Trafficking of lipid-modified proteins to specialised membrane domains

Yasmin ElMaghloob, MSc

Submitted in fulfilment of the requirements for the Degree of Doctor of Philosophy

Supervised by Dr Shehab Ismail

Institute of Cancer Sciences
College of Medical, Veterinary and Life Sciences
University of Glasgow

September 2019

Abstract

Protein localisation is an important determinant of its function; trafficking mechanisms which bring about this localisation regulate signalling. These are crucial in functional membrane domains which remain continuous with the rest of the bilayer yet retain a distinct composition. This thesis presents my work as part of our investigation into the trafficking of lipid-modified proteins to two of these domains. These are the immune synapse, which is formed at the interface of immune cells with their targets, and the primary cilium, which is a cell surface microtubule-based sensory organelle. Using biochemical, structural, and imaging approaches, we study the trafficking of lipid-modified proteins to these domains. First, we attempt to answer the question of how the lymphocyte-specific kinase (LCK) is targeted to the $CD4^+$ T cell synapse and then retained in the domain, a process which remains not fully understood. In the second part of the thesis, we demonstrate the clinical relevance of ciliary lipid-associated cargo trafficking and the underlying biochemical pathology due to a novel Joubert syndrome patient mutation.

Although synapse-forming lymphocytes do not have primary cilia, the two membrane domains have been shown to share structural and functional similarities. We show that the LCK trafficking to the immune synapse involves GDI-like solubilising factor (GSF)-mediated transport, which has been previously described in the primary cilium. The GSF UNC119A facilitates LCK extraction from the membranes into the cytoplasm. LCK release occurs specifically at the synapse under the action of the G protein ARL3 and the regulation of the synapse-localised ARL13B. Retention is mediated by phosphoregulation of the LCK-UNC119A interaction. A very similar system operates in the cilium, and therefore it is another shared feature between cilia and synapses. Furthermore, we show that a novel ARL3 mutation identified by our collaborators interferes with GSF-mediated trafficking and disrupts maintenance of ciliary composition. Finally, I present my preliminary investigations into using GSF-mediated trafficking via PDEδ to manipulate Hedgehog signalling in the primary cilium.

The flexibility of GSF-mediated trafficking results in efficient cellular transportation, as well as far-reaching consequences in case of its impairment. Our work provides insights into potential avenues of manipulating signalling pathways through affecting the underlying transport.

Table of Contents

List of Tables

List of Figures

Acknowledgements

I would like to thank Shehab Ismail for giving me the chance to join the lab and being a hugely positive part of this four year journey. Through marathon protein purifications and multi-figure whiteboard discussions, I have learned a great deal on many different levels, for which I am entirely grateful.

I am very lucky to be a part of R03, and I would like to thank its members, past and present: Michael McIlwraith and Louise Stephen, who patiently helped me through endless questions in my first days (questions which continued, but hopefully decreased with the passage of time). It is very important to have a solid foundation in the learning of new skills, and with respect to protein purification and cell culture and many other aspects, Mike and Louise were instrumental. Esther Garcia-Gonzalez, who has also been the patient recipient of many questions, on microscopes and chocolates and everything in between. Tamas Yelland, the other half of the much-maligned "fun side of the lab", who has helped me greatly with protein crystallography. Youhani Samarakoon, the best student, horror film, and post-6 pm lab buddy anyone can ask for.

I would like to thank CRUK for the generous funding. The Beatson Institute central services are an immense help every single day.

The past four years have not been easy, but I know that they have been made easier by several orders of magnitude thanks to my friends at the Beatson Institute and beyond. They are, thankfully, too many to fully name here, but I would like to express my gratitude to Frances and Gary Sibbet, who have been the most generous, kind, and admirable friends; to Patricia Castro Sanchez, who is the best in the world, the Egyptians in Glasgow, who are the most reliable source of good cheer and conversation (and ice cream!), and to my GUC friends, Mirna and Sofana, whom I am lucky to have.

My family is my bedrock. No words are sufficient to express gratitude to my parents, who have supported me in all things, and who I hope to have made proud. My brothers are a terrific force of nature, in all senses of the word, and I am very glad they are mine.

Author’s Declaration

I declare that this dissertation is the result of my own work, except where stated otherwise. This thesis does not include work that has been submitted for consideration for another degree at the University of Glasgow or any other institution.

Yasmin ElMaghloob

Abbreviations

°C	Degrees Celsius
Å	Ångström
AC	Adenylyl cyclase
Ag	Antigen
APC	Antigen-presenting cell
ARF	ADP ribosylation factor
ARL	ADP-ribosylation factor(ARF)-like
ATP	Adenosine triphosphate
BBSome	Bardet-Biedl Syndrome proteins
BLAST	Basic local alignment search tool
bp	Base pair
c/p/dSMAC	Central/peripheral/distal supramolecular activation cluster
CaM	Calmodulin
CBP	CSK-binding protein
CD	Cluster of differentiation
CDC42	Cell division control protein 42
CMAC	7-amino-4-chloromethylcoumarin
CoA	Coenzyme A
Cr	*Chlamydomonas reinhardtii*
CSK	C-terminal SRC-specific kinase
CTL	Cytotoxic T lymphocytes
CTLA4	Cytotoxic T lymphocyte antigen 4
CTS	Ciliary targeting sequence
DCs	Dendritic cells
DLG	Disc large
DTT	Dithiothreitol
DZ	Deltazinone
EB1	End-binding protein 1
F/R primers	Forward/reverse primers
F-actin	Filamentous actin
FBS	Fetal bovine serum
FCS	Forward scatter
FL	Full-length
FL	Full-length
FMNL1	Formin-like protein 1
FP	Fluorescence polarisation
FTase	Farnesyl transferase
GANT	GLI antagonist
GAP	GTPase-activating protein
GDF	GDI-like displacement factor
GDI	GDP-dissociation inhibitor
GEF	Guanine nucleotide exchange factor
Ger	Geranyl
GFP	Green fluorescent protein
GGTase	Geranylgeranyl transferase
GLI	Glioma-associated proteins

GLIA/R	GLI activator/repressor
GNAT1	Transducin-α
GPI	Glycophosphatidylinositol
GPR161	G protein coupled receptor 161
GSF	GDI-like solubilising factor
GSH	Glutathione
GST	Glutathione S-transferase
GTP/GDP	Guanosine tri/diphosphate
GUCA1C	Guanylyl cyclase-activating protein 3
Gαs	Alpha subunit of the stimulatory G protein
HH	Hedgehog
HPLC	High-performance liquid chromatography
hr	hour
HRAS	Harvey rat sarcoma
Hs	*Homo sapiens*
ICAM-1	Intracellular adhesion molecule-1
ICL	Idiopathic CD4 lymphopenia
ICMT	Isoprenylcysteine carboxymethyltransferase
IFT	Intraflagellar transport
INPP5E	Inositol polyphosphate-5-phosphatase E
IPTG	Isopropyl ß-D-1-thiogalactopyranoside
ITAMs	Immunoreceptor tyrosine-based activation motifs
JBTS	Joubert syndrome
kb	Kilobase pair
kDa	Kilodaltons
KIF17	Kinesin family member 17
KRAS	Kirsten rat sarcoma
LAT	Linker for the activation of T cells
LB	Lysogeny broth
LCK	Lymphocyte-specific protein tyrosine kinase
LFA-1	Integrin lymphocyte function associated-1
LR	Localisation ratio
MAL	Myelin and lymphocyte protein
mantGDP	2'/3'-O-(N-methyl-anthraniloyl)-guanosine-5'-diphosphate
MARCKS	Myristoylated alanine-rich C kinase substrate
MBOAT	Membrane-bound O-acyl-transferases
mCh	mCherry
MDCK	Madin-Darby canine kidney cells
MHC	Major histocompatibility complex
min	Minute
Mm	*Mus musculus*
MTOC	Microtubule-organising centre
MW	Molecular weight
Myr	Myristoyl
NK cells	Natural killer cells
NMT	N-myristoyltransferase
NPHP3	Nephrocystin 3
NRAS	Neuroblastoma rat sarcoma

PAG1	Phosphoprotein associated with glycosphingolipid-enriched microdomains 1
Pam	Palmitoyl
PAR	Partition defective
PAT	Palmitoyl acyl transferase
PBS	Phosphate-buffered saline
PCR	Polymerase chain reaction
PDB	Protein database
PDEδ	Phosphodiesterase 6 subunit δ
PI(4)P	Phosphatidylinositol 4-phosphate
$PI(4,5)P_2$	Phosphatidylinositol 4,5-biphosphate
PKA	Protein kinase A
PKC	protein kinase C
PKD	Polycystic kidney disease
PLCγ1	Phospholipase C γ1
PM	Plasma membrane
PTCH1	Patched 1
R110	Rhodamine 110
RAB	Rat sarcoma-related protein in brain
RAC1	Ras-related C3 botulinum toxin substrate 1
RAN	RAS-related nuclear protein
RAS	Rat sarcoma protein
RE	Restriction digestion
RHO	RAS homologous protein
RHOGDI	RHO GDP-dissociation inhibitor
RP2	Retinitis pigmentosa protein 2
RT	Reverse transcriptase
s	Second
SAG	Smoothened agonist
SCRB	Scribble
SDM	Site-directed mutagenesis
SDS-PAGE	Sodium dodecyl sulphate - polyacrylamide gel electrophoresis
SEE	Staphylococcal enterotoxin E
SFK	SRC family kinase
SH	SRC homology
SHP1	SH2-containing phosphatase 1
SLP76	SH2 domain–containing leukocyte protein of 76 kDa
SMO	Smoothened
SRCIN1	SRC kinase signalling inhibitor 1
SSC	Side scatter
SSTR3	Somatostatin receptor 3
SUFU	Suppressor of Fused
TBAB	Tetra-n-butylammonium bromide
TCR	T cell receptor
TULP3	Tubby-like protein 3
UNC119	Uncoordinated-119
WT	Wild-type
ZAP70	TCR zeta chain-associated protein kinase of 70 kDa
ß-ME	ß-mercaptoethanol

Chapter 1 Introduction

At the molecular level, the vast intricacies of cellular signalling are held up by a delicate balance of a wide array of proteins and other signalling molecules being in the right place at the right time. Understanding how this is achieved is critical for precise targeting of these pathways as a therapeutic avenue in disease. In some cases, the right place is a defined cellular compartment that is separated by membranes from the rest of the cell, such as in the case of mitochondria. In others, however, it is harder to define and delineate.

1.1 Functional membrane domains

Our understanding of the cell membrane has evolved from the fluid mosaic model of a viscous fluid-like structure in which proteins can laterally diffuse resulting in their random distribution in the membrane as shown in **Figure 1-1A** (Singer and Nicolson, 1972). Diffusion rate constants of various lipids and proteins have been found to differ greatly when measured in artificial bilayers as compared to similar biological membranes, which showed much slower rates. This indicates that free diffusion in the bilayer is not the sole governor of the movement of proteins and lipids in biological membranes (Kusumi et al., 2005). As a result, the membrane exhibits lateral heterogeneity, consisting of different subdomains of distinct protein and lipid compositions. Membrane domains vary in size, from nanoscale domains comprising a few proteins clusters, such as those formed by activated rat sarcoma (RAS) proteins in the membrane, all the way up to microscale domains (Trimble and Grinstein, 2015, Murakoshi et al., 2004). Examples of the latter domains include the immune synapse, which is the interface formed between immune cells and their targets (Paul and Seder, 1994), and the primary cilium, which is a microtubule-based structure on the surface of many cell types that acts as a hub of signal detection and transduction (Singla and Reiter, 2006). These membrane domains of immune synapses and primary cilia will be discussed in further detail in later chapters as they are the focus of this thesis.

Through the formation of membrane domains, signalling molecules arrive at the "right place" to participate in signal transduction. These domains act as

functional nodes with distinct signalling pathways that can be regulated and fine-tuned by adjusting the composition of the domain. This segregation of signalling molecules allows their efficient participation in cellular signalling pathways taking place in what would otherwise be the open compartment of the cell membrane. The advantages of compartmentalisation also include the increased local concentration of signalling molecules which results in rapid activation compared to that obtained with random diffusion (Bray, 1998). In addition, unintended inhibition of signal transduction is avoided via the exclusion of molecules with opposing activities within membrane domains, such as in the case of kinases and phosphatases in T cells (Dustin and Groves, 2012).

The formation and maintenance of membrane domains depends on preferential recruitment and/or exclusion of molecules, as well as the restriction of their movement within the domain by the so-called diffusion barriers.

1.1.1 Active processes driving membrane domain formation

Increasing the concentration of a protein at a specific locus, or the removal of the same protein from regions surrounding the same locus, will result in the formation of a concentration gradient of that protein. Examples of opposing processes bringing about the formation of localised concentrations in the membrane are shown in **Figure 1-1B**.

Among these is the separation of enzymes catalysing the synthesis and degradation of a certain protein. The aforementioned exclusion of phosphatases in T cell areas of contact with target cells is accompanied by recruitment of kinases. This results in regions of high levels of protein phosphorylation in the cell membrane at the synapse (Davis and van der Merwe, 2006). Various interactions between membrane proteins and lipids can result in preferential recruitment or exclusion due to attraction or repulsion, respectively. Phosphatases with bulky extracellular domains in the T cell membrane have been reported to be excluded from areas of T cell contact with target cells due to steric hindrances. The separation of kinases and phosphatases is the basis for the "kinetic segregation" model of the triggering of TCR signalling (van der Merwe et al., 2000). This particular example of the immune synapse shows how multiple processes working in concert can affect the composition of the same membrane domain.

Local protein concentrations within membrane domains can also be generated by localised exocytosis of a protein to the cell membrane in an area surrounded by regions where that same protein is removed by endocytosis. The formation of primary cilia is dependent on exocytosis of ciliary vesicles that dock to the mother centriole at the base of the cilium. Following fusion with the cell membrane, these vesicles form the ciliary membrane (Sorokin, 1962). Following the formation of the cilia, targeting of some membrane proteins destined for the cilia has been proposed to take place via the exocytosis of vesicles from the Golgi to the base of the cilium in a process mediated by the GTPase rat sarcoma-related protein in brain 8 (RAB8) (Nachury et al., 2007). In addition, the ciliary pocket surrounding the base of the primary cilium has been reported in some cell types to have clathrin-coated pits which are actively involved in endocytosis (Molla-Herman et al., 2010). Focused endocytosis and exocytosis at the T cell interface with target cells, which is termed the immune synapse, has also been reported as a mechanism by which T cells fine-tune the level of TCRs in the synapse (Patino-Lopez et al., 2008).

Electrostatic interactions between membrane phospholipids and transmembrane or membrane-associated proteins can occur in proteins recruited to or repelled by the membrane domain. Regions of negative charge as imparted by phospholipids in the cell membrane are more likely to attract proteins with positively charged domains. An example of such interactions is the C-terminal domain of tubby proteins which has a positively-charged cavity that preferentially binds to the doubly phosphorylated membrane phospholipids phosphatidylinositol 4,5-bisphosphate ($PI(4,5)P_2$) (Santagata et al., 2001).

Lipid modification of proteins is another method by which they can be targeted to cellular membranes. Depending on the type of linkage and the lipid group added, these modifications may or may not be reversible, and they impart different affinities to the membrane. In addition, they act in concert with other hydrophobic or electrostatic interactions formed by the protein to impart specificity to the membrane binding (Peitzsch and McLaughlin, 1993, Hancock et al., 1990). The transport of lipid-modified proteins in the aqueous environment of the cytoplasm requires the masking of the hydrophobic lipid group. This can be achieved by transporter proteins with hydrophobic pockets that can bind the lipid groups, such as GDP-dissociation inhibitor (GDI) and GDI-like proteins,

which will be discussed in further detail in later sections. The specificity of these transporters and the mechanisms by which lipid-modified cargo are released from the transporter complexes help fine-tune the targeting of these proteins to the target membrane domains.

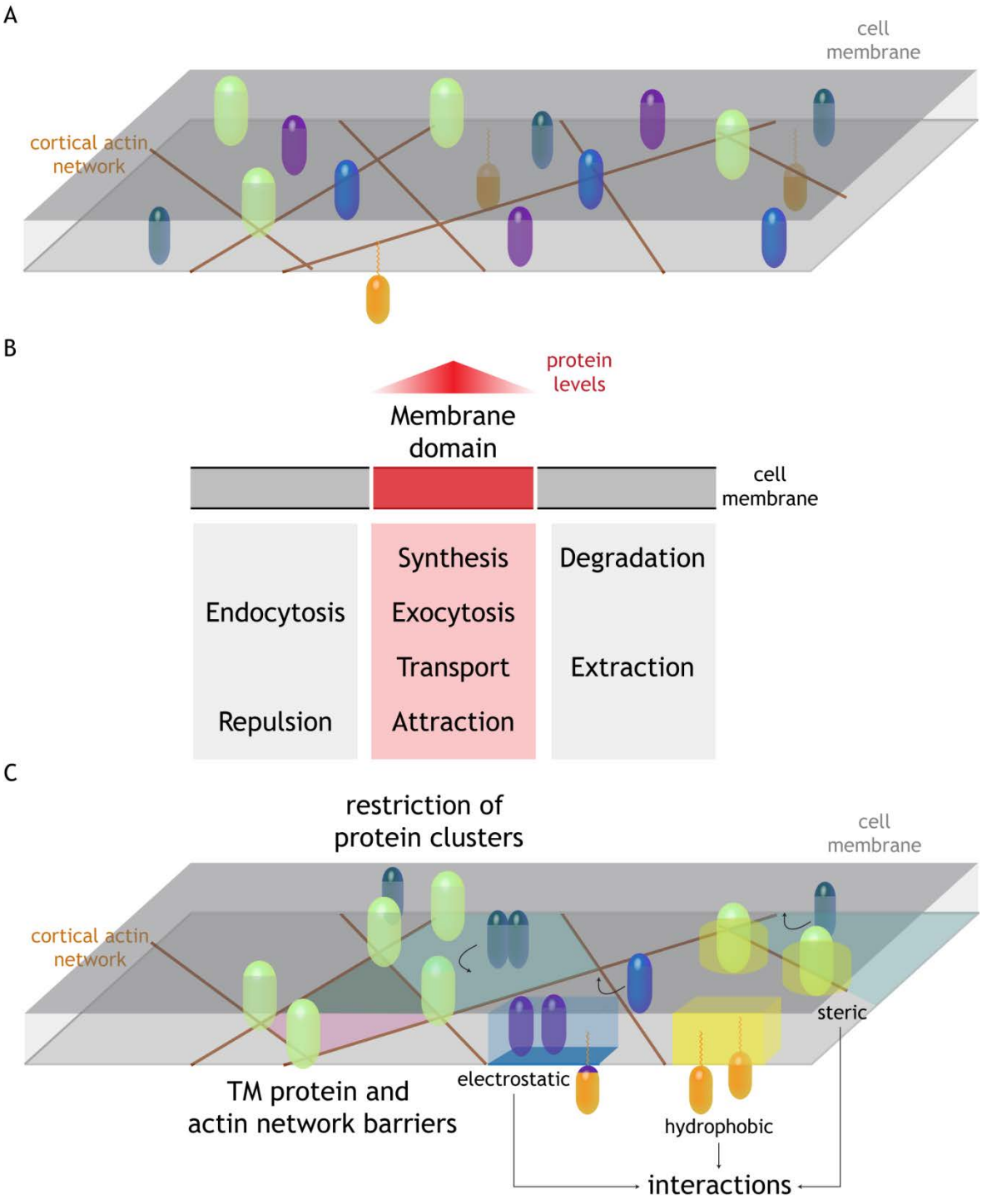

Figure 1-1 The cell membrane displays lateral inhomogeneity, with subdomains having distinct compositions.

(A) The cell membrane, as first proposed by the fluid mosaic model, is composed of a phospholipid bilayer matrix in which proteins embedded in or associated with the membrane can freely diffuse, resulting in their random arrangement. **(B)** Concentration gradients of proteins

present in membrane domains can be generated via processes that increase the localisation of the protein within the domain (red), or decrease its levels in regions surrounding the domain (grey), or both. **(C)** Diffusion barriers restrict the movement of molecules in the membrane (black arrows) and help maintain their local concentrations in the various subdomains. These include electrostatic, hydrophobic, and steric interactions between transmembrane proteins, lipids and membrane-associated protein. In addition, the cortical actin network restricts the movement of transmembrane proteins; together, they divide the membrane into regions between which diffusion of molecules is restricted. Clustering of proteins in the membrane makes them more likely to undergo steric hindrances, and therefore restricts their movement in the membrane.

1.1.2 Diffusion barriers in the membrane

The formation and maintenance of the distinct compositions of membrane domains is also aided by the presence of diffusion barriers. These oppose isotropic diffusion in the membrane, which would otherwise result in the abolishment of concentration gradients.

The reduction of diffusion rates of lipids and proteins in the membrane is attributed to the presence of structures or processes that oppose their free diffusion in the membrane. These are termed diffusion barriers and though they are not fully understood, they appear to exist in different forms in various domains and membranes. These barriers also vary in the duration of their presence in the membrane; some barriers form transiently to bound short-term domains, while others have longer half-lives. Examples of diffusion barriers in the membrane are shown in **Figure 1-1C**.

Restriction of molecule diffusion in the membrane can be due to the presence of physical obstacles that prevent or slow down the free movement of particles. Potential candidates include membrane proteins, the extracellular matrix, and the cytoskeletal network underlying the plasma membrane.

High resolution single particle tracking of an unsaturated phospholipid on the surface of rat kidney fibroblasts showed that it underwent two types of movement. Diffusion that was similar in rate to that observed in artificial settings was observed, but only within specific compartments. Localised fast diffusion within a compartment was followed by movement to an adjacent compartment, where localised diffusion took place again, in a process that was

called hop diffusion. These compartments were in the 200 nm diameter range, and they were found to be dependent on the presence of the actin cytoskeleton. A network of barriers is therefore formed by membrane proteins that are held in place by the underlying actin mesh, together forming the anchored-protein picket fence. The immobilised proteins oppose molecule diffusion both through direct collision with molecules and forming a zone of higher friction in the phospholipid bilayer. These hindrances restrict movement between compartments, resulting in the observed "hops" occurring less frequently across the barriers, or during the reorganisation of the dynamic network (Fujiwara et al., 2002). Restriction of diffusion becomes more likely with the formation of protein clusters in the membrane, trapping them within the compartments (Kusumi et al., 2005).

Electrostatic interactions described in the previous section can also act as diffusion barriers, curtailing the movement of charged molecules by attraction or repulsion depending on the charge. A good example is the membrane-associated protein known as myristoylated alanine-rich C kinase substrate (MARCKS). MARCKS associates to the membrane through its lipid myristoyl moiety and a stretch of positively charged lysine residues that bind to the negatively charged membrane. Phosphorylation of three serine residues by protein kinase C (PKC) in the polybasic stretch results in weakening of its electrostatic interaction with the membrane, and hence its release into the cytoplasm (Thelen et al., 1991). Interaction of the MARCKS basic domain with calcium/calmodulin (Ca^{2+}/CaM) results in reversal of its charge, thereby also releasing MARCKS to the cytoplasm due to repulsion with membrane (Kim et al., 1994). Furthermore, MARCKS itself has been shown to sequester the negatively charged $PI(4,5)P_2$ molecules in the membrane (Gambhir et al., 2004). The barrier that the localisation of MARCKS presents to the free diffusion of PIP_2 can be therefore counteracted by either PKC-catalysed phosphorylation or an increase in local Ca^{2+} concentration.

Through targeting of molecules whose diffusion is restricted in the membrane, concentration gradients in membrane domains are generated and maintained. Molecules are therefore segregated, which leads to a range of signalling pathways being triggered and regulated within domains in the dynamic cell membrane. A major route of targeting to the membrane is through lipid

modification of proteins. The transport of some of these proteins in the cytoplasm is facilitated by solubilising factors that mask the lipid moiety to allow transit (Ismail, 2017). This work focuses on the solubilising factor-mediated trafficking of lipid-modified proteins to the target membrane domains of the immune synapse and the primary cilia. Despite occurring on different cell types, several similarities have been reported for these two domains, which are described in the next section.

1.1.3 Primary cilia and immune synapses

As previously mentioned, the primary cilium is present on the surface of most cells which receives and transduces a myriad of extracellular signals. Lymphocytes are one of the few cell types to lack primary cilia; however, the observation that both immune synapses and primary cilia involve centrosomal membrane docking at the point of formation identified a distinct structural similarity between the two domains (Stinchcombe et al., 2006). Additional parallels reported include the polarisation of organelles, secretory granules, and cytoskeletal elements to the docked centrosome. Both membrane domains are sites of focused endocytosis and exocytosis guided by the docked centrosome (Griffiths et al., 2010). Furthermore, several ciliary intraflagellar transport (IFT) components have been reported to play a role in the delivery of recycled TCRs to the synapse through an endosomal route (Finetti et al., 2009). More recently, the membrane phosphoinositide composition in both domains exhibits localised depletion of bi- and tri-phosphorylated phosphoinositides (PI(4,5)P_2, and PI(3,4,5)P_3, respectively) (Gawden-Bone et al., 2018, Chávez et al., 2015).

1.2 Lipid modifications of proteins

Lipid-modified proteins comprise a widespread part of the proteome with significant functional implications. Through the addition of one or more lipophilic moieties to a protein during and/or after the translation process, cells can change the physicochemical properties of a protein. As a result, the localisation, activity, stability, and interactions of a polypeptide chain can be manipulated by the cell to perform and adapt to a range of functions and situations (Hentschel et al., 2016). **Figure 1-2** shows the general structure of

some of these modifications, and an overview of their properties is summarised in **Table 1-1**.

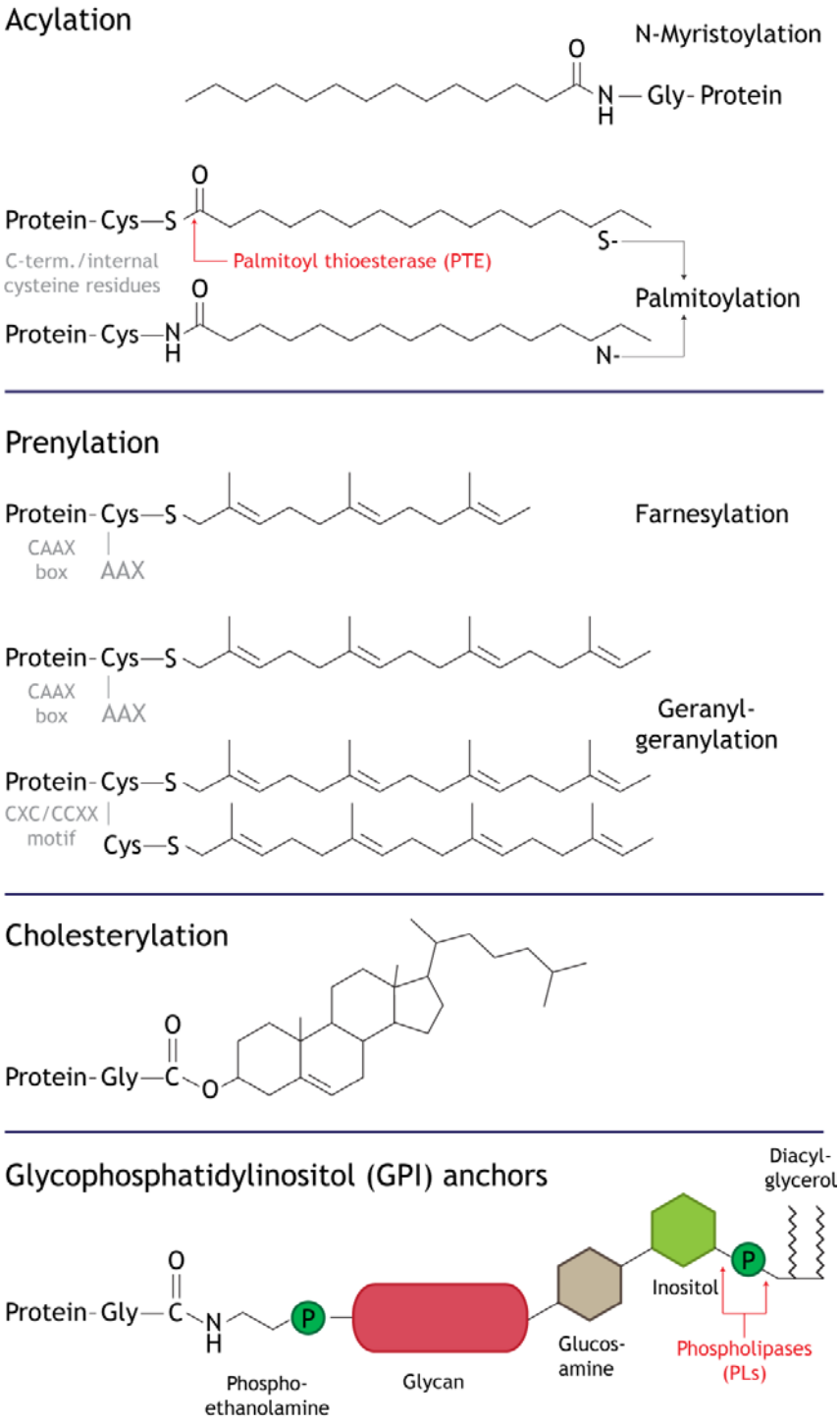

Figure 1-2 Protein lipid modifications.

The general structure of each lipid modification, and the linkage formed with the modified protein is shown. While N-myristoylation is restricted to N-terminal glycine, palmitoylation can occur at an internal cysteine residue. Prenylation occurs at cysteine residues present in a C-terminal CAAX motif. Some geranylgeranylated proteins, such as RAB, have two cysteines in CXC or CCXX motifs, in which case both cysteine residues are modified. Indicated in red are the enzymes which remove S-palmitoyl groups and GPI anchors. A scheme of the general structure showing the main components of GPI anchors is shown.

Table 1-1 Common lipid modifications of proteins.

Modification	Moiety	Enzyme(s)	Reversible?	Plasma membrane localisation	Example
Acylation					
•Myristoylation	N-terminal glycine → 14-carbon saturated myristate fatty acid	N-myristoyl transferase (NMT)	No (amide linkage)	Cytoplasmic leaflet	Lymphocyte-specific kinase (LCK) (Caron et al., 1992)
•Palmitoylation	Cysteine → 16-carbon saturated palmitate fatty acid	Palmitoyl acyl transferases (PATs) Membrane-bound O-acyl-transferases (MBOATs)	S-palmitoyl: Yes (thio-esterases) N-palmitoyl: No (amide linkage)	Cytoplasmic leaflet and transmembrane	LCK (Paige et al., 1993) Hedgehog (HH) (Pepinsky et al., 1998)
Prenylation					
•Farnesylation	Cysteine in C-terminal CAAX box → 15-carbon isoprenoid group	- Farnesyl transferase (FTase) - CAAX prenyl protease - Isoprenyl-cysteine carboxymethyl-transferase (ICMT)	No (thioether linkage)	Cytoplasmic leaflet	Kirsten rat sarcoma (KRAS) (Hancock et al., 1989)
•Geranyl-geranylation	Cysteine in C-terminal CAAX box or CxC/CC-containing proteins → 20-carbon isoprenoid group(s)	- Geranyl-geranyl transferase (GGTase) - CAAX prenyl protease - Isoprenyl-cysteine carboxymethyl-transferase (ICMT)	No (thioether linkage)	Cytoplasmic leaflet	RAS homologous protein (RHO) (Yoshida et al., 1991) Rat sarcoma-related protein in brain (RAB) (Farnsworth et al., 1991)
Cholesterylation	Glycine at cleavage site → 27-carbon sterol	N/A (reaction initiated by autoproteolysis of Hedgehog at Gly-Cys-Phe site)	No (ester linkage)	Exoplasmic leaflet	Hedgehog (HH) (Porter et al., 1996)
Glycophosphatidyl-inositol (GPI) anchors	C-terminal glycine → GPI glycolipids	Multiple (GPI transamidase complex)	Yes (phospho-lipases)	Exoplasmic leaflet	Alkaline phosphatase (Low et al., 1986)

1.2.1 Regulation of membrane binding of lipid-modified proteins

The most obvious effect of the addition of a lipophilic moiety to a protein is allowing its direct anchoring to membranes in the cell. However, this localisation is dynamic and undergoes regulation through various mechanisms. As shown in **Table 1-1**, the attachment of lipid groups is generally irreversible, with few exceptions. The dynamic nature of the association of these modified proteins to the membrane seems contradictory to the permanence of the lipid modification. However, this was explained by the discovery that a second binding signal is required for stabilisation of the membrane interaction of myristoylated proteins (Peitzsch and McLaughlin, 1993). This second signal could be in the form of a reversible lipid modification **(Figure 1-3A)**. Alternatively, electrostatic interactions with other domains of the protein can regulate the interaction between the lipid group and the membrane, thereby switching it on and off **(Figure 1-3B)**.

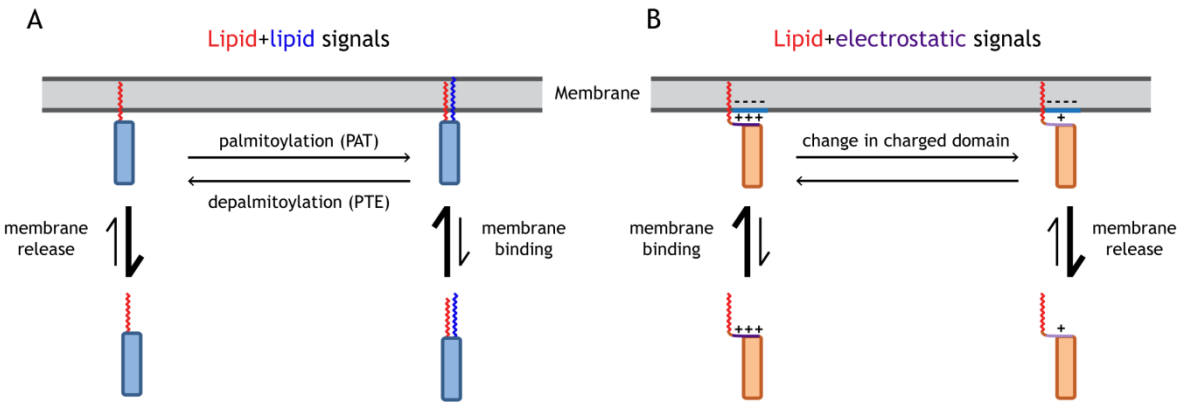

Figure 1-3 Two signal hypothesis of membrane binding of lipid-modified proteins.

Reversible membrane association of proteins with permanent lipid modifications is facilitated by the inability of the lipid group to maintain the association on its own. A second signal is required for membrane binding, which imparts reversibility to the binding. **(A)** The addition of a palmitoyl group to a lipid-modified protein results in the formation of sufficient hydrophobic interactions to stabilise membrane binding. Enzymatic removal of the palmitoyl group reverses the binding. Palmitoylation can therefore help retain lipid-modified proteins at the membrane. **(B)** Electrostatic interactions between phospholipids and charged domains in the protein can act as a second signal, which can be removed by reducing or reversing the charge.

Some SRC family kinases (SFKs), such as the lymphocyte-specific kinase (LCK), undergo post-translational palmitoylation of conserved N-terminal cysteine residues following co-translational myristoylation (Paige et al., 1993).

Palmitoylation of myristoylated proteins upon their arrival at the membrane has been proposed to result in increasing their residence at the membrane, according to the bilayer trapping hypothesis **(Figure 1-3A)**. The interaction of the membrane with both groups counteracts the transient nature of the interaction with each group on its own. Depalmitoylation of the protein would subsequently result in its release from the membrane (Shahinian and Silvius, 1995). This step-wise acylation has been shown to result in fast transport to the membrane followed by retention. In contrast, doubly-palmitoylated proteins exhibit slow membrane binding (van't Hof and Resh, 1997). Palmitoylation has also been shown to affect protein activity independent of its membrane localisation (Osterhout et al., 2003).

In addition, the availability of the myristoyl group itself for membrane interaction can be regulated by various myristoyl switches. Membrane binding of the aforementioned MARCKS protein **(Section 1.1.2)** can be reversed by reducing the charge of the polybasic stretch, as in the case of phosphorylation or the binding of Ca^{2+}/CaM. The weakening of the electrostatic interaction renders the myristoyl unable to stabilise the membrane interaction of the protein; this known as a myristoyl-electrostatic switch **(Figure 1-4A)**. **Figure 1-4B** shows two cases where the myristoyl moiety becomes sequestered within the protein itself. The conformational change of the myristoyl moiety due to ligand binding occurs in myristoyl-ligand switches, as in the case of the ADP ribosylation factor (ARF) protein ARF-1. GTP binding of ARF-1 results in displacement of the myristoylated N-terminus from a surface hydrophobic groove, which otherwise shields against membrane binding (Amor et al., 1994). Alternatively, the masking of the myristoyl group can be due to proteolysis of the protein to form a cleaved protein that sequesters the lipid group (Hermida-Matsumoto and Resh, 1999).

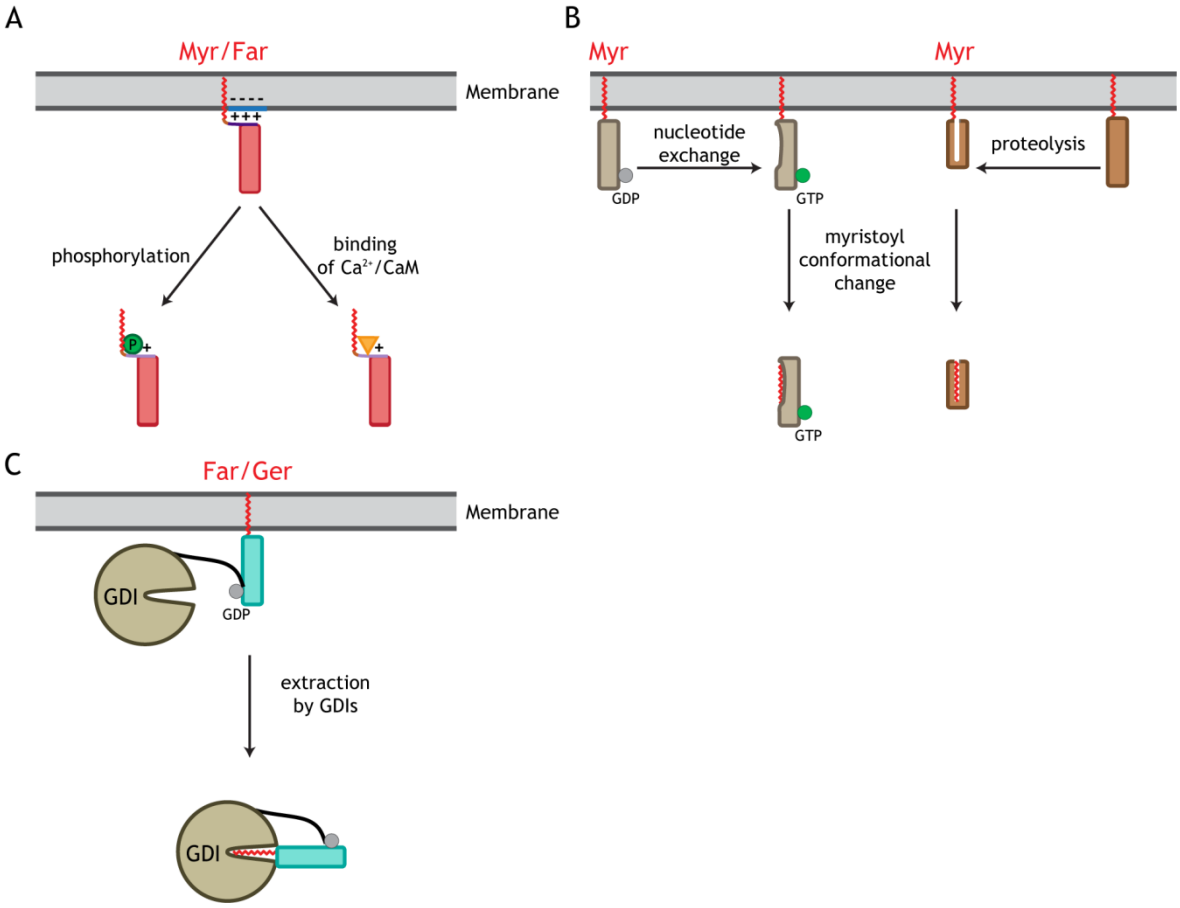

Figure 1-4 Lipid-modified proteins can associate with the membrane in a reversible manner.

(A) Reducing or reversing the positive charge of a polybasic stretch in the protein weakens the electrostatic interaction formed with the membrane, resulting in dissociation of the protein. Both myristoylated and farnesylated proteins have been shown to exhibit this type of electrostatic switch. **(B)** The myristoyl moiety may become unavailable for membrane binding due to sequestration within the protein itself, resulting in release. The protein can undergo a conformational change due to nucleotide binding or proteolysis, whereby a hydrophobic pocket in the protein accommodates the lipid group. **(C)** GDP-dissociation inhibitors (GDIs) can extract prenylated proteins from the membrane by sequestering the lipid moiety within a hydrophobic pocket, thereby forming a soluble complex. CaM, calmodulin; Myr, myristoyl; Far, farnesyl; Ger, geranylgeranyl; GDI, GDP-dissociation inhibitor.

Farnesylated RAS proteins have also been shown to require a second signal for membrane binding, where KRAS has a poly-lysine stretch **(Figure 1-4A)**, while Harvey and neuroblastoma RAS proteins (HRAS and NRAS, respectively) undergo palmitoylation of cysteine residues in their C-termini (Hancock et al., 1989, Hancock et al., 1990). Geranylgeranylated proteins, such as those of the RHO family, can anchor to the membrane via the geranylgeranyl group alone, as the lipid moiety is sufficiently hydrophobic for stable membrane association (Resh,

2013). However, this membrane binding can still be reversed through the action of GDP-dissociation inhibitor (GDI) proteins. GDIs, as shown in **Figure 1-4C**, associate with the prenyl moiety of the protein, and form a soluble complex that moves into the cytoplasm (Araki et al., 1990).

GDI and GDI-like proteins also facilitate the reversible membrane binding of lipid-modified proteins in the absence of switches which modulate the exposure of the lipid group. These proteins can interact with the lipid group and mask it from the aqueous surroundings, thereby facilitating the transport of lipid-modified proteins in the cytoplasm, playing a vital role in the trafficking to and from membrane domains.

1.3 GDI and GDI-like solubilising factors

1.3.1 GDP-dissociation inhibitors

As the name suggests, GDIs were first identified as binding partners of small GTPases whose binding opposed the dissociation of GDP (Fukumoto et al., 1990, Sasaki et al., 1990). GDIs are specific to either RAB or RHO GTPases, which belong to the RAS superfamily of proteins and are involved in a wide range of cellular processes. GDIs are a fine example of the efficient economy of proteins in the cell. In humans, only two RABGDI (-α and –ß) and three RHOGDI (-1 through -3) isoforms are expressed. However, they are capable of binding all of over 60 RAB GTPases and 20 RHO GTPases, respectively. RAB and RHO GTPases can associate with cellular membranes through prenyl groups present in their C-termini, as mentioned in **Table 1-1**.

As shown in **Figure 1-5**, these small GTPases function as molecular switches, cycling between an active, GTP-bound state and an inactive GDP-bound state, formed by GTP hydrolysis. Nucleotide exchange results in the conformational change of the switch regions of the protein, resulting in different interactions with downstream effectors. Activation of GTPases involves the release of GDP, a slow process that is catalysed by guanine nucleotide exchange factors (GEFs). GEFs also stabilise the nucleotide-free GTPase, allowing the binding of GTP that is present in excess in the cell compared to GDP. Conversely, GTPase-activating proteins (GAPs) enhance the intrinsic GTPase activity of the G protein, thereby

switching off its activity. Binding of GDIs therefore results in the stabilisation of the inactive form of these GTPases (Bos et al., 2007).

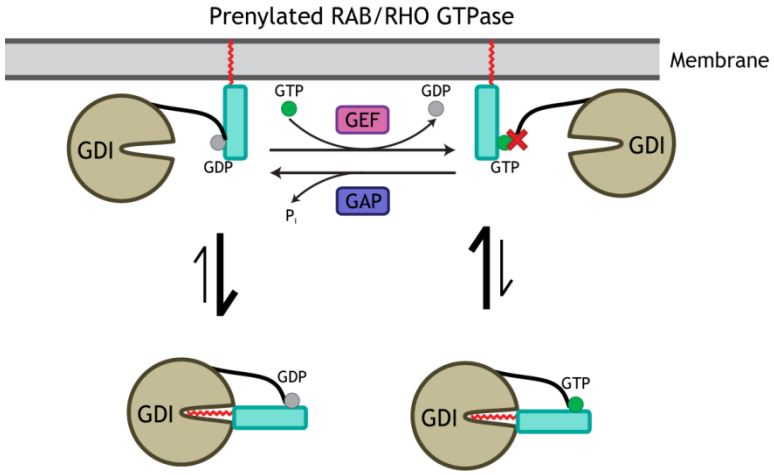

Figure 1-5 GDIs bind to GTPases in a nucleotide-dependent manner.

Prenylated RAB and RHO GTPases exist in two forms dependent on their nucleotide state. GDIs have a higher affinity to the GDP-bound form, and are able to extract it from the membrane by masking the lipid group within a hydrophobic pocket. The localisation of the GEF at the target membrane therefore traps the GTPase by opposing GDI-mediated extraction. GDI, GDP-dissociation inhibitor; guanosine nucleotide exchange factor; GAP, GTPase-activating factor.

In addition to inhibition of GDP dissociation, the binding of RHOGDI1 to cell division control protein 42 (CDC42) was also found to result in the extraction of the prenylated membrane-bound cognate RHO protein, CDC42. This results in a cytosolic pool of soluble CDC42 in complex with RHOGDI1 (Leonard et al., 1992). This extraction is facilitated by the binding of the hydrophobic pocket of GDI to the C-terminal lipid group of the GTPase. This prenyl-binding pocket is a barrel-like structure comprising nine ß-strands arranged in two sheets, which is known as an immunoglobulin-like ß-sandwich fold. In addition, an N-terminal domain of GDI interacts with the switch regions of the GTPase. This interaction has been shown in RABGDIs to be regulated by the nucleotide state of the extracted RAB GTPases, with a much higher affinity to the GDP-bound form compared to the GTP-bound counterpart (Wu et al., 2010). A similar nucleotide-dependent mode of interaction has been reported for the binding of RHOGDI with RHOA and Ras-related C3 botulinum toxin substrate 1 (RAC1) (Sasaki et al., 1993).

The majority of RHO GTPases are localised in the cytoplasm, which is only possible due to the solubilisation of the prenyl group by RHOGDIs (Boulter et al.,

2010). The masking of the prenyl group in the cytoplasm also protects the protein from degradation. It is this chaperone function of GDIs that allows the rapid cycling of prenylated RAB and RHO GTPases between different target membranes and the cytoplasm. This, in turn, facilitates correct membrane targeting and hence normal function of the proteins in the cell.

The relative scarcity of different isoforms of GDIs compared to the number RAB and RHO GTPases seems incompatible with the precise targeting of each of these GTPases to various target membrane domains in the cell. How do these few GDIs sort their cargo to various cellular destinations? The presence of GDI displacement factors (GDFs) has been suggested as a possible answer, whereby specific GDFs localised at the target membrane interact with the GDI-GTPase complex and specifically release the targeted RHO or RAB GTPase (Garcia-Mata et al., 2011, Collins, 2003). However, it remains unclear how the currently identified potential GDFs would be able to specifically target individual GTPases for release from the general pool of GTPase-GDI complexes (Blümer et al., 2013). Recently, it has been shown that the localisation of these RAB GTPases is actually dependent on that of their GEFs. This is not due to active release of the RAB GTPase from the complex that is facilitated by the GEF, but rather due to the formation of the GTP-bound form of the RAB proteins, to which GDIs have a much lower affinity (Schoebel et al., 2009). As a result, the GTPases are retained at the target membrane until hydrolysis of the GTP and the formation of the inactive protein, which can then be extracted again by the GDI **(Figure 1-5)**.

1.3.2 GDI-like solubilising factors

The ß-sandwich fold-based hydrophobic pocket of GDIs is also present in proteins of the evolutionarily conserved unccordinated-119 (UNC119) supergene family. This group comprises the phosphodiesterase 6 subunit δ (PDEδ) and the uncoordinated paralogues UNC119A and UNC119B (Zhang et al., 2012, Constantine et al., 2012). Consequently, they act as chaperones for lipid-modified proteins, and have been named GDI-like solubilising factors (GSFs) (Chandra et al., 2012, Ismail, 2017). PDEδ has been shown to bind prenylated GTPases of the RAS family and to facilitate their trafficking to the plasma membrane. However, unlike GDIs, these interactions are independent of the

nucleotide state of the shuttled GTPases (Nancy et al., 2002, Chandra et al., 2012). On the other hand, UNC119A and UNC119B are acyl-binding proteins, and are involved in the trafficking of myristoylated proteins. UNC119A has been shown to transport transducin-alpha to the outer segments of rod photoreceptors (Zhang et al., 2011). Its paralogue UNC119B is involved in the trafficking of nephrocystin-3 (NPHP3) to the primary cilium, a membrane domain which was previously mentioned in **Section 1.1** (Wright et al., 2011a).

GSFs bind to the small G proteins ARF-like 2 and 3 (ARL2 and ARL3) in a nucleotide-dependent manner, favouring the GTP-bound forms (Linari et al., 1999, Kobayashi et al., 2003). However, this binding takes place despite the lack of lipid modifications of the ARL proteins, indicating that GSFs do not function as chaperones in this case. Instead, PDEδ and the UNC119 proteins undergo conformational changes upon the binding of ARL2 and ARL3 at a site distal to the lipid-binding pocket. This results in the reduction of the affinity of the hydrophobic pocket to the lipid group. Although ARL binding can result in cargo release from both GSFs, this is achieved via two opposing mechanisms. ARL binding induces the closing of the prenyl-binding pocket of PDEδ, resulting in steric clash with the prenylated cargo and hence its release (Ismail et al., 2011). In contrast, the UNC119 hydrophobic pocket increases in size upon ARL binding, resulting in the reduced affinity to and the release of the acylated cargo (Ismail et al., 2012). In this way, ARL2 and ARL3 function as the GDI-like displacement factors (GDFs) for PDEδ and UNC119.

Further regulation is exerted on the release of cargo from PDEδ and UNC119 proteins which is based on the affinity of the lipid-modified protein to the GSF. The strength of the binding of the lipid group to the hydrophobic pocket is dependent on the residues immediately following the acyl group or preceding the prenyl group. High affinity cargo of PDEδ and UNC119, such as inositol polyphosphate-5-phosphatase E (INPP5E) and NPHP3, respectively, can only be released from the complex via the binding of GTP-bound ARL3 and not ARL2-GTP. Conversely, low affinity cargo for PDEδ and UNC119, such as the respective KRAS and c-SRC, are released by both ARL2 and ARL3. These differences in release are the key to directed targeting of different lipid-modified proteins to various domains (Wright et al., 2011a, Ismail et al., 2012, Fansa et al., 2016).

GTP-bound ARL3 is inactivated by its specific GAP, retinitis pigmentosa protein 2 (RP2) (Veltel et al., 2008). **Figure 1-6** shows a simplified scheme of this process.

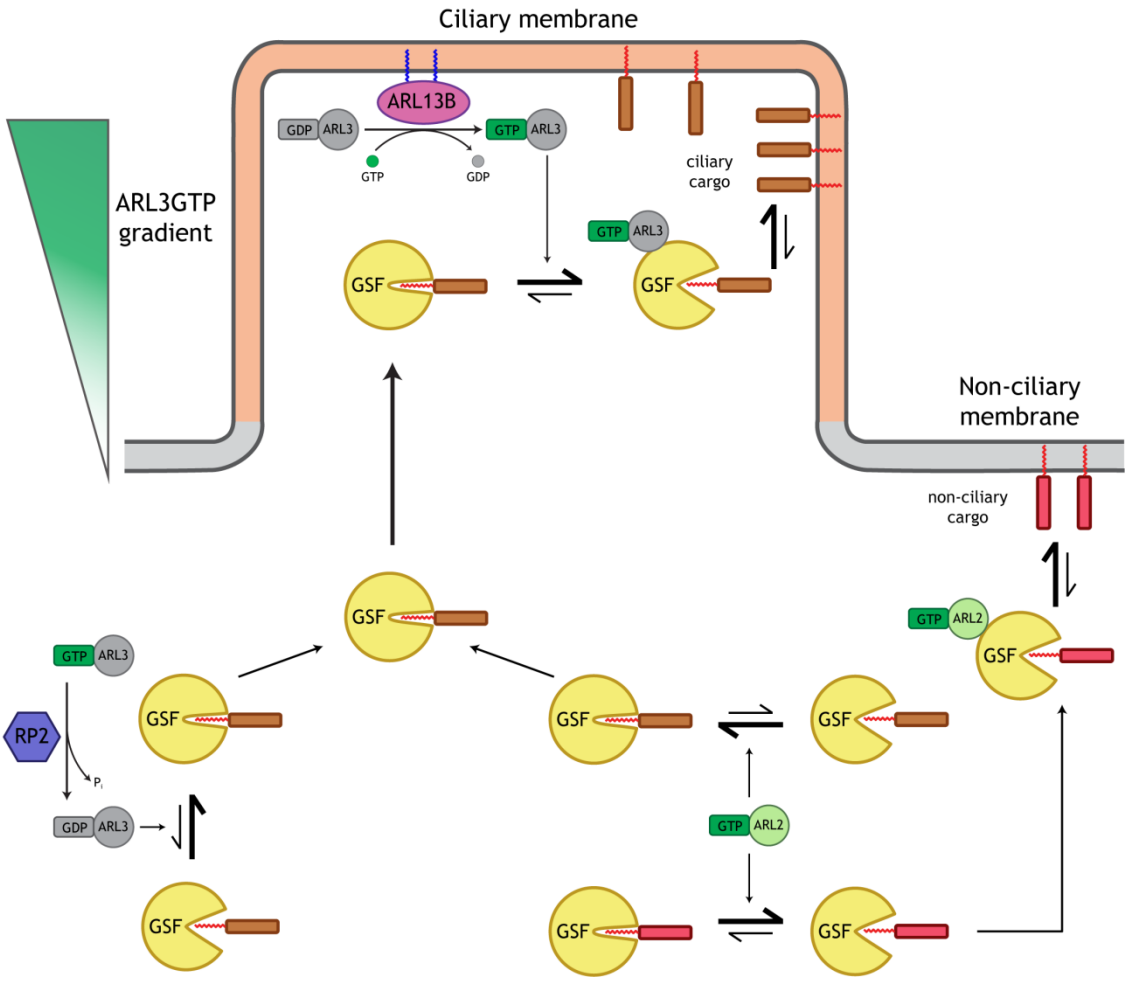

Figure 1-6 GSF trafficking of acylated/prenylated ciliary cargo to the ciliary domain.

PDEδ and UNC119 bind prenylated and acylated proteins, respectively, with ciliary cargo having higher binding affinities to the GSFs. Outside the ciliary domain, only non-ciliary proteins can be released from the GSF complex due to the presence of ARL2GTP, which is able to release low affinity cargo which then anchors to non-ciliary membranes. In addition, ARL3 is inactivated by the presence of its GAP, RP2. The ARL3GEF, ARL13B, localises to the ciliary membrane, which results in the formation of a local concentration of ARL3GTP. Complexes of GSF and ciliary cargo will therefore be disrupted in the cilia, and the cargo will released to anchor to the ciliary membrane. GSF, GDI-like solubilising factor; RP2, retinitis pigmentosa protein 2; ARL, ARF-like protein.

Specific cargo release at target domains has been attributed in the case of the primary cilium to the restricted localisation of the GEF for ARL3, ARL13B. This GEF localisation, in addition to the exclusion of the ARL3GAP, RP2, results in the formation of a concentration gradient with high levels of GTP-bound ARL3

present within the cilium. As a result, complexes of GSFs and lipid-modified cargo are disrupted in the cilium, resulting in cargo release followed by anchoring to the ciliary membrane via prenyl/acyl groups (Gotthardt et al., 2015) **(Figure 1-6)**.

UNC119 and PDEδ will be discussed in further details in the following chapters with respect to their roles in the trafficking lipid-modified cargo to target domains in the membrane.

Chapter 2 Materials and Methods

2.1 Materials

2.1.1 General reagents

PBS, PE, TAE and LB medium were made in-house at the Beatson Institute. All restriction enzymes and CutSmart® buffer were purchased from NEB. LB-agar plates with ampicillin or kanamycin were prepared in-house.

Reagent	Supplier	Reference
0.45 µm Durapore membrane filter	Millipore	10527862
16% Formaldehyde, Methanol-free	Pierce™	28908
2-Mercaptoethanol	Sigma Aldrich	M6250-100ML
5 µm Durapore membrane filter	Millipore	10136630
Activated full-length human LCK-6xHis protein	Merck/Millipore	14-842
Agarose	Melford	MB1200
Alkaline Phosphatase	Roche	10108138001
Amersham Protran 0.2 µm nitrocellulose Western blotting membranes	GE Healthcare	10600001
Amicon Ultra 15 mL 10 K centrifugal filter	Millipore	UFC901024
Amicon Ultra 4 mL 10 K centrifugal filter	Millipore UK	UFC801024
Ampicillin sodium	Formedium	AMP100
ATP lithium salt hydrate	Sigma	A2647-5MG
Betaine	Sigma	B0300-1VL
Blocking buffer for fluorescent Western blotting	Rockland™	MB-070-010
Chloramphenicol	Formedium	CLA02
CMAC blue cell tracking dye	Invitrogen™	C2110
Complete EDTA-free Protease inhibitor	Roche	11873580001
DAPI	Sigma	D9542
Deltazinone 1	Chemical Diversity Lab	E854-6463
DMEM	Gibco™	21969-035
DMSO	Sigma	D2650
Donkey Serum	Sigma	D9663
Fast SYBR™ Green Master Mix	Applied Biosystems™	4385612
Fetal bovine serum	Gibco™	10270
Flow cytometry staining buffer	eBioscience	00-4222-57
GANT61	Sigma Aldrich	G9048
GDP	Sigma	G7127
GelRed nucleic acid stain	Biotium	BT41003

Glutathione Sepharose 4 Fast Flow	GE Healthcare	17-5132-01
Glycine	Millipore	357002
GppNHp	Jena Bioscience Gmbh	NU-401-10
GSTrap HP Columns, (5 x 5ml)	GE Healthcare	17-5282-02
High Density Nickel resin	Agarose Bead Technologies	6BCL-QHNI-25
HisTrap HP Columns	GE Healthcare	17-5248-02
HiTrap Benzamidine FF columns	GE Healthcare	17-5143-01
IPTG	Formedium	IPTG100
Kanamycin monosulphate	Formedium	KAN0025
L-Glutamine	Gibco™	25030024
mantGDP	BioLog Life science Institute	M041-05
MEM	Sigma	M2279
NuPAGE® MES running buffer (20X)	Novex	NP0002
NuPAGE™ 4-12% Bis-Tris Protein Gels	Invitrogen™	NP0321BOX
Methanol	fisher scientific	67-56-1
Myristoyl Coenzyme A lithium salt	Sigma	M4414
NeXtal tubes suite $AmSO_4$	Qiagen	130705
NeXtal tubes suite Classics	Qiagen	130701
NeXtal tubes suite PEGs	Qiagen	130704
NeXtal tubes suite PEGs II	Qiagen	130716
Nuclease-free, non-DEPC-treated water	Ambion	AM9937
PageRuler Prestained Protein Ladder	Fermentas	11812124
PD-10 desalting columns	GE Healthcare	17-0851-01
Penicillin/Streptomycin	Gibco™	15140122
Poly-L-lysine solution	Sigma	P4707
ProLong™ Gold Antifade Mountant with DAPI	Invitrogen™	P36931
Protein Assay Dye Reagent Concentrate	Bio-Rad	500-0006
Q5 High Fidelity 2X Master Mix	NEB	M0492S
Q5® High-Fidelity 2X Master Mix	NEB	M0492S
QIAshredder homogeniser spin columns	Qiagen	79654
ReBlot Plus Mild Solution	Millipore UK	2502
Reduced glutathione	fisher scientific	11483074
RNase-Free DNase Set	Qiagen	79254
RPMI medium	Gibco™	31870-025
SAG	Calbiochem	566660
SAG•2HCl	Sigma	SML1314
Sodium chloride	fisher scientific	7647-14-5
Sodium Deoxycholate	Sigma	D6750-25G
Squarunkin A	Glixx labs Inc	GLXC-10229
Staphylococcal Enterotoxin E (SEE)	Toxin Technology Inc.	ET404
Superdex 200 Increase 10/300 GL	GE Healthcare	28-9909-44

Tetrabutylammonium bromide	Sigma	193119
Thrombin	Sigma	T4648
Tris base	Melford	T60040
Triton X-100	Sigma	X100
UltraComp eBeads™	eBioscience	01-2222-41
Zeba™ Spin Desalting Columns, 7K MWCO, 0.5 mL	ThermoFisher	89882

2.1.2 Buffers

Buffer	Composition
HisTrap-wash	25 mM Tris (pH 7.5), 300 mM NaCl, 2 mM ß-ME
HisTrap-elute	25 mM Tris (pH 7.5), 300 mM NaCl, 300 mM imidazole, 2 mM ß-ME
GSTrap-wash	30 mM Tris (pH 7.5), 300 mM NaCl, 2 mM DTT
Glutathione (GSH)	25 mM Tris (pH 7.5), 200 mM NaCl, 20 mM GSH, 2 mM DTT
Gel filtration	25 mM Tris (pH 7.5), 150 mM NaCl, 2 mM DTT
RIPA	10 mM Tris (pH 8.0), 140 mM NaCl, 1 mM EDTA (pH 8.0), 1% Triton X-100, 0.1% SDS, 0.1% sodium deoxycholate, 1:100 protease inhibitors
Pull-down-wash	50 mM Tris (pH 8.0), 1 mM $MgCl_2$, 0.02% Triton X-100, 1 mM DTT
FP buffer	20 mM Tris (pH 7.5), 150 mM NaCl, 5 mM $MgCl_2$, 2 mM DTT
Transfer buffer	25 mM Tris, 192 mM Glycine, 20% Methanol
Pull-down-wash	25 mM Tris (pH 7.5), 200 mM NaCl, 2 mM DTT
HPLC running buffer	100 mM K_3PO_4 (pH 6.5), 10 mM Tetra-n-butylammonium bromide (TBAB)

2.1.3 Cell lines

2.1.3.1 Bacterial strains

Strain	Supplier	Reference
BL21-CodonPlus (DE3)-RIL competent cells	Agilent Technologies	230245
BL21(DE3)pLysS competent cells	Promega	L1195
One Shot™ TOP10 chemically-competent cells	Invitrogen™	C404003
DH5α competent cells	Invitrogen™	18265017

2.1.3.2 Mammalian cell lines

Cell line	Supplier	Reference
NIH/3T3	ATCC®	CRL-1658
Jurkat, clone E6-1	ATCC®	TIB-152
Raji	DSMZ	ACC 319
Madin-Darby canine kidney (MDCK)	ATCC®	CCL-34

2.1.4 Primers

2.1.4.1 Site-directed mutagenesis (SDM)

Primers were designed using the online tool NEBaseChanger™ to produce non-overlapping primers spanning the mutagenesis site (indicated in lowercase), which were used with the Q5® site-directed mutagenesis kit (New England Biolabs). Primers used in this work are listed in the following table, and are named as gene name_mutation_F/R, where _F and _R denote forward and reverse primers, respectively. All primers were synthesised by IDT.

Primer name	Sequence (5’ to 3’)
ARL3_Q71L_F	CATTGGTGGActgAGGAAAATCAG
ARL3_Q71L_R	TCCCATACATTCAGTTTAAAAC
ARL2_Q70L_F	TGTGGGTGGCctgAAGTCCCTGC
ARL2_Q70L_R	TCCCAGATGTTCAGCTTGAATCCTC
KRas4B_C185A_F	AAAGACAAAGgccGTAATTATGTAAATGACTG
KRas4B_C185A_R	GACTTCTTTTTCTTCTTTTTACC
KRas4B_G12D_F	AGTTGGAGCTgacGGCGTAGGCA
KRas4B_G12D_R	ACCACAAGTTTATATTCAGTCATTTAC
KRas4B_K182A+K184A_F	AgccTGTGTAATTATGTAAATGACTG
KRas4B_K182A+K184A_R	GTggcTGACTTCTTTTTCTTCTTTTTAC
KRas4B_K182S+K184I_F	AatcTGTGTAATTATGTAATAGGG
KRas4B_K182S+K184I_R	GTggaTGACTTCTTTTTCTTCTTTTTAC
LCK_K273R_F	GGTGGCGGTGaggAGCCTGAAGC
LCK_K273R_R	TTCGTGTGCCCGTTGTAGTACC
LCK_Y181F_F	GGTGAAACATttcAAGATCCGTAATCTG
LCK_Y181F_R	ACCTCTCCCTGGTTCTGG
LCK_Y192F_F	CGGTGGCTTCttcATCTCCCCTC
LCK_Y192F_R	TTGTCCAGATTACGGATCTTGTAATG
LCK_Y25F_F	GAACTGCCATttcCCCATAGTCC
LCK_Y25F_R	TCACACACATCGATGTTTTC
LCK_Y263F_F	GTGGATGGGGttcTACAACGGGC
LCK_Y263F_R	ACCTCCCCGAACTGTCCAG
LCK_Y313F_F	GGAGCCCATCttcATCATCACTG
LCK_Y313F_R	TGGGTGACCACAGCGTAG
LCK_Y360F_F	AGAGCGGAATttcATTCATCGTGAC
LCK_Y360F_R	TCAATGAATGCCATGCCTTC
LCK_Y394F_F	GGACAACGAGttcACAGCCAGGG
LCK_Y394F_R	TCAATGAGGCGTGCTAGG
LCK_Y414F_F	AGCCATTAACttcGGGACATTCAC
LCK_Y414F_R	TCTGGCGCTGTCCACTTA
LCK_Y470F_F	AGAGGAGCTGttcCAACTCATGAGG
LCK_Y470F_R	GGACAGTTGTCAGGGCGC
LCK_Y489F_F	CACCTTTGACttcCTGCGCAGTGTGCTGG
LCK_Y489F_R	GGCCGGTCCTCTGGGCGC
UNC119A_G22V_F	GGGGCCCTCGgtgCAGAGCGTGG
UNC119A_G22V_R	GGAGCGGACTCCGTCGCC

2.1.4.2 Quantitative PCR

Primers were designed for canine (1) and murine (2) sequences of the analysed genes for quantifications in MDCK and NIH/3T3 cells, respectively. Primer-BLAST

(Ye et al., 2012) was used to design primers for each template. The following search parameters were applied: 70–200 bp amplicon size, 60°C-63°C primer melting temperature, and spanning exon-exon junctions. The best primer pairs were chosen from the results based on the presence of 3' G/C bases, 40-60% GC content, and minimal self-complementarity. These were then tested by carrying out endpoint PCR and confirming that the obtained amplicon size matched that predicted by Primer-BLAST. All primers were synthesised by IDT.

Primer name	Sequence (5' to 3')
GAPDH_F1	CCATCACTGCCACCCAGAAG
GAPDH_R1	CCAGTGAGCTTCCCGTTCAG
GLI1_F1	GCAGACAGTTATCCGCACCT
GLI1_R1	TTTAGCTGGCAAGTCGGGAG
PTCH1_F1	GGGATCATTGTGACGGTGCT
PTCH_R1	ACGGCTCTGCGGTTCTTATC
GAPDH_F2	GGCCTTCCGTGTTCCTAC
GAPDH_R2	TGTCATCATACTTGGCAGGTT
GLI1_F2	CCAAGCCAACTTTATGTCAGGG
GLI1_R2	AGCCCGCTTCTTTGTTAATTTGA
PTCH1_F2	ACTGTCCAGCTACCCCAATG
PTCH_R2	CATCATGCCAAAGAGCTCAA

2.1.5 Kits

Kit	Supplier	Reference
DNA Ligation Kit, Mighty Mix	TaKaRa	6023
Amaxa® Cell Line Nucleofector® Kit V	Lonza	VCA-1003
RNeasy Mini Kit	Qiagen	74104
High-Capacity RNA-to-cDNA™ Kit	Applied Biosystems™	4387406
Q5 Site Directed Mutagenesis kit	New England BioLabs	E0554S
ProFluor® Src-Family Kinase Assay	Promega	V1270
Endo-free plasmid maxi kit	Qiagen	12362
QIAquick gel extraction kit	Qiagen	28704
QIAquick PCR purification kit	Qiagen	28104

2.1.6 Antibodies

Antibody	Supplier	Reference
Primary antibodies		
anti-6xHis, monoclonal (mouse)	TaKaRa	631212
anti-GST, polyclonal (goat)	GE Healthcare	27457701V
anti-LCK, polyclonal (rabbit)	Sigma-Aldrich	HPA003494
anti-LCK (pY394), monoclonal (mouse)	abcam	ab201567
anti-FMNL1 (rabbit)	Bethyl Laboratories	A304-869A
anti-Phosphotyrosine, clone 4G10® (mouse)	Sigma-Aldrich	05-321
anti-Human ZAP70 (pY493) (mouse)	R&D Systems	MAB7694
anti-CD28 clone CD28.2 (mouse)	BD	555726
anti-acetylated tubulin (mouse)	Sigma Aldrich	T7451
anti-vinculin, monoclonal (rabbit)	Abcam	ab129002
anti-ARL3, polyclonal (rabbit)	Proteintech	10961-1-AP
anti-ARL13B, polyclonal (rabbit)	Proteintech	17711-1-AP
anti-UNC119, monoclonal (mouse)	Sigma	SAB1404669
Secondary antibodies		
IRDye® 800CW Donkey anti-Goat IgG	Li-Cor	926-60874
IRDye® 680RD Donkey anti-Rabbit IgG	Li-Cor	926-68073
IRDye® 800CW Donkey anti-Mouse IgG	Li-Cor	926-32212
Goat anti-Rabbit IgG (H+L), Alexa Fluor 546	ThermoFisher	A-11035
Donkey anti-Mouse IgG (H+L), Alexa Fluor 488	ThermoFisher	A-21202
Goat anti-Mouse IgG (H+L), Alexa Fluor 555	ThermoFisher	A-21424
Conjugated antibodies		
APC-anti-CD69, monoclonal (CH/4)	ThermoFisher	MHCD6905
Alexa Fluor® 488-anti-GFP	BioLegend UK	338007

2.1.7 Peptides

Lyophilised peptides were reconstituted in DMSO to prepare 20 mM stock solutions, which were further diluted as required. All solutions were stored at -20°C.

Peptide	Sequence		Supplier
LCK WT	Myr-GCGCSSHPED	-K(5/6-Fluorescein)-amide	Alta Bioscience, University of Birmingham
LCK G4Q	Myr-GCQCSSHPED		
LCK G4N	Myr-GCNCSSHPED		
LCK C3Q	Myr-GQGCSSHPED		
LCK C3N	Myr-GNGCSSHPED		
LCK C5Q	Myr-GCGQSSHPED		
LCK C5N	Myr-GCGNSSHPED		
FMNL1	Myr-GNAAGSAEQPAG		
FMNL3	Myr-GNLESAEGVPGE		
LCK WT	Myr-GCGCSSHPED-OH		JPT peptide technologies

2.1.8 Constructs

All inserts are of full-length proteins unless otherwise specified. All pET20-based constructs encode 6xHis-tagged proteins unless 12xHis-tag is specified. Tyrosine-to-phenylalanine mutants of 12xHis-tagged LCK are listed as one entry with a compiled list of the positions where the mutations were generated. Cloning was carried out either by polymerase chain reaction and restriction digestion (PCR/RE) or site-directed mutagenesis (SDM). All constructs were generated for this work and have been published (Stephen et al., 2018, Alkanderi et al., 2018). The expression vectors used in this work are: pET-20b(+) (Novagen, ampicillin resistance), pGST-4T-1 (Amersham, ampicillin resistance), and pEGFP-N1 (Clontech, kanamycin resistance).

Vector	Insert	Cloning method
pET-20b(+)	*Mm*ARL2	PCR/RE (HindIII, BamHI)
	*Mm*ARL3	PCR/RE (XhoI, BamHI)
	*Mm*ARL3^{R149H}	SDM
	*Cr*ARL3	PCR/RE (EcoRI, HindIII)
	*Cr*ARL3^{R148H}	SDM
	*Hs*ARL13B$^{18-278}$-12xHis	PCR/RE (NdeI, HindIII)
	*Hs*LCK$^{1-121}$ (LCK SH3)	PCR/RE (NdeI, HindIII)
	*Hs*LCK$^{1-226}$ (LCK SH3-SH2)	PCR/RE (NdeI, HindIII)
	*Hs*LCK$^{(1-226)\ G4Q}$	SDM
	*Hs*HCK$^{(1-243)}$ (HCK SH3-SH2)	PCR/RE (NdeI, HindIII)
	*Hs*HCK$^{(1-243)\ R4G}$	SDM
	*Hs*LCK$^{225-509}$ (LCK kinase)	PCR/RE (HindIII, XhoI)
	*Hs*LCK-12xHis	PCR/RE (NdeI, XhoI)
	*Hs*LCK-12xHis Y-to-F mutants: 25, 181, 360, 394, 414, 489, 505, 394+505, 394+414	SDM
pGST-4T-1	*Hs*UNC119A	PCR/RE (BamHI, EcoRI)
	*Hs*UNC119A^{G22V}	SDM
	*Hs*UNC119A$^{54-240}$ (UNC119A-Δ54)	PCR/RE (BamHI, EcoRI)
	*Hs*UNC119B	PCR/RE (BamHI, EcoRI)
	*Hs*FMNL1$^{1-458Δ172-198}$ (FMNL1Δ)	PCR/RE (BamHI, EcoRI)
	*Cr*ARL13B$^{18-278}$	PCR/RE (EcoRI, XhoI)
	*Cr*ARL13B$^{(18-278)E86R}$	SDM
pEGFP-N1	*Hs*ARL2	PCR/RE (HindIII, BamHI)
	*Hs*ARL2^{Q70L}	SDM
	*Hs*ARL3	PCR/RE (XhoI, BamHI)
	*Hs*ARL3^{Q71L}	SDM
	*Hs*LCK	PCR/RE (HindIII, AgeI)
	*Hs*LCK^{G4Q}	SDM

2.1.9 Software and algorithms

Name	Source
BLAST	NIH
Fiji	NIH
FlowJo software 10.4.2	FlowJo, LLC
GraFit	Erithacus software
Image Studio™ Lite	LI-COR
MolRep	CCP4 program suite
NetPhos 3.1	DTU Bioinformatics
Prism	GraphPad Software
Pymol	Schrödinger, LLC
Refmac5	CCP4 program suite
StepOne™ software	ThermoFisher
Unicorn 5	GE Healthcare
WinCoot	PHENIX

2.2 Methods

2.2.1 Biochemistry and structural biology

2.2.1.1 Cloning

All inserts encoding proteins listed in **2.1.8** were cloned into the respective vector by polymerase chain reaction (PCR) amplification followed by restriction digestion and ligation with the vector after digestion with the same endonucleases. PCR amplification reactions were set up as shown below before checking the amplicon size by agarose gel electrophoresis of a sample of the reaction.

Component		Final concentration	Thermocycler settings
2X Q5 master mix	25 µL	1X	98°C for 1 min
10 µM F primer	2.5 µL	0.5 µM	98°C for 10 s 65°C for 30 s 72°C for 30 s/kb — 35 cycles
10 µM R primer	2.5 µL	0.5 µM	
5 M Betaine	10 µL	1 M	
DNA	100 ng	2 ng/µL	72°C for 10 min
Water	to 50 µL	-	hold at 4°C

PCR reactions were purified using the Qiagen purification kit. Restriction digestion reactions of the insert and vector were then set up in 1X CutSmart® buffer with 1 µL enzyme/25 µL reaction volume. Reactions were incubated at 37°C for 1 hr before performing gel purification as per the QIAquick kit instructions. Purified DNA was then analysed using a DeNovix DS-11+ spectrophotometer (DeNovix Inc.). 5–10 µL ligation reactions were set up using the Mighty mix ligation kit with ~ 1:5 ratio of vector to insert. These were incubated at room temperature for 30 min before being used for transformation of competent TOP10 *E. coli* cells. The transformed cells were plated on LB-agar plates with the appropriate antibiotic. Subsequent DNA purification and sequencing was performed by the Molecular Technology Services at the Beatson Institute. Sequences were confirmed by carrying out alignment against the template using BLASTn.

2.2.1.2 Site-directed mutagenesis

Site-directed mutagenesis (SDM) was carried out using the Q5® SDM kit and the recommended protocol. PCR reactions were set up as below. The annealing temperature was set as recommended by NEBaseChanger™ used for primer design. Following PCR amplification, reactions were used for KLD digestion and transformation of competent *E. coli* cells. These were then plated on LB-agar plates with appropriate antibiotic selection and colonies were picked for small-scale culturing, DNA purification, and sequencing. Sequence alignment with the template was carried out using BLASTn.

Component		Final concentration	Thermocycler settings	
2X Q5 master mix	12.5 µL	1X	98°C for 30 s	
10 µM F primer	1.25 µL	0.5 µM	98°C for 10 s 50-72°C for 30 s 72°C for 30 s/kb	25 cycles
10 µM R primer	1.25 µL	0.5 µM		
DNA	10-15 ng	0.4-0.6 ng/µL		
Water	to 25 µL	-	72°C for 2 min hold at 4°C	

2.2.1.3 Bacterial cell culture and protein expression

Expression vectors with their respective cloned inserts were used to transform competent BL21 *E. coli* expression strains. pET-20b(+) constructs were expressed in BL21(DE3)pLysS cells, while pGST-4T-1 constructs were expressed in BL21(DE3)CodonPlus cells. A ~200 mL starter culture was initially grown overnight at 37˚C in LB media with the addition of 100 µg/mL ampicillin and 25 µg/mL chloramphenicol. This was then used to inoculate 1 L cultures that were grown at 37°C until OD_{600} of 0.4-0.5 before cooling the cultures to 16°C and inducing the expression by the addition of 250 µM isopropyl ß-D-1-thiogalactopyranoside (IPTG). Protein expression was allowed to continue overnight before harvesting the cells by centrifuging at 4500 ×g for 15 min at 4°C using a JS-4.2 swinging-bucket rotor (Beckman Coulter).

2.2.1.4 Protein purification

Harvested cells were resuspended in ~100-150 mL of HisTrap- or GSTrap-wash buffer, for His- and glutathione S-transferase (GST)-tagged proteins, respectively **(section 2.1.2)**, with the addition of 1 tablet of Protease inhibitor/50 mL buffer. Cells were then lysed using the M-110P microfluidiser (Microfluidics™) at 20 000 PSI. Cell debris was removed by centrifuging at 48300 ×g for 1 h at 4°C using a JA-25.50 fixed-angle rotor (Beckman Coulter). The supernatant was then passed through a 5 µm filter. The lysate was then loaded on the affinity chromatography column using an ÄKTA purifier system (GE Healthcare). The column was then washed with the wash buffer until UV absorbance of the flow-through was stabilised. This was followed by step and gradient elution for GST- and His-tagged proteins, respectively, with fraction collection. 12xHis-tagged proteins were washed with 20% HisTrap-elution buffer before performing the

gradient elution. The correct fractions were selected based on the UV elution profile. These were pooled and concentrated by centrifugal filters to reduce the volume to 10 mL for injecting on to the gel filtration column. Elution was performed using the gel filtration buffer; the required fractions were pooled and concentrated as aforementioned. The purified protein was then checked by SDS-PAGE electrophoresis and quantified by spectrophotometry before snap-freezing the aliquots in liquid nitrogen and storing at -80°C. Full-length LCK proteins and ARL13B proteins were purified and stored with the addition of 10% glycerol to all buffers.

2.2.1.5 Crystallisation and structure determination

Complex formation of UNC119A and *in vitro* myristoylated LCK is described in **section 3.2.2.1**. Purified recombinant full-length and truncated UNC119A at concentrations of 466 µM and 746 µM, respectively, were mixed with 20 mM solution of myristoylated N-terminal peptide LCK in a 1:1 molar ratio. UNC119A proteins were in gel filtration buffer. Crystallisation screens were set up in 3 lens crystallisation midi plates (SWISSCI) for sitting-drop vapour diffusion. 38 µL of the NeXTal crystallisation suites $AmSO_4$, Classics, PEGs, and PEGs II was pipetted to each reservoir well. 200 nL of reservoir and protein were added to and mixed in the crystallisation drop wells using a mosquito® crystal nanolitre robot (TTP Labtech). The plates were carefully sealed and then stored and imaged using a ROCK IMAGER® (FORMULATRIX®) at 4°C and 19°C. Crystals were formed in one of the conditions of the PEGs screen, with a composition of 20% (w/v) PEG 3350 and 0.2 M KH_2PO_4. These crystals were flash-frozen in 25% (v/v) glycerol diluted in the mother liquor.

Data collection was carried out the Diamond Light Source using beamline I04 (λ= 0.9795 Å). Integration was then carried out using automated XDS, and the CCP4 program suite was used for scaling. Molrep was used for molecular replacement using a previously reported structure of UNC119 (PDB code 3RBQ) as a search model (Zhang et al., 2011). Refinement was carried out using Refmac5 and WinCoot was used to build the model. Finally, Pymol was used for model visualisation.

2.2.1.6 *In vitro* myristoylation

In vitro myristoylation of recombinant wild-type and mutant LCK and HCK was carried out in the presence of GST-tagged UNC119 as previously reported (Padovani et al., 2013). Typical reactions were set up as shown below, and were incubated at room temperature for 3 hrs before using them for pull-down assays.

Component	Final concentration/amount
Tris (pH 8.0)	50 mM
$MgCl_2$	1 mM
GST-UNC119	30 – 100 µg
LCK/HCK	100 – 200 µg
Myristoyl CoA	100 µM
NMT	2.5 µM
DTT	1 mM

2.2.1.7 Nucleotide exchange of G proteins

Recombinant ARL2 and ARL3 were loaded with the non-hydrolysable GTP analogue, GppNHp, as shown below. Reactions were incubated overnight at 15°C before removing excess unbound nucleotides by carrying out size exclusion chromatography, with 5 mM $MgCl_2$ added to the gel filtration buffer. ARL-GppNHp was quantified by performing High-performance liquid chromatography (HPLC) using a reverse phase C18 column (Dionex) and an UltiMate 3000 HPLC system (ThermoFisher Scientific).

Component	Final concentration
ARL2 or ARL3	400 µM
GppNHp	2 mM
Alkaline Phosphatase	0.14 U/µL
Gel filtration buffer	to 500 µL

Recombinant ARL13B was loaded with GppNHp and ARL3 with fluorescently-labelled mantGDP by setting up the following reactions with incubation for 2 hrs at room temperature.

Component	Final concentration	Component	Final concentration
ARL13B	100 µM	ARL3	100 µM
GppNHp	500 µM	mantGDP	200 µM
EDTA	50 mM	EDTA	50 mM
Gel filtration buffer	to 500 µL	Gel filtration buffer	to 500 µL

All exchange reactions were stopped by the addition of $MgCl_2$ to a final concentration of 100 mM. PD-10 desalting column were used to remove excess nucleotides and the proteins were concentrated using centrifugal filters and quantified using the colourimetric protein assay dye reagent as per the manufacturer's instructions.

2.2.1.8 Pull-down assays

50 µL of glutathione sepharose slurry was washed thrice in spin columns with 400 µL pull-down-wash buffer by spinning at 1×10^3 ×g for 1 min; the column was then blocked. 50 µL reactions involving *in vitro* myristoylation as previously described, or without myristoylation as shown below, were added to the washed beads and incubated for 15 min at room temperature. For pull-down assays with Jurkat cell lysate, the lysate was incubated with the beads for 1 hr at 4°C with constant rotation. The columns were then unblocked and washed 5 times with 400 µL pull-down-wash buffer before eluting with 30 µL of glutathione buffer. Elutes were then analysed using SDS-PAGE electrophoresis and Western blotting.

Component	Final concentration/amount
Tris (pH 8.0)	50 mM
$MgCl_2$	1 mM
GST-UNC119	30 – 100 µg
LCK/HCK/ARL3	2 – 200 µg
Triton X-100	0.02%
DTT	1 mM
Water	to 50 µL

2.2.1.9 Western blotting

Lysates or pull-down assay samples were separated by sodium dodecyl sulphate - polyacrylamide gel electrophoresis (SDS-PAGE) using NuPAGE™ 4-12% Bis-Tris gels run at 150 V for ~60 min. The separated proteins were then transferred on to Amersham Protran 0.2 µm NC nitrocellulose membrane; transfer was performed at 30 V for 60 min. The membrane was then blocked in 5 mL Rockland blocking buffer for 1 hr at room temperature. Primary antibodies were added at a 1:1000 dilution and incubated overnight at 4°C. The membrane was then washed three times with 50 mL PBS-T (PBS + 0.1% Tween-20) for 10 min at room temperature. Secondary antibodies were added at a dilution of 1:5000 and incubated for 1 hr at room temperature before repeating the washing steps. The membrane was washed one final time in PBS before imaging using an Odyssey® CLx system (LI-COR); images were analysed using Image Studio™ Lite software.

2.2.1.10 Fluorescence polarisation

Fluorescence polarisation (FP) was measured using a QuantaMaster 8000 fluorimeter (PTI) with excitation and emission set as follows:

Fluorophore	Excitation (nm)	Emission (nm)
Fluorescein	485	530
Mant	366	450

All measurements were carried out in 500 µL FP buffer at room temperature and were maintained for at least 100 s before any addition of another component of the reaction. The exact amounts used in each of the assay are described in the captions of the relevant figures in the following chapters.

ARL-mediated release assays involved the addition of UNC119A to a solution of fluorescently-labelled peptide followed by GppNHp-loaded ARL2 or ARL3. Measurement of binding affinity to UNC119 was carried out by measuring the resultant FP due to consecutive additions of increasing amounts of UNC119. The data was analysed using GraFit to estimate the binding affinity. Assessment of guanine nucleotide exchange activity of ARL13B was performed by monitoring FP measurements following the addition of ARL13B to a mixture of ARL3-mantGDP and unlabelled GppNHp.

2.2.1.11 Measurement of kinase activity of LCK

The kinase activity of the recombinant wild-type and mutant LCK was assessed in flat-bottom black 96 well plates using the Pro-Fluor Src kinase assay kit, as per the manufacturer's protocol. Briefly, serial dilutions of LCK were made in the substrate solution across 12 wells with a maximum concentration of 100 ng/µL. ATP solution was added and the plate was incubated for 1 hour at room temperature in the dark, followed by the addition of the protease solution and incubating for a further hour. Fluorescence measurements were then made at a wavelength of 485 nm using a Tecan Safire 2 multi-mode plate reader. The fluorescence of the substrate following phosphorylation and proteolytic digestion is inversely correlated to the phosphorylation of the substrate.

2.2.2 Cell biology

2.2.2.1 Mammalian cell culture

Jurkat and Raji cells were maintained in suspension at a concentration of 0.5 – 2×10^6 cells/mL in RPMI medium supplemented with 10% heat-inactivated fetal bovine serum (FBS), 1% penicillin-streptomycin, and 2 mM L-glutamine. Cells were split three times a week by diluting the culture or changing the medium as required; in the latter case, cells were spun down at 180 ×g for 5 min using a swinging-bucket A-4-44 rotor (Eppendorf).

NIH/3T3 and MDCK adherent cells were maintained in DMEM and MEM media, respectively. The culture medium was supplemented with 10% fetal bovine serum, 1% penicillin-streptomycin, and 2 mM L-glutamine. Cultures were split three times a week as follows: the cells were washed with PBS before adding a minimum volume of trypsin solution (prepared by diluting the 50× stock in PE buffer) such that the entire cell layer was covered. Cells were left to stand at room temperature until detachment of 70% of cells. Trypsin was then inactivated by the addition of 5 volumes of FBS-supplemented medium and the cells were pelleted by centrifugation at 180 ×g as above for 3 min to change the medium. Cells were then seeded at 0.1×10^6 cells/mL.

2.2.2.2 Nucleofection of Jurkat cells

Jurkat cells were transfected with the various pEGFP-N1 constructs using the Amaxa® Nucleofector™ II Kit V as per the kit instructions. 24 hours before transfection, cells were seeded at 0.5×10^6 cells/mL. On the day of transfection, 2×10^6 cells were used per construct; 2 µg DNA was added to 100 µL kit transfection reagent, and the mixture was used to resuspend the cell pellet before transferring to the Nucleofector™ cuvette and electroporating with the Nucleofector™ 2b Device with the program X-001. Transfected cells were then carefully transferred from the cuvette to a 12 well plate with 2 mL of complete medium per well that was pre-incubated at 37°C for 15 min. GFP expression was assessed by fluorescence microscopy after 24 hours of incubation.

2.2.2.3 Jurkat-Raji conjugate formation

13 mm glass coverslips were coated with poly-L-lysine as follows: 100 µL of poly-L-lysine diluted 1:1 in PBS was added per coverslip before incubating them at 37°C for 30 min. Coverslips were then washed in PBS and left to dry at room temperature. CMAC-stained and superantigen-coated Raji B cells were prepared by incubating them at a concentration of 1×10^6 cells/mL in complete medium with the addition of 10 µM CMAC and 1 µg/mL staphylococcal enterotoxin E (SEE) for 1 hour at 37°C. Raji cells were then washed thrice with 5 mL complete medium before resuspending them in complete medium at a concentration of 2×10^6 cells/mL. An equivalent number of Jurkat T cells at the same concentration were then added and mixed. 50 µL of the cell suspension (~10^5 cells) was added per poly-L-lysine-coated coverslip and incubated at 37°C for 10 minutes to allow conjugates to form and settle onto the glass. Cells were then fixed in ice-cold methanol for 2 min and washed thrice in PBS.

2.2.2.4 Preparation of MDCK and 3T3 coverslips

MDCK and 3T3 cells were seeded at 0.1×10^6 cells/mL on 13 mm glass coverslips placed in 12 well plates. Cells were allowed to reach confluence overnight in complete medium (10% FBS-supplemented). DMSO or deltazinone (DZ) was added to the wells for 6 hours prior to serum starvation. Complete medium was then removed and the coverslips washed with PBS. 0.5% FBS-supplemented medium was added along with the previous amount of DMSO/DZ. Serum starvation was carried out for 24 hours before fixation. Coverslips were fixed with pre-warmed 4% paraformaldehyde in PBS for 15 min at room temperature before washing 3 times with PBS.

2.2.2.5 Immunofluorescence staining

Fixed Jurkat-Raji conjugates were incubated in blocking solution (5% donkey serum and 0.01% triton X-100 in PBS-T) for 1 hour at room temperature. Primary antibodies (diluted 1:100 in blocking solution) were added and the coverslips were incubated overnight at 4°C. This was followed by three washing steps in PBS before the addition of secondary antibodies (diluted 1:500 in blocking solution) and incubating the coverslips for 1 hour at room temperature in the dark. The coverslips were then washed thrice in PBS before mounting them on

glass slides using ProLong Gold mountant. Slides were left to set for at least 24 hours before imaging.

Fixed MDCK cells and NIH/3T3 fibroblasts were stained using a similar protocol with the exception of the use of a different blocking solution (10% donkey serum and 0.3% triton X-100 PBS-T). In addition, DAPI was added to the secondary antibodies at a dilution of 1:2000.

2.2.2.6 Microscopy

Optical sectioning of fixed cells was performed using confocal laser scanner microscopes LSM 710 or LSM 880 with Airyscan (Zeiss) at 63X. Z-stacks were taken of the entire immune synapse or cilium, using pZAP70 or acetylated tubulin staining, respectively, as a guide. Images were viewed and analysed using Fiji. For quantification of immune synapse protein localisation, maximal intensity projections of the immune synapse z-stacks were used with the plugin SynapseMeasures (Calabia-Linares et al., 2011) to measure the relative localisation of LCK at the synapse compared to the rest of the membrane **(section 3.2.4)**.

Maximal intensity projections of cilia images were also used for analysis. Numbers of cilia and nuclei in each image were counted manually. The total area of cilia and nuclei was measured by adjusting the channel threshold manually to encompass only the respective structure before measuring the total marked area. The Fiji plugin Coloc2 was used to measure colocalisation.

2.2.2.7 Flow cytometry analysis of T cell activation

2.2.2.7.1 In-plate stimulation of Jurkat T cells

Flat-bottom 96 wells plates were coated with anti-CD3 antibody by incubating 100 µL of 10 µg/mL solution per well (diluted in PBS; 1 µg anti-CD3/well) overnight at 4°C. Following the incubation, the antibody solution was removed and the wells were washed with PBS and left to dry at room temperature. Jurkat T cells to be stimulated were suspended in complete medium at a concentration of 1.5×10^6 cells/mL and anti-CD28 antibody was added to a final concentration of 1.5 µg/mL. 100 µL of cell suspension was added per well (0.15 µg anti-CD28/well) and the plate was incubated at 37°C for 4 hrs.

2.2.2.7.2 Staining for flow cytometry analysis

100 µL stimulated Jurkat cells were transferred to V-bottom 96 well plate with the addition of 100 µL cold PBS per well. Cells were pelleted by centrifugation at 300 ×g for 3 min at 4°C. The supernatant was removed and the pellets resuspended by vortexing. 50 µL/well APC-conjugated anti-CD69 antibody solution was added at a dilution of 1:50 in PBS followed by 30 min incubation at 4°C in the dark. Cells were then washed thrice in cold PBS before resuspending them in 50 µL PBS and transferring to FACS tubes containing 200 µL flow cytometry staining buffer. Single-colour controls for GFP and APC were prepared using GFP-transfected Jurkat cells and UltraComp beads stained with the conjugated antibody as above, respectively. Samples were analysed using the Attune NxT flow cytometer (ThermoFisher) and the data was gated and quantified using FlowJo software (FlowJo, LLC). Further details of the analysis performed are given in **section 3.2.4.3**.

2.2.2.8 Stimulation of Hedgehog pathway in MDCK and 3T3 cells

MDCK and 3T3 cells were seeded in 6 well plates at 0.3×10^6 cells/mL in complete medium (10% FBS-supplemented) and allowed to reach confluence overnight. Cells were then treated with the required DMSO/drug concentrations for 6 hours prior to serum starvation. Following the pre-treatment, complete medium was removed from the wells, the cells were washed with PBS, and 0.5% FBS-supplemented medium with or without smoothened agonist (SAG) was added to the cells along with the previous amount of DMSO/drug. Serum starvation was carried out for 24 hours before RNA isolation.

2.2.2.9 RNA isolation

RNA was isolated from MDCK and 3T3 cells grown in 6 well plates using the RNeasy mini kit and following the manufacturer's instructions. Cell lysis was carried out by the addition of RLT lysis buffer and scraping the cells to aid the recovery of cell lysate. QIAshredder spin columns were used to homogenise the cell lysate. On-column DNase-I treatment was performed to ensure complete removal of genomic DNA. Following the RNA isolation steps, RNA was eluted from the RNeasy columns in 30 µL RNase-free water and analysed using a DeNovix DS-11+ spectrophotometer (DeNovix Inc.) to assess the quantity (A_{260}) and quality of the purified RNA.

2.2.2.10 Reverse transcription

cDNA was reversed transcribed from the isolated RNA using the High Capacity RNA-to-cDNA kit. Contamination with genomic DNA was ruled out by preparing controls lack the reverse transcriptase (RT) enzyme. Reactions and –RT controls were set up on ice as follows:

Component		Thermocycler settings
2X RT buffer mix	10 µL	37°C for 60 min
20X RT enzyme mix	1 µL (except in –RT control)	95°C for 5 min
RNA	0.5 µg	hold at 4°C
Nuclease-free water	to 20 µL	

2.2.2.11 Quantitative PCR

cDNA samples were diluted 1:5 before using for quantitative PCR (qPCR). 20 µL qPCR reactions were set up using the Fast SYBR™ Green master mix in 96 well plates, with each sample set up in triplicate. A master mix of reaction components excluding the template was prepared for each pair of forward (F) and reverse (R) primers (*GAPDH*, *GLI1*, and *PTCH1*). An example of an experimental set-up for 10 wells/sample is shown below. Data collection and analysis was done using the StepOne™ Real-Time PCR system and software.

Component		Master mix (x10 wells)	Amounts /well	Thermocycler settings
2X SYBR green master mix	10 µL	100 µL		95°C for 20 s
5 µM F+R primer mix	2 µL	20 µL	18 µL	
Water	6 µL	60 µL		95°C for 3 s 60°C for 30 s 40 cycles
cDNA	2 µL	-	2 µL	

2.2.2.12 Statistical methods

Statistical analysis was carried out using GraphPad Prism software. The statistical test employed, along with sample sizes and p-values are mentioned in the relevant figure legends, and the error bars indicate standard deviation.

Immune synapse localisation ratio data were analysed with the non-parametric Mann-Whitney U test, where the analysed data sets were not assumed to follow a normal distribution. For FACS data, $\%CD69^{+}GFP^{+}$ of ARL3-GFP transfected Jurkat cells was compared for each construct tested with that of GFP-transfected controls following stimulation. Analysis was carried out using an unpaired t-test, as the compared groups are distinct.

Chapter 3 LCK trafficking to the immune synapse

3.1 Introduction

The formation of functional plasma membrane domains is especially crucial in the immune response. It is here that the vanguard of the immune signalling machinery is directed. Dependent on these membrane domains is the both the rapid recognition of targets as well as the regulation of the subsequent response to avoid damage to healthy bystander cells. These membrane domains were first observed in the activation of T lymphocytes, a critical part of the adaptive immune response which requires direct cell-cell interaction. In scanning the surrounding tissue for targets, the T cell forms transient contacts with surrounding cells. These interactions allow the engagement of the T cell receptor (TCR) to antigen-derived peptides bound to major histocompatibility (MHC) molecules on the surface of antigen-presenting cells (APCs). The latter can either be professional APCs, such as B lymphocytes or dendritic cells (DCs), or non-professional APCs, which include all nucleated cells in the body. Antigen-derived peptides are bound to MHC class II molecules on professional APCs, and to MHC class I molecules on their non-professional counterparts. Following TCR binding to peptide-MHC complexes (pMHC), the T cell interaction stabilises to form an isolated interface with the antigen-presenting cell. In doing so, the T cell assembles a specialised membrane domain to which adhesion, signal transduction, and secretion machinery are recruited; this has been termed the immune synapse (Norcross, 1984, Paul and Seder, 1994).

3.1.1 The immune synapse

While immune synapses were first described for T cells, they are also formed by B lymphocytes and natural killer (NK) cells (Davis et al., 1999, Batista et al., 2001). Immune synapses form between communicating immune cells, or between immune cells and infected or transformed target cells. This is an important part of the constant surveillance carried out by these cells to identify individual targets amongst the multitude of healthy cells. The synapse allows the targeted secretion of mediators both in the contexts of regulation between immune cells, and cytotoxicity in the case of target cells (Davis and Dustin,

2004). As discussed later in this section, the formation of the synapse involves the targeting of many signalling, adhesion, and cytoskeletal components to the membranes. Among these are many proteins with lipid modifications, whose presence aids in their targeting and membrane localisation (Udenwobele et al., 2017, Yount et al., 2013). This chapter focuses on our study of the trafficking of a lipidated protein to the immune synapse, specifically that formed by $CD4^+$ T lymphocytes.

3.1.1.1 Topography

The sequence of events occurring during immune synapse formation was first studied using glass-supported lipid bilayers bearing labelled MHC class II and adhesion molecules. Supported bilayers allow the lateral diffusion of the antigen-presenting and adhesion molecules, and hence they provide a simplified mimic of the professional APC surface for studying the immune synapse. $CD4^+$ T cells forming synapses with this bilayer were found to organise pMHC-engaged TCR molecules in the form of a ring enclosing a central cluster of interacting adhesion molecules. This configuration is inverted as the synapse stabilises, with adhesion molecules forming the outer ring (Grakoui et al., 1999). Further studies in cytotoxic $CD8^+$ T cells showed that their synapses start to form as small integrin-ringed TCR clusters which merge later on to form a larger domain, as described below (Somersalo et al., 2004).

As shown in **Figure 3-1**, within the mature synapse, T cell surface molecules segregate into concentric regions known as supramolecular activation clusters (SMACs) (Monks et al., 1998). pMHC-bound TCRs as well as costimulatory and checkpoint molecules localise to the central cluster (cSMAC), which is surrounded by adhesion molecules that are enriched in the peripheral cluster (pSMAC). The cells engaged in the synapse are held together by interactions between the T cell integrin lymphocyte function associated-1 (LFA-1) and the APC intracellular adhesion molecule-1 (ICAM-1) (Grakoui et al., 1999, Yokosuka et al., 2008). On the outskirts of the synapse, the distal cluster (dSMAC) comprises filamentous actin (F-actin) and the phosphatase CD45 which are cleared from the centre of the synapse (Johnson et al., 2000). The latter, as previously mentioned in **section 1.1.1**, is excluded by kinetic segregation, which is driven by steric hindrances against its extracellular domain (van der Merwe et

al., 2000). This “bull’s eye”-like structure is called the Kupfer-type immune synapse and is the predominant type of synapse formed; non-Kupfer synapses lacking the organisation of concentric activation clusters have been observed in some cases with cytotoxic T cells (Barcia et al., 2008).

Below the surface, the cytoskeleton plays crucial roles in the formation of the immune synapse. The initial scanning contacts formed by the T cell are driven by the interaction of adhesion molecules and actin-based protrusions. These push the T cell membrane within close proximity to the target cell membrane, counteracting the steric hindrance caused by bulky glycoproteins which cover the surfaces of both cells. As a result, the TCR is positioned at a suitable distance from the surface of the APC to allow contact with pMHCs. The initial TCR recognition of pMHCs immediately triggers cytoskeletal remodelling. This functions to halt the transient T cell scanning contacts and form a more stable and extensive interaction with the target cell engaged in the synapse. Driven by actin polymerisation, the interface grows as the T cell spreads on the surface of the APC, with TCR-pMHC microclusters forming at the periphery of the interaction. This is followed by the actin-myosin-mediated contraction of the interface. Concurrently, actin retrograde flow due to polymerisation at the leading edge pushes actin filaments backwards and drives TCR microclusters, which associate with cortical F-actin, towards the centre of the synapse. Actin dynamics are therefore considered to be critical for the accumulation of TCR microclusters in the cSMAC (Kumari et al., 2014, Comrie and Burkhardt, 2016).

In addition, the secretory machinery of the cell is polarised towards the synapse. These include the Golgi and the microtubule-organising centre (MTOC), the latter of which docks to the membrane at the periphery of the cSMAC. The docked centrosome directs polarised exocytosis to the synapse membrane for secretion of mediators into the isolated interface. In the case of $CD8^+$ T cells, a secretory domain is formed at the point of centrosomal docking, wherein cytotoxic effector molecules are delivered. The release of cytotoxic mediators towards the target cell is further facilitated by the clearance of cortical F-actin at the centre of the synapse (Stinchcombe et al., 2001, Stinchcombe et al., 2006).

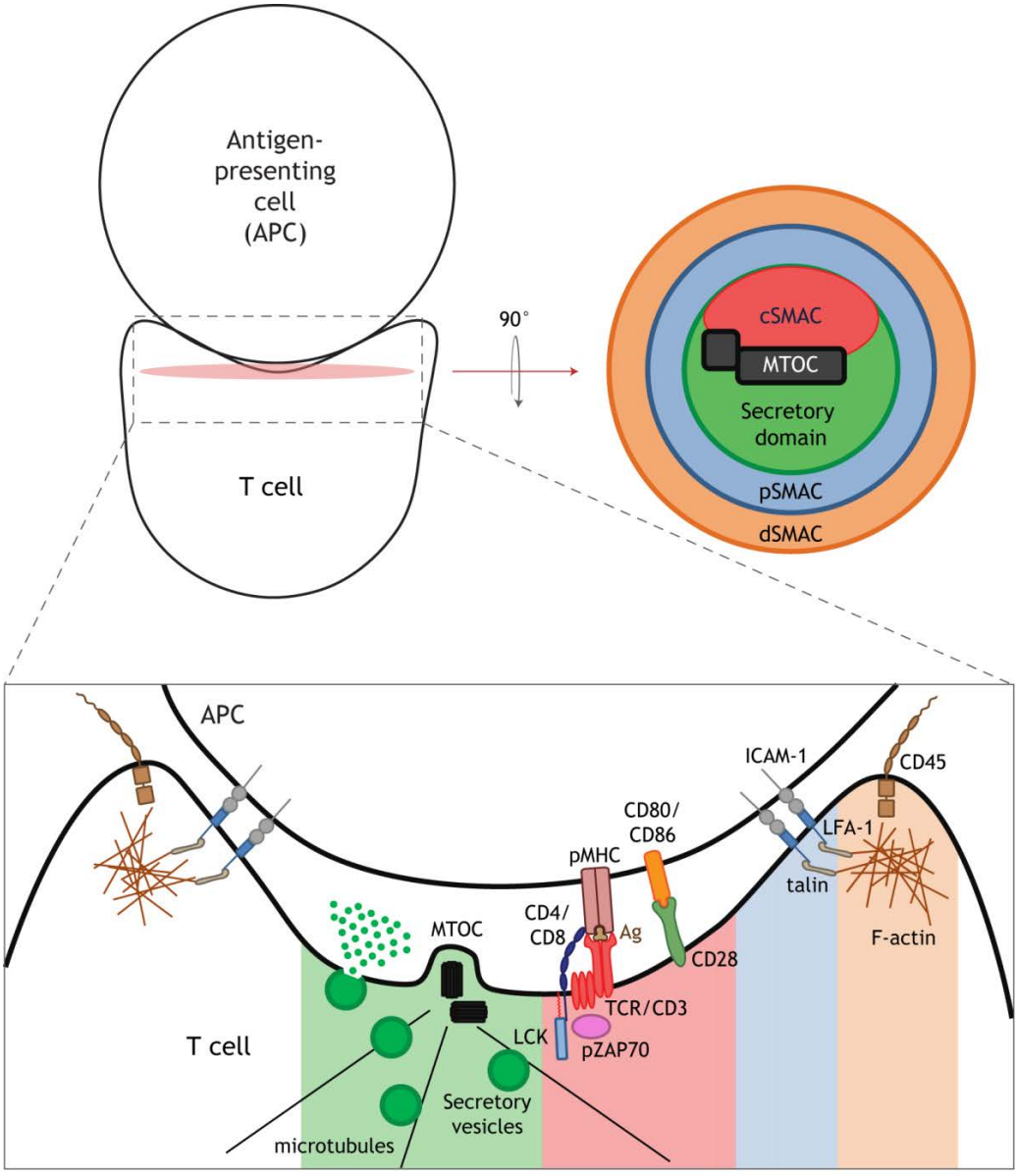

Figure 3-1 The T cell immune synapse.

The specialised membrane domain formed at the interface between a T cell and its target antigen-presenting cell exhibits the segregation of signalling molecules and cytoskeletal elements into three concentric regions. As shown in the top view schematic (right), these are the central, peripheral, and distal supramolecular activation clusters (cSMAC, pSMAC, and dSMAC, respectively). The secretory domain (green), where cytotoxic perforins and granzymes are released, is specific to synapses formed by cytotoxic T lymphocytes (CTLs); it forms at the point of centrosomal docking to the membrane. The central cluster (red) harbours TCRs bound to peptide/MHC complexes and costimulatory molecules like CD28. Integrins bound to APC adhesion molecules are in the peripheral cluster (blue). Finally, filamentous actin and phosphatases such as CD45 are cleared out to the distal cluster (orange). Talins and other adaptor proteins connect integrins to the cytoskeleton. APC, antigen-presenting cell; MTOC, microtubule-organising centre; LCK, lymphocyte-specific kinase; TCR, T cell receptor; pMHC, peptide-major histocompatibility complex; Ag, antigen; pZAP70, phosphorylated zeta-chain- associated protein kinase 70 kDa; LFA-1, lymphocyte function associated 1; ICAM-1, intracellular adhesion molecule-1; F-actin, filamentous actin.

3.1.1.2 Function

While the formation of the T cell immune synapse has been studied in various systems and through different approaches, the roles it plays in the immune response remain a matter of debate. The significance of the immune synapse to T cell function is not unanimously reported *in vitro*, and studying immune synapses *in vivo* is a challenging undertaking (Dustin et al., 2010). This section presents an overview of the synapse functions attributed to signal detection and effector mechanisms of the immune response.

3.1.1.2.1 Stable and specific target cell interactions

Synapse formation has been shown to result in slowing down of T cell movement as the interaction with the target cell is stabilised. Reduction in cell motility is achieved through cytoskeletal reorganisation, Ca^{2+}-influx, and upregulation of surface adhesion molecules. Furthermore, the interactions of adhesion molecules in the pSMAC form a sealed interface between the T cell and its target. The integrin ring surrounds the cSMAC which is cleared of F-actin, allowing the unimpeded release of mediators through exocytosis. In cytotoxic $CD8^+$ T cells, the immune synapse has been proposed to provide a directed route for delivery of cytotoxic mediators that can kill only the target cell engaged in the synapse (Stinchcombe et al., 2001). However, it has also been reported that the $CD8^+$ T cell response mounted against murine brain tumours was not dependent on the formation of Kupfer-type synapses (Yang et al., 2010). The use of the synapse as a targeting system for the cytotoxic response of the cell has therefore been suggested to be dependent on the context of the target and the appropriate immune response therein (Mitxitorena et al., 2015). Stable interactions have also been linked to $CD8^+$ T cell acquisition of memory rather than cytokine release or cell division, (Scholer et al., 2008), although the impact of prolonged contact may differ depending on the context of antigen presentation.

3.1.1.2.2 Mechanical communication

The continuous cytoskeletal reorganisation taking place throughout the formation of the immune synapse results in the generation of relatively significant mechanical forces. These are exerted in part on the T cell, resulting in the aforementioned changes in shape, motility, and organisation of surface

molecules. In addition, they are also transmitted via the adhesive interactions to the target cell engaged in the synapse. These forces are not a simple by-product of a dynamic cytoskeleton, but they are an important regulatory mechanism of protein-protein interactions and signal transduction.

The T cell-APC synapse is maintained by the pSMAC, in which T cell integrins interact with adhesion molecules on the surface of APCs, hence holding the two cells in contact. The binding of integrins to extracellular ligands requires their initial activation by the binding of intracellular cytoskeletal adaptor complexes to the integrin cytoplasmic domains. The binding requires further enhancement through the application of tensile forces on the integrin-ligand interface. This mode of binding is exhibited by the so-called catch bonds, and it has been shown for the binding between LFA-1 and ICAM-1. Retrograde F-actin flow during immune synapse formation pulls LFA-1 molecules towards the centre of the synapse, thereby enhancing their affinity to APC ligands and strengthening the adhesion (Comrie and Burkhardt, 2016). Through the synaptic adhesion, forces exerted by T cell cytoskeleton will also be transmitted to the APC. These have been proposed to enhance the efficiency of $CD8^+$ T cell cytotoxicity, where increased APC membrane tension resulted in better cell killing as mediated by cytolytic granules (Basu and Huse, 2017).

In addition, sensitivity to mechanical forces also extends to the TCR-pMHC binding; this was first reported in studies showing that the stiffness of the antigen-presenting surface affected the intensity of the $CD4^+$ T cell response in a cytoskeleton-dependent process (Judokusumo et al., 2012). Later studies have suggested that the TCRs form catch bonds, but only with their genuine pMHC ligands. Tensile forces exerted by the synapse can therefore serve as a selection criteria for specific TCR antigens (Liu et al., 2014). These mechanical forces have also been proposed to aid in triggering TCR signalling following pMHC interaction. This is suggested to occur through the induction of conformational changes in the TCR and/or associated molecules which allow the initiation of downstream transduction events, described in **section 3.1.2**.

3.1.1.2.3 A multifaceted signalling platform

The polarisation of various surface and cytoplasmic proteins to the immune synapse allows it to serve as a platform for the efficient and regulated

transduction of signalling pathways. The binding of TCR molecules to cognate pMHCs results in the activation of a myriad of signalling networks which bring about T cell activation and effector function as well as regulation of the immune response.

The formation of the immune synapse is closely linked to TCR activation and downstream signalling. As previously mentioned, synapse formation helps to actively maintain the close cell-cell contact necessary for TCR-pMHC engagement, which takes place across a gap of approximately 15 nm (Garcia et al., 1996). The formation of a synapse is required to counteract the effect of steric hindrance exerted by nearby larger surface molecules, the low TCR affinity to the pMHC, and the likelihood of disruption due to T cell movement (Shaw and Dustin, 1997). The accumulation of TCRs and associated molecules in the cSMAC was initially expected to result in initiation of the signalling. However, it has been shown that it is the formation of TCR microclusters at the periphery of the early synapse which is concurrent with the initial burst of T cell activation (Krummel et al., 2000). In contrast, the cSMAC has been shown to exhibit lower TCR signalling compared to its surrounding periphery (Lee et al., 2003). However, the aforementioned results are complicated by the fact that variations in the strength of the initial stimulus can affect the level of TCR signalling in different regions of the synapse (Monks et al., 1998).

Following initiation of TCR signalling, the cSMAC of the mature synapse has been reported to be involved in the modulation of the elicited response, as well as its termination. Components of the ubiquitin pathway have been reported to localise at the cSMAC, indicating its role in the degradation of TCR molecules following their endocytosis (Wiedemann et al., 2005). In addition, the recruitment of immune checkpoint molecules such as the cytotoxic T lymphocyte antigen 4 (CTLA4) also ensures that T cell activation is kept within appropriate levels (Balagopalan et al., 2009, Chen and Flies, 2013). In general, the synapse is posited to maintain the balance between initiation and termination of TCR signalling depending on the circumstances of the antigen recognition event.

As previously mentioned, the $CD8^+$ T cell cytotoxic response is greatly dependent on the secretion of cytolytic granules. These granules are targeted to the immune synapse membrane by the action of the docked centrosome and

associated microtubules (Stinchcombe et al., 2006). The secretion of granules through the membrane, however, is under the control of the cortical actin network present below the plasma membrane. Actin clearance occurs at the synapse within one minute of T cell contact with the target, allowing the passage of granules (Ritter et al., 2015). Conversely, secretion is terminated by the reformation of the synaptic actin network, which prevents the granules from reaching the membrane. Actin dynamics at the synapse are regulated by the levels of the phosphoinositide $PI(4,5)P_2$ at the membrane of the immune synapse (Ritter et al., 2017). These changes are mediated by the activation of phospholipase C γ1 (PLCγ1), which degrades PIP_2. As this phosphoinositide functions in the recruitment of F-actin, its reduction at the synapse results in F-actin clearance. Furthermore, the membrane becomes less negatively charged with the loss of the biphosphorylated phospholipid, which results in the exclusion of the phosphatidylinositol 4-phosphate (PI(4)P) 5-kinase, which produces PIP_2. Regeneration of the latter is therefore inhibited, thereby maintaining its low levels at the synapse. As a result, TCR stimulation influences the synaptic cortical actin through the manipulation of the membrane phosphoinositide composition (Gawden-Bone et al., 2018).

Furthermore, TCR stimulation has been shown to result in the activation of the Hedgehog pathway in $CD8^+$ T cells (de la Roche et al., 2013). The initiation of this signalling pathway in mammalian cells has been considered to be exclusive to the functional membrane domain of the primary cilium (Bangs and Anderson, 2017), which is the focus of the next chapter. Although T lymphocytes do not have primary cilia, TCR activation at the $CD8^+$ immune synapse resulted in the stimulation of the Hedgehog pathway within intracellular compartments which translocated towards the synapse. Hedgehog signalling was also associated with the polarisation of the centrosome in a process mediated by RAC1, which is a regulator of the actin cytoskeleton (de la Roche et al., 2013).

3.1.1.2.4 Establishment of T cell asymmetry

One of the consequences of antigen recognition by T cells is their subsequent division into effector- and memory-fated daughter cells. In this way, the effector function is carried out in parallel with the production of self-renewing memory cells for long-term protection. This divergence of daughter cell fates is brought about by the process of asymmetric cell division, wherein specific fate-

determining factors are unequally distributed on either side of the mitotic plane. The formation of the immune synapse and subsequent polarisation of surface molecules and secretory organelles brings about this biased distribution. Synapse formation is therefore considered to trigger asymmetry in subsequent cell divisions (Chang et al., 2007). While not fully understood, this role is further supported by the bipolar distribution of polarity-mediating proteins in proliferating T cells following antigen presentation. These include the partition defective (PAR) proteins and the Scribble-Disc Large (SCRB-DLG) adaptor protein complexes. The aforementioned proteins are involved in the establishment of epithelial cell polarity and the mediation of asymmetric cell division. These proteins segregate to the synapse and the opposite end of the cell, and remain polarised in the T cell for up to 40 hours following antigen recognition, which is consistent with the occurrence of asymmetric cell division (Huse, 2012).

3.1.2 TCR signal initiation and transduction

TCR signalling is initiated by the recognition of antigen-derived peptides bound to MHC molecules by the TCRαß heterodimer, which together with CD3 proteins, makes up the TCR complex. CD3 proteins, which comprise three dimers (ζζ, εγ, and εδ), associate with the TCR via hydrophobic interactions (Weiss, 1993). While the CD3 proteins do not participate in antigen recognition, they are responsible for the ensuing signal transmission (Irving and Weiss, 1991). This is mediated by the presence of 10 immunoreceptor tyrosine-based activation motifs (ITAMs) in their cytosolic domains. These motifs have the general sequence of YxxL/Ix(6-8)YxxL/I, where two tyrosine residues each followed by leucine or isoleucine in the +3 position (YxxL/I) are separated by 6 – 8 residues (Cambier, 1995). Phosphorylation of these tyrosine residues by the lymphocyte-specific kinase (LCK) results in the recruitment of the kinase TCR zeta chain-associated protein of 70 kDa (ZAP70) (Weiss, 1993). ZAP70 interacts with the phosphorylated ITAMs via its two SRC homology 2 (SH2) domains, which recognise the phosphotyrosine residues (Gauen et al., 1994). The recruited ZAP70 is in turn phosphorylated by LCK, thereby becoming activated and phosphorylating the palmitoylated transmembrane scaffolding protein linker for the activation of T cells (LAT) and the SH2 domain–containing leukocyte protein of 76 kDa (SLP76) (Weil et al., 1995, Zhang et al., 1998, Wardenburg et al., 1996). These two proteins recruit various adaptors and effector enzymes and assemble a

multimolecular signalling network termed the LAT signalosome that drives multiple signal transduction pathways. As a result, T cell proliferation, cytoskeletal rearrangement, cytokine production, and other effector functions are activated (Balagopalan et al., 2010) **(Figure 3-2)**.

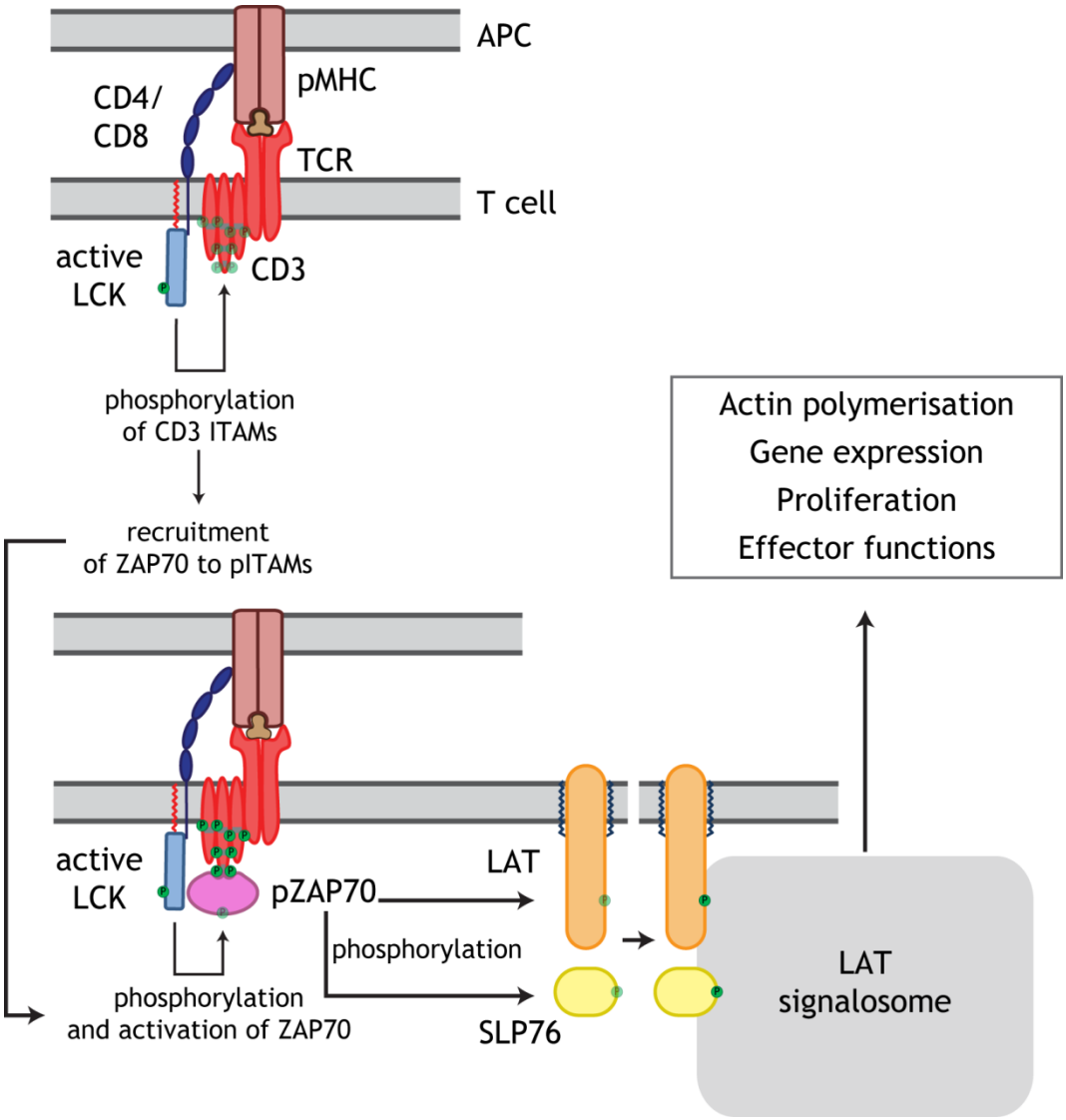

Figure 3-2 TCR signal transduction.

A simplified scheme of the events following pMHC recognition by the TCR: activated LCK phosphorylates (green circles) immunoreceptor tyrosine based activation motifs (ITAMs, grey) present on the cytosolic CD3 domains. The kinase ZAP70 is recruited and subsequently phosphorylated by LCK, resulting in its activation. pZAP70 then phosphorylates the linker for the activation of T cells (LAT) and the SH2 domain–containing leukocyte protein of 76 kDa (SLP76). The LAT signalosome is formed by the subsequent recruitment of multiple adaptors and enzymes, which drive different signalling pathways resulting in T cell activation. pITAM, phosphorylated ITAMs; APC, antigen-presenting cell; LCK, lymphocyte-specific kinase; TCR, T cell receptor; pMHC, peptide-major histocompatibility complex; pZAP70, phosphorylated zeta chain-associated protein kinase of 70 kDa.

Being responsible for the initial phosphorylation step following antigen recognition by the TCR, the recruitment and activation of LCK are critical processes for TCR signalling. It is therefore of no surprise that the activation of LCK undergoes tight phosphoregulation, which will be described in the next section. Two models have been proposed regarding the timing of LCK activation with respect to that of the TCR. Based on the presence of a pool of activated LCK in T cells prior to TCR activation, the "standby model" proposes that TCR activation does not affect LCK activation, but rather allows the function of already activated LCK. This may be due to the recruitment of active LCK to the TCR, or the exposure of ITAMs to the active LCK (Nika et al., 2010). The exposure of CD3 ITAMs has been suggested to be a consequence of mechanical forces applied by the reorganising cytoskeleton and/or the formation of catch bonds between TCRs and high affinity pMHCs (Comrie and Burkhardt, 2016). The proportion of active LCK in the cell has been disputed, however, due to the difficulty of accurate quantification of the pool of active LCK in the cell (Ballek et al., 2015). It has therefore been suggested by the "de novo activation model" that TCR activation triggers that of LCK, hence initiating signalling (Philipsen et al., 2017). Induction of LCK activation has been attributed by the "kinetic segregation model" to the exclusion of large phosphatases, which inhibit LCK, from the zone of close contact between the TCR and the APC at the immune synapse, as mentioned in **section 1.1.1**.

3.1.3 Lymphocyte-specific kinase (LCK)

LCK belongs to the SRC family of tyrosine kinases, whose members are involved in the regulation of various signal transduction pathways in different cell types. They are so named because the first identified member of the family, c-SRC, was discovered as an oncogene product in studies of the Rous sarcoma virus (Martin, 2001).

3.1.3.1 Domain organisation and function

The arrangement of LCK domains, which is conserved amongst members of the SRC kinase family (SFKs), is shown in **Figure 3-3**. The N-terminus targets the protein to the membrane, on account of the presence of acyl lipid modifications that help stabilise hydrophobic interactions. The glycine residue at position 2,

which is the myristoylation site, is conserved among SFKs. Cysteine residues at positions 3 and 5 of LCK undergo reversible palmitoylation (Caron et al., 1992, Paige et al., 1993). The N-terminal unique domain following the acylation sites spans about 60 residues and exhibits the most divergence of amino acid sequences between the different SFKs. A CxxC motif with cysteine residues at positions 20 and 23 mediates the Zn^{2+}-dependent association of LCK with a C-terminal CxCP motif present in the T cell surface molecules CD4 and CD8 (Turner et al., 1990, Kim et al., 2003). The N-terminal unique domain is followed by the SRC homology domains 3 and 2 (SH3 and SH2, respectively). These mediate intermolecular as well as intramolecular interactions.

The SH3 domain, which spans about 60 residues, recognises short polyproline PxxP motif-containing sequences that are present on other proteins as well as on LCK itself, which is important for regulation. The recognition site is a ß-strand–based structure with a hydrophobic interface to which the PxxP sequence binds to in a helical conformation (Yu et al., 1992, Yu et al., 1994). The SH2 domain comprises a central ß-sheet flanked by two α-helices which form binding pockets for a phosphotyrosine residue and a C-terminal hydrophobic side chain (Eck et al., 1993). Phosphotyrosine binding is also involved in intramolecular binding with the C-terminus of LCK.

The SH domains are connected to the kinase domain by a PxxP-containing linker which forms intramolecular interactions with the SH3 domain as described above. The kinase domain has a bi-lobed structure with the two lobes connected by a short hinge segment. The catalytic site where ATP binding and phosphate transfer takes place is located in the pocket between the two lobes. The C-terminal lobe also contains a regulatory activation loop of about 20 residues. Following the kinase domain is a short C-terminal tail, which is important for autoinhibition of the kinase as described in the next section (Boggon and Eck, 2004).

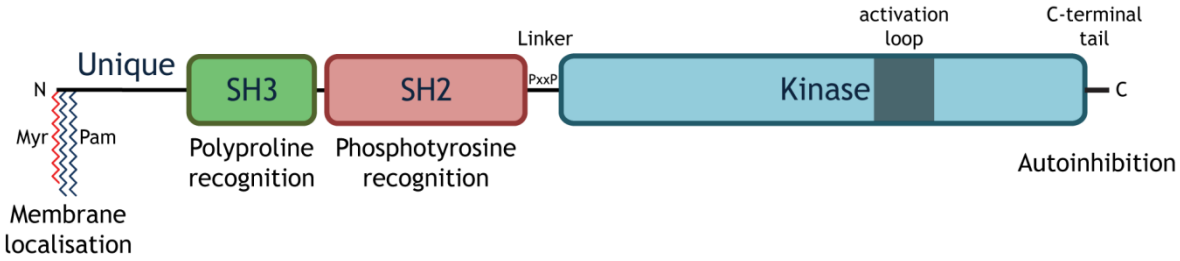

Figure 3-3 Domain structure of LCK.

The N-terminal acylation sites mediate membrane binding of LCK. The SH3 and SH2 domains recognise PxxP and phosphotyrosine sequences, respectively, and mediate interactions within the protein and with other binding partners. A PxxP-containing linker connects the kinase domain to the SH2 domain. The activation loop and the C-terminal tail contain the sites of the regulatory tyrosine residues. Myr, myristoyl; Pam, palmitoyl; SH, SRC homology domain.

3.1.3.2 Phosphoregulation of the kinase domain

The regulation of the activity of the kinase domain of SFKs is subject to the phosphorylation status of two conserved tyrosine residues, each of which mediates the activation or inhibition of the kinase. These are located in the activation loop near the catalytic site, and in the C-terminal tail following the kinase domain, respectively **(Figure 3-4A)**.

In LCK, phosphorylation of tyrosine 505 in the C-terminus results in the formation of a closed conformation due to the binding of the SH2 domain to the phosphotyrosine residue. Further intramolecular interactions between the SH3 domain and the PxxP-containing SH2-kinase linker further stabilise this conformation, as depicted in **Figure 3-4B**. While the SH3 and SH2 domains do not the block the active site of the kinase domain, the kinase domain undergoes conformational changes in the N-terminal lobe. These oppose the formation of a salt bridge that is important for the coordination the ATP phosphate groups (Xu et al., 1997). In addition, the normally disordered activation loop adopts a helical conformation that blocks the active site of the kinase domain and protects the activating tyrosine residue from phosphorylation (Xu et al., 1999).

Dephosphorylation of the inhibitory tyrosine 505 breaks open the autoinhibited conformation and restores the kinase domain to a more active state, with disordering of the activation loop. Trans-autophosphorylation of tyrosine 394 further enhances the activity of the kinase domain via stabilising the activation

loop in a conformation which is compatible with substrate binding to the pocket (Yamaguchi and Hendrickson, 1996) **(Figure 3-4C)**.

The phosphoregulation of LCK places its activity under the control of various kinases and phosphatases, some of which are shown in **Figure 3-4D**. Inhibitory phosphorylation of Y505 is catalysed by the C-terminal SRC-specific kinase (CSK) (Nada et al., 1991), and inhibitory dephosphorylation of Y394 is mediated by the SH2-containing phosphatase 1 (SHP1) (Chiang and Sefton, 2001). The phosphatase CD45 functions as both an activator and an inhibitor of LCK, depending on the site of dephosphorylation (Mustelin et al., 1989, D'Oro and Ashwell, 1999); although, it has been reported that the latter function is performed more efficiently by CD45 (McNeill et al., 2007). In the same way, trans-autophosphorylation catalysed by other LCK molecules can either enhance or decrease the kinase activity**.**

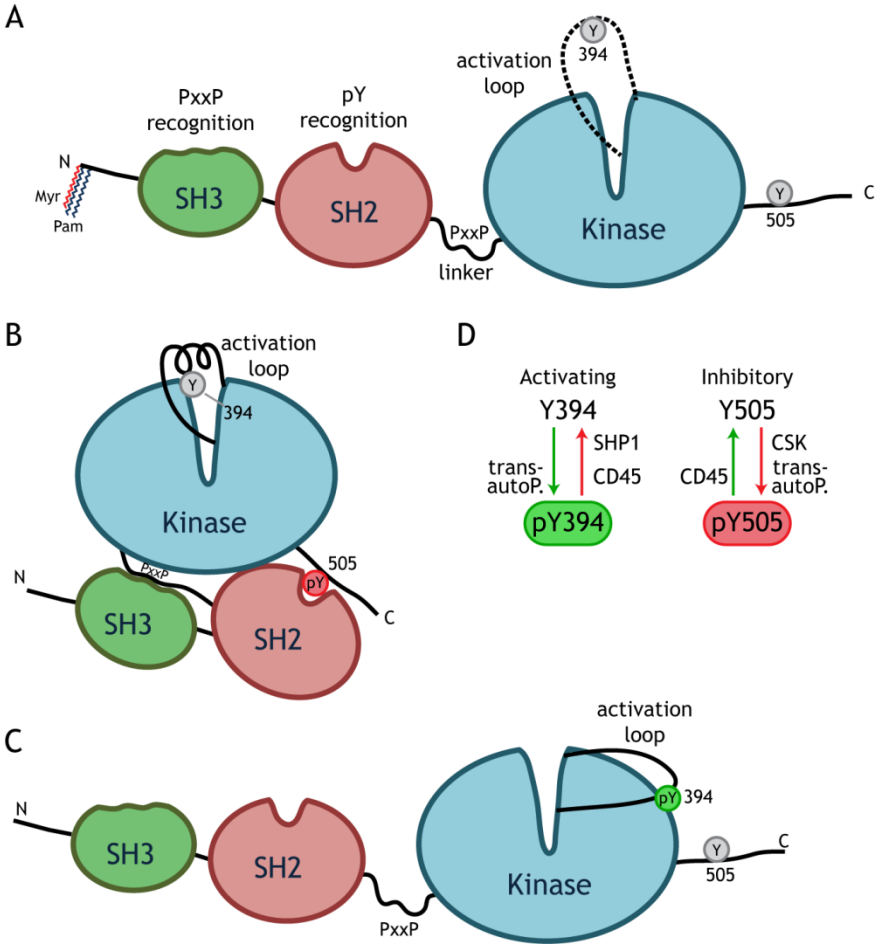

Figure 3-4 Phosphoregulation of the kinase domain of LCK.

(A) The phosphorylation status of two conserved tyrosine residues (grey circles) regulates the activity of the kinase domain: Y394 in the activation loop of the kinase domain and Y505 in the

C-terminal tail of the protein. In absence of Y394 phosphorylation, the activation loop is disordered. **(B)** Phosphorylation of the inhibitory Y505 (red circle) results in the formation of a closed conformation due to phosphotyrosine (pY)-SH2 domain and PxxP linker-SH3 domain intramolecular interactions. The activation loop, in absence of Y394 phosphorylation, obstructs the active site of the kinase domain. **(C)** Dephosphorylation of Y505 and phosphorylation of Y394 (green circle) results in the formation of the open, active conformation of LCK, with the activation loop stabilised away from the kinase domain active site. **(D)** CD45, CSK, SHP1, and LCK itself can all affect the phosphorylation status of Y394 and/or Y505; green arrows indicate activation of LCK while red arrows indicate inhibition. Trans-autoP., trans-autophosphorylation; CSK, C-terminal SRC-specific kinase, SHP1, SH2-containing phosphatase 1.

3.1.3.3 Recruitment to the immune synapse

Being the initiator of TCR signalling, the arrival of LCK to the site of pMHC recognition and immune synapse formation is critical. LCK has been shown to localise to the plasma membrane in resting Jurkat T cells (Ley et al., 1994). Membrane association of LCK is made possible via its N-terminal myristoyl and palmitoyl groups. LCK has also been reported to associate to the T cell coreceptors CD4 and CD8, whose extracellular domains in turn bind to MHC molecules (Veillette et al., 1988). However, this association is not the sole reason for LCK membrane localisation, as LCK expressed in fibroblasts which lack T cell-specific proteins also localised to the membrane. Membrane localisation was found to be dependent on the presence of the N-terminal acylation sites (Bijlmakers et al., 1997).

The endosomal pathway has been proposed as the route of LCK trafficking. Studies in Jurkat T cells tracing protein localisation following synthesis showed that both LCK and CD4 localise rapidly to intracellular membranes after synthesis, followed by membrane localisation via a slower process. The rate of LCK membrane association was primarily affected by the palmitoylation of the N-terminus and not by the absence of CD4. Membrane association was also slowed down but not abrogated by the inhibition of the exocytic pathway via Brefeldin A treatment. These results implicated vesicle trafficking in LCK targeting but also suggested a role for another independent pathway (Bijlmakers and Marsh, 1999). Endosomal proteins RAB11 and CD222 have also been reported to affect LCK trafficking and the myelin and lymphocyte (MAL) protein has been reported to associate with LCK on endosomes (Gorska et al., 2009, Pfisterer et

al., 2014, Antón et al., 2008). Later studies using single molecule fluorescence microscopy showed the presence of a cytosolic soluble fraction of LCK that exhibited free diffusion in the cytoplasm until trapping at the membrane by subsequent palmitoylation (Zimmermann et al., 2010).

The rapid trafficking of LCK to the immune synapse followed by its retention in the specialised membrane domain remains not fully understood. As discussed in **section 1.3.2**, myristoylated cargo is trafficked to the specialised domain of the primary cilium via a system comprising the GDI-like solubilising factor UNC119 and the small G proteins ARL3 and ARL13B. Despite being absent from the surface of lymphocytes, primary cilia have been shown to share several structural similarities as mentioned in **section 1.1.3**.

While UNC119 has been reported to be involved in LCK trafficking, it was in the context of activating RAB11 in the endocytic pathway (Gorska et al., 2009) and not via the solubilisation of the myristoyl moiety. The observation of the presence of a soluble fraction of LCK in the cytoplasm gives rise to the question if that is achieved by the binding of UNC119. We therefore set out to investigate the possibility of a role for ciliary trafficking machinery in the transportation of LCK to the membrane domain of the immune synapse.

3.2 Results

3.2.1 LCK binds to the GDI-like solubilising factor UNC119A

3.2.1.1 Ciliary proteins are expressed in Jurkat T cells

The possibility of whether LCK is being trafficked to the immune synapse by way of ciliary machinery primarily depends on the presence of these cilia proteins in T cells, which lack primary cilia. **Figure 3-5A** shows Western blots in which UNC119, ARL13B, and ARL3 were detected in Jurkat T cell lysate.

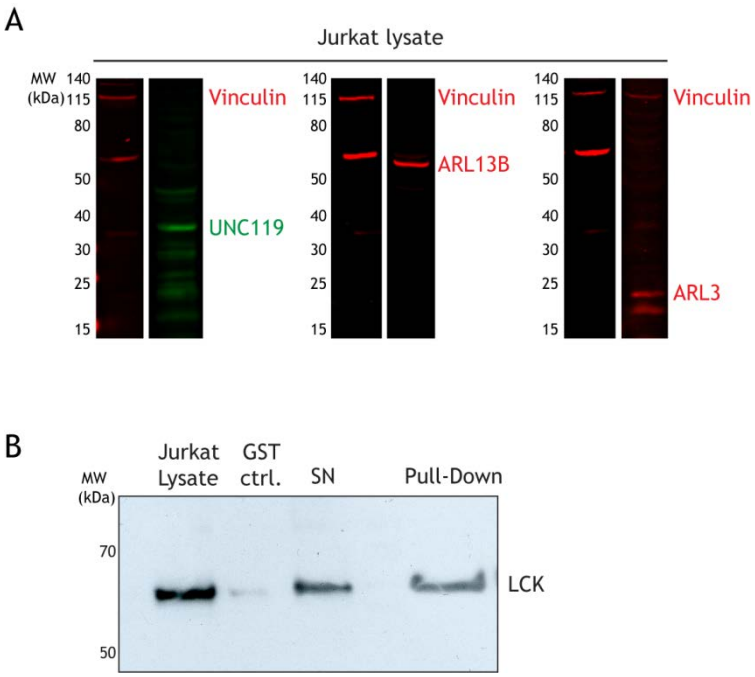

Figure 3-5 Ciliary proteins are present in Jurkat T cells.
(A) Protein concentration of Jurkat T cell lysate was quantified and 50 µg of total protein was loaded per lane. Antibodies against UNC119, ARL13B, ARL3, and vinculin were used on separate lanes to detect the proteins. Anti-vinculin staining is shown in the first lane of each pair. **(B)** 30 µg GST-tagged full-length UNC119A was used with glutathione sepharose beads in a GST pull-down assay with Jurkat cell lysate. The Western blot shows the presence of LCK in the lysate, the supernatant fraction (SN), and the pull-down, but not in the UNC119A negative control (GST ctrl.), where GST was added to the beads instead of GST-UNC119A.

With the presence of these ciliary proteins confirmed in Jurkat T cells, the next step was to investigate if the GDI-like solubilising factor UNC119A is able to interact with LCK in the T cell lysate. Recombinant GST-tagged full-length UNC119A was expressed in and purified from BL21(DE3)CodonPlus *E. coli* cells

and used in a GST pull-down assay with Jurkat T cell lysate. LCK was detected in the elute only when GST-UNC119A had been loaded on to the glutathione sepharose beads, indicating that UNC119A is capable of binding LCK amongst other T cell proteins **(Figure 3-5B)**.

3.2.1.2 UNC119A binding is specific to LCK

To test whether the UNC119A binding to LCK was due to a specific and direct interaction between these two proteins, I used a fluorescence polarisation assay to assess the binding of an LCK peptide to UNC119A. Polarisation of a fluorescently-labelled peptide in solution inversely correlates to its size, and therefore the increase in polarisation upon addition of UNC119A to the peptide gives an indication of the binding between them **(Figure 3-6A)**.

Through monitoring the fluorescence polarisation during the addition of increasing amounts of UNC119A to a solution of fluorescently-labelled LCK peptide, the binding affinity of UNC119A to the peptide can be measured. In this way, I measured the binding affinity of a fluorescently-labelled, myristoylated N-terminal peptide of LCK to UNC119A, and compared it to that of a similar c-SRC peptide. c-SRC is another member of the SRC family of kinases to which LCK belongs. If the binding of UNC119A is specific to LCK, then there should be a difference in the binding affinity of UNC119A to LCK compared to that of c-SRC. Indeed, by titrating in UNC119A to solutions of the peptides, LCK showed a much higher binding affinity to UNC119A compared to that of c-SRC. **Figure 3-6B** shows the fluorescence polarisation values obtained with the addition of increasing amounts of UNC119A. Fluorescence polarisation for both peptides was plotted against UNC119A concentration and the data was fitted to a quadratic equation. The binding affinities were calculated as 2.2 ± 0.7 nM for LCK and 125 ± 69 nM for c-SRC **(Figure 3-6C)**. LCK therefore has an affinity to UNC119A 50 times higher than that of c-SRC, indicating the specificity of the binding of LCK to UNC119A.

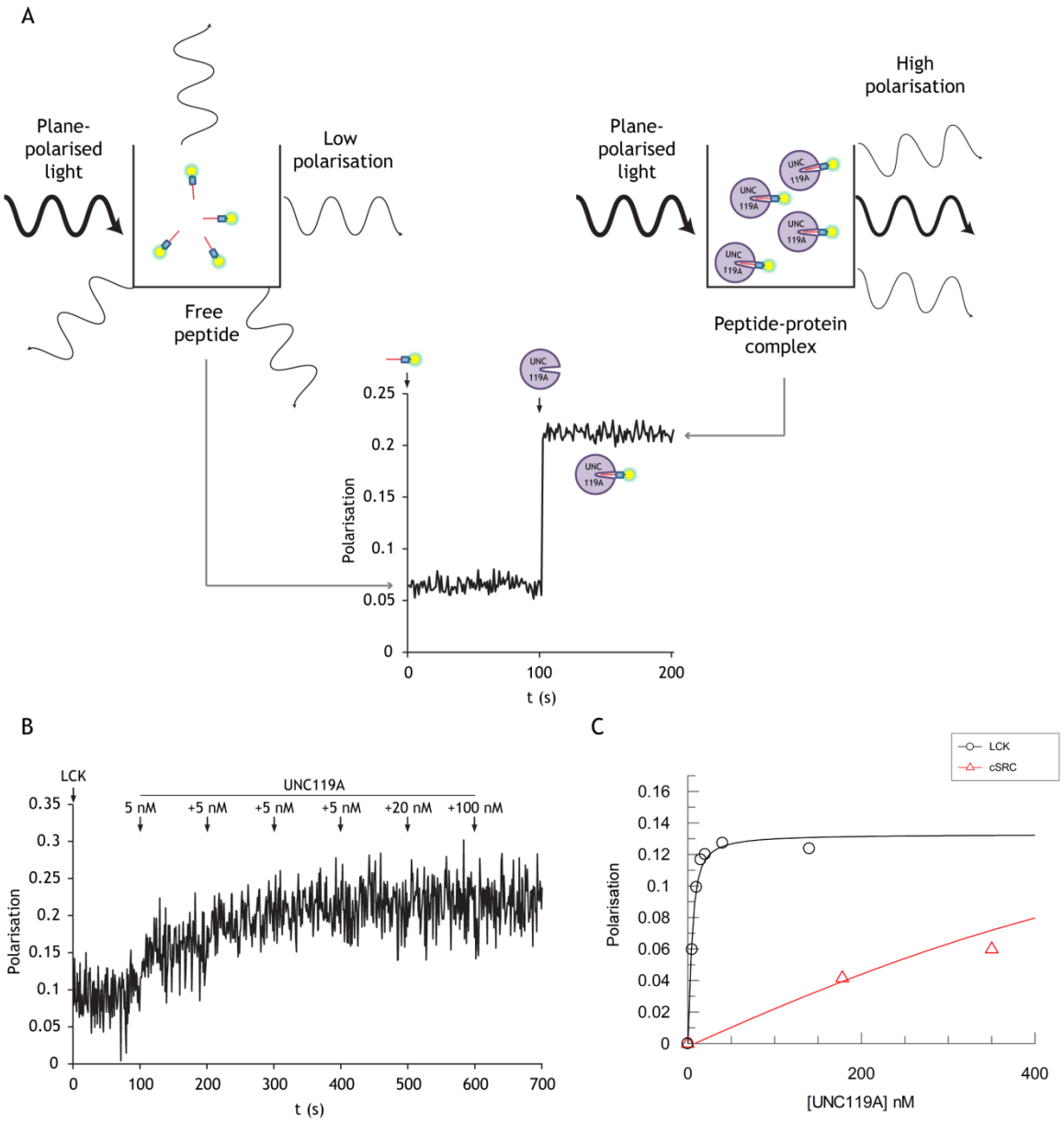

Figure 3-6 Using fluorescence polarisation to assess LCK-UNC119A binding.
(A) Fluorescence polarisation gives an indication of peptide-protein interaction. Free fluorescently-labelled peptide in solution is small in size and will therefore have a high rate of tumbling, which results in depolarisation of the emitted light. Binding of a larger protein to the peptide increases its size and slows down its tumbling, thereby increasing the probability of light being emitted in the same plane as the plane-polarised excitation light. **(B)** Full-length UNC119A was added as indicated every 100 s to a 5 nM solution of fluorescein-labelled myristoylated N-terminal peptide of LCK and fluorescence polarisation was measured. **(C)** Average changes in fluorescence polarisation were plotted against the concentration of UNC119A added to solutions of 5 nM LCK (black) or 0.5 µM c-SRC (red) fluorescently-labelled peptides. Binding affinities for LCK and c-SRC were calculated as 2.2 ± 0.7 nM and 125 ± 69 nM, respectively. The data was fitted to a quadratic equation using GraFit analysis software (Erithacus Software).

3.2.1.3 Interaction between UNC119A and LCK is myristoylation-dependent

LCK undergoes myristoylation, a lipid modification which is catalysed by the enzyme N-myristoyl transferase (NMT) following the removal of the initiator methionine residue **(Figure 3-7A)**. While the N-terminal LCK peptide used in the polarisation experiments was myristoylated, its length only spanned residues 2 - 11. To further investigate the interaction between UNC119A and LCK, I used recombinant GST-tagged UNC119A to pull down two longer 6×His-tagged LCK constructs comprising the N-terminal domains up to the SH3 domain (LCK^{1-121}, LCK SH3) and to the SH2 domain (LCK^{1-226}, LCK SH3-SH2) **(Figure 3-7B)**. These were expressed in BL21(DE3)pLysS cells, which do not have N-myristoyltransferase, and therefore the purified proteins were not myristoylated. To overcome this problem, the purified proteins were used for *in vitro* myristoylation, whose conditions were optimised previously in our lab. The various LCK constructs were incubated with recombinant NMT and myristoyl coenzyme A, and then added to GST-UNC119A and glutathione sepharose beads. Two constructs of GST-UNC119A were used, one being full-length (UNC119A-FL) and the other having an N-terminal truncation ($UNC119A^{54-240}$, UNC119A-Δ54) **(Figure 3-7B)**. **Figure 3-7C** shows the results of these pull-downs, where LCK SH3 and SH3-SH2 were pulled down with full-length and truncated GST-UNC119A following *in vitro* myristoylation in the presence and absence of NMT. The pull-downs showed that both N-terminal LCK constructs only bound to UNC119A when NMT was present in the myristoylation reaction. This indicates that the interaction depends on LCK myristoylation, and occurs independently of the SH2 domain, as both LCK SH3-SH2 and LCK SH3 show binding.

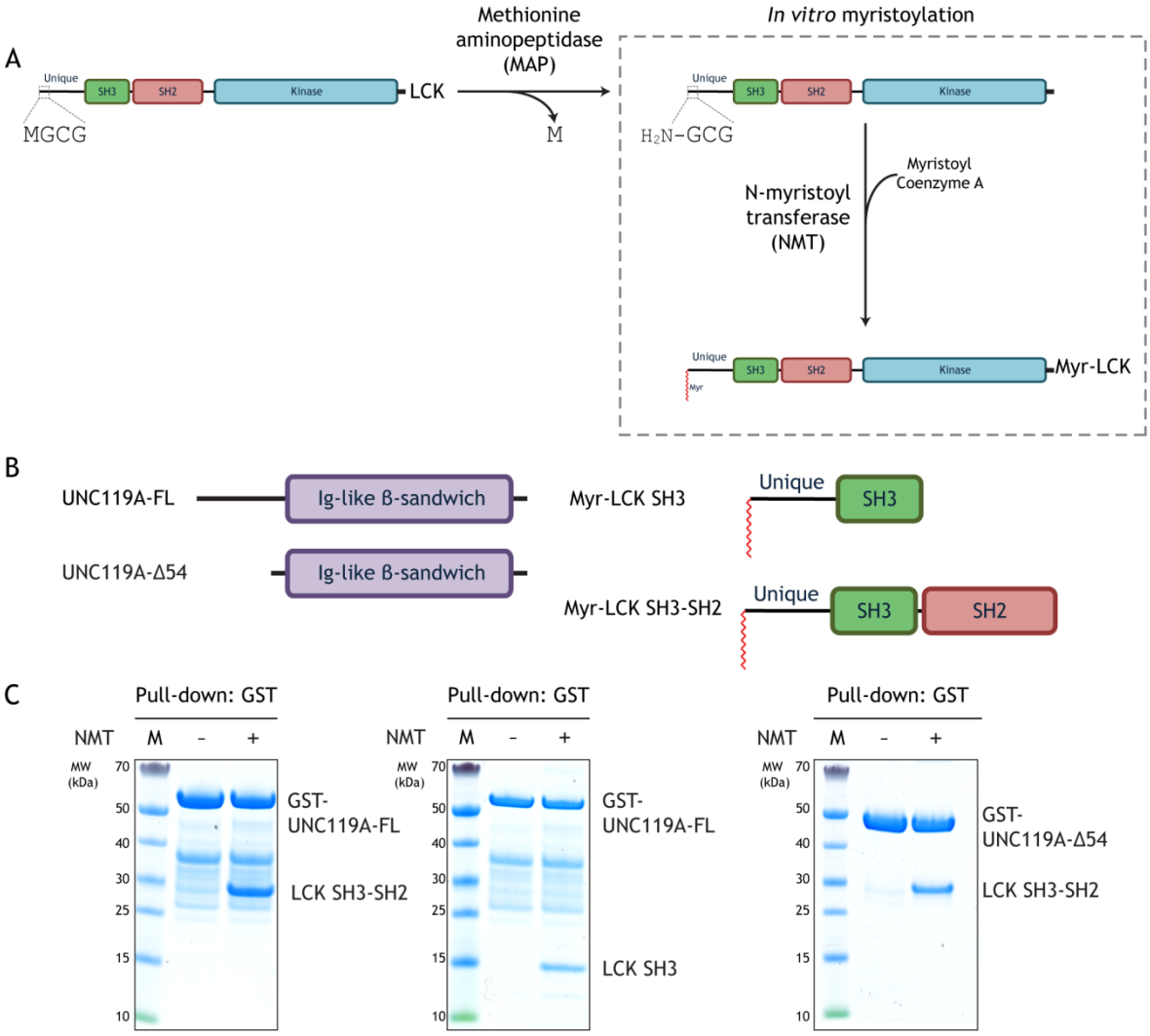

Figure 3-7 UNC119A binds to the N-terminal domains of LCK in a myristoyl-dependent manner.

(A) Myristoylation is a co- and post-translational modification which involves the removal of the initiator methionine residue, followed by the addition of a 14-carbon saturated myristoyl group to the amino group of the remaining N-terminal glycine residue. **(B)** LCK and UNC119A constructs used to map the myristoyl-dependent interaction with UNC119A. **(C)** 100 µg GST-tagged full-length UNC119A was used to pull down 200 µg purified LCK SH3 or LCK SH3-SH2 after *in vitro* myristoylation with 2.5 µM NMT and 100 µM Myristoyl-CoA. The pull-down was also carried out with UNC119A-Δ54 and LCK SH3-SH2. The elutes were run on SDS-PAGE and stained with Coomassie. FL, full-length; M, protein ladder; NMT, N-myristoyltransferase; UNC119A-Δ54, N-terminally truncated UNC119A; Ig, immunoglobulin.

3.2.1.4 UNC119A-LCK binding is disrupted specifically by ARL3

High affinity ciliary proteins that are transported by UNC119A have been shown to be specifically released by the nucleotide-dependent binding of the small G protein ARL3 and not its non-ciliary homologue ARL2 (Wright et al., 2011b). The allosteric binding of ARL3GTP induces a conformational change mediated by its

N-terminal amphipathic helix that opens the UNC119A pocket and results in the release of the myristoylated cargo (Ismail et al., 2012). To test the effect of ARL3 on the LCK-UNC119A binding, fluorescence polarisation measurements were carried out where UNC119A was added to the fluorescein-labelled LCK peptide, followed by ARL3 or ARL2 that was loaded with the non-hydrolysable GTP analogue GppNHp. As previously mentioned, a decrease in polarisation following ARL addition would indicate that the peptide was released from UNC119A and has regained its small size, resulting in depolarisation. LCK was released from UNC119A by GppNHp-loaded ARL3 but not ARL2 **(Figure 3-8A)**. In contrast, c-SRC was released from UNC119A by both ARL2 and ARL3, which is consistent with its lower affinity to UNC119A.

To further demonstrate the difference between ARL2 and ARL3 with respect to LCK release, GppNHp-loaded ARL proteins were titrated against UNC119A-LCK peptide complexes. Monitoring fluorescence polarisation shows that while increasing concentrations of ARL3 resulted in partial LCK release, the same was not true for addition of ARL2 **(Figure 3-8C,** right**)**. The polarisation measurements also showed that complete release of the LCK peptide was not achieved, even with the addition of 200-fold excess of ARL3 compared to UNC119A **(Figure 3-8C,** left**)**. The partial release by ARL3 in both of the previous experiments shows that the ARL3-mediated release is due to an allosteric interaction with UNC119A, forming a ternary complex with a lower affinity to LCK. In addition, ARL2 and ARL3 on their own cannot bind to the LCK peptide, and therefore this release is due to their effect on UNC119A **(Figure 3-8D)**.

ARL3-mediated release was also evident in the case of the binding between UNC119A and *in vitro* myristoylated LCK SH3-SH2. Pulling down *in vitro* myristoylated LCK SH3-SH2 is reduced in the presence of ARL3, but not with ARL2, confirming that ARL3 specifically releases this myristoylation-dependent interaction **(Figure 3-8E)**.

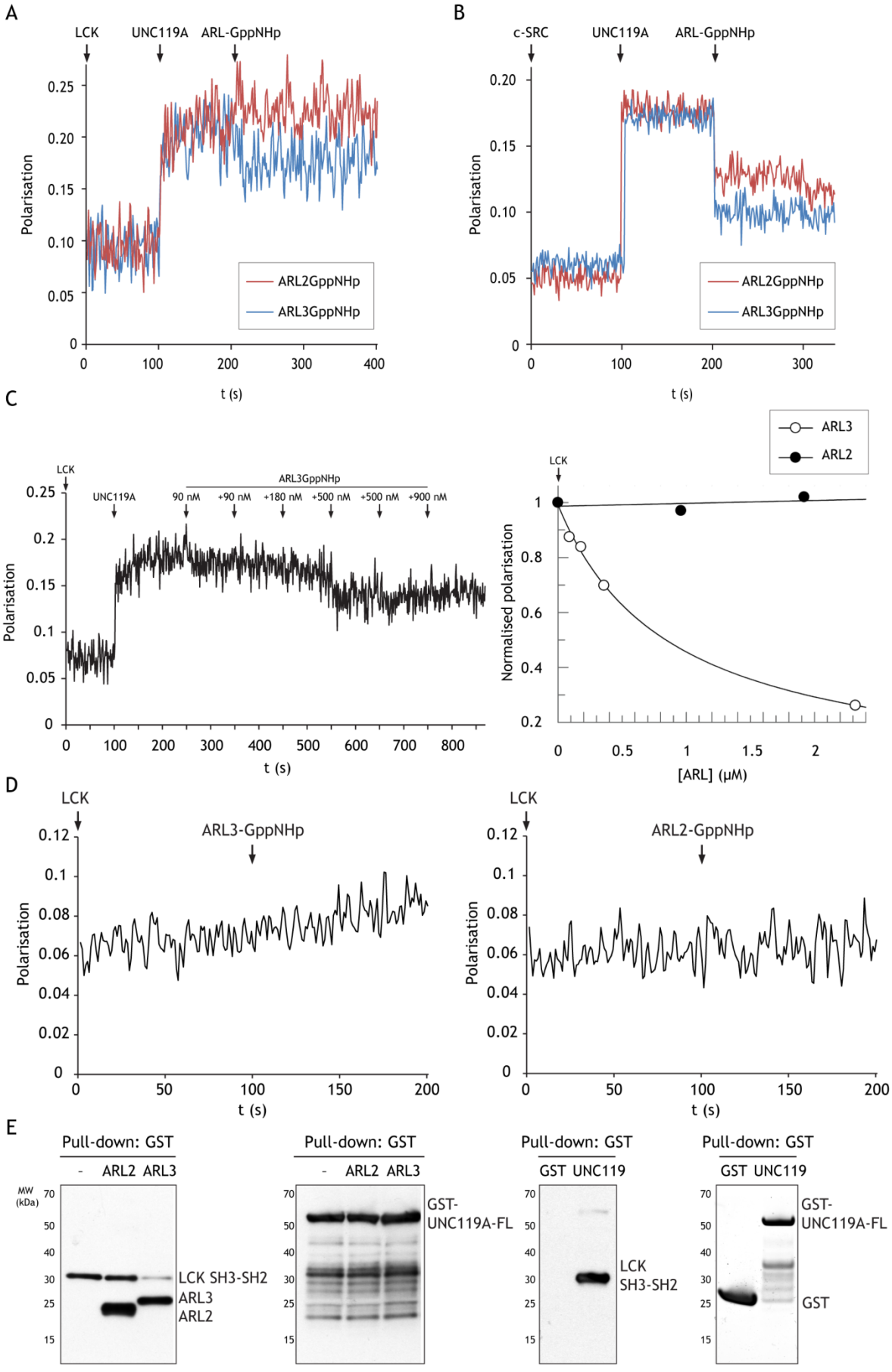

Figure 3-8 ARL3 specifically releases LCK from UNC119A.

(A) Fluorescence polarisation measurements where 10 nM full-length UNC119A was added to 5 nM fluorescein-labelled LCK peptide, followed by 500 nM GppNHp-loaded ARL2 (red) or ARL3 (blue). **(B)** The previous experiment was repeated, but with 0.5 µM full-length UNC119A added to 0.5 µM fluorescein-labelled c-SRC peptide, followed by 5 µM ARL2- or ARL3-GppNHp (red and blue curves, respectively). **(C)** Left, 10 nM UNC119A was added to 10 nM LCK peptide, followed by the indicated concentrations of ARL3GppNHp; fluorescence polarisation was measured throughout. Right, the same experiment was repeated but with ARL2GppNHp, and the average polarisation values normalised to the maximum value obtained in each experiment were plotted against the concentration of ARL added to the UNC119A-LCK complex. **(D)** 5 µM GppNHp-loaded ARL3 (left) or ARL2 (right) was added to a 20 nM solution of LCK peptide, and fluorescence polarisation was monitored. **(E)** 100 µg GST-tagged full-length UNC119A was used to pull down *in vitro* myristoylated LCK SH3-SH2 with the pull-downs carried out in the presence and absence of 200 µg GppNHp-loaded ARL2 and ARL3 (panels 1 and 2). Myristoylated LCK SH3-SH2 was also pulled down using 50 µg GST (panels 3 and 4). LCK, ARL2, and ARL3 were visualised using an anti-His antibody, while GST and GST-UNC119A were visualised using an anti-GST antibody.

3.2.2 Structural basis of high UNC119A affinity to LCK

3.2.2.1 Purification of UNC119A-LCK SH3-SH2 complexes

We carried out crystallisation screens at 4°C and 19°C using purified complexes of UNC119A with LCK SH3-SH2. The complex was attempted with both full-length and N-terminally truncated UNC119A (UNC119A$^{54-240}$). The shorter UNC119A construct was also tested as the presence of the N-terminus of UNC119A has been previously shown to oppose crystallisation due to its being disordered (Ismail et al., 2012). His-tagged LCK SH3-SH2 was used for *in vitro* myristoylation in the presence of GST-tagged UNC119A. The complex was bound to a glutathione sepharose GSTrap column to remove the components of the myristoylation reaction. Thrombin was then used to cleave the GST-tag of UNC119A and elute the complex. Further purification was carried out by a nickel affinity chromatography step, followed by size exclusion chromatography. The purification workflow is summarised in **Figure 3-9**.

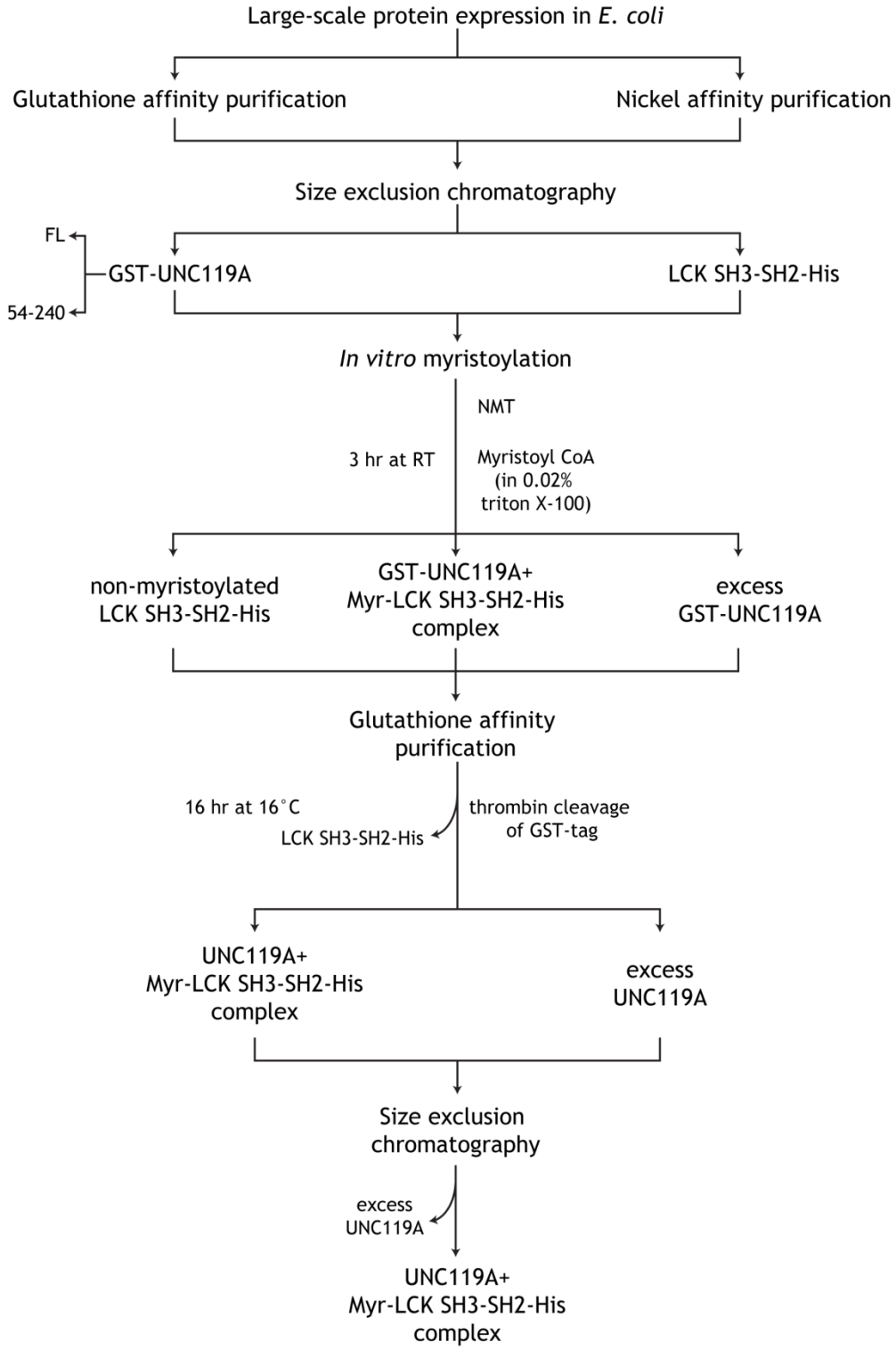

Figure 3-9 Purification of LCK SH3-SH2 complexes with UNC119A.

GST-tagged full-length and N-terminally truncated UNC119A and His-tagged LCK SH3-SH2 were expressed in competent *E. coli* cells. The tagged proteins were then separated from bacterial cell lysates by the appropriate affinity purification, followed by size exclusion chromatography. *In vitro* myristoylation reactions were set up with the purified LCK and UNC119A, in addition to NMT and myristoyl coenzyme A in a solution of 0.02% triton X-100. The reactions were incubated for three hours at room temperature before removing non-myristoylated LCK SH3-SH2 by glutathione affinity chromatography. The bound GST-UNC119A+LCK complex and excess GST-

UNC119A were eluted by cleaving the GST-tag through digestion with thrombin digestion, which was pumped through the column in a closed loop for 16 hours at 16°C. Finally, the complex was separated from excess UNC119A by size exclusion chromatography.

However, all attempts with these complexes failed to crystallise, possibly due to the harsh conditions of the *in vitro* myristoylation reaction, which involved incubating the protein for three hours at room temperature in the presence of 0.02% triton X-100.

3.2.2.2 Structure of UNC119A-LCK peptide complex

Data collection and analysis described in this section were carried out by Shehab Ismail, Michael McIlwraith, and Tamas Yelland and are included here with their permission.

Crystallisation screens were also carried out using 1:1 complexes of a myristoylated N-terminal peptide of LCK spanning residues 2 – 11 with full-length and truncated UNC119A. While the LCK peptide is much shorter than the LCK SH3-SH2 construct, it allowed the formation of a complex without having to carry out *in vitro* myristoylation of LCK. Of these attempts, crystals were obtained with the UNC119A$^{54-240}$-LCK peptide complex. Crystals were observed at 4°C in a screen using the PEGs suite (Qiagen), with the hit condition comprising 20% (w/v) PEG 3350 and 0.2 M KH_2PO_4. The crystals were flash-frozen in 25% (v/v) glycerol diluted in the mother liquor.

Following data collection, integration was done using automated XDS, and scaling using the CCP4 program suite. Using the structure of UNC119A in complex with transducin-α (GNAT1) (PDE code 3RBQ) as a search model, molecular replacement was performed using Molrep. Refinement was carried out using Refmac5 and model building was done in WinCoot. The refined structure of the complex was at 2 Å resolution **(Figure 3-10A)**. The asymmetric unit contained three molecules of the UNC119A-LCK complex, only one of which showed LCK residues beyond position 5. The first four amino acids of the LCK peptide were visible in all three molecules, and had the same structure. The myristoyl group and the first three residues of the LCK peptides were enclosed in the UNC119A pocket **(Figure 3-10B)**. Data collection and refinement statistics are summarised in **Table 3-1**.

The UNC119A structure is composed of residues 59 – 238, excluding residues 109-121 due to absence of observed electron density. The UNC119A pocket is formed by an immunoglobulin-like ß-sandwich fold, similar to that previously reported in the UNC119A-GNAT1 complex structure (PDB code 3RBQ). This is composed of nine ß-strands (ß1-ß9) that form two beta sheets (with four and five strands, respectively) which make up the Greek key motif. Strands ß3-ß4 and ß7-ß8 are connected by short α-helical loops, α1 and α2, respectively. These loops are situated on the side opposite to that of the entrance of the pocket **(Figure 3-10C)**. Together, these ß-strands form a barrel-like structure whose interior is lined with hydrophobic residues that form the myristoyl-binding pocket.

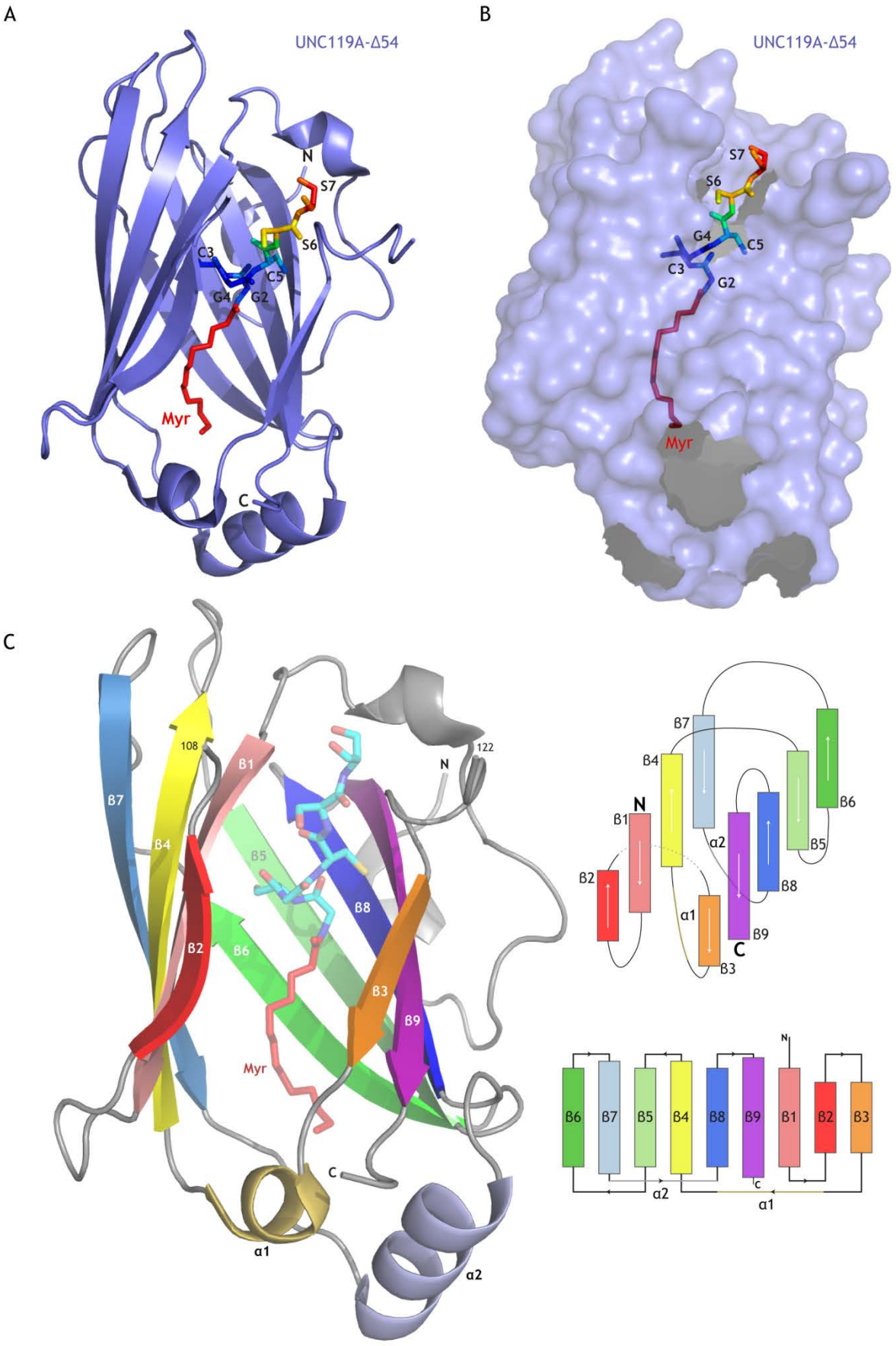

Figure 3-10 Crystal structure of UNC119A$^{54-240}$-LCK peptide complex.

(A) Crystal structure of UNC119A (purple cartoon) bound to a myristoylated N-terminal LCK peptide (myristoyl group in red and peptide in blue to red, indicating increasing B-factors

ranging from 23.95 to 74.91). LCK peptide residues are labelled with their amino acids and positions, and the N- and C-termini of UNC119A are indicated. **(B)** UNC119A$^{54-240}$-LCK peptide structure with UNC119A shown in surface representation. Serine residues 6 and 7 of LCK are shown protruding outside the UNC119A pocket opening. **(C)** Left, cartoon representation of the structure of the immunoglobulin-like ß-sandwich fold of UNC119A, with its nine ß-strands labelled and marked in pale red to violet (N-terminus to C-terminus). The loop connecting ß2-ß3 (P108-D122) is missing from the structure. The N- and C-termini are labelled, as are the α-helical loops α1 and α2, which connect strands ß3-ß4 and ß7-ß8, respectively. Right, schematic representations of the ß-strands in the fold and their connecting loops (top) and the Greek key motif formed by the ß-strands (bottom). PDB code 6H6A (Stephen et al., 2018).

Table 3-1 Data collection and refinement statistics.

R_{work} was calculated using 95% of the total reflections; the remaining 5% were used to calculate R_{free} and test the model in an unbiased manner. Highest resolution values are represented in parenthesis.

Data Collection	
Space group	$P2_12_12_1$
Cell dimensions	
a, b, c (Å)	50.09, 63.62, 188.16
α, ß, γ (°)	90, 90, 90
Resolution (Å)	94.08 – 2.00 (2.05 – 2.00)
R_{sym}	0.09 (0.54)
I/σ(I)	12.4 (3.9)
Completeness (%)	99.8 (99.74)
Redundancy	6.5 (6.4)
Refinement	
No. of reflections	39393
R_{work} / R_{free}	17.10/21.220
No. of atoms	
Protein	4316
Ligand/ion	105
Water	270
B-factors	
Protein	31.84
Ligand/ion	40.59
Water	36.19

The UNC119A-LCK peptide crystal structure was compared to those previously reported of UNC119 in complex with NPHP3 (Jaiswal et al., 2016) and with a transducin-α-(GNAT1)-mimicking peptide (Zhang et al., 2011). Superimposition of these structures with that of the UNC119-LCK complex shows that LCK peptide adopts a similar conformation to that of the ciliary proteins within the UNC119 pocket **(Figure 3-11)**.

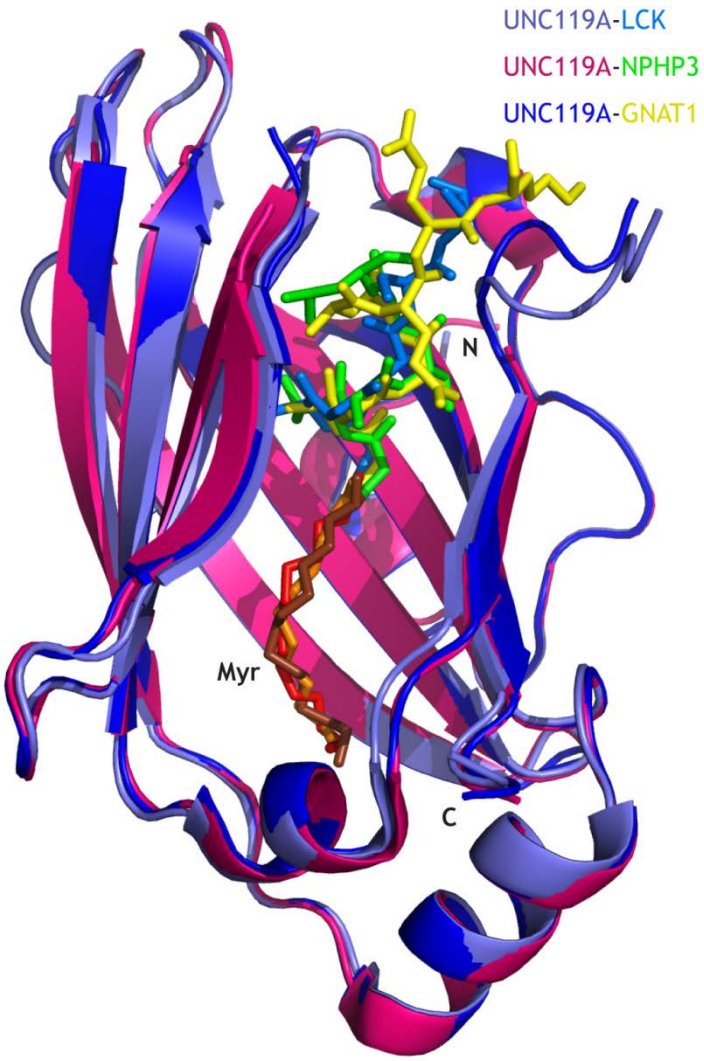

Figure 3-11 Structures of UNC119-peptide complexes.

Superimposition of UNC119 structures (cartoon representations) in complex with peptides of LCK (PDB code 6H6A (Stephen et al., 2018)) and NPHP3 (PDB code 5L7K (Jaiswal et al., 2016)), and a GNAT1-mimicking peptide (PDB code 3RBQ (Zhang et al., 2011)). The N- and C-termini of UNC119 are labelled and the myristoylated peptides are shown in stick representation.

3.2.2.3 ARL3-mediated release of LCK from UNC119A

To study the ARL3-mediated release of LCK, I superimposed of the structure of UNC119A in complex with LCK with that of UNC119 in complex with ARL3 (PDB code 4GOJ) (Ismail et al., 2012). ARL3 binds to UNC119 through the interaction of ß2 of ARL3 and ß7 of UNC119A. As shown in **Figure 3-12A**, superimposition of the structures of UNC119A-ARL3 and UNC119A-LCK shows that the binding site of ARL3 does not interfere with the opening of the UNC119A pocket. This supports the allosteric mechanism of release indicated by the fluorescence polarisation LCK peptide release assays **(Figure 3-8)**.

The structures show that the release of LCK is similar to that of ciliary cargo, where the binding of ARL3 results in conformational changes of residues within the hydrophobic pocket **(Figure 3-12A)**. The ciliary protein NPHP3 has previously been shown to bind to UNC119B, which is a homologue of UNC119A with 55% sequence identity **(Figure 3-12B)**. This binding has been shown to be crucially dependent on the hydrophobic interactions formed with the conserved phenylalanine residues 144, 148, and 207 (Wright et al., 2011b). Through sequence alignment, I identified the respective equivalent residues in UNC119A to be F133, F137, and F196. Comparing the conformations of these residues in the presence and absence of ARL3 binding to UNC119A shows that all three side chains move away from the myristoyl moiety, resulting in disruption of their hydrophobic interactions. ARL3 binding also results in the movement of loop λ9 away from the pocket, and the conformational change of Y194, which is part of the UNC119A hydrophobic pocket. As a result of this conformational change, Y194 moves away from the myristoyl moiety, and the pocket is widened **(Figure 3-12C)**. The disruption of interactions with the myristoyl moiety, in addition to the increased size of the UNC119A pocket, result in the reduction of UNC119A affinity to the myristoylated LCK N-terminus, and hence its release.

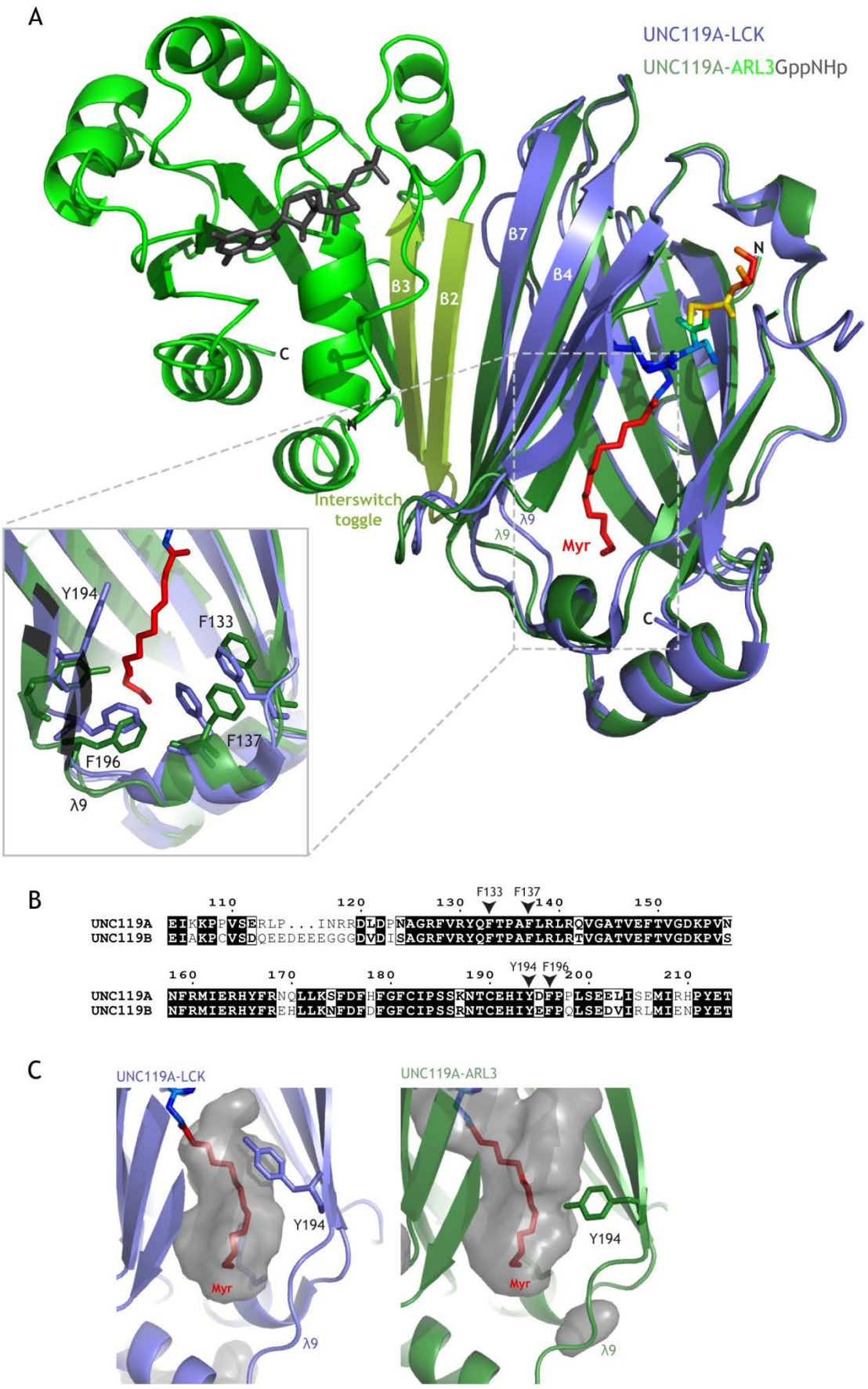

Figure 3-12 Mechanism of ARL3-mediated release of LCK from UNC119A.

(A) Superimposition of structures of UNC119A in complex with LCK (purple) and ARL3GppNHp (green); PDB codes 6H6A (Stephen et al., 2018) and 4GOJ (Ismail et al., 2012), respectively. LCK

peptide in the former is shown in stick presentation with the myristoyl moiety in red. ARL3 in the latter complex is shown in bright green cartoon representation, with GppNHp as grey sticks. Interacting ß-strands ß7 of UNC119A and ß2 of the interswitch toggle region of ARL3 are labelled. Loop λ9 in both UNC119A structures is also indicated, as are N- and C-termini of both UNC119A and ARL3. Conformational changes of F133, F137, F196, and Y194 in the hydrophobic pocket upon ARL3 binding are shown in the grey box. **(B)** Alignment of UNC119A and UNC119B sequences forming part of their hydrophobic pockets. Residues shown to be crucial to myristoyl binding are labelled with black arrows. **(C)** Close-up view of the UNC119A pocket in complex with LCK peptide (purple) and ARL3GppNHP (green). The pocket cavity is shown in grey surface representation, and residue Y194 is shown as sticks in both structures.

3.2.2.4 Basis of high affinity of LCK to UNC119A

The crystal structure of UNC119A in complex with the LCK peptide shows that, beyond the myristoyl group, only the first few amino acids of LCK are situated within the UNC119A pocket. Investigating the basis for the high affinity of the LCK peptide to UNC119A would therefore have to start at the N-terminal sequence of LCK. A closer look at the structure shows that space inside the UNC119A pocket is limited, but the peptide is accommodated as its N-terminal amino acids are small in size (glycine residues at positions 2 and 4; cysteine residues at positions 3 and 5). Aligning the N-terminal sequence of LCK with that of known ciliary cargo proteins of UNC119 reveals that the small size of N-terminal residues (positions 2 – 5) is a common feature **(Figure 3-13)**. In contrast, other members of the SRC kinase family did have larger residues in these N-terminal positions; for example, arginine 4 in HCK and lysine 5 in c-SRC. These large residues are likely to cause steric clashes within the UNC119 pocket, and therefore may be the reason for the low affinity to UNC119.

Figure 3-13 N-terminal sequences of UNC119 cargo proteins.

Alignment of N-terminal sequences of LCK and examples of SRC family kinases with those of reported UNC119 ciliary cargo proteins. Residues at positions 3 – 5 are marked in red.

Mutating these N-terminal residues in LCK to larger amino acids is expected to affect its UNC119A affinity. To investigate the effect of increasing the amino acid size at positions 3 – 5, I used fluorescein-labelled N-terminal myristoylated peptides of LCK in a fluorescence polarisation assay. The release of the peptides from UNC119A upon addition of an excess of ARL2GppNHp was compared. ARL2, which can only release low affinity cargo such as c-SRC, will only release those mutants with a reduced UNC119A affinity. Therefore, the UNC119 pocket can be mapped for its tolerance of increasing the size of cargo N-terminal amino acids. Cysteine residues at positions 3 and 5, and glycine at position 4 were individually mutated to either asparagine, or glutamine. This was to test the effect of having medium- and large-sized amino acids, respectively.

The mutations at position 4 were modelled in Pymol, and the four most common rotamers for each mutation along with the resultant predicted steric clashes with neighbouring UNC119A residues are shown in **Figure 3-14**.

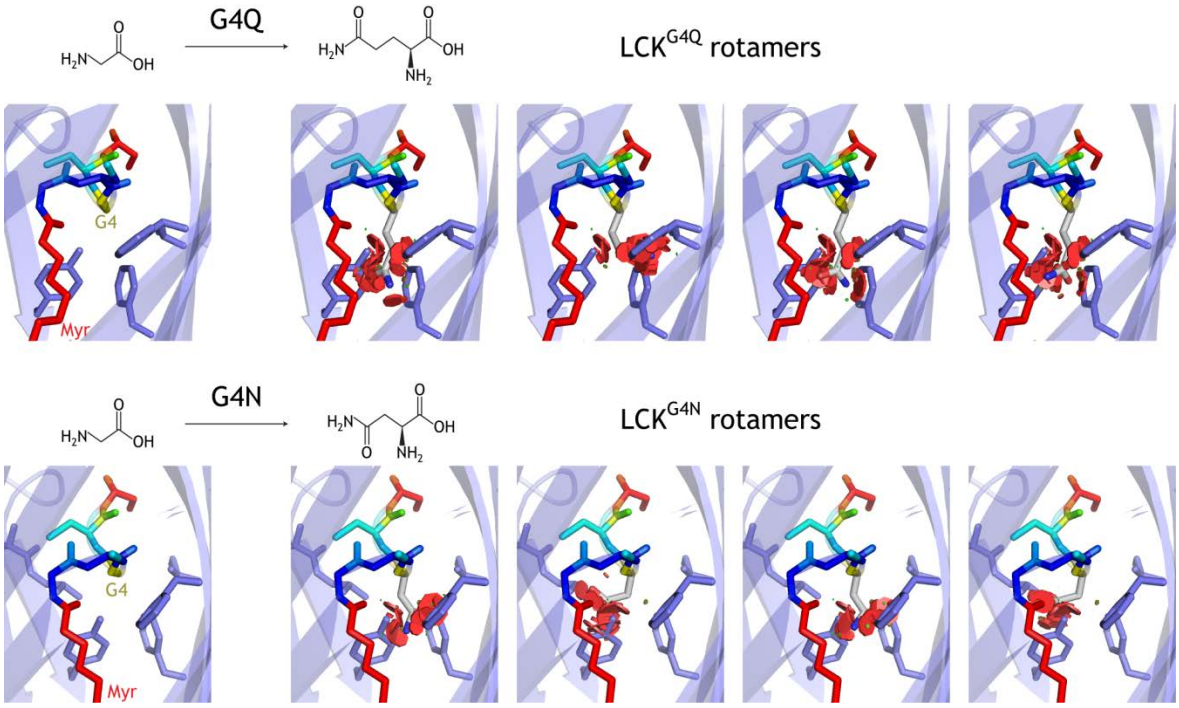

Figure 3-14 Mutating glycine 4 of LCK within the UNC119A pocket.
LCK glycine 4 was mutated to glutamine and asparagine in Pymol, and the four most common rotamers for each are shown. UNC119A residues adjacent to LCK G4 are as represented as sticks. The red disks indicate the steric clashes calculated for each rotamer.

Although smaller in size, the asparagine mutation was still predicted to result in steric clashes in the UNC119A. However, the actual effect of this mutation

would need to be tested via the ARL2-mediated release of the mutant peptides and comparing them to high affinity wild-type LCK and low affinity c-SRC. To facilitate comparing between the different peptides, each experiment was normalised to the baseline polarisation of the peptide solution and to the maximum polarisation upon UNC119A addition; this is demonstrated in **Figure 3-15A**. **Figure 3-15B** shows the normalised polarisation values following ARL2 addition for c-SRC and mutant and wild-type peptides. The asparagine mutants exhibit a similar level of polarisation as wild-type LCK, indicating that the medium-sized amino acid did not affect the affinity to UNC119A regardless of its position among residues 3 – 5. The glutamine mutation, however, resulted in a decrease in polarisation, which becomes more evident the closer the residue is to the N-terminus, and therefore deeper in the UNC119A pocket. Consequently, the affinity to UNC119A is dependent on the size of amino acids immediately following the myristoylated glycine.

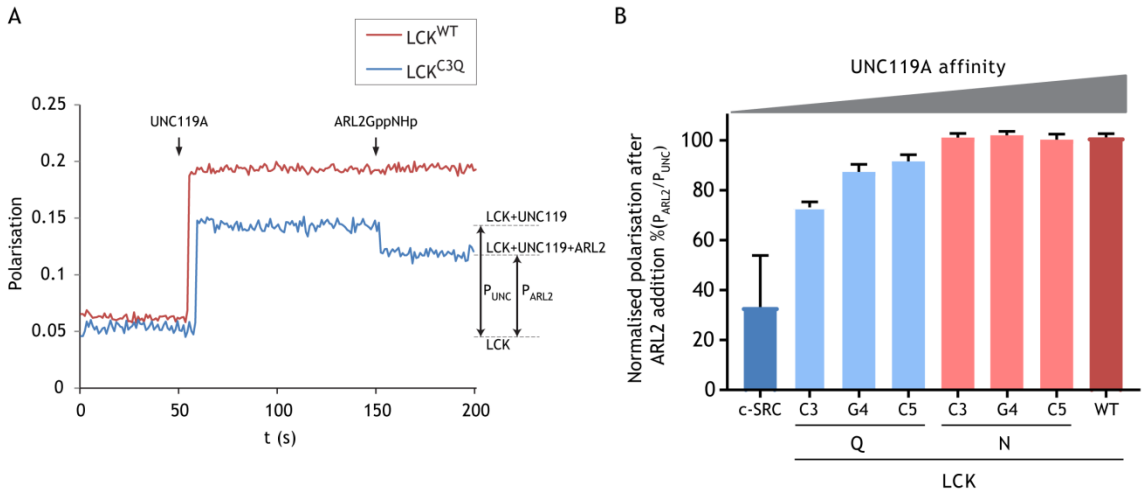

Figure 3-15 Mapping the effect of amino acid size of N-terminal residues of LCK on UNC119A affinity.

(A) Fluorescence polarisation measurements of 100 nM LCK^{WT} and LCK^{C3Q} peptides to which an equal amount of UNC119A was added, followed by 500 nM ARL2GppNHp. The baseline peptide polarisation was subtracted from the average polarisations following addition of UNC119A and ARL2. These values were then used to calculate normalised polarisation after the addition of ARL2. **(B)** The experiment was repeated for the indicated LCK peptides as well as a c-SRC peptide. Average polarisation following ARL2 addition is plotted for each peptide (n=3).

To support the effect of residue size of position 4, we looked at the N-terminal sequence of HCK, which is a SRC family kinase that does not localise to the immune synapse **(Figure 3-16A)**. HCK has a bulky arginine at position 4, and is

therefore expected to have low UNC119A affinity. Repeating the previously described pull-down assays, I used purified HCK SH3-SH2 for *in vitro* myristoylation in the presence of UNC119A-GST and GppNHp-loaded ARL2 or ARL3. Consistent with its N-terminal sequence, HCK was released with both G proteins **(Figure 3-16B)**. Upon mutating arginine 4 to glycine as in the LCK N-terminal sequence, the mutant HCK^{R4G} was only released in the pull-down assay by ARL3 and not by ARL2. The affinity of UNC119A was therefore increased by reducing the size of residue at position 4, reducing steric clashes between the N-terminus of HCK and UNC119A pocket.

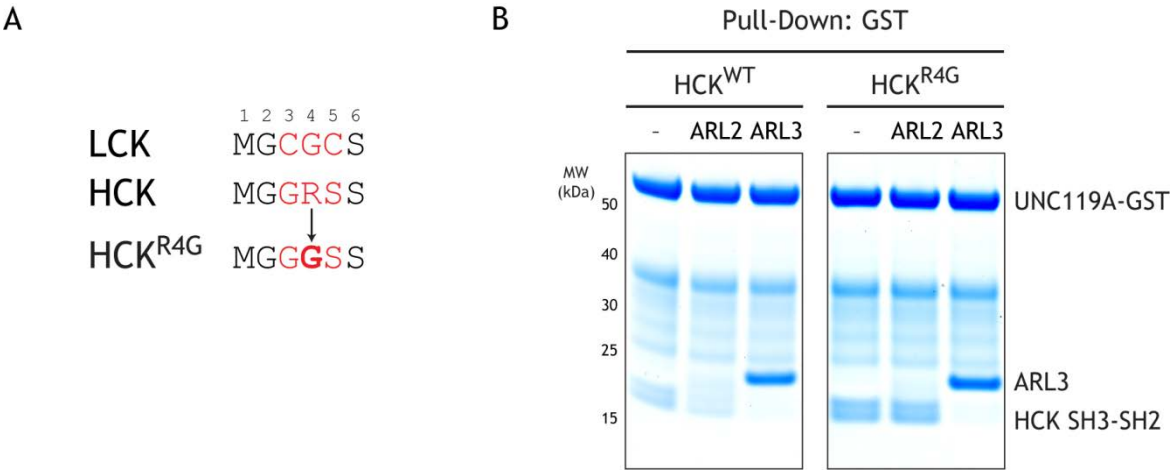

Figure 3-16 Manipulation of UNC119A affinity of HCK.

(A) Arginine 4 in HCK was mutated to glycine to mimic the N-terminal sequence of LCK. **(B)** 100 µg GST-tagged full-length UNC119A was used to pull-down 200 µg purified *in vitro* myristoylated HCK^{WT} or HCK^{R4G} SH3-SH2 in the presence or absence of 200 µg of GppNHp-loaded ARL2 or ARL3. The elutes were run on SDS-PAGE and stained with Coomassie.

3.2.3 Motif-based search for potential UNC119 cargo

The commonality of having small N-terminal residues following a myristoylation site shown by LCK and ciliary proteins may aid in the identification of other myristoylated cargo proteins of UNC119. The obvious requirement for a potential cargo of UNC119 would be the presence of N-terminal myristoylation. A consensus pattern for myristoylation has been derived from known N-myristoylated proteins and synthetic peptide studies. The myristoylation motif is described in the PROSITE motif database (Sigrist et al., 2012) as PROSITE:PDOC00008 G-{EDRKHPFYW}-x(2)-[STAGCN]-{P}. The N-terminal glycine in position 1 should therefore be followed by small, uncharged residues in positions 2 and 5, and with no proline in position 6 **(Figure 3-17A)**. The N-

terminal sequences of LCK and ciliary cargo proteins of UNC119 demonstrate the same general pattern, but with the additional restriction of the absence of large residues in the three positions following the N-terminal glycine. We therefore carried out a motif-based search for proteins that can undergo myristoylation and then filtered them for candidates with suitable residue sizes in the N-terminus. The N-terminal sequences of four such proteins are shown in **Figure 3-17B**.

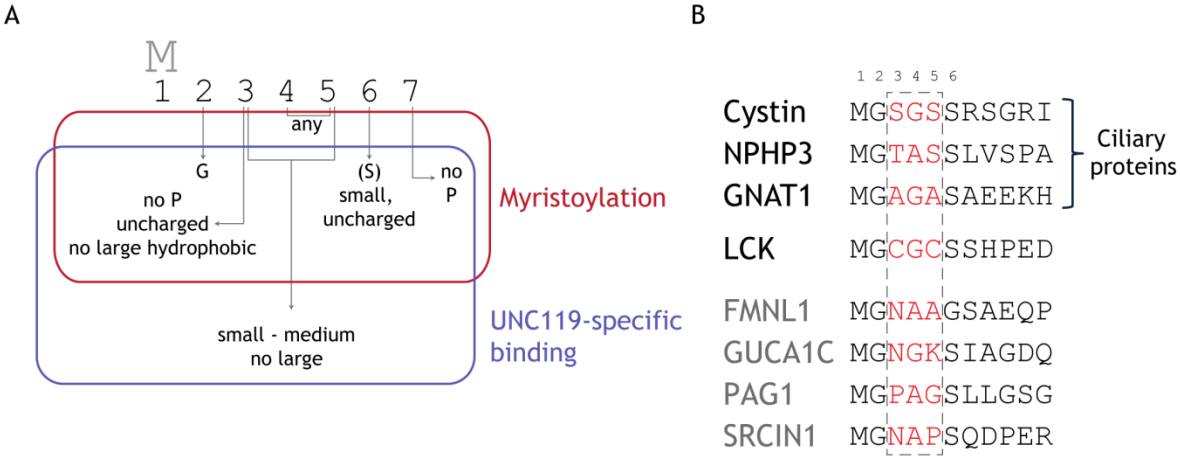

Figure 3-17 Sequence-based identification of potential cargo proteins of UNC119. **(A)** Consensus pattern for N-myristoylated proteins: an N-terminal glycine, followed by an uncharged residue (large hydrophobic residues and proline absent), then any two amino acids. These should be followed by a small uncharged residue, preferably serine, and finally proline should be absent from the next position. Specific cargo proteins of UNC119 generally follow the same rules, with the addition that the three residues following the N-terminal glycine should be small to medium in size. **(B)** Sequence alignment of ciliary cargo proteins, LCK and four hits obtain by the sequence homology search. FMNL1, formin-like protein 1; GUCA1C, Guanylyl cyclase-activating protein 3; PAG1, Phosphoprotein associated with glycosphingolipid-enriched microdomains 1; SRCIN1, SRC kinase signalling inhibitor 1.

A brief description of these identified putative UNC119 binders is given in **Table 3-2.** Of the candidate cargo proteins identified, FMNL1 was of particular interest due to its reported role in the positioning of the microtubule-organising centre (MTOC) at the immune synapse, which is crucial for the polarisation of secretory granules and target cell killing (Gomez et al., 2007, Stinchcombe et al., 2006). Confirming that FMNL1 is a specific binder of UNC119 would help paint a more complete picture of the role of UNC119 at the immune synapse.

Table 3-2 Potential UNC119 specific cargo proteins.

Name	Myristoylation reported?	Function
Formin-like protein 1 (FMNL1)	Yes (Han et al., 2009)	Involved in actin filament dynamics and the relocation of the MTOC to the immune synapse in the cytotoxic T cell response (Gomez et al., 2007).
Guanylyl cyclase-activating protein 3 (GUCA1C)	Yes (Haeseleer et al., 1999)	Ca^{2+}-dependent stimulation of guanylyl cyclases GC1 and GC2 in photoreceptors to restore cGMP following phototransduction (Haeseleer et al., 1999).
Phosphoprotein associated with glycosphingolipid-enriched microdomains 1 (PAG1)/CSK-binding protein (CBP)	No	Binds CSK in a phosphorylation-dependent manner to target it to the membrane where it inhibits SRC-family kinases, including LCK. Becomes phosphorylated upon T cell activation and dissociates from CSK, resulting in reduced SRC inhibition (Brdicka et al., 2000, Kawabuchi et al., 2000).
SRC kinase signalling inhibitor 1 (SRCIN1)	No	Activates CSK which in turn inhibits SRC via phosphorylation of its C-terminus. SRC signalling and cell motility are therefore reduced (Di Stefano et al., 2007).

3.2.3.1 Investigating FMNL1 as a potential high affinity UNC119A cargo

Similar to LCK, our investigation of FMNL1 began with testing whether GST-UNC119A is able to bind FMNL1 present in Jurkat T cell lysate. The pull-down assays were carried out in the presence and absence of GppNHp-loaded ARL2 and ARL3. **Figure 3-18** shows that UNC119A was able to bind FMNL1 on its own and in the presence of ARL2, but less FMNL1 was pulled down in the presence of ARL3. UNC119A can therefore bind FMNL1, but it releases its cargo upon binding of ARL3.

Figure 3-18 UNC119A pulls down FMNL1 from Jurkat T cell lysate.
30 µg GST-tagged full-length UNC119A was used in a GST pull-down assay with Jurkat cell lysate; the pull-down was also repeated with the addition of 30 µg ARL2- or ARL3-GppNHp. The GST control was carried out using 15 µg of GST. Presence of FMNL1 was tested by Western blot.

I then used fluorescein-labelled N-terminal myristoylated peptides of FMNL1 and FMNL3 for fluorescence polarisation assays to assess UNC119A affinity and ARL3-specific release. FMNL3 belongs to the same family of formin-like proteins as FMNL1, but it is not involved in the immune synapse and does not localise to it. Therefore, FMNL3 would not be expected to bind UNC119A with a high affinity.

Titrating UNC119A into a solution of FMNL1 resulted in increasing fluorescence polarisation as the UNC119A-FMNL1 peptide complex was formed. Polarisation values reached a plateau beyond the addition of 250 nM of UNC119A, which is about 1.25×FMNL1, indicating the saturation of the peptide **(Figure 3-19A and B)**. FMNL3, on the other hand, did not reach saturation under the same conditions. This is explained by the difference in the binding affinity, which was calculated for FMNL1 to be about 80-fold higher than that of FMNL3 (binding affinities calculated as 10.1 ± 3.5 nM and 856 ± 156 nM, respectively).

The higher affinity of FMNL1 would be further confirmed by undergoing ARL3-specific release. I used the peptides in another fluorescence polarisation assay where UNC119A was added to a solution of either FMNL1 or FMNL3, followed by GppNHp-loaded ARL2 and ARL3. The former was only released by ARL3, while FMNL3 was released by both ARL2 and ARL3. Furthermore, FMNL1 showed a 4-fold increase in polarisation upon UNC119A addition, compared to less than 2-fold for the lower affinity FMNL3, indicating more UNC119A complex formation with the FMNL1 peptide **(Figure 3-19C and D)**.

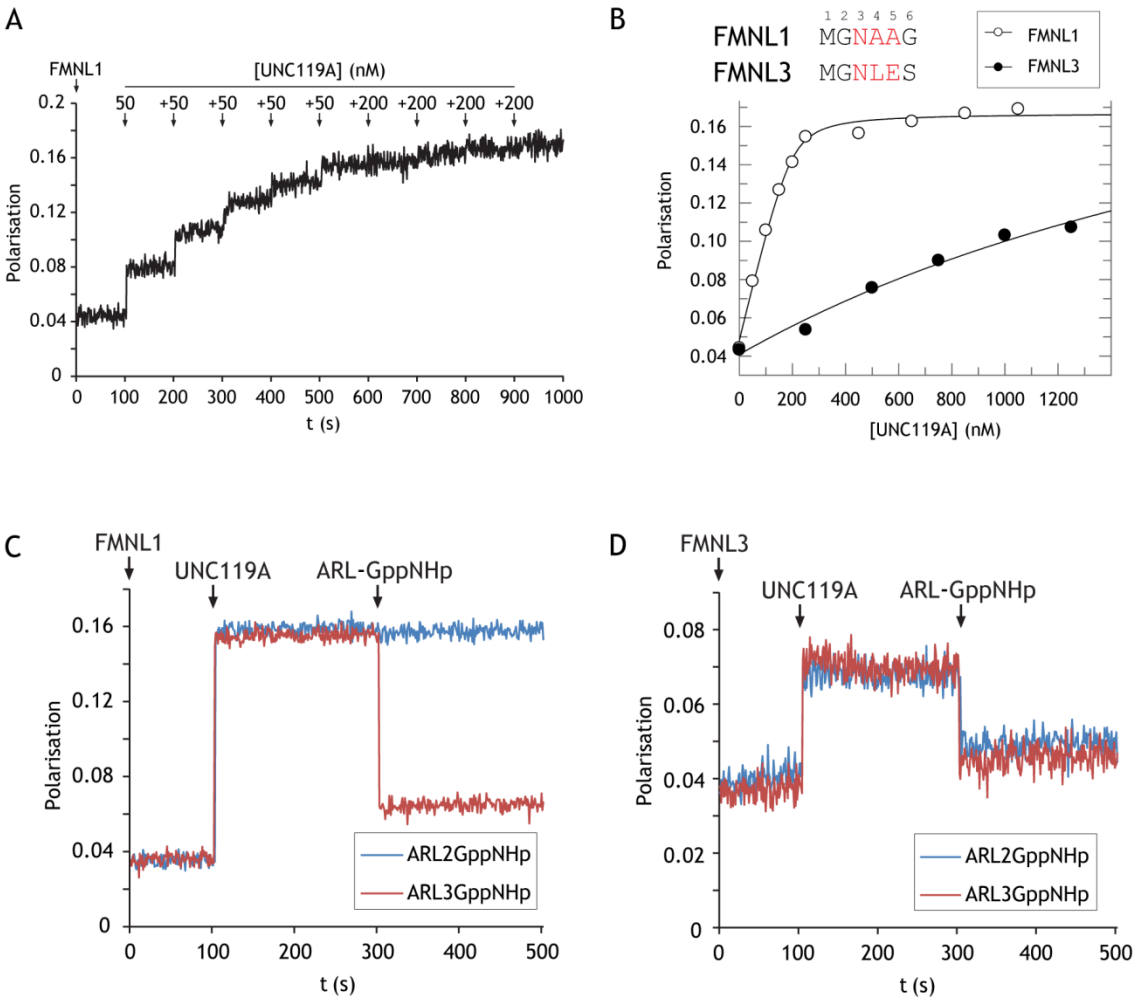

Figure 3-19 FMNL1 binds specifically to UNC119A.
(A) Fluorescence polarisation measurements taken during stepwise addition of UNC119A as indicated to a 0.2 µM solution of fluorescein-labelled myristoylated FMNL1 peptide. **(B)** Increasing concentrations of full-length UNC119A were added to 0.2 µM solutions of fluorescent FMNL1 (○) or FMNL3 (●) peptides. Binding affinities for FMNL1 and FMNL3 were calculated as 10.1 ± 3.5 nM and 856 ± 156 nM, respectively. The N-terminal six residues of both proteins are also shown, with positions 3 – 5 marked in red. **(C and D)** 0.5 µM full-length UNC119A was added to 0.5 µM fluorescein-labelled myristoylated FMNL1 **(C)** or FMNL3 **(D)** peptide followed by 5 µM ARL2- or ARL3-GppNHp, and fluorescence polarisation was measured throughout.

I next wanted to test if the binding between UNC119 and the N-terminus of FMNL1 is also dependent on myristoylation. As full-length FMNL1 is difficult to express and purify, I used a construct of GST-tagged FMNL1$^{1–458(\Delta 172-198)}$ (FMNL1Δ) **(Figure 3-20A)** that has been previously reported to be successfully expressed in *E. coli* and used for structural studies (Kühn et al., 2015).

While GST-FMNL1Δ expression in BL21(DE3)CodonPlus cells was successful, I experienced problems in removing the GST-tag from FMNL1. The removal of the

N-terminal GST-tag was necessary to allow *in vitro* myristoylation of the protein. While the GST-tag was successfully removed by thrombin digestion **(Figure 3-20B)**, in all conditions tested, this resulted in FMNL1 being eluted in the void volume of the size exclusion chromatography column, indicating aggregation of the protein. **Figure 3-20C and D** show an example of one such purification, with the separation of FMNL1 and GST in the elution profile.

Despite this setback, there was still a possibility that the N-terminus of the protein was available for myristoylation. I therefore attempted the *in vitro* myristoylation of FMNL1 in the presence of full-length GST-UNC119A. As **Figure 3-20E** shows, FMNL1 was indeed pulled down by UNC119A, but only when NMT was added to the myristoylation reaction.

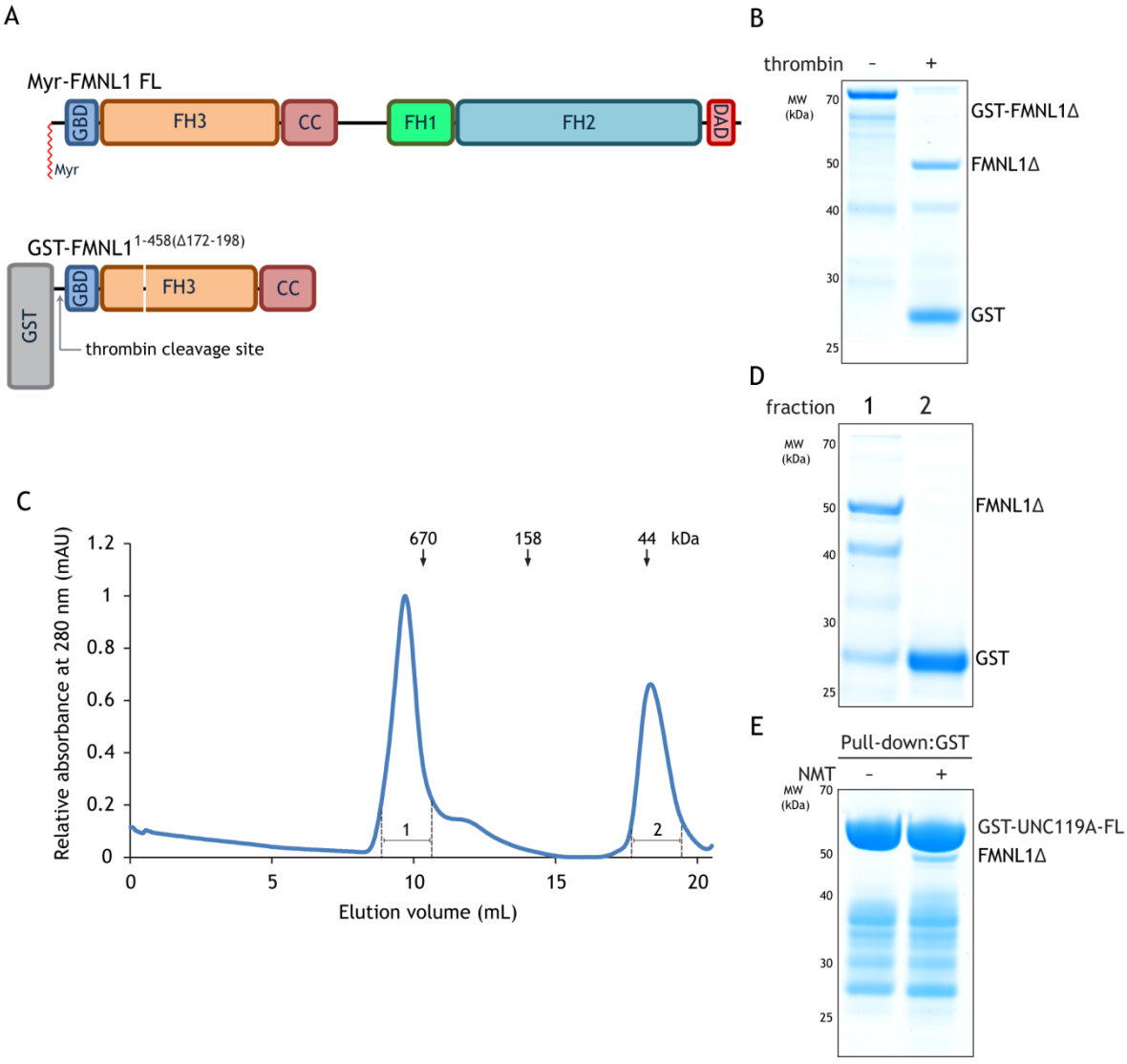

Figure 3-20 Purification of FMNL1$^{1-458(\Delta172-198)}$ and pull-down with UNC119A.

(A) Domain organisation of full-length and truncated FMNL1, the latter of which was used for expression in *E. coli*. **(B)** Eluted GST-FMNL1$^{1-458(\Delta172-198)}$ was incubated in 200 mM NaCl and 0.015 mg/mL thrombin at 4°C for 16 hours. Samples of the protein with and without thrombin were

run on SDS-PAGE and stained with Coomassie. **(C)** Size exclusion chromatography elution profile of thrombin-digested FMNL1. Two peaks were obtained: FMNL1$^{1-458(\Delta 172-198)}$ running higher than 670 kDa, and dimerised GST eluting at around 40 kDa. Samples of both fractions were run on SDS-PAGE and are shown in **(D). (E)** 150 µg of FMNL1 fraction 1 from **(C)** was used for *in vitro* myristoylation in the presence of 200 µg of full-length UNC119A before carrying out the GST pull-downs. The elutes were run on SDS-PAGE and stained with Coomassie. GBD, GTPase binding domain; FH, formin homology domain; CC, coiled coil; DAD, Diaphanous-autoregulatory domain.

Together with the fluorescence polarisation assays, our pull-downs would indicate that FMNL1 binds specifically to UNC119A, in a manner that is possibly myristoylation-dependent. However, given the difficulty encountered in purifying properly-folded FMNL1, this line of investigation was halted to refocus on LCK and its localisation at the immune synapse.

3.2.4 Localisation of LCK to the immune synapse is affected by its UNC119A affinity

3.2.4.1 The Jurkat-Raji immune synapse model system

The localisation of LCK to the immune synapse formed between immune cells and their targets is an important event in T cell receptor signalling (Straus and Weiss, 1992). Having shown that, compared to other SRC kinases, LCK has a high binding affinity to UNC119A, we wanted to investigate if the affinity to UNC119A has an influence on the localisation of LCK to the immune synapse. To study the localisation of LCK and other proteins at the immune synapse, we employed a cell line model wherein Jurkat leukaemia-derived T cells were conjugated with Raji lymphoblast-like B cells. Prior to addition of Jurkat cells, Raji cells were stained with 7-amino-4-chloromethylcoumarin (CMAC) and coated with staphylococcal enterotoxin E (SEE). Several major histocompatibility complex class II alleles can present SEE to the T cell receptor via the binding of the superantigen outside the MHC peptide-binding groove (Jardetzky et al., 1994). In addition, SEE binding to the T cell receptors depends on the presence of specific Vß sequences, rather than the sequences of both α and ß chains, that is, the TCR αß clonotype (Kappler et al., 1989). Consequently, SEE is considered to be a superantigen that is capable of activating a greater proportion of T cells compared to peptide-MHC complexes, which would only activate a specific clone of T cell. Therefore, SEE-presentation by Raji cells would result in the formation

of more T-B cell immune synapses which are all in response to the same antigen, and should therefore be similar in nature.
However, the use of this model presents some disadvantages, chief among which is the use of transformed Jurkat and Raji cells which may exhibit variations in the expression of adhesion and accessory molecules as compared to primary cells. An alternative approach is the use of mouse-derived primary T cells that are engineered for stimulation by a specific peptide that can be expressed by antigen presenting cells, such as OT-II cells (Barnden et al., 1998); these may provide more physiologically relevant immune synapses. However, primary cells present more difficulties given that they require continuous isolation from mice due to their shorter lifespans compared to immortalised cell lines. Furthermore, they are inefficient targets for transfection. Therefore, we decided to use the Jurkat-Raji model as an initial step in our investigation of the role of UNC119A in the immune synapse.

Jurkat and Raji cells were mixed and seeded onto poly-L-lysine coated glass coverslips for a set period of time before fixing the coverslips and staining them for immunofluorescence microscopy. On imaging the conjugates, immune synapses were identified using phosphoZAP70 (pZAP70) as a marker, as its localisation is restricted to the immune synapse following TCR stimulation (Chan et al., 1991). Therefore, the presence of pZAP70 at the interface between a CMAC-stained Raji cell and a Jurkat cell marks it as an immune synapse. We quantified the localisation of various proteins to these immune synapses using the Fiji plugin SynapseMeasures that was developed by the Veiga-Chacón lab (Calabia-Linares et al., 2011). The plugin takes into consideration the fluorescence at several regions of interest: the T cell synapse, the T cell membrane opposite the synapse, the B cell membrane, and finally the background surrounding the two cells. The calculated localisation ratio (LR) for a certain protein is a measure of the amount of that protein at the synapse, relative to the amount in the cell membrane outside of the synapse. A ratio of 1 indicates an equal localisation of the protein both inside and outside the synapse; if the localisation ratio is more than 1, then more protein is in the synapse than outside, and vice versa **(Figure 3-21A)**.

To investigate the localisation of different mutants of LCK, we transfected the Jurkat T cells with LCK constructs bearing a C-terminal GFP tag prior to

conjugate formation. The GFP fluorescence was then used to calculate the localisation ratio of the protein at the synapse relative to the rest of the cell membrane **(Figure 3-21B)**.

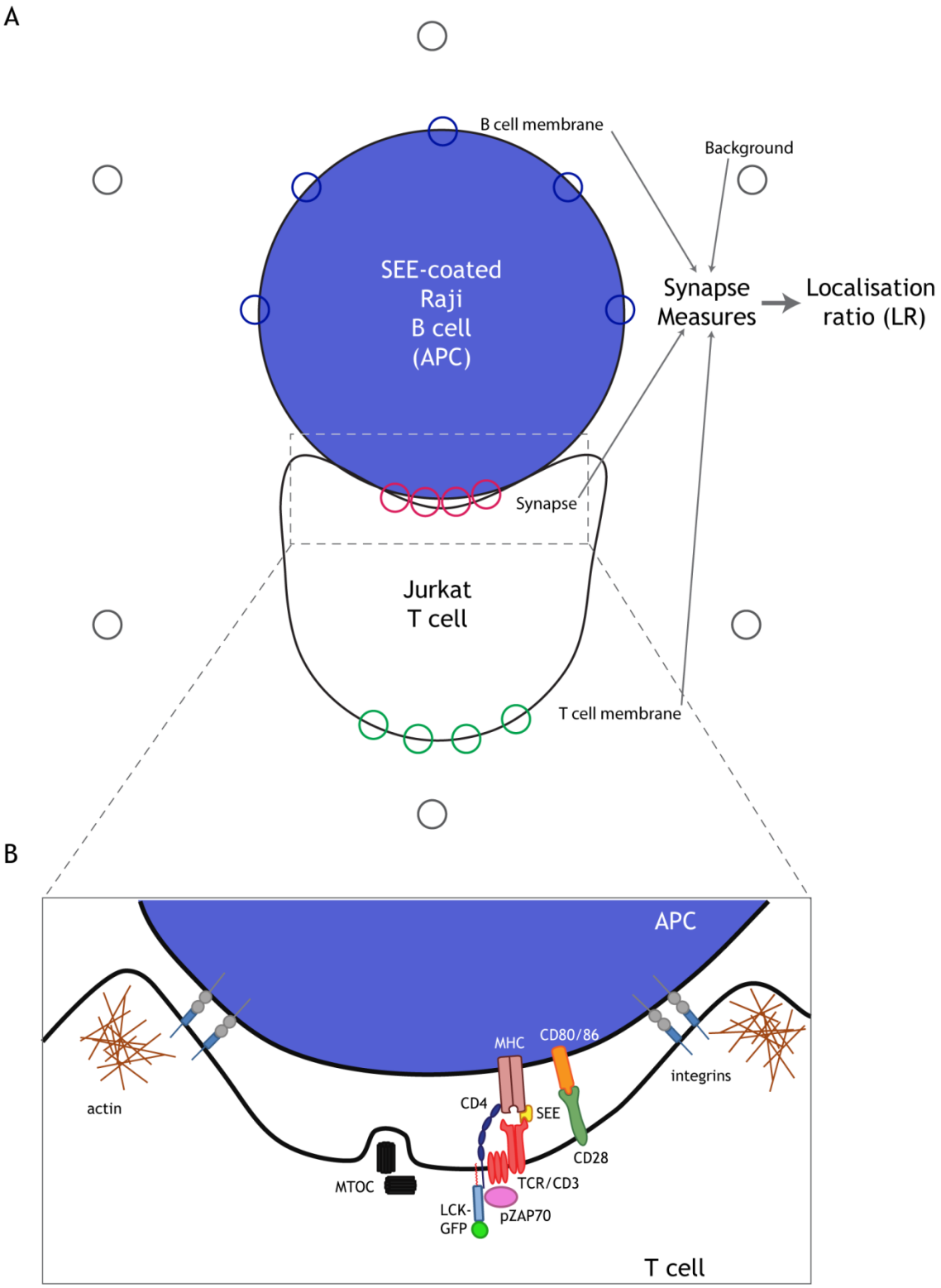

Figure 3-21 Quantification of protein localisation at the immune synapse.

(A) Conjugates are formed between CMAC-stained, SEE-loaded Raji B cells and Jurkat T cells. Protein localisation at the synapse is quantified from conjugate images by measuring fluorescence obtained by staining of that protein at various regions of interest as shown. These are then used by the plugin SynapseMeasures in Fiji to calculate the localisation ratio of the

protein: LR = 1, equal localisation in the synapse as in the rest of the cell membrane; LR > 1, more localisation in the synapse; LR < 1, more localisation in the cell membrane outside of the synapse. **(B)** The superantigen SEE, upon presentation to the T cell, binds to specific Vβ sequences in the TCR, thereby triggering the formation of an immune synapse. The centrosome docks at the interface membrane to direct polarisation of the cytoskeleton and organelles. Various proteins localise to the synapse, including LCK, which recruits and subsequently activates ZAP70 via phosphorylation. pZAP70 is then used to identify the synapse in the conjugate images. MHC, major histocompatibility complex; MTOC, microtubule-organising centre, SEE, staphylococcal enterotoxin E.

3.2.4.2 Decreasing UNC119A affinity to LCK results in reduced LCK focusing at the immune synapse

Based on the crystal structure of UNC119A in complex with an N-terminal LCK peptide, we found that the size of the N-terminal residues of the cargo affects its UNC119A affinity. However, as LCK undergoes myristoylation at G2 and palmitoylation at C3 and C5, only mutations at glycine 4 can be tested in a cellular setting, to avoid affecting lipid modifications of LCK that aid in its localisation **(Figure 3-22)**.

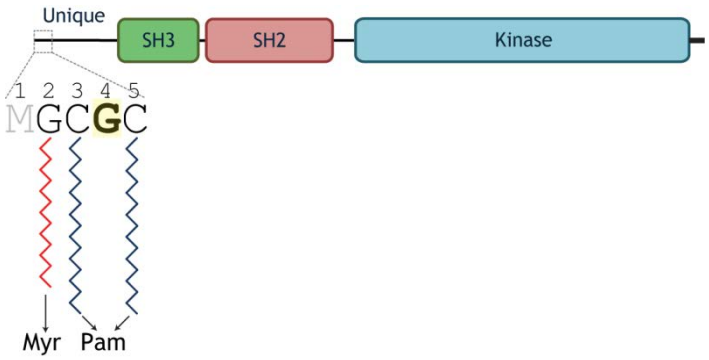

Figure 3-22 N-terminal lipid modifications of LCK.
LCK is myristoylated at glycine 2 following the removal of the initiator methionine, and is palmitoylated at cysteine residues 3 and 5. As these modifications affect membrane localisation of LCK, testing the effect of reducing UNC119A by mutating LCK N-terminal residues was limited to glycine 4. Myr, myristoyl; Pam, palmitoyl; SH, SRC homology.

A glycine-to-glutamine mutation at position 4 in LCK resulted in decreasing its UNC119A affinity in *in vitro* assays, where LCK^{G4Q} was released from the complex by the small G protein ARL2, which is only able to release weaker binders of UNC119A **(Figure 3-15B)**. In the aforementioned fluorescence polarisation assay, LCK^{G4Q} was released about 14% more than LCK^{WT} by ARL2. As this mutation

should not affect the lipid modifications of LCK, we could therefore investigate its behaviour in T cells that are forming immune synapses.

We utilised the aforementioned immune synapse model in which SEE-loaded Raji B cells were conjugated with Jurkat cells that were transfected with wild-type and mutant GFP-tagged LCK. Conjugates were allowed to form for 10 minutes before fixing the coverslips and proceeding with immunofluorescence staining. An example of the synapse images is shown in **Figure 3-23**.The localisation ratio of LCK to the immune synapse relative to the rest of the T cell membrane was quantified for multiple images. While the mutant LCK^{G4Q} did have localisation ratio that was more than 1, LCK^{WT} showed a relative localisation that was about 1.6-times higher than that of the lower UNC119A affinity mutant.

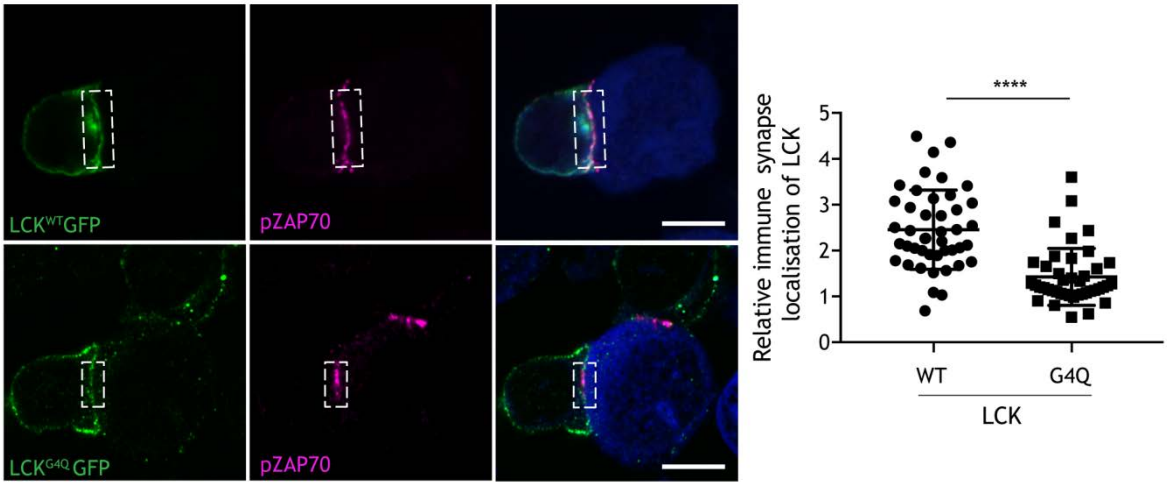

Figure 3-23 Immune synapse localisation of the low affinity mutant LCK^{G4Q}.
T-B conjugates comprising transfected Jurkat T cells and Raji B cells that have been pre-incubated in CMAC and SEE. T cells were transfected with GFP-tagged wild-type or low affinity mutant LCK (LCK^{WT}GFP and LCK^{G4Q}GFP, respectively. Relative immune synapse localisation was calculated to be 2.45 (n=45) for LCK^{WT}, and 1.40 for LCK^{G4Q} (n=42). Mann-Whitney $P \leq 0.0001$; scale bars represent 5 µm. Immune synapses as indicated by pZAP70 staining are marked by the white rectangles in the conjugate images.

To confirm these results, we employed the use of a previously-reported UNC119A inhibitor, squarunkin A (Mejuch et al., 2017). This molecule has been shown to bind the hydrophobic pocket of UNC119, thereby interfering with the binding of myristoylated cargo peptides **(Figure 3-24A)**. To demonstrate the effect of squarunkin A on the N-terminal peptide of LCK, I added a mixture of UNC119A and excess squarunkin A to a solution of the fluorescein-labelled peptide; measurement of fluorescence polarisation showed no increase in

polarisation upon addition of the UNC119A+squarunkin A mixture. Adding a mixture of UNC119A and DMSO, however, did result in an increase in polarisation, indicating the binding of UNC119A to the LCK peptide, which was inhibited in the presence of squarunkin A **(Figure 3-24B)**.

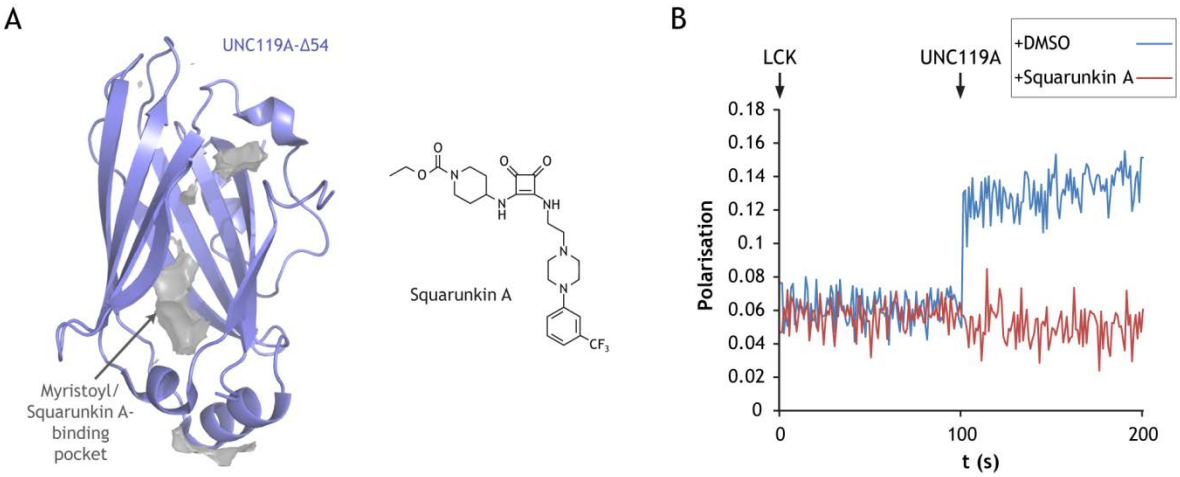

Figure 3-24 Squarunkin A binds the UNC119A pocket and prevents LCK binding.
(A) Structure of UNC119A in cartoon representation with the binding pocket shown in grey (left). The structure of the UNC119A inhibitor squarunkin A is shown in the right panel.
(B) Fluorescence polarisation measurement where a mixture of 20 nM UNC119A and either 20μM of the UNC119A-inhibitor squarunkin A (red) or DMSO (blue) was added to a 20 nM solution of fluorescein-labelled myristoylated LCK N-terminal peptide.

Therefore, we decided to use this small molecule to lower the affinity of LCK to UNC119A and study its effect on the localisation of LCK to the immune synapse. Jurkat cells were treated with either DMSO or squarunkin A before adding Raji cells that were pre-incubated with CMAC and SEE. The cells were given 10 minutes to form conjugates before fixing the coverslips and staining them for endogenous LCK and pZAP70. Quantification of the relative localisation of LCK to the immune synapse showed a 2-fold decrease in the squarunkin A-treated Jurkat cells compared to those treated with DMSO **(Figure 3-25)**.

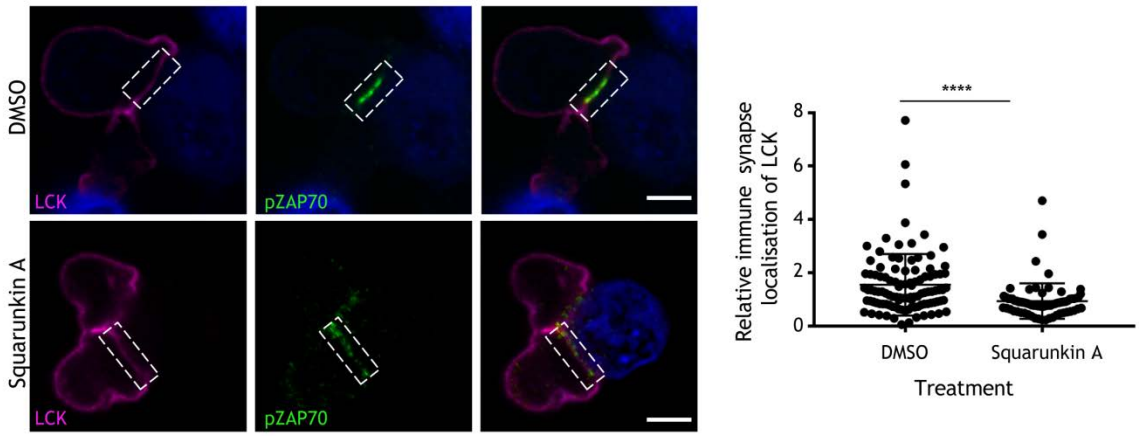

Figure 3-25 Treatment with squarunkin A reduces LCK localisation to the immune synapse. T-B conjugates were formed using Raji B cells that have been pre-incubated in CMAC and the superantigen SEE, and Jurkat T cells treated with either DMSO or 2 μM squarunkin A. Relative immune synapse localisation was calculated to be 1.54 for DMSO-treated cells (n=105) and 0.71 for squarunkin A-treated cells (n=71). Mann-Whitney P≤0.0001; scale bars represent 5 μm, and immune synapses, as detected by the presence of pZAP70, are marked by white rectangles.

From these results, we could say that impairing the affinity of UNC119A to LCK, whether by N-terminal mutation of LCK or chemical inhibition of UNC119A, resulted in a decreased focusing of LCK at the immune synapse. The synapse localisation of LCK is therefore facilitated, at least in part, by the high affinity binding of UNC119A, which echoes its role in the ciliary localisation of cargo like NPHP3. In the cilia, however, UNC119 works in concert with proteins such as ARL3 to bring about this specific localisation. This lead to the question: which proteins assist UNC119A in trafficking LCK to the immune synapse?

3.2.4.3 ARL3 activity in Jurkat cells affect LCK immune synapse localisation

We began with investigating the localisation of the small G protein ARL3, which is able to release high affinity cargo such as LCK from the UNC119A complex. We formed conjugates between Raji and Jurkat cells as previously described and stained for endogenous ARL3 and pZAP70. These were compared to conjugates formed in the same way, but with no SEE loaded on the Raji cells, and therefore no true synapses should form between these cells. This is confirmed by the absence of pZAP70 at the interface between the cells **(Figure 3-26A**, bottom panels**).** Loading the Raji cells with SEE did result in the formation of immune synapses and the localisation of pZAP70; however, ARL3 showed no change in its localisation at the synapse, remaining present throughout the T cell **(Figure**

3-26A, top panels**)**. This is in stark contrast to LCK, which localises to the synapses formed in the presence of SEE, resulting in a 2-fold increase in its localisation ratio compared to the SEE- conjugates **(Figure 3-26B and C)**.

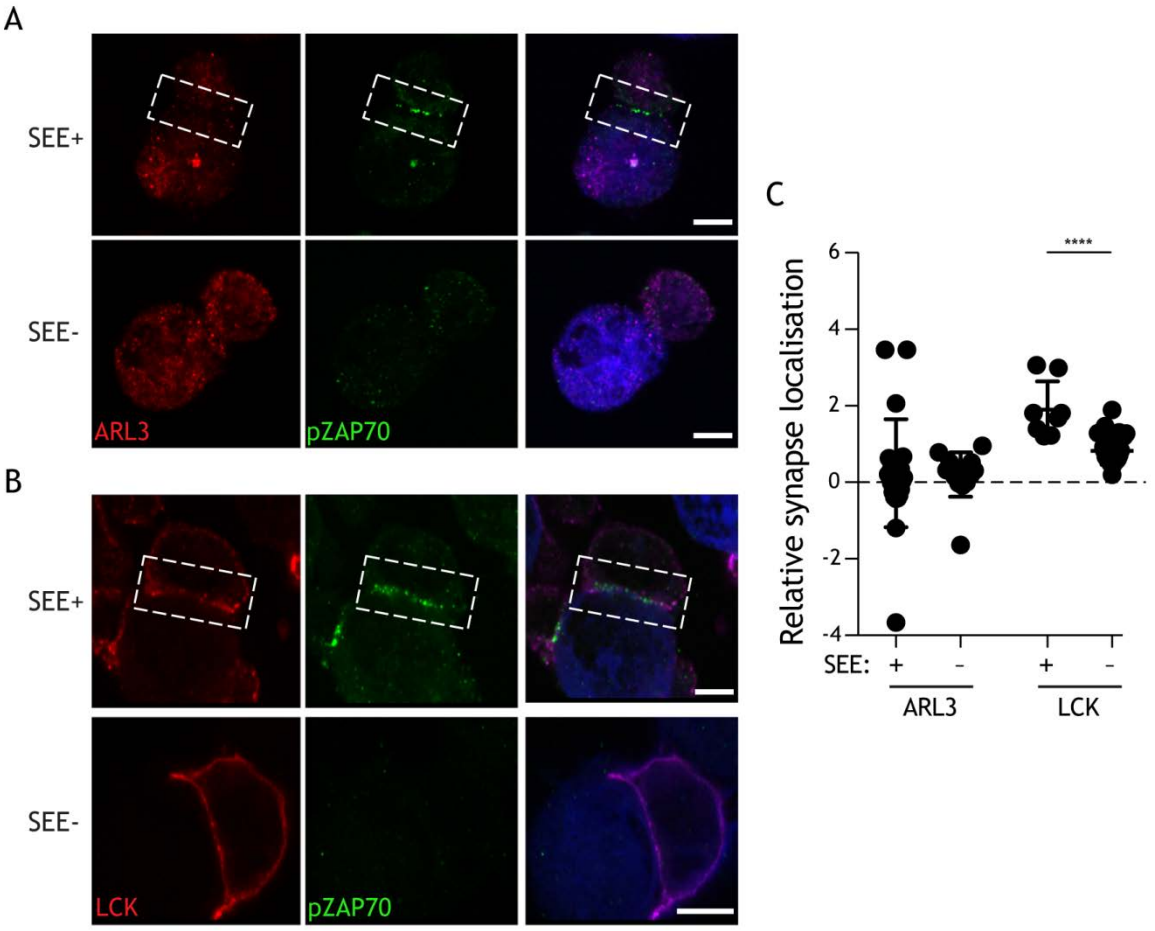

Figure 3-26 ARL3 does not localise to the immune synapse upon its formation.
T-B conjugates formed between Jurkat T cells and CMAC-incubated Raji B cells in the presence or absence of SEE were stained with anti-phosphoZAP70 and anti-ARL3 **(A)** or –LCK **(B)** antibodies. **(C)** The relative immune synapse localisation was quantified for each protein in conjugates formed in the presence and absence of SEE. ARL3 shows no synapse localisation (LR = 0.3) in both sets of conjugates (n=38). LCK shows a localisation ratio of 1.9 in SEE+ conjugates and 0.7 in SEE- conjugates (n=42; P≤0.0001). Immune synapses as indicated by pZAP70 staining are marked by the white rectangles in the conjugate images; scale bars represent 5 µm. Differences in localisation were analysed using the Mann-Whitney U test.

The lack of ARL3 focusing at the synapse raised the question of whether ARL3 is releasing LCK from the UNC119A complex, and if so, how the specific localisation of LCK is maintained when it is not matched by that of ARL3. To first test if ARL3 is involved in LCK localisation, we attempted to manipulate its activity in the T cell by overexpression of GFP-tagged constructs of wild-type ARL3, and the constitutively-active mutant, $ARL3^{Q71L}$, which remains in the active GTP-bound

form as the mutation impairs its GTP hydrolysis (Linari et al., 1999). Sequence alignment shows that glutamine 71 in ARL3 is equivalent to glutamine 61 in KRas; this latter residue has been shown to be crucial in GTP hydrolysis of KRas, due to its role in the stabilisation of the transition state formed during the reaction (Prive et al., 1992). Mutation of the equivalent Q71 in ARL3 would therefore interfere with GTP hydrolysis of ARL3, resulting in increased ARL3 activity in the cell.

The transfected Jurkat cells were then mixed with CMAC-stained, SEE-coated Raji cells to form conjugates before performing immunofluorescence staining for endogenous LCK and phosphoZAP70. **Figure 3-27** shows representative images for each of the constructs and the quantification of LCK localisation to the synapse, relative to that of untransfected cells. Overexpression of the constitutively-active ARL3^{Q71L} mutant resulted in a 50% decrease in the localisation of LCK at the immune synapse relative to the rest of the T cell membrane.

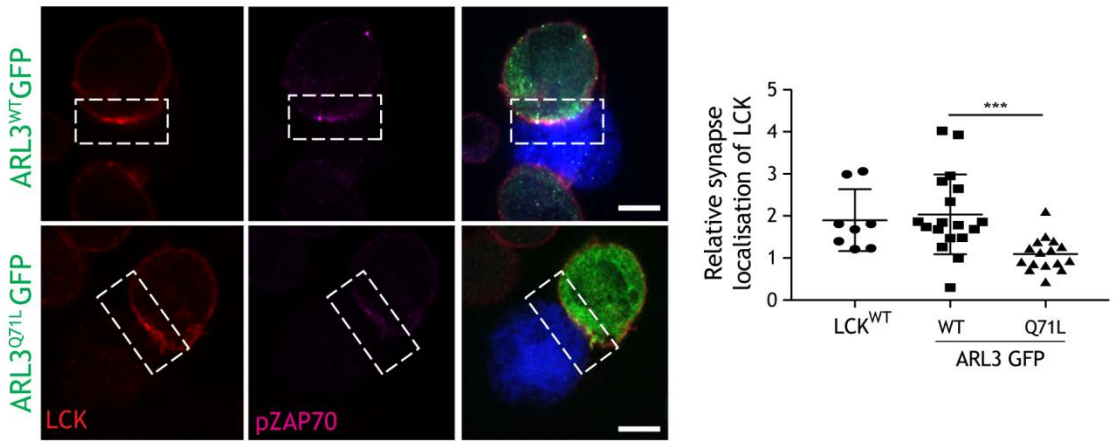

Figure 3-27 Effect of ARL3 activity on LCK immune synapse localisation.
Jurkat cells were transfected with GFP-tagged wild-type or constitutively active mutant of ARL3. These were then used to form conjugates with Raji cells that were incubated in SEE and CMAC and the conjugates were stained for LCK and pZAP70. Synapse localisation of LCK was quantified in both and compared to that shown by immune synapses of untransfected Jurkat cells (LCK^{WT}). LCK still showed synapse localisation of 2 (n=18) in cells expressing ARL3^{WT}, while expression of the mutant ARL3^{Q71L} resulted in the reduction of LCK synapse localisation to 1 (n=16, Mann-Whitney P=0.0002). Immune synapses as identified by the presence of pZAP70 are marked by white rectangles, and the scale bars represent 5 μm.

We also tested the effect of increasing the ARL3 activity and resulting LCK mislocalisation on the activation of T cells. Following transfection with various GFP-tagged ARL constructs, Jurkat cells were stimulated using anti-CD3 and anti-CD28 antibodies. As a marker of T cell activation, we used the expression of CD69. This is a surface glycoprotein that exhibits rapid upregulation following lymphocyte stimulation, reaching detectable protein levels within 2 -3 hours post-stimulation (Lopez-Cabrera et al., 1993). Four hours following stimulation, CD69 expression levels on the surface of GFP-positive cells were measured by flow cytometry **(Figure 3-28A and B)**. Transfection of ARL3^{Q71L}GFP resulted in a significant increase in surface CD69 expression levels on Jurkat cells compared to those transfected with GFP. In contrast, overexpression of wild-type ARL3, as well as wild-type and constitutively-active ARL2, had no significant effect on CD69 expression **(Figure 3-28C)**. Therefore, it is the specific activity of ARL3 that has an effect on Jurkat T cell activation upon stimulation with antibodies.

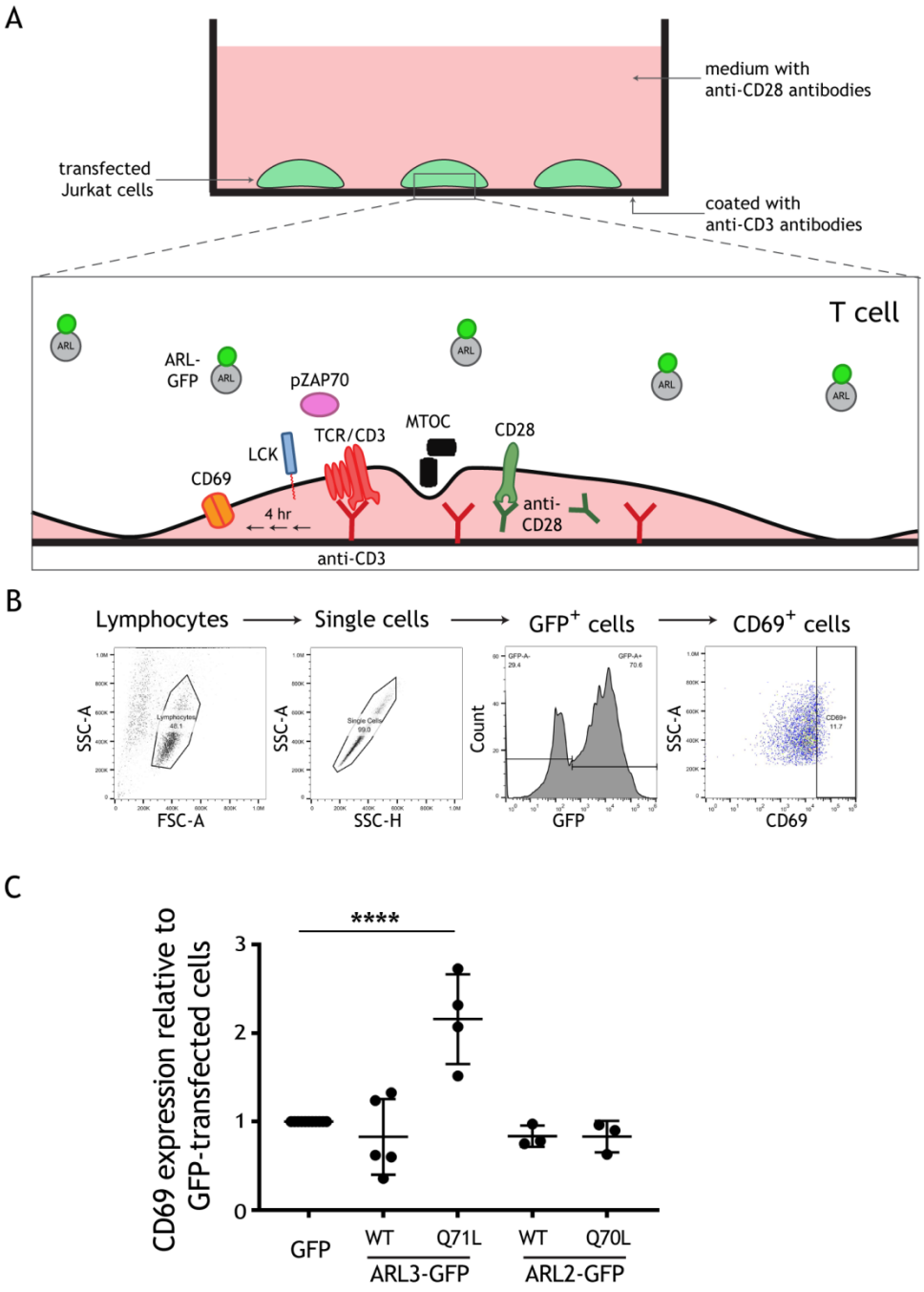

Figure 3-28 Effect of ARL3 activity on T cell stimulation.

(A) Transfected Jurkat T cells were stimulated *in vitro* by using anti-CD3 and –CD28 antibodies for 4 hours at 37°C. Following activation of the TCR, CD69 is expressed on the surface of the T cells, which was then measured by flow cytometry. **(B)** Gating strategy for flow cytometry analysis of CD69 expression: lymphocytes were distinguished from cell debris based on their size and granularity, as indicated by forward (FSC) and side scatter (SSC), respectively. Doublets were then excluded from the lymphocytes based on the area and height of the side scatter peaks. GFP-positive single cells were then used to measure the level of CD69 expression. **(C)** Jurkat cells transfected with the indicated GFP-tagged constructs and stimulated with anti-CD3 and –CD28 antibodies were analysed for increase in surface CD69 expression upon stimulation. Increase in CD69 expression level for each construct was normalised against that of GFP alone. P-values were as follows: $ARL3^{Q71L}$ ($P \leq 0.0001$), $ARL3^{WT}$ ($P=0.004$) $ARL2^{WT}$ ($P=0.02$) and $ARL2^{Q70L}$ ($P=0.03$), and refer to unpaired t-test data.

3.2.4.4 Ciliary ARL13B localises to the immune synapse and results in specific LCK release

Overexpression of constitutively-active ARL3 resulted in the mislocalisation of LCK and increased expression of CD69. This indicated that ARL3 is indeed involved in the localisation of LCK at the immune synapse and the subsequent T cell stimulation. However, the effect is mediated by the activity of ARL3, rather than the general localisation of total ARL3, which points at another level of regulation. This is most likely exerted by the GEF for ARL3, which catalyses its nucleotide exchange. The ARL3 GEF has been shown to be the ciliary G protein ARL13B (Gotthardt et al., 2015), whose restricted ciliary localisation mediates the specific release of ciliary cargo from UNC119 only in the ciliary compartment.

Jurkat T cells, despite lacking primary cilia, do express the ciliary protein ARL13B **(Figure 3-5A)**. We therefore investigated the localisation of endogenous ARL13B in immune synapses formed between Jurkat T cells and Raji B cells as aforementioned. Upon immune synapse formation with SEE-loaded Raji cells, ARL13B displayed a localisation that was markedly focused at the synapse compared to the rest of the cell membrane. This localisation was 3-times higher than that observed at the T-B interface when the Raji cells were not loaded with SEE, indicating that it is specific to the formation of the immune synapse **(Figure 3-29A)**.

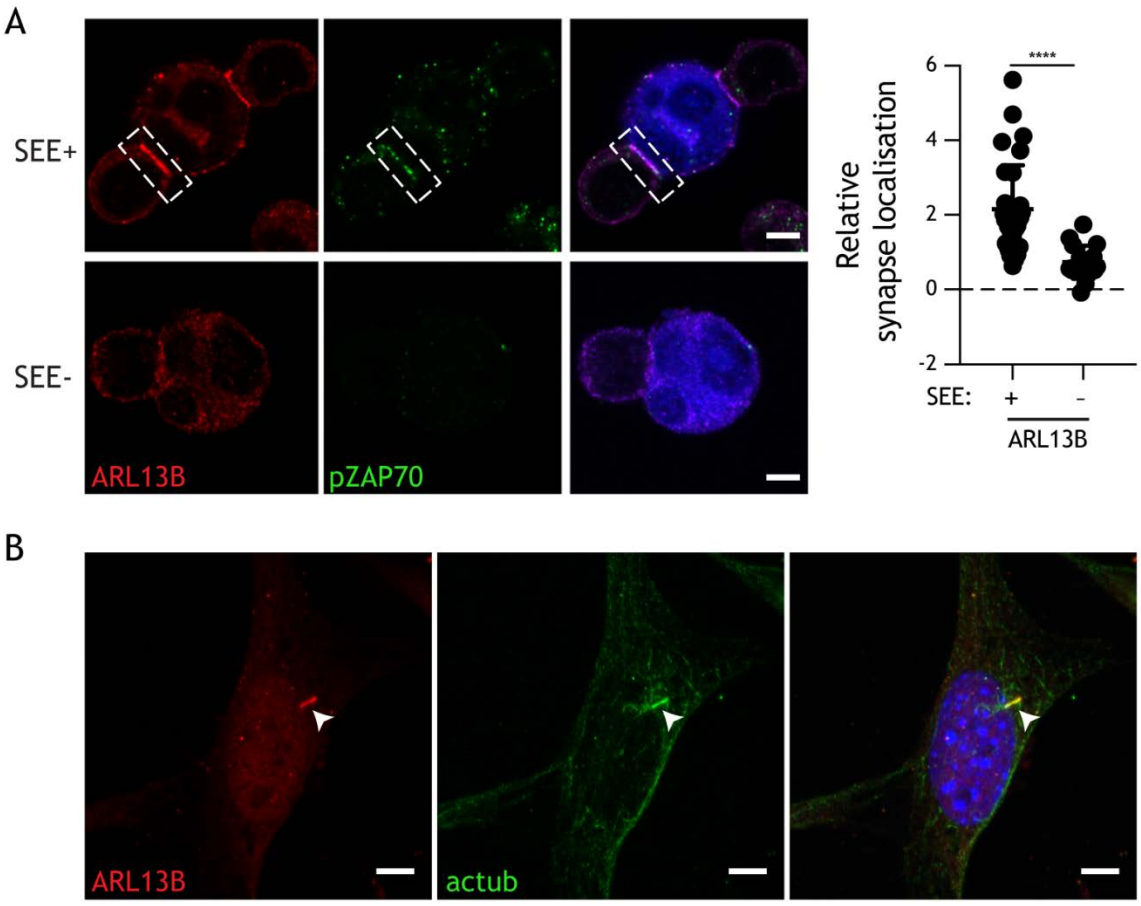

Figure 3-29 ARL13B localises to the immune synapse.

(A) T-B conjugates were formed between Jurkat T cells and Raji B cells in the presence and absence of SEE on the surface of Raji cells. Immunofluorescence staining was performed for ARL13B and phosphorylated ZAP70. Immune synapse localisation relative to the rest of the cell membrane is shown in the right panel. ARL13B shows a localisation of 2 to the synapse in the presence of SEE (n=32) which dropped to 0.6 in the absence of the superantigen (n=16; P≤0.0001). The difference in localisation was analysed using the Mann-Whitney U test.
(B) NIH/3T3 fibroblasts were serum-starved overnight to induce ciliogenesis and, following fixation, were stained with DAPI and antibodies against ARL13B and acetylated tubulin (actub). White rectangles and arrows indicate immune synapses and cilia, respectively, and the white bars represent 5 μm.

This membrane domain-restricted localisation is reminiscent of that seen in primary cilia as shown in **Figure 3-29B**, and is therefore a feature that is exhibited by both of the specialised membrane compartments of primary cilia and immune synapses. This focusing of ARL13B at the synapse would result in the formation of a pool of active ARL3, which specifically releases LCK from UNC119A at the immune synapse, irrespective of the localisation of total ARL3.

3.2.5 UNC119A and LCK form additional interactions independent of myristoylation

Having shown that the myristoyl moiety of LCK binds the hydrophobic pocket of UNC119A with a high affinity, we expanded our interaction studies to include the full-length sequences of both proteins. This was to identify if LCK and UNC119A form additional interactions outside the myristoyl-pocket binding that we have seen in our *in vitro* pull-downs. Although this binding occurs with a high affinity *in vitro*, within the context of the cell, UNC119A must successfully compete against the entirety of cellular membranes and extract LCK. The presence of an additional interaction would aid in this extraction by increasing the local concentration of UNC119A in the vicinity of LCK proteins anchored to the membrane **(Figure 3-30)**.

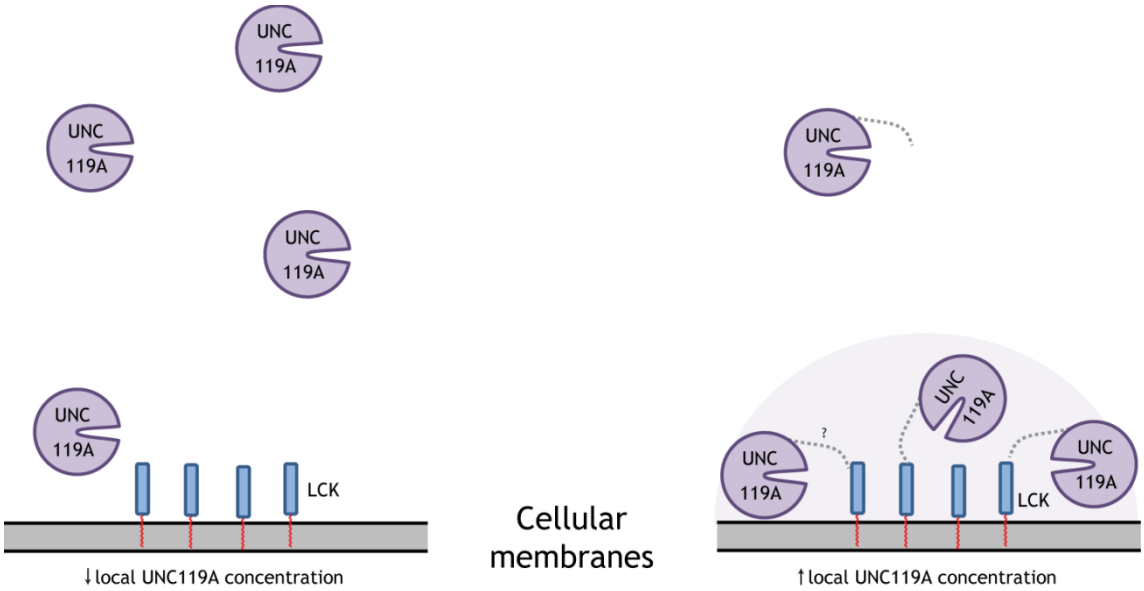

Figure 3-30 UNC119A-LCK additional interaction hypothesis.
LCK is anchored to cellular membranes via the myristoyl moiety. As a result, UNC119A local concentration must be high enough to successfully compete and bind to LCK. This would be aided by the presence of an additional interaction (dashed line) that does not involve the bound myristoyl moiety (red).

3.2.5.1 Purification of recombinant full-length LCK

Obtaining recombinant full-length LCK is a challenge. Commercial sources of full-length LCK and previous structural studies of the kinase domain of LCK (Yamaguchi and Hendrickson, 1996) employed the use of baculoviral infection of Sf21 insect cells.

We had previously used *E.coli* cells to express and purify GST-tagged full-length UNC119A and 6xHis-tagged N-terminal constructs of LCK **(Figure 3-7C)**. Using the same strategy with full-length LCK, however, resulted in low yields due to poor separation of the expressed protein from the rest of the lysate during nickel affinity chromatography. To improve the purification, we increased the length of the C-terminal His-tag to 12 residues to improve the affinity to the column and thereby the subsequent separation. This proved to be a highly successful strategy as I could then wash the column with a higher concentration of imidazole following binding of the lysate **(Figure 3-31A)**. As a result, the obtained LCK-12xHis peak is clearly separated and could be easily further purified. **Figure 3-31B** shows the size exclusion chromatography profile of the 12xHis-LCK fraction: full-length LCK is eluted at a size of around 50 kDa, and was obtained at a yield and purity that was suitable carrying out *in vitro* assays. The advantage of using *E. coli* instead of insect cells as an expression system is that bacteria are faster to transfect and express proteins, thereby allowing the generation of many mutants in a short period of time.

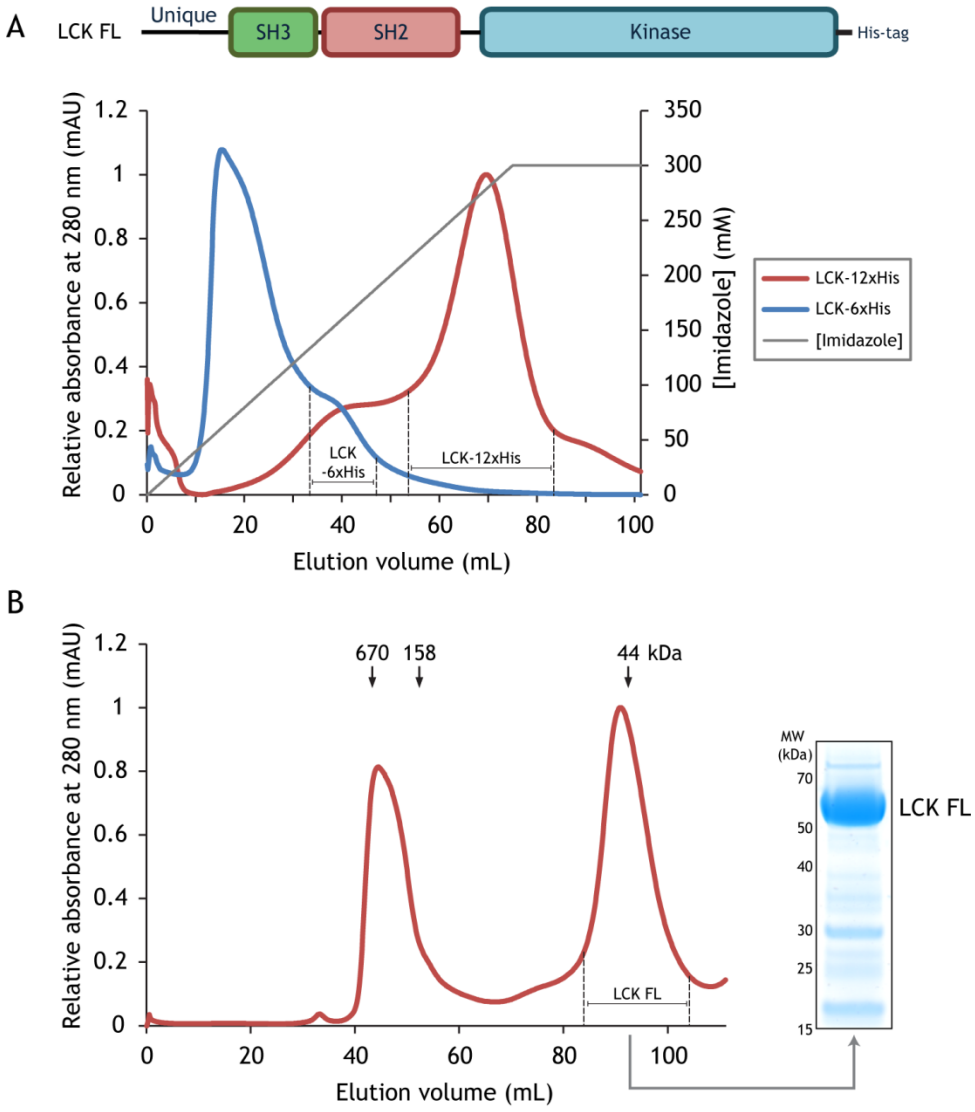

Figure 3-31 Purification of recombinant full-length LCK.

(A) Full-length LCK proteins tagged with 6 and 12 histidine residues were expressed in BL21-CodonPlus (DE3)-RIL competent cells and purified by nickel affinity chromatography. The elution profile of both proteins upon increasing the imidazole concentration is shown. The obtained fractions for each protein are marked by black dashed lines. **(B)** Size exclusion chromatography profile of LCK-12xHis fraction obtained from the nickel affinity column. The LCK FL fraction was separated on SDS-PAGE and stained with Coomassie.

To confirm that the full-length LCK protein obtained from *E. coli* was properly folded, I tested its kinase activity using the ProFluor® Src-Family Kinase Assay (Promega). The assay utilises a rhodamine 110 (R110) bisamide that acts as the SRC kinase substrate. The phosphorylation step is followed by proteolysis, in which the protease removes amino acids to release the fluorescent R110. The protease cannot remove phosphorylated amino acids, however, and the measured R110 fluorescence is inversely proportional to the phosphorylation of the peptide **(Figure 3-32A)**. I compared the kinase activity of *E. coli*-expressed

LCK to that of a commercially-available full-length LCK that was expressed in Sf21 insect cells and was further activated by incubation with Mg^{2+}/ATP (Merck). As shown in **Figure 3-32B**, the kinase activities of the two proteins were comparable, exhibiting a similar activity at concentrations above 0.05 ng/µL. Therefore, the *E. coli*-expressed LCK was functioning as a kinase, indicating that it was folded correctly, and can be used for *in vitro* assays.

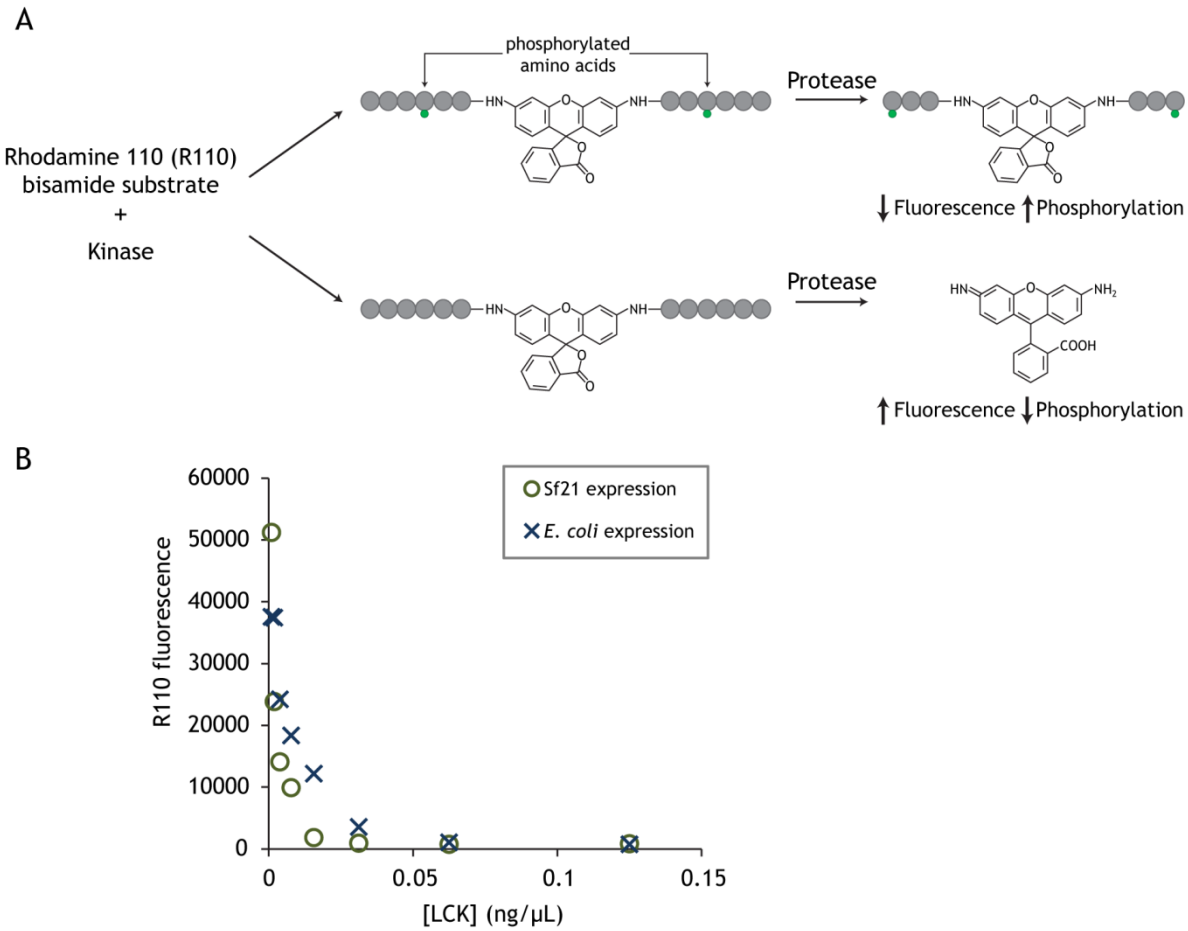

Figure 3-32 Measurement of LCK kinase activity.

(A) Phosphorylation of rhodamine 110 bisamide substrate blocks the protease activity which generates the fluorescent R110. Fluorescence is therefore inversely correlated with the phosphorylation of the substrate obtained by incubation with the tested kinase. **(B**) Kinase activity of the LCK protein expressed in and purified from *E. coli* cells was evaluated and compared to a commercially-available purified LCK which was expressed in Sf21 insect cells and activated during purification by on-column incubation of Mg^{2+}/ATP.

3.2.5.2 The UNC119A N-terminus and the LCK kinase interact independent of myristoylation

To investigate interactions occurring outside of the myristoyl-UNC119A pocket binding, I used full-length LCK expressed in *E. coli* without carrying out *in vitro*

myristoylation. Any binding that occurs in this case excludes the myristoyl moiety, and indicates the presence of an additional interaction.

I started with attempting to pull down LCK with full-length UNC119A, and observed that binding did occur even in the absence of myristoylation **(Figure 3-33A)**. To ensure that the result observed was not due to a non-specific interaction, I repeated the pull-down with N-terminally truncated UNC119A (UNC119A-Δ54), which failed to bind to LCK. Another control used was UNC119B, being an UNC119A homologue that differs mainly in its N-terminal sequence, which also did not appear to bind to full-length non-myristoylated LCK **(Figure 3-33B and C)**. The failure of these two proteins to bind LCK in absence of the myristoyl moiety indicated that the N-terminus of UNC119A was involved in the interaction with LCK, as it is the main difference between these proteins.

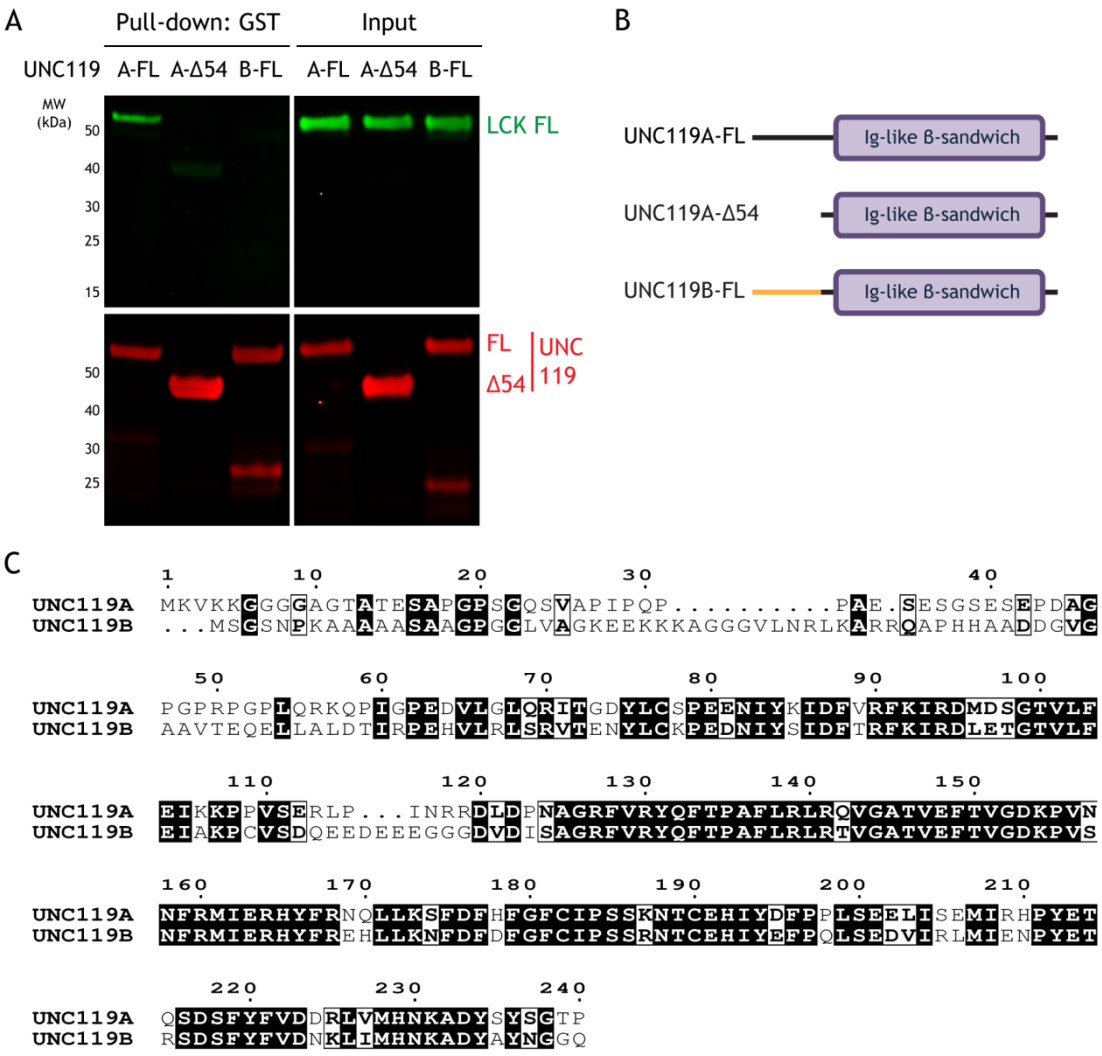

Figure 3-33 The N-terminus of UNC119A binds LCK in absence of the myristoyl moiety. **(A)** UNC119A constructs used in pull-down assays with full-length non-myristoylated LCK. **(B)** 30 µg of the indicated GST-tagged UNC119A or UNC119B proteins were used in a pull-down assay

with 2 µg of purified full-length, non-myristoylated 12xHis-tagged LCK. Proteins were detected by Western blotting using antibodies against GST and His. **(C)** Sequence alignment of full-length UNC119A and UNC119B, which share 55% sequence identity; residues shared by both sequences are marked in black. FL, full-length; Δ54, N-terminally truncated; Ig, immunoglobulin.

The next step was to identify the LCK domain interacting with the N-terminus of UNC119A. The N-terminal constructs of LCK (LCK SH3-SH2 and LCK SH3) had previously been shown to require *in vitro* myristoylation for binding to UNC119A to occur **(Figure 3-7C)**. I therefore tested a construct encoding the LCK kinase domain ($LCK^{229-509}$) in pull-down assays with full-length and N-terminally truncated GST-tagged UNC119A **(Figure 3-34A)**. As shown in **Figure 3-34B**, the LCK kinase domain did bind to full-length but not truncated UNC119A, similar to the full-length LCK. LCK SH3-SH2, on the other hand, did not bind either construct of UNC119A in the absence of N-terminal myristoylation **(Figure 3-34C)**.

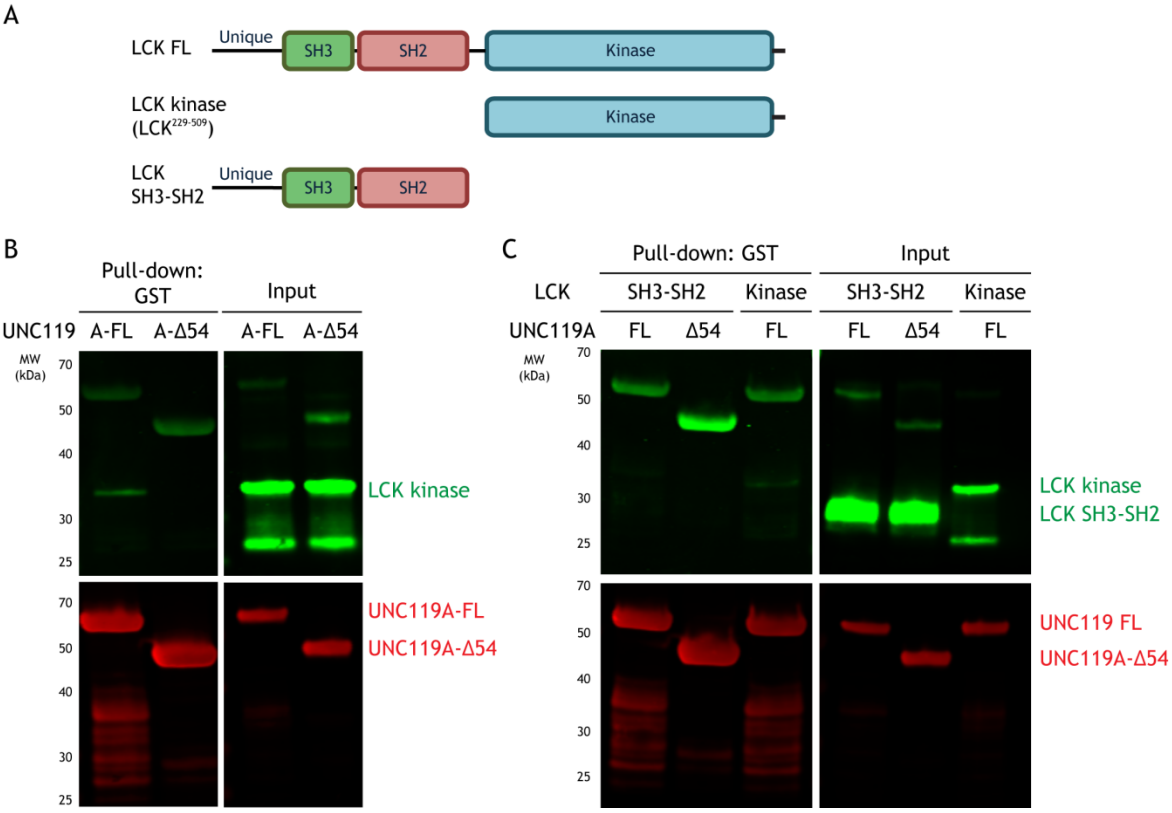

Figure 3-34 The kinase domain of LCK interacts with the N-terminus of UNC119A.
(A) LCK constructs used in pull-down assays with GST-tagged full-length and N-terminally truncated UNC119A. **(B)** 30 µg of GST-tagged full-length and N-terminally truncated UNC119A was used to pull down 12 µg of purified His-tagged LCK kinase domain. The same pull-down was repeated in **(C)** with 12 µg of purified LCK SH3-SH2 also being used. Proteins were detected by Western blotting with antibodies against GST (UNC119 FL and Δ54) and His (LCK kinase and SH3-SH2). All LCK proteins used were non-myristoylated.

Together, these results point to the presence of another interaction between UNC119A and LCK, involving their respective N-terminus and kinase domain. All reported UNC119 structures do not include its N-terminus, due to its high flexibility, so we have no structural data as yet on this interaction.

However, an UNC119A mutation was reported in a patient with idiopathic CD4 lymphopenia (ICL) (Gorska and Alam, 2012). The patient exhibited a reduction in TCR stimulation due to mislocalisation of LCK to RAB11^{+} endosomes as well as decreased LCK activity. This was attributed to the disruption in binding between LCK and the mutant UNC119A^{G22V}. This glycine-to-valine mutation at position 22 is located in the N-terminus of UNC119A, and so it should not affect the binding between the hydrophobic pocket and the myristoyl moiety. I tested the mutant in a fluorescence polarisation assay with the fluorescently-labelled myristoylated N-terminal LCK peptide, and found that binding still occurs despite the mutation **(Figure 3-35A)**. However, the mutant fails to pull down non-myristoylated full-length LCK in a pull-down assay, as shown in **Figure 3-35B**. It is the additional interaction that is therefore disrupted in the case of this mutation and not the high affinity binding to the myristoyl group. However, the disruption remains sufficient to cause impaired immune function in the patient, which points to the importance of this interaction.

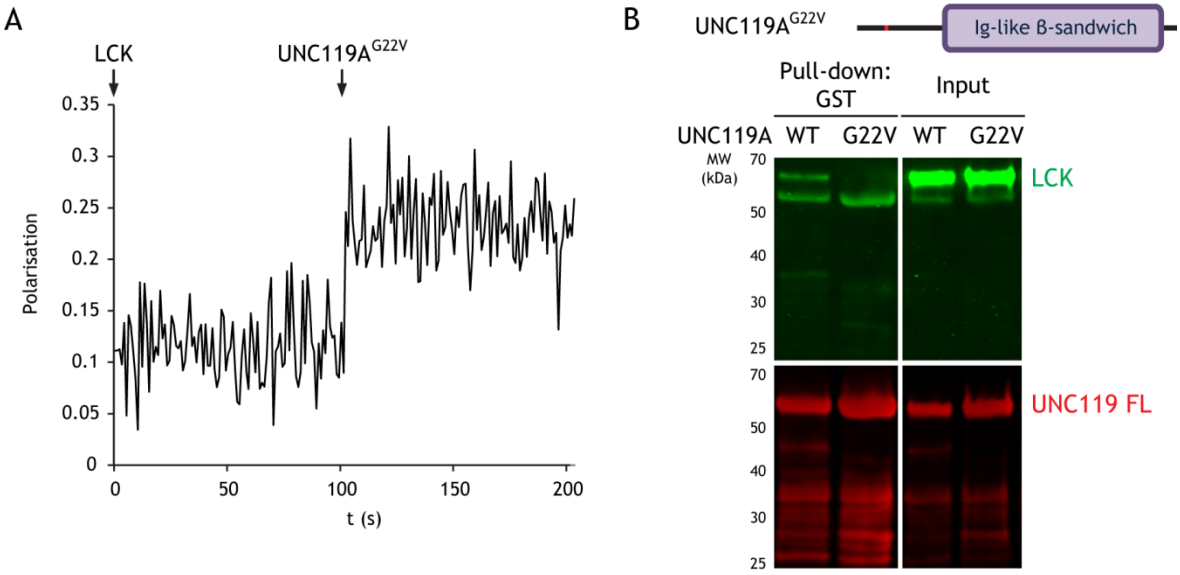

Figure 3-35 N-terminal patient mutation of UNC119A affects its additional interaction to LCK. **(A)** 0.5 μM full-length GST-UNC119A^{G22V} was added to a 5 nM solution of fluorescein-labelled myristoylated N-terminal peptide of LCK, and fluorescence polarisation was measured. **(B)** 30 μg of GST-tagged wild-type and mutant UNC119A were used to pull down 2 μg of full-length LCK. UNC119 and LCK were visualised with antibodies against GST and His, respectively. Ig, immunoglobulin.

UNC119A shares structural similarities to RHO GDP-dissociation inhibitors (RHOGDIs) which bind lipid-modified RHO proteins, thereby extracting them from membranes into the cytoplasm. This extraction take place over two steps, the first of which involves the binding of N-terminal regulatory arm to the cytoplasmic switch regions of the membrane-anchored RHO protein, as shown in **Figure 3-36**. This is followed by binding of the C-terminal lipid tail to the hydrophobic pocket of the GDI, which is correctly oriented next to the lipid tail due to the initial binding step (Hoffman et al., 2000). Furthermore, the binding of the regulatory arm of RABGDI, whose pocket binds prenylated RAB proteins, has been shown to be dependent on the nucleotide state of RAB, with over 600-fold higher affinity to GDP-bound RAB than the GTP-bound form (Wu et al., 2010). This led us to the question of whether the N-terminal interaction of UNC119A with the kinase domain of LCK is subject to a similar regulation.

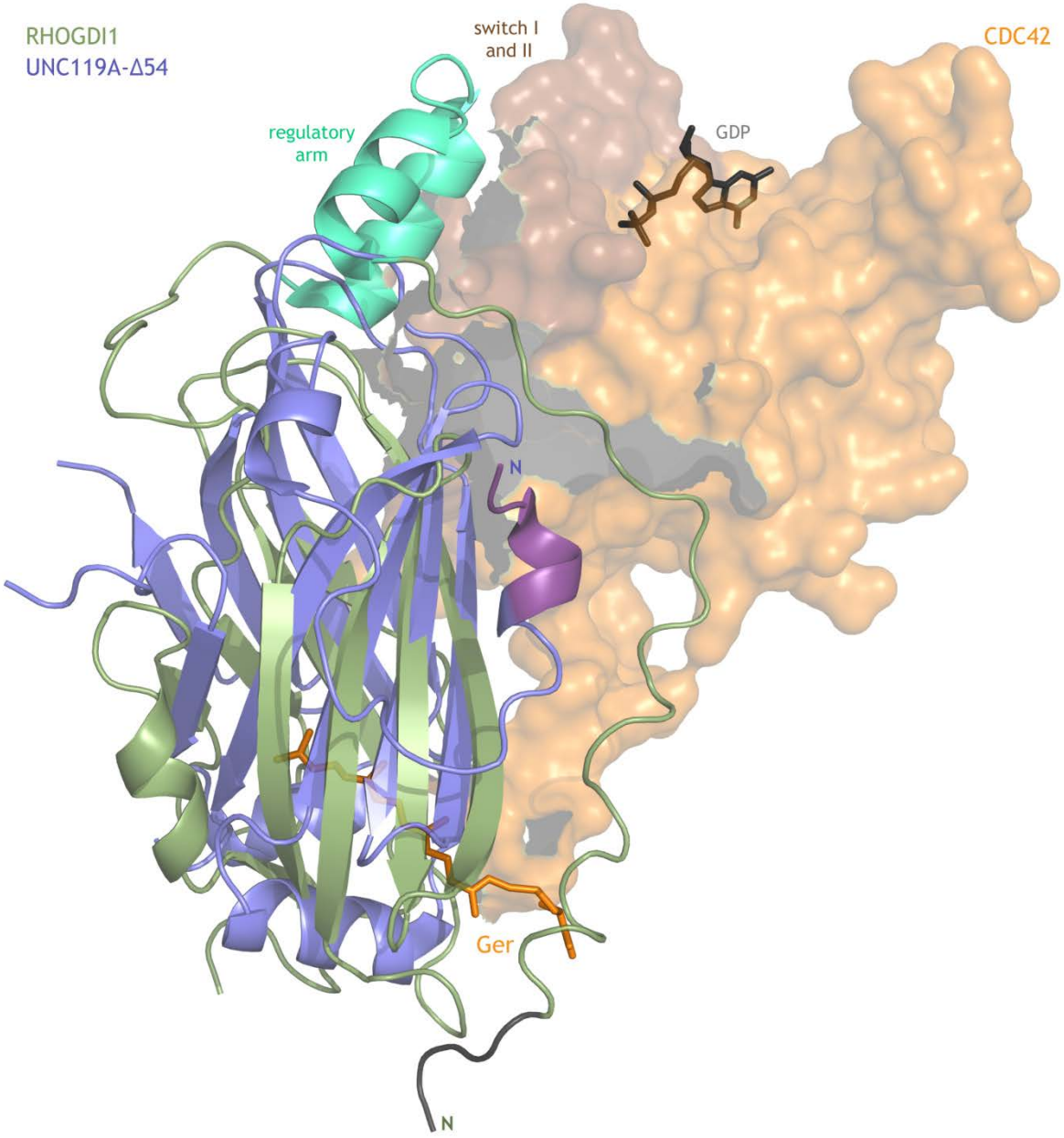

Figure 3-36 N-terminal regulatory arm of RHOGDI1.
Superimposition of cartoon representations of the structures of UNC119A-Δ54 (purple) and RHOGDI1 (green), with the latter in complex with CDC42 (orange surface representation). The N-terminal regulatory arm of RHOGDI1 (cyan) interacts with the switch regions of CDC42 (brown surface). The C-terminal geranylgeranyl (Ger) moiety of CDC42 is shown in orange stick form within the RHOGDI1 pocket and the bound GDP nucleotide is shown as grey sticks. The UNC119A N-terminus is missing its first 58 residues, and is marked in dark purple. PDB codes: UNC119A, 6H6A (Stephen et al., 2017); RHOGDI1-CDC42, 1DOA (Hoffman et al., 2000).

3.2.5.3 Phosphoregulation of the UNC119A-LCK additional interaction

The kinase domain of LCK undergoes phosphoregulation, where the phosphorylation status of conserved tyrosine residues can enhance or inhibit its kinase activity **(section 3.1.3.2)**. If the UNC119A additional interaction with the

kinase domain is regulated by the activity of the cargo, perhaps its binding to LCK may be phosphorylation-dependent. I therefore repeated the pull-down assays between full-length UNC119A and non-myristoylated LCK in the presence and absence of ATP. As shown in **Figure 3-37A**, the interaction did appear to be inhibited in the former case, when ATP was present in the pull-down. However, the presence of ATP with both proteins gives rise to the possibility that both proteins were phosphorylated, which resulted in the inhibition. To narrow down the cause of the inhibition, I incubated UNC119A and LCK with ATP as in the previous assay, before separating each of the proteins from the rest of the phosphorylation reaction **(Figure 3-37B)**. As a result, the pull-down assay could be carried out with the phosphorylated proteins in the absence of ATP. The pull-downs were successful only in the absence of pLCK, regardless of whether UNC119A was phosphorylated **(Figure 3-37C)**, which points to the phosphorylation of LCK resulting in the inhibition of the N-terminal interaction of UNC119A.

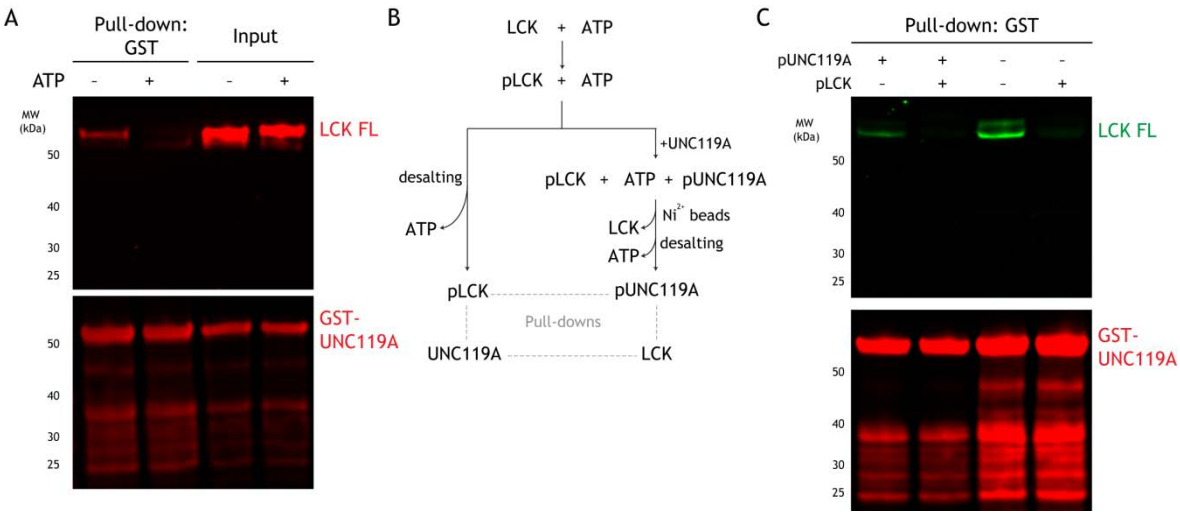

Figure 3-37 The additional interaction between UNC119A and LCK is inhibited by phosphorylation of LCK.

(A) 2 µg of non-myristoylated, full-length LCK was incubated with 1 mM ATP for 6 hours on ice and was then used in a pull-down with 30 µg of full-length GST-UNC119A. Proteins were detected in the Western blots with antibodies against LCK and GST. **(B)** LCK and UNC119A were phosphorylated and separated from the remaining components of the phosphorylation reactions. Grey dashed lines indicate proteins tested together in pull-down assays. **(C)** 4 µg of full-length, His-tagged LCK was incubated overnight on ice with 1 mM ATP and then was incubated with 60 µg GST-UNC119A FL for 3 hrs at room temperature. LCK and ATP were then removed using high density nickel resin and Zeba™ spin desalting columns, respectively. The remaining potentially-phosphorylated UNC119A (pUNC119A) was divided in two and used to pull-down 2 µg of LCK that was incubated overnight on ice in 1 mM ATP (pLCK) or water. 2 µg of LCK full-length, His-tagged

LCK was incubated overnight on ice in the presence or absence of 1 mM ATP. ATP was removed by dialysis before carrying out GST pull-downs with 30 µg of untreated GST-UNC119A. Proteins were detected in the Western blots with antibodies against His (LCK in **C**) and GST (LCK in **A** and GST-UNC119A).

The next step was to identify the tyrosine residue or residues whose phosphorylation resulted in the inhibition of the binding. We started with mass spectrometry analysis of full-length LCK following ATP incubation, which identified 11 phosphotyrosine residues in the LCK sequence regions covered by detected peptides, which are shown in **Figure 3-38A**. I also analysed the LCK sequence using the NetPhos 3.1 server to identify predicted sites of tyrosine phosphorylation in LCK (Blom et al., 1999). The NetPhos analysis helped to narrow down the mass spectrometry results by filtering out tyrosine sites with low phosphorylation potentials, such as Y51, Y209, and Y264, all of which scored below the 0.5 threshold. The analysis also identified two sites with high phosphorylation potential in regions that were not covered by identified peptides in the mass spectrometry analysis: Y313 and Y360 **(Figure 3-38B)**.

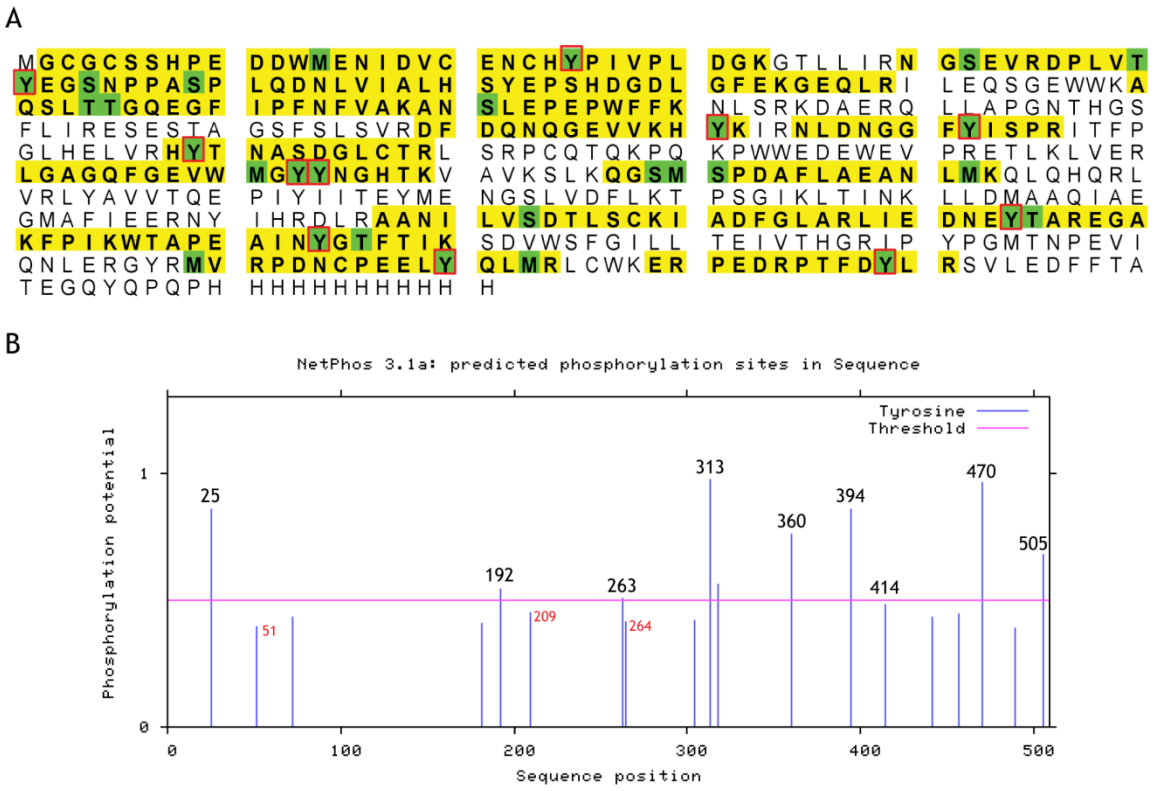

Figure 3-38 Identification of phosphorylated LCK tyrosine residues following ATP incubation. **(A)** Detection of phosphotyrosine residues in 12 µg of non-myristoylated, full-length LCK incubated at room temperature in 1 mM ATP for 15 minutes was carried out by mass spectrometry following tryptic digestion. Tyrosine residues outlined in red were found to be

phosphorylated (residues 25, 51, 181, 192, 209, 263, 264, 394, 414, 470, and 489). Yellow shading indicates peptide coverage. **(B)** The LCK sequence was run through the NetPhos 3.1 server to predict potential phosphotyrosine residues in the sequence. Of the predicted residues that were not identified by the mass spectrometry analysis, Y313 and Y360 were predicted to be high probability sites (scores of 0.973 and 0.755, respectively). Positions marked in red indicate residues that were identified by the mass spectrometry analysis but scored phosphorylation potentials below the threshold.

Based on these results, I identified 11 tyrosine residues to investigate as the regulatory phosphotyrosine(s). These included the eight residues that were identified by mass spectrometry and were predicted by the NetPhos analysis to be high probability phosphorylation sites (residues 25, 181, 192, 263, 394, 414, 470, and 489). In addition, the two highest scoring residues from the NetPhos analysis (Y313 and Y360) were considered to be potential regulatory sites. Finally, I also investigated Y505, which is the conserved inhibitory tyrosine of LCK, and whose phosphorylation results in the autoinhibition of the protein. These sites are summarised in **Figure 3-39A**.

To identify the regulating tyrosine, I mutated each of the tyrosine residues into phenylalanine to block phosphorylation at that site. I then compared the mutants against the wild-type protein in GST pull-downs with full-length UNC119A. The purified recombinant wild-type LCK exhibits a high level of phosphorylation even without pre-incubation with ATP, as detected by an anti-phosphotyrosine antibody **(Figure 3-39B**, LCK^{WT} input lane**)**. This is due to its high kinase activity, and it means that the regulating tyrosine is likely to be phosphorylated to a certain extent in the wild-type protein, reducing its ability to bind UNC119A in the absence of myristoylation. Blocking this phosphorylation through mutation would therefore result in stronger binding to UNC119A despite having a similar level of phosphorylation.

Of the 11 investigated positions, three mutants failed to be expressed by the *E. coli* **(Figure 3-39A)**. I tested the remaining mutants in pull-down assays, and the results are shown in **Figure 3-39B**. Tyrosine-to-phenylalanine mutants at positions 394 and 414 appeared to show stronger binding to UNC119A compared to the wild-type protein. The LCK double mutant at positions 394 and 505 also showed stronger binding, but LCK^{Y505F} did not, indicating that it was due to the mutation of Y394.

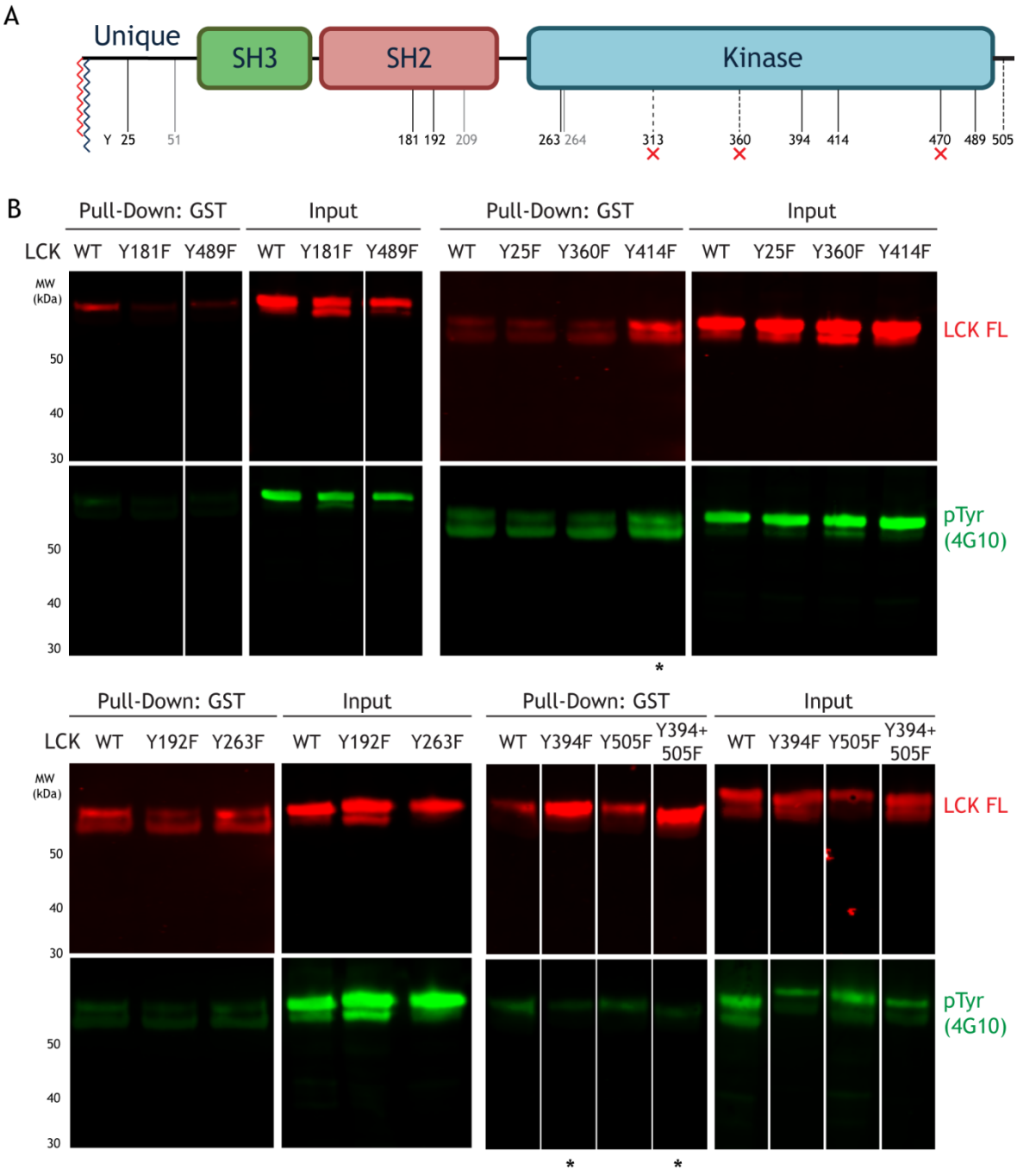

Figure 3-39 Screening for phosphotyrosine LCK residues regulating the interaction with the UNC119A N-terminus.

(A) Domain organisation of LCK showing positions of the 11 phosphotyrosines detected by mass spectrometry (solid lines). Eight of these tyrosine residues were mutated to phenylalanine and expressed in *E. coli* (black solid lines); of these mutants, LCK^{Y470F} failed to be expressed. Y313 and Y360 were predicted by the NetPhos 3.1 server to be high probability phosphorylation sites with scores of above 0.75, and so they were also mutated, along with the inhibitory tyrosine 505 (all three residues are indicated with dashed lines); of these, only LCK^{Y505F} was successfully expressed. **(B)** GST pull-downs in which 60 µg of full-length GST-UNC119A was used to pull down 12 µg of full-length non-myristoylated LCK. In all pull-downs, wild-type LCK was compared to Y→F mutants at the indicated positions. Asterisks indicate mutants that appear to show stronger

binding to UNC119A. Proteins were detected using antibodies against LCK and pTyr(4G10). White lines indicate irrelevant lanes that were spliced out.

The identification of Y394 as a potential regulatory site for the interaction with UNC119A was promising, as Y394 is the conserved tyrosine residue of LCK, whose phosphorylation enhances its kinase activity. This would be the equivalent of the inhibition of the regulatory arm binding to the active RAB-GTP protein, and would indicate that the N-terminal regions of UNC119A and GDIs have similar functions. However, the role of Y394 in enhancing LCK kinase activity complicates matters, as LCK^{Y394F} has lower kinase activity than the wild-type protein, resulting in less phosphorylation as detected by anti-pTyr staining **(Figure 3-39B**, LCK^{Y394F} input lane**)**. The stronger binding of LCK^{Y394F} could therefore be due to lower phosphorylation of another unidentified residue and not due to the blocking of Y394 phosphorylation.

To further investigate the effect of Y394 phosphorylation on the UNC119A interaction, I used LCK^{K273R}, a mutant with an attenuated kinase activity. **Figure 3-40A** shows the kinase activities of LCK^{K273R}, LCK^{WT}, and LCK^{Y394F}, as measured using the previously described assay. Increasing the concentration of all three proteins resulted in decreasing the substrate fluorescence, indicating its phosphorylation. However, all tested concentrations of LCK^{K273R} resulted in much greater R110 fluorescence values, compared to those obtained with both the wild-type LCK and even the Y394F mutant. The kinase activity of LCK^{K273R} is therefore severely attenuated. I then compared the binding of LCK^{WT} and LCK^{K273R} with full-length UNC119A in a GST pull-down assay **(Figure 3-40B)**. LCK^{K273R} showed a much stronger binding to UNC119A compared to the wild-type protein, and had a much lower level of phosphorylation as detected by anti-pTyr staining. This was in line with our previous observations: LCK^{K273R}, having attenuated kinase activity, exhibits less phosphorylation of its tyrosine residues, including the regulatory residue(s). Its interaction with the N-terminus of UNC119A is therefore not inhibited, resulting in stronger binding.

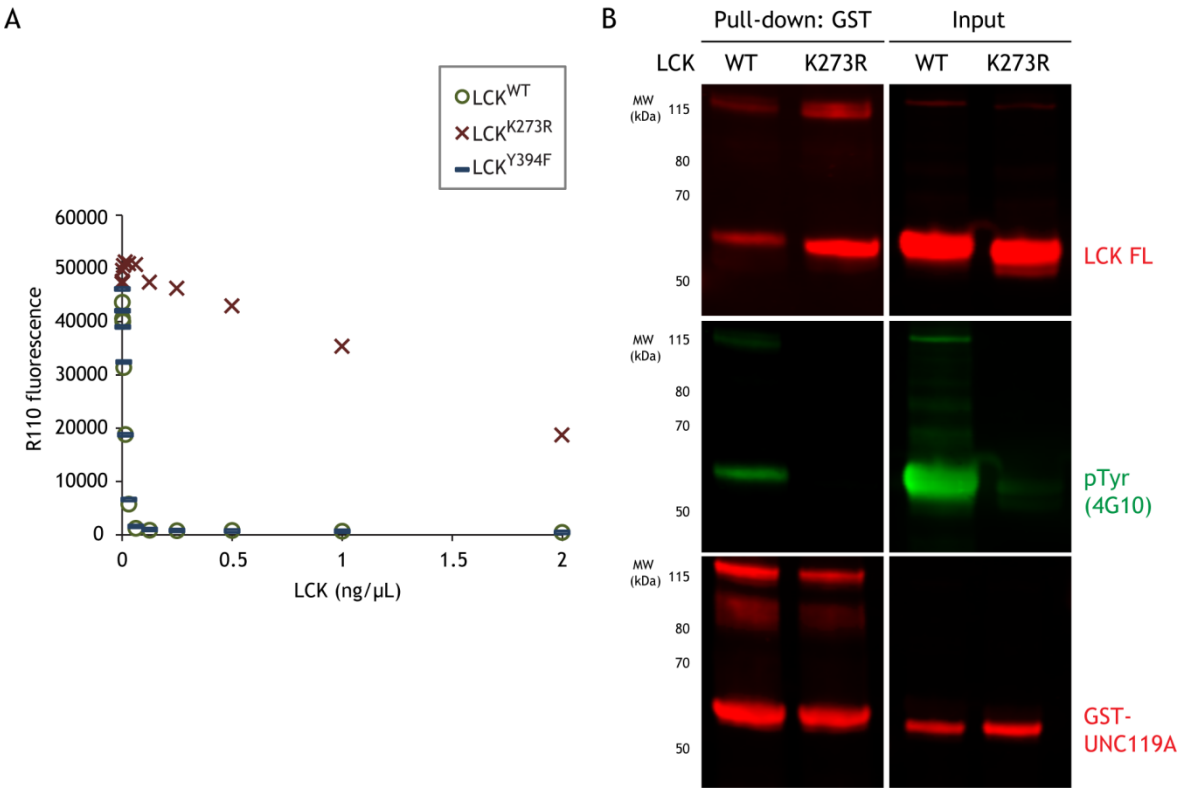

Figure 3-40 Attenuation of LCK kinase activity results in increased UNC119A binding. **(A)** Kinase assay of LCK^{WT}, LCK^{K273R}, and LCK^{Y394F}, where the R110 fluorescence is inversely proportional to the substrate phosphorylation. **(B)** 12 µg of full-length, non-myristoylated LCK^{WT} and LCK^{K273R} were pulled down by 30 µg of full-length, GST-tagged UNC119A. Antibodies against LCK, phosphotyrosine (4G10), and GST were used to detect the proteins.

The next step was to test LCK^{K273R} binding to UNC119A in the presence of ATP. Taking the attenuated kinase activity of the protein into consideration, LCK^{K273R} was used in pull-down assays with UNC119A at different time points during its incubation with ATP. **Figure 3-41A** shows that within 15 minutes of incubation with ATP, LCK^{K273R} binding to UNC119A is greatly reduced, and is almost completely inhibited after two hours. The binding to UNC119A shows an inverse relationship with its level of phosphorylation, confirming the previous results. The reduction of UNC119A binding after 15 minutes of incubation with ATP was of particular interest, because despite the low level of phosphorylation, the binding was still inhibited, indicating the phosphorylation of the regulating residue(s). We therefore used these conditions for identification of LCK phosphotyrosine residues by mass spectrometry analysis, in the hopes of obtaining less background phosphorylation compared to the wild-type protein. Indeed, only three phosphotyrosine residues were identified, at positions 181, 394, and 489 **(Figure 3-41B)**. All three residues were identified by the LCK^{WT}

analysis, but Y181 and Y489 were ruled out by the pull-down assays. We had therefore identified Y394 again as a potential regulatory site for the UNC119A interaction.

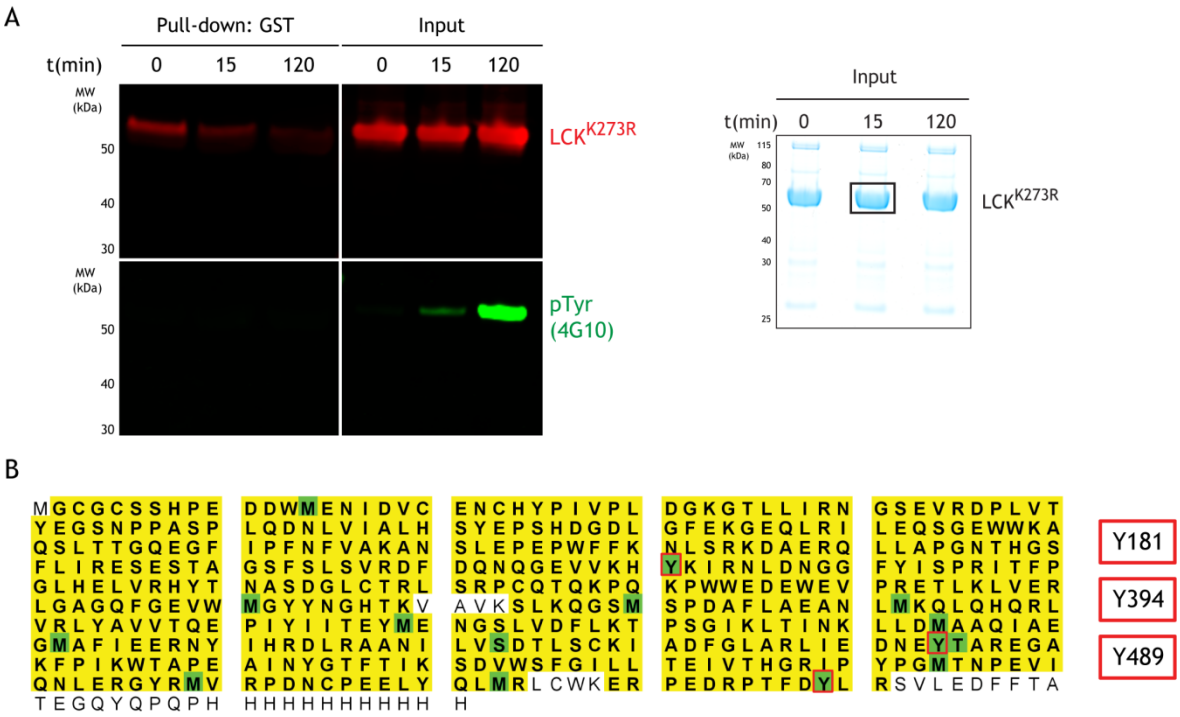

Figure 3-41 Binding of LCK^{K273R} is also inhibited by phosphorylation.
(A) 12 µg of LCK^{K273R} was incubated at room temperature in 1 mM ATP for the indicated times before being pulled down by 60 µg GST-UNC119A. Antibodies against LCK and pTyr(4G10) were used to detect the proteins and samples from the inputs were also stained with Coomassie. **(B)** Detection of phosphotyrosines in the 15 minute LCK^{K273R}+ATP reaction from **(A)** by mass spectrometry following tryptic digestion.

While pY414 was not identified in the LCK^{K273R} mass spectrometry analysis, it may be due to the low level of phosphorylation of the protein. In any case, the attenuated kinase activity of LCK^{K273R} provided a tool to rule out the possibility of the Y394F mutation resulting in increased UNC119A binding due to simply reducing the overall phosphorylation of the protein. LCK mutants with blocked phosphorylation at Y394 and Y414 were compared with LCK^{K273R} in pull-downs with UNC119A. The LCK proteins were tested before and after 15 minutes of incubation with ATP, to allow for the phosphorylation of LCK^{K273R} **(Figure 3-42)**. While LCK^{K273R} binding was inhibited after 15 minutes of incubation, the two single mutants at Y394 and Y414, as well as the double mutant all still showed UNC119A binding even after incubation with ATP. The higher phosphorylation level of these mutants compared to LCK^{K273R} confirms that the effect is due to

the blocking of the phosphorylation of these specific residues, and not due to an overall reduction of LCK phosphorylation.

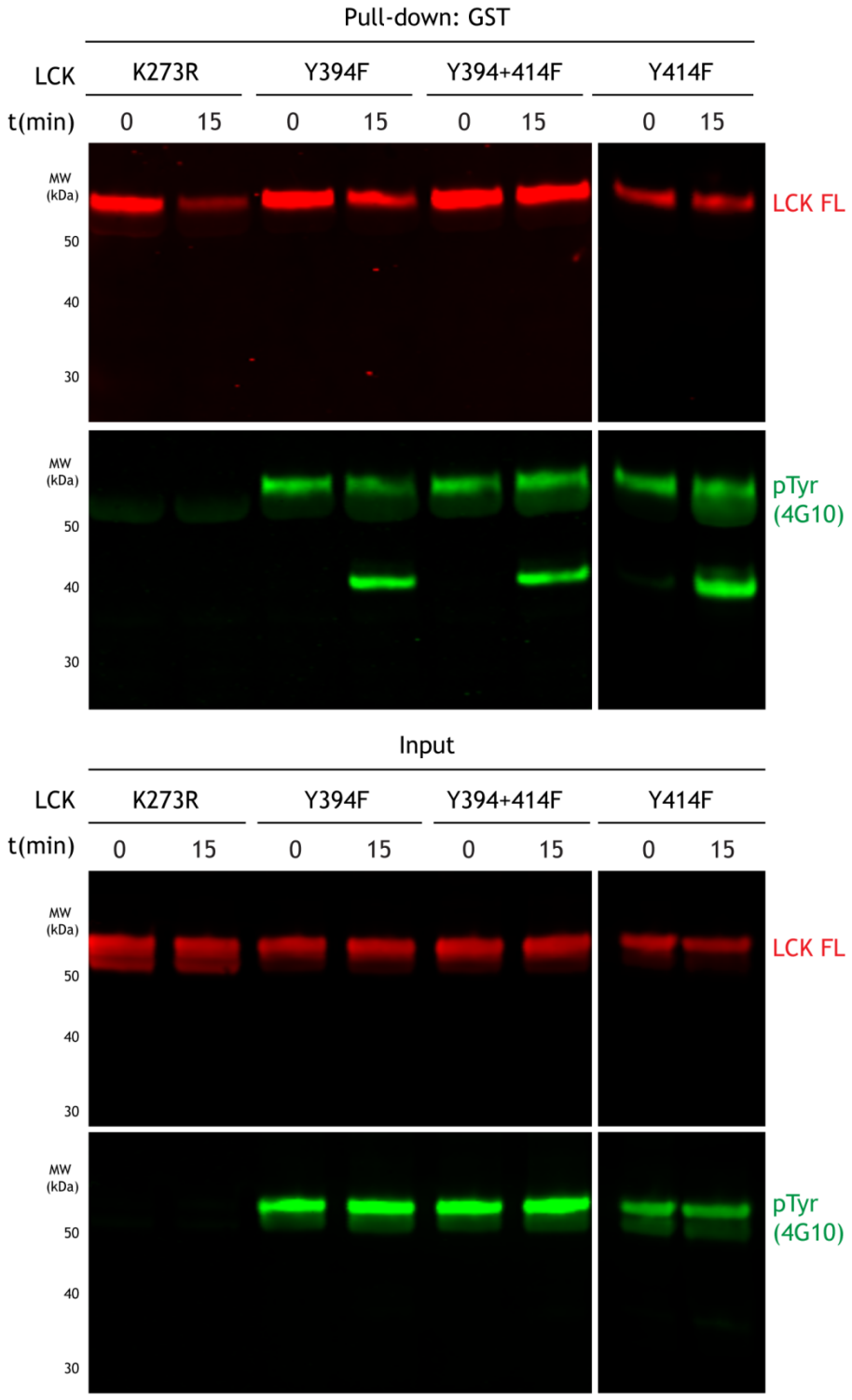

Figure 3-42 Identification of phosphotyrosine residues regulating the interaction with the UNC119A N-terminus.

GST pull-downs with 60 µg full-length GST-UNC119A and 12 µg of the indicated LCK mutants, carried out before and after 15 minutes of incubation at room temperature in 1 mM ATP. Proteins were detected by antibodies against LCK and pTyr(4G10).

The structure of the LCK kinase domain with phosphorylated Y394 (Yamaguchi and Hendrickson, 1996) shows that, in this LCK conformation, Y394 and Y414 are in close proximity **(Figure 3-43)**. In contrast, Y394 in absence of phosphorylation is oriented away from Y414 (Gommermann et al., 2010) due to the different conformation of the LCK activation loop. This perhaps hints to UNC119A binding in the vicinity of Y414, an interaction which may be feasibly inhibited by the phosphorylation of Y414 in addition to that of the activating tyrosine 394.

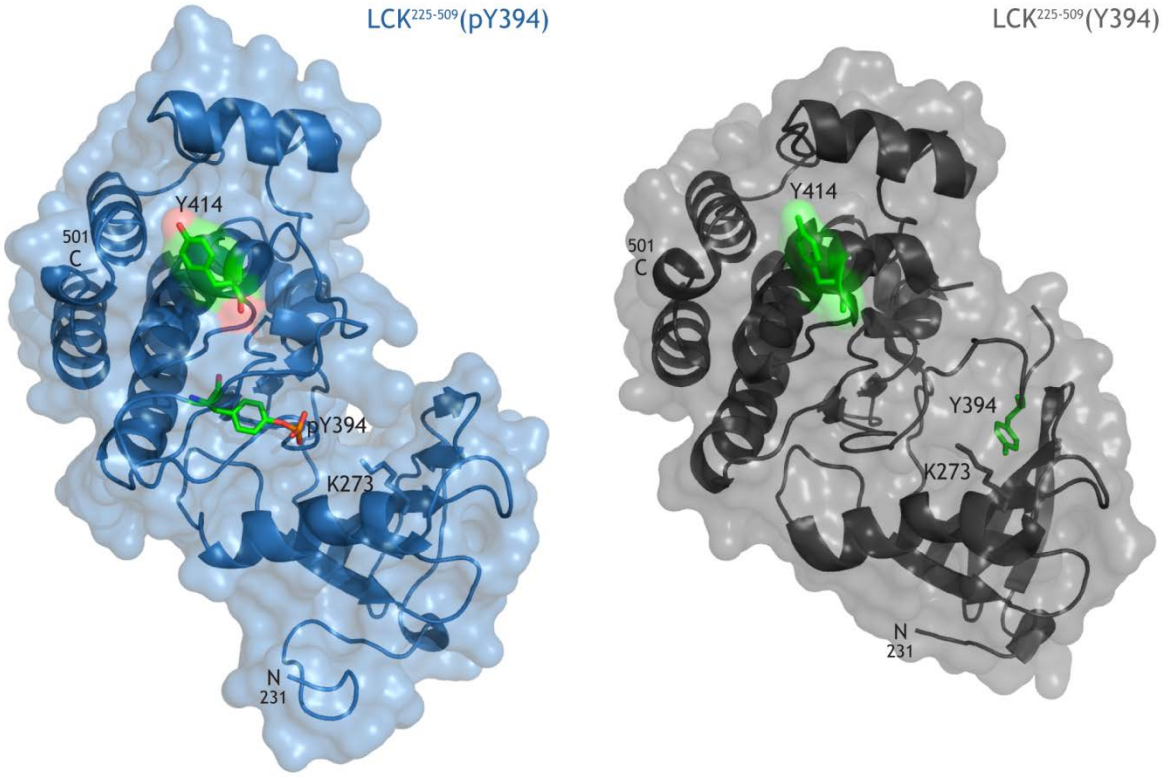

Figure 3-43 Structure of the kinase domain of LCK.
Structures of the LCK kinase domain (residues 225 – 509) in the presence (blue) and absence (grey) of Y394 phosphorylation. Residues Y394, Y414, and K273 in both structures are shown as sticks, with the tyrosine residues coloured in green. PDB codes 3LCK and 3MPM, respectively (Yamaguchi and Hendrickson, 1996, Gommermann et al., 2010).

3.2.5.4 UNC119A binding, LCK autophosphorylation, and LCK immune synapse localisation

LCK autophosphorylation at Y394 resulted in reduced UNC119A N-terminal binding. This gave rise to the question of whether the UNC119A N-terminal interaction had a reciprocal effect on the autophosphorylation of LCK. To investigate, I used LCK^{K273R} as its initial low level of phosphorylation and

attenuated kinase activity allows monitoring of its autophosphorylation under different conditions.

Figure 3-44A shows the autophosphorylation of LCK^{K273R} at different time points following the addition of ATP in the presence and absence of full-length UNC119A. Anti-phosphotyrosine staining of samples taken from both reactions showed no obvious difference in the level of phosphorylation of LCK. However, as LCK^{K273R} is non-myristoylated, UNC119A can only bind through the N-terminal interaction, which has a much lower affinity compared to the binding to the myristoyl moiety. To circumvent this limitation, I used LCK^{K273R} for *in vitro* myristoylation in the presence of N-terminally truncated and full-length UNC119A prior to addition of ATP. In this case, UNC119A will bind the myristoyl moiety of LCK with a high affinity, but the additional interaction can only occur in the presence of full-length UNC119A. LCK^{K273R} showed higher levels of autophosphorylation in the presence of UNC119A-Δ54, which cannot interact with the kinase domain **(Figure 3-44B**, left panel**)**. In contrast, LCK autophosphorylation was reduced in the presence of full-length UNC119A, particularly in the samples taken at earlier time points, as shown in the right panel of **Figure 3-44B**.

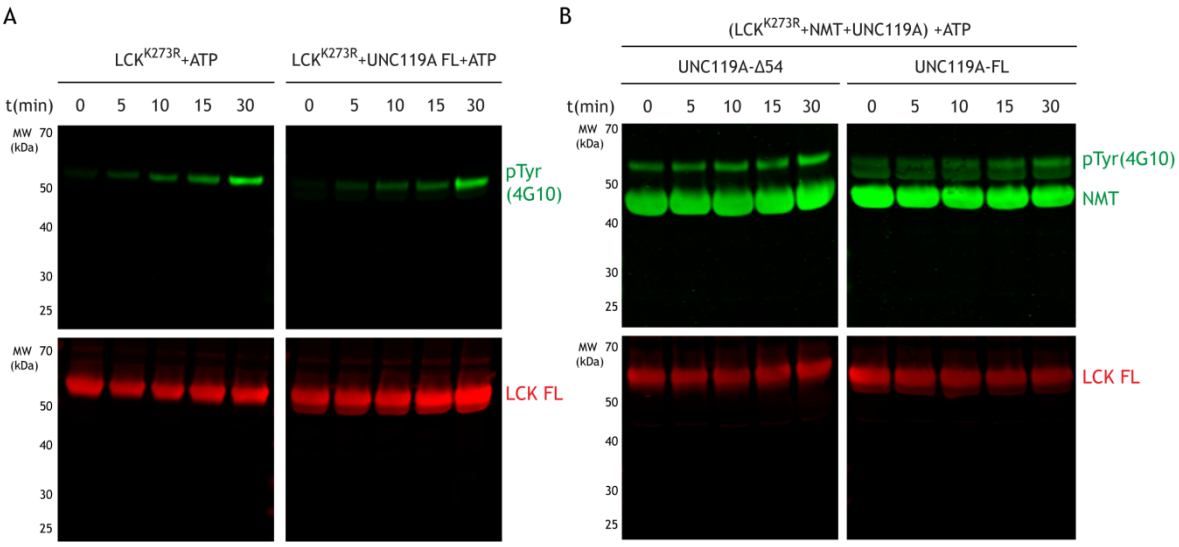

Figure 3-44 Effect of the additional interaction on LCK autophosphorylation.
(A) 6 µg full-length LCK^{K273R} was incubated in 1 mM ATP at room temperature in the presence or absence of full-length UNC119A. Samples were taken at the indicated time points and autophosphorylation was monitored by Western blotting. **(B)** The same experiment was repeated, this time using LCK^{K273R} that underwent *in vitro* myristoylation in the presence of UNC119-Δ54 (left) or UNC119A-FL (right) before ATP incubation. Antibodies against LCK and pTyr(4G10) were used for visualisation.

Finally, we have shown that LCK immune synapse localisation is affected by its affinity to UNC119A. Furthermore, the affinity to the N-terminal region of UNC119A is affected by LCK autophosphorylation at Y394. Due to its effect on affinity to UNC119A, we hypothesised that LCK phosphorylation is likely to affect its immune synapse localisation.

We therefore studied the localisation of LCK at the immune synapse with respect to its phosphorylation status. Immune synapses were formed between Jurkat T cells transfected with LCK^{Y394F}GFP and SEE-loaded Raji B cells as previously described. LCK^{Y394F}GFP showed a much reduced immune synapse localisation relative to the rest of the T cell membrane **(Figure 3-45)**. This is especially evident in comparison to endogenous LCK phosphorylated at Y394 (^{pY394}LCK), which showed a much higher immune synapse localisation.

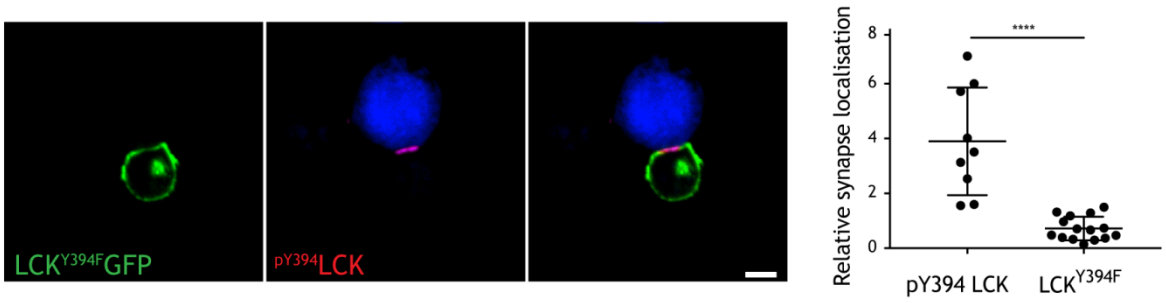

Figure 3-45 LCK phosphorylation and immune synapse localisation.
T-B conjugates were formed using Jurkat T cells transfected with GFP-tagged LCK^{Y394F} and Raji B cells that were incubated in CMAC and SEE. The conjugates were stained with an anti-pY394 LCK antibody. LCK phosphorylated at Y394 localised to the immune synapse with a ratio of 3.89, while the mutant LCK^{Y394F} showed a ratio of 0.72 ($p<0.0001$). Scale bars represent 5 µm.

3.3 Discussion

The assembly of the immune synapse population of proteins, cytoskeletal elements, and organelles is a highly orchestrated undertaking on the part of the T cell. The nature of the immune synapse as a functional domain in the plasma membrane dictates that three conditions must be met in the trafficking of these synapse components. Namely, they must take place at the appropriate speed, be directed to the targeted destination, and finally, allow post-delivery retention for the duration of the synapse localisation of the cargo.

This chapter presented our work on investigating the trafficking of LCK to the immune synapse via a potential UNC119A-mediated route. Two main approaches were employed: the interaction of LCK and UNC119A was characterised using structural and biochemical studies of recombinant proteins. In parallel, preliminary testing of our hypotheses was carried out using the synapse model system of Jurkat T cells and SEE-coated Raji B cells. We used the information obtained from these studies to suggest a model of UNC119A-mediated transport of LCK to the immune synapse **(Figure 3-46)**, which fulfils the aforementioned requirements.

In building a model from our results, we also outline the subsequent studies required to confirm its validity and circumvent the limitations of our previous work. The use of the Jurkat-Raji model poses the disadvantage of using transformed cells which do not fully reflect the repertoire of adhesion and accessory molecules expressed by primary cells (Huppa and Davis, 2003). Further studies in our lab are currently utilising engineered primary T cells ($CD4^+$ OT-II and $CD8^+$ OT-I cells) to study synapses formed with APCs stably expressing their cognate antigenic peptide.

While our structural studies of the UNC119A-LCK peptide complex identified the requirements for high affinity binding in the hydrophobic pocket, the additional interaction requires more work. The crystal structure of the complex of full-length UNC11A and LCK is crucial to dissect how this interaction takes place and is regulated by LCK phosphorylation. However, several challenges are involved, chief among which is the fact that the full-length structures of both proteins has

not been solved. It is possible that complex formation can stabilise the proteins and reduce domain flexibility to aid in crystallisation. Formation of the complex is also not straightforward. Our previous attempts of using *in vitro* myristoylated LCK constructs failed to produce crystals. Two solutions are possible: first, to forgo the myristoylation and depend on the N-terminal interaction to hold the complex together. It might be beneficial in this case to utilise the low kinase activity of LCK^{K273R} to minimise its phosphorylation and maximise the interaction with UNC119A. Alternatively, we can attempt LCK expression in mammalian HEK-293 cells, which can produce myristoylated LCK. Further dephosphorylation by using CD45 or another phosphatase may increase the homogeneity of the purified LCK with respect to the presence of phosphotyrosine residues.

Furthermore, the interaction itself remains to be confirmed in the physiological setting. This can be attempted though investigating the effect of manipulating the expression of UNC119A and other proteins implicated in the pathway. In addition, studying protein localisation to the synapse in fixed cells is very likely to miss important dynamics as the synapse organisation and composition changes over time. Imaging of live cells is crucial to track the transport of LCK to the synapse in the context of the UNC119A-mediated pathway. With these limitations in mind, follow-up investigations required to confirm the model and answer open questions will be mentioned throughout this chapter.

3.3.1 An early phase of rapid LCK transport

The formation of the immune synapse is a temporally dynamic process, with different components arriving at different time points and exhibiting different localisations with the passage of time. Trafficking mechanisms must therefore deliver each component within the appropriate time frame. The role of LCK as the initiator of TCR signalling requires its rapid localisation to the synapse following TCR-pMHC recognition.

The presence of active LCK with phosphorylated Y394 has been detected at the $CD4^+$ T cell-APC synapse within 2 min of TCR stimulation (Holdorf et al., 2002). Previous reports of LCK trafficking to the synapse have implicated a $RAB11^+$ endosomal route with the possible contribution of another endosome-independent route (Bijlmakers and Marsh, 1999, Gorska et al., 2009). In

addition, later studies of the recovery of LCK following photobleaching using single molecule fluorescence microscopy reported an early phase of recovery mediated by a cytosolic fraction of LCK rather than lateral diffusion. This recovery was maintained even in the inhibition of endosomal transport, supporting the presence of an endosome-independent delivery route (Zimmermann et al., 2010).

We have shown that the GDI-like solubilising factor UNC119A can bind the myristoyl moiety of LCK with a high affinity (Stephen et al., 2018), which would allow its free movement in the aqueous environment of the cytoplasm. The extraction of membrane-associated LCK and the formation of a soluble UNC119A-LCK complex can account for the presence of a freely-diffusing cytosolic fraction. Solubilisation is the critical factor in this case because LCK undergoes co-translational myristoylation (Caron et al., 1992), and so will need to mask the myristoyl moiety throughout its presence in the cytoplasm. c-SRC, which belongs to the same family as LCK, has been deemed unlikely to have a myristoyl switch (whose mechanism is demonstrated in **Figure 1-4B**), as disrupting its potential myristoyl-binding pocket did not affect the membrane binding, unlike in the case of known myristoyl-switching proteins (Patwardhan and Resh, 2010). LCK has not been reported to be able to sequester its own myristoyl moiety, and given the c-SRC study, this is unlikely to be the case. Therefore, LCK diffusion in the cytoplasm will be hampered by binding to membranes unless the lipid moiety is masked from the aqueous surroundings.

The aforementioned endosomal pathway may serve as a slow mechanism for LCK transport to the plasma membrane, such as that required for continuous recycling of immune synapse components for sustained TCR signalling (Onnis and Baldari, 2019). However, the rapid delivery to the synapse at the onset of TCR stimulation requires a different transport mechanism. Faster transport may be achieved either by lateral diffusion from regions in the plasma membrane surrounding the assembling synapse or via the cytoplasm. It has been reported that the diffusion of wild-type LCK in the membrane is slower compared to that of the Y394F mutant (Wan et al., 2019). The authors suggested that wild-type LCK is more prone to clustering, resulting in its slowed movement in the membrane.

Delivery of LCK through the cytoplasmic route by way of soluble UNC119A complexes can circumvent slow transport through the endosomal route. It can also aid in speeding up lateral diffusion in the membrane, hence allowing the rapid delivery of the kinase to the membrane to initiate signal transduction following TCR stimulation. Live cell imaging studies have shown that the TCR itself accumulates at the $CD8^+$ cSMAC in two phases. Initial TCR clustering occurs at the same time as the clearance of synaptic actin within 1 minute of contacting the target cell. This is then followed a few minutes later by vesicle-mediated transport alongside the polarising centrosome, which docks at the synapse 6 minutes after the initiation of synapse formation (Ritter et al., 2015).

The two-phase formation of the cSMAC gives rise to the question if it also applies to the delivery of LCK to the synapse. If that is the case, the exact role(s) of the UNC119A-mediated pathway need to be elucidated. This can be attempted through live cell imaging studies of LCK transport to the synapse in T cells where the UNC119A pathway is disrupted via the deletion of various components. The differences in the spatiotemporal organisation of LCK can give indications as to the role of UNC119A and its associated proteins in relation to the endosomal delivery of LCK. Furthermore, how would disrupting the pathway affect the downstream effector functions of T cells, such as cytokine release and cytotoxicity of $CD4^+$ and $CD8^+$ cells, respectively?

3.3.2 Specific delivery of LCK

In addition to the speed of transport, LCK delivery must be targeted for precise initiation of TCR signalling following the recognition of pMHCs. Spatial segregation of various components of the immune signalling machinery has been suggested as a mechanism by which regulation of T cell activity is achieved. One aspect of this segregation is the proposed exclusion of the negative LCK regulator CD45 from the synapse upon TCR stimulation (Rossy et al., 2012). Targeted delivery of LCK to the synapse would avoid CD45-mediated inhibition and increase the efficiency of TCR signal transduction.

We have demonstrated *in vitro* that the high affinity binding between LCK and UNC119A is specifically released by the action of the active small G protein ARL3GTP and not by its homologue ARL2. In addition, our imaging studies of

Jurkat-Raji conjugates showed the specific localisation of the ciliary protein ARL13B at the immune synapse. Furthermore, overexpressing an ARL13B-independently active ARL3 also resulted in LCK synapse mislocalisation, confirming the role of ARL13B (Stephen et al., 2018). This finding adds to the similarities shared between immune synapses and primary cilia as specialised membrane domains formed at the docking of the centrosome to the membrane (Stinchcombe et al., 2006). The function of ARL13B as the guanine nucleotide exchange factor for ARL3 provides a mechanism for the synapse-specific release of LCK from UNC119A complexes through the local generation of active ARL3GTP. This is the same strategy employed by the primary cilium to specifically release high affinity cargo from GSFs inside the ciliary compartment (Gotthardt et al., 2015).

This mechanism of specific delivery to the synapse was supported by the observation that the relative LCK immune synapse localisation was decreased upon reducing LCK affinity to UNC119A, both by chemical intervention or mutational studies. The latter were facilitated by structural information obtained from the UNC119A-LCK peptide complex, which suggested a requirement for the presence of small residues following the myristoyl moiety (Stephen et al., 2018).

The identification of the role of the ciliary ARL13B in the synapse localisation of LCK still leaves the open question of how and when ARL13B itself localises to the synapse. Our studies of fixed synapses show that it is enriched at the synapse within 10 minutes of contact, which remains a relatively long period of time in the highly dynamic lifetime of the synapse. Careful dissection of this initial phase of protein localisation is necessary to unravel how ARL13B and the TCR bring about LCK polarisation. Furthermore, how is ARL13B restricted to the domain of the immune synapse? Ciliary localisation of ARL13B is not fully understood, but it has been reported to depend on the palmitoylation of N-terminal sites (Hori et al., 2008). In addition, disruption of various ciliary intraflagellar transport (IFT) components in *C. elegans* resulted in some mislocalisation of ARL13B to membranes surrounding the cilium (Cevik et al., 2013). TCR clustering to the immune synapse has been linked to some IFT components (Finetti et al., 2009), so perhaps their function in the immune synapse extends to ARL13B localisation as well.

3.3.3 Retention at the immune synapse

The immune synapse is a functional domain with no overt boundaries from the surrounding membrane. Local concentrations of proteins in such domains exist against the concentration gradient, and so must be actively maintained by the cell to prevent equilibration either to the cytoplasm or the surrounding membrane.

LCK is known to associate with the TCR coreceptors, which on Jurkat T cells is CD4. Coreceptors localise to the pMHC-bound TCR by binding to the antigen-presenting MHC molecules (Veillette et al., 1988). The association of LCK to CD4 may serve to restrict LCK localisation to the TCR. However, it has been shown using super-resolution imaging of activated $CD4^+$ T cells that active ^{pY394}LCK clusters do not colocalise with those of CD4 coreceptors at the interface with the activating surface (Roh et al., 2015).

Membrane association of myristoylated LCK is stabilised by palmitoylation, as catalysed by the palmitoyl acyltransferase DHHC-21 (Akimzhanov and Boehning, 2015). This provides the second signal which together with the myristoyl moiety stabilises hydrophobic interactions with the membrane, which is known as bilayer trapping (Shahinian and Silvius, 1995). However, the transient nature of palmitoylation predicts that a fraction of LCK at the synapse will only have the myristoyl moiety, and can therefore be extracted from the membrane by UNC119A. This would result in the leakage of the immune synapse fraction of LCK to the cytosol. In our investigation of the biochemistry of the binding between UNC119A and LCK, we have identified an additional interaction that occurs independently of the myristoyl moiety. Furthermore, this binding between the N-terminus of UNC119A and the kinase domain of LCK was inhibited by the phosphorylation of LCK, specifically at tyrosine 394 (Stephen et al., 2018). The additional interaction is posited to aid in the extraction of membrane-associated LCK by UNC119A, as it would form a region of high local concentration around the anchored LCK. As previously mentioned, active LCK present at the immune synapse exhibits phosphorylation at tyrosine 394. It is therefore likely that the inhibition of the additional interaction would allow the retention of this active LCK at the immune synapse. In addition, retention against lateral diffusion may occur due to the formation of larger clusters of LCK

as it becomes more activated (Wan et al., 2019). The slower diffusion rate and the higher likelihood of being impeded by various barriers in the membrane can help prevent its dissemination to the wider plasma membrane.

The possible roles of the additional interaction with UNC119A in maintaining the retention of LCK in the immune synapse need to be confirmed by monitoring LCK localisation with the disruption of this interaction. Would the N-terminally truncated UNC119A protein be able to rescue LCK localisation following deletion of UNC119A? It would also be interesting to test the effect of different truncation lengths on the function of UNC119A, perhaps to narrow down the possible location of the site of the interaction. Our experiments with the UNC119A ICL patient mutation (Gorska and Alam, 2012) point to glycine 22 being an important site, as the G22V mutant was unable to form the additional interaction **(Figure 3-35)**. The UNC119^{G22V} mutation was shown to affect the proliferation of CD4^{+} cells as well as the localisation of LCK in resting cells. A few questions arise from these data: is the reduced proliferation a direct consequence of UNC119 impaired function, or is it due to LCK mislocalisation? How would T cells with mutant UNC119 behave in the presence of target cells? Would LCK localisation be restricted to the slower endosomal pathway? Studying the downstream effects of replicating this mutation both in CD4^{+} and CD8^{+} cells can help unravel the role of UNC119A N-terminal interaction at the immune synapse.

3.3.4 Model of UNC119A-mediated transport of LCK to the immune synapse

The GDI-like solubilising factor UNC119A is able to extract anchored LCK from intracellular and plasma membranes; this results in the formation of a soluble complex that can diffuse freely in the cytoplasm. LCK release is mediated by the UNC119 displacement factor ARL3 upon its activation by the GEF ARL13B. Prior to immune synapse formation, ARL13B does not appear to be specifically localised in the Jurkat T cell **(Figure 3-29A**, lower panels**)**. As a result, activation of ARL3 will not occur at a specific region to drive localised LCK release **(Figure 3-46A)**. As the TCR recognises the pMHC, the T cell-APC interface begins to transition into the immune synapse. The process involves the localisation of the ciliary GEF ARL13B, which we observed to be localised at the

synapse within 10 minutes of mixing the Jurkat and Raji cells **(Figure 3-29A)**. ARL3 is therefore activated at this domain, resulting in LCK release. However, no retention occurs as UNC119A is still able to sequester LCK back into the cytoplasm **(Figure 3-46B)**. Activation of LCK through the phosphorylation of tyrosine 394 inhibits the N-terminal interaction of UNC119A. The local concentration of UNC119A surrounding the membrane-associated LCK is reduced, hampering the ability of UNC119A to compete with the membrane to successfully extract LCK. As a result, active LCK is retained at the immune synapse **(Figure 3-46C)**.

As the synapse matures and TCR signalling is terminated, the cSMAC LCK fraction does not exhibit Y394 phosphorylation (Lee et al., 2002). This should allow its removal from the membrane by UNC119A, allowing the redistribution of LCK once more.

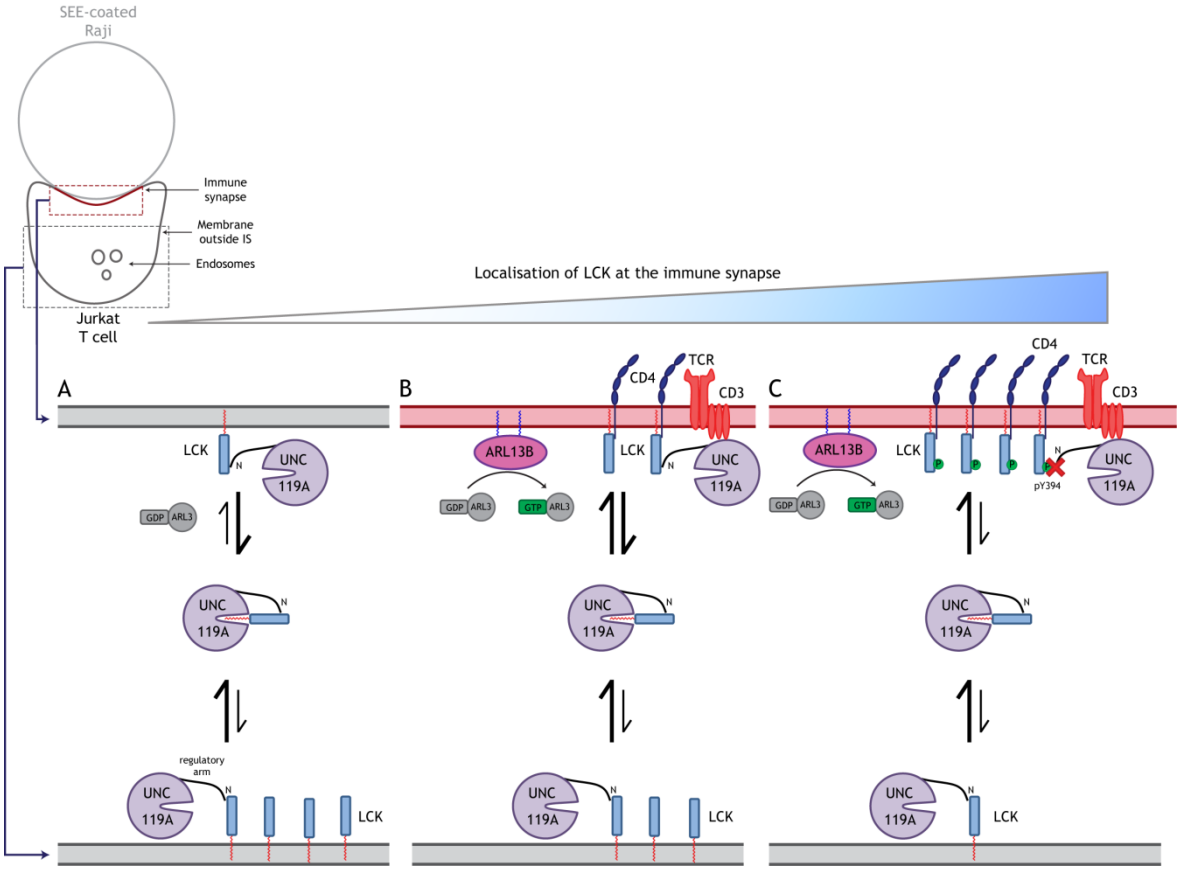

Figure 3-46 Model of UNC119A-mediated trafficking of LCK to the immune synapse.
Our working model of the interplay between ciliary ARL3, UNC119A-mediated trafficking and LCK phosphorylation is described. The lipid modification of LCK confers its membrane association. Within the T cell, LCK can associate either with intracellular membranes such as endosomes, or with the plasma membrane. We have studied the trafficking of LCK to the region of the plasma membrane forming the immune synapse (red box) with the superantigen-coated Raji B cell. We therefore distinguish between the immune synapse and all other membrane regions, including intracellular membranes and the plasma membrane outside of the synapse (grey box). The lower panels describe the proposed events in each of these regions in different stages of the localisation of LCK to the immune synapse. **(A)** UNC119A can extract LCK from intracellular and plasma membranes. This is mediated through the interaction of the N-terminal regulatory arm interaction with the LCK kinase domain and the binding of the UNC119A hydrophobic pocket to the LCK myristoyl moiety (red). However, prior to antigen recognition, there is no localised generation of active ARL3GTP at the plasma membrane as the synapse is yet to form, and hence no specific release of LCK occurs. **(B)** As the immune synapse forms along with the specific localisation of ARL13B, active ARL3GTP levels increase at the synapse, driving LCK release from cytoplasmic UNC119A complexes. No retention occurs, however, as the N-terminal regulatory arm interaction allows UNC119A to re-extract LCK from the membrane. **(C)** The phosphorylation of regulatory tyrosine residues inhibits the N-terminal interaction, preventing the formation of high local concentration of UNC119A and opposing the LCK extraction from the membrane. LCK is therefore retained at the functional membrane domain of the immune synapse. SEE, staphylococcal enterotoxin E; IS, immune synapse; LCK, lymphocyte-specific kinase; UNC119A, uncoordinated 119A; ARL, ARF-like protein; TCR, T cell receptor.

3.3.5 Identification of potential UNC119A immune synapse cargo

The UNC119A-LCK peptide structure revealed the requirement imposed by the UNC119A pocket for small N-terminal cargo residues in order to form a high affinity binding. These restrictions can be applied to other proteins reported or predicted to undergo myristoylation in order to identify potential high affinity cargo of UNC119A, some of which may be localised to the immune synapse. A small-scale search identified several possible cargo proteins **(Table 3-2).** Of these, the formin-like protein 1 (FMNL1) was of particular interest due to its reported role in MTOC positioning at the $CD8^+$ T cell immune synapse (Gomez et al., 2007).

3.3.6 Potential avenues for manipulating the immune response

Inhibiting the hydrophobic pocket binding of UNC119A to LCK by using squarunkin A (Mejuch et al., 2017) resulted in a more diffuse membrane localisation of LCK with less restriction to the synapse. At the same time, Jurkat cells transfected with $ARL3^{Q71L}$-GFP exhibited greater activation as measured by CD69 expression following stimulation by antibodies **(Figure 3-28C)**. It remains to be seen if this LCK mislocalisation results in enhanced or reduced T cell function against the target cell. In either case, UNC119A may provide a new way by which T cell responses can be manipulated.

It has been shown that the use of the immune synapse in the cytotoxic effector function of $CD8^+$ T cells is not universal, and seems to depend on the antigenic context. In responding to murine brain tumours, $CD8^+$ T cells did not form the canonical Kupfer-type synapses (Yang et al., 2010). While the sealed structure of these synapses provides a directed route of secretion towards the target cell, the mediated cytotoxicity is accomplished by one-on-one cell killing. It would therefore be more suited when targeted cytotoxicity is required, as has been reported for viral clearance. Non-specific killing of all surrounding cells may be the more effective strategy in the context of the tumour, and so the T cell does not employ the immune synapse in this case (Mitxitorena et al., 2015). UNC119A inhibition might be a way through which T cells can be biased towards this kind of multi-directional effector strategy.

Chapter 4 Inhibition of trafficking of lipid-modified proteins to the primary cilium

4.1 Introduction

A striking case of the compartmentalisation of the membrane into specialised domains is evident in cilia. These are motile and nonmotile structures which protrude from the surface of the cell with an underlying microtubular scaffold; the latter nonmotile structures are called primary cilia, so named as they were observed to develop before their motile counterparts. It is these primary cilia that are the major focus of this chapter. Despite being continuous with the rest of the cell, the composition of these organelles, both on the membrane and within the cilium, remains distinct from the rest of the cell. It is this segregation that drives many of the functions carried out by cilia. In particular, the nonmotile primary cilium has been identified as a crucial signal detection and transduction cellular hub.

4.1.1 The primary cilium

A primary cilium can be found on most nondividing mammalian cell types; exceptions include lymphocytes, as previously mentioned, and hepatocytes (Seeley and Nachury, 2010). The near-ubiquitous cellular incidence of cilia combined with its involvement in multiple cellular functions highlights its importance as an organelle. Since the first studies of their role in phototransduction (De Robertis, 1956), cilia are now known to be involved in a wide range of processes including development, tissue homeostasis and cell cycle regulation.

4.1.1.1 Formation and structure

Cellular assembly of the cilium has been elucidated via ultrastructural studies of the process (Sorokin, 1962, Sorokin, 1968). Primary cilium formation occurs at the point of centrosomal docking to the membrane. The centrosome, which acts as the microtubule-organising centre (MTOC) of the cell, comprises two centrioles embedded in a matrix of pericentriolar material. Each centriole

consists of nine microtubule triplets (each comprising A, B, and C tubules) arranged in a barrel-like structure. Of these, the mother centriole, which is inherited by the cell from the previous mitotic cycle, docks to the cortical actin network attached to the plasma membrane (Kobayashi and Dynlacht, 2011). Centriole docking is mediated via distal appendages which are only present on the mother centriole, hence its ability to form the cilium (Vorobjev and Yus, 1982). Vesicles dock to the plus-ends of microtubules at the distal end of the mother centriole during the transport of the centrioles towards the membrane and the central shaft of the cilia extends into the lumen of the vesicles. The membranes of these vesicles will fuse with the plasma membrane and form the ciliary membrane, which encloses the central axoneme **(Figure 4-1A)**.

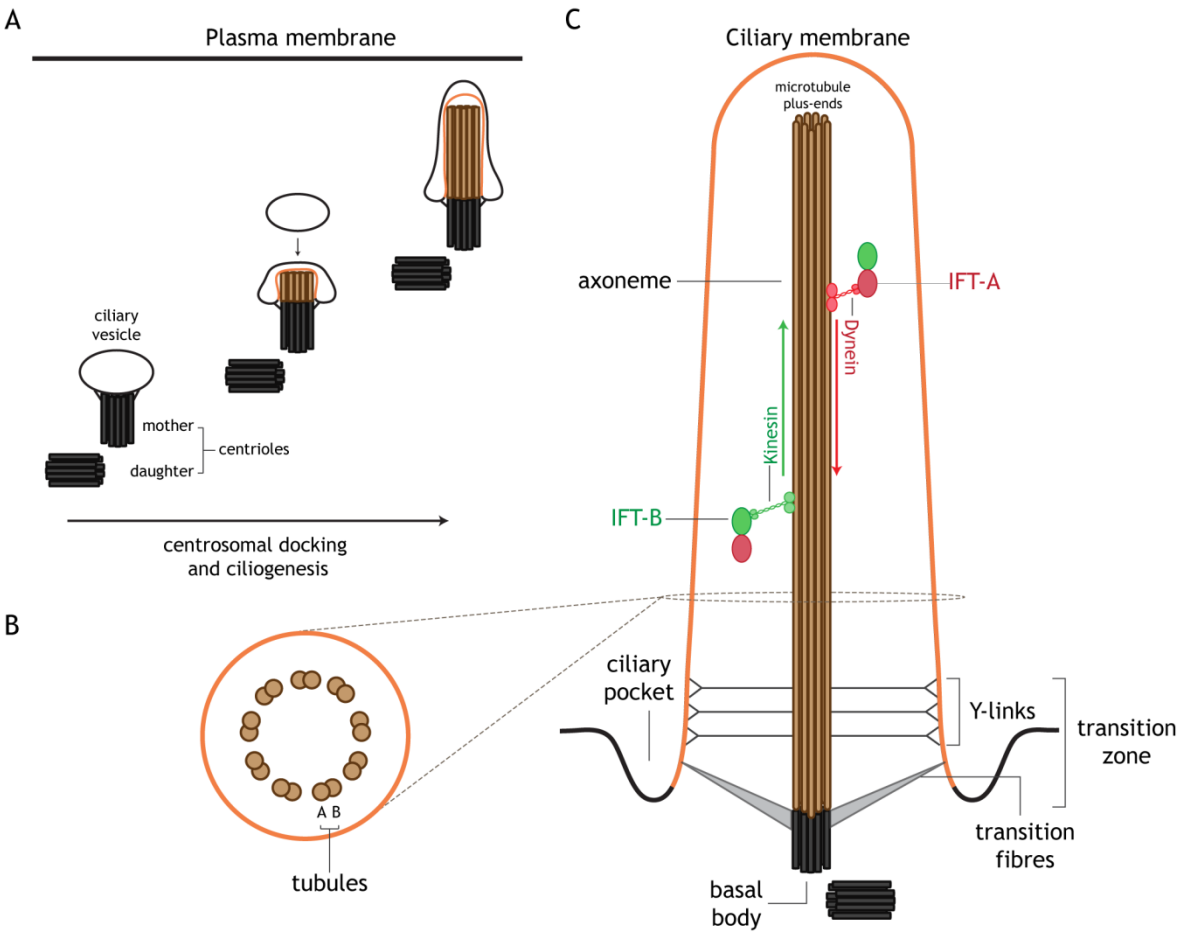

Figure 4-1 The primary cilium.

(A) Formation of the primary cilium involves the migration of the centrioles towards the cell membrane, and the docking of ciliary vesicles to the distal side of the mother centriole. The basal body nucleates the formation of the axoneme, which extends into the lumen of the vesicle via plus-end growth. Upon fusion with the cell membrane, the axoneme protrudes from the surface of the cell, enclosed by the vesicle membrane which has now become the ciliary sheath. **(B)** Cross-section of the cilium showing arrangement of microtubule doublets with each

comprising A and B tubules. **(C)** Structure of the primary cilium: the axoneme extends from the basal body and its doublets provide microtubular tracks for anterograde and retrograde intraflagellar transport (IFT). Y-links and transition fibres facilitate membrane attachments with the axonemal base and the basal body, respectively; the base of the axoneme forms the transition zone. Primary cilia on some mammalian cell types protrude from a membrane invagination, which is termed the ciliary pocket.

The axoneme extends from the basal body, which comprises the docked mother centriole. The growing axoneme is made up of nine parallel microtubule doublets, each of which comprises an A tubule attached to an incomplete B tubule **(Figure 4-1B)**. The outer doublets of the axoneme serve as microtubular tracks for cargo transport by intraflagellar transport (IFT) trains. Bidirectional transportation of proteins along the axoneme is carried out by large IFT complexes functioning as transport trains that are powered by protein motors. As shown in **Figure 4-1C**, IFT-B complexes are transported outwards to the distal tip of the cilium by the motor protein kinesin, while IFT-A complexes move inwards towards the basal body due to the action of dynein. During cilia assembly, anterograde IFT transportation of precursors to the growing tip of the axoneme is essential for ciliogenesis (Pazour and Rosenbaum, 2002).

Distal to the basal body, the base of the axoneme forms the transition zone, which is connected to the ciliary membrane via Y-links **(Figure 4-1C)**. The basal body is connected to the membrane and cytoplasmic microtubules by transition fibres and basal feet, respectively. Transition fibres, which are also called alar sheets, arise from the distal appendages of the basal body. The membrane surrounding the basal body has been reported to associate with a ring structure composed of the self-assembling GTP-binding septin proteins, which possibly aids in restricting lateral diffusion in the membrane to and from the cilium (Hu et al., 2010, Chih et al., 2012). The transition zone and associated structures such as Y-links and the transition fibres separate the inner ciliary compartment from the rest of the cytoplasm. This region is known as the ciliary gate, and it is here that access to the cilium to and from the cytoplasm is regulated.

Transition fibres form sheet-like structures that attach between each of the nine microtubule triplets of the centriole and the membrane. The resulting arrangement is similar to that of a propeller fan with its blades spaced ~60 nm

apart around the circumference of the basal body. The size of these inter-transition fibre spaces prohibits the passage of vesicles (Nachury et al., 2010).

The importance of the ciliary gate formed in part by the transition zone is made evident by the consequences of mutations of its components. Many transition zone proteins are considered to be ciliopathy proteins. This means that mutations of their encoding genes and the resultant impairment in the regulation of ciliary composition gives rise to a host of genetic disorders known as ciliopathies (Garcia-Gonzalo and Reiter, 2017).

The base of primary cilia on the surface of some mammalian cell types is surrounded by a membrane invagination termed the ciliary pocket (Malicki and Avidor-Reiss, 2014). As mentioned in **section 1.1.1**, this pocket has been reported to form an endocytic domain at the base of the cilium, which is also involved in regulating ciliary entry (Molla-Herman et al., 2010).

4.1.1.2 Maintenance of ciliary composition

The cilium cannot synthesise its own proteins and must rely on translational machinery present in the cytoplasm. A targeted delivery system for ciliary proteins is therefore essential for their correct localisation in a functional cilium. Furthermore, ciliary function is dependent on maintaining the appropriate balance of signalling molecules on the surface and within the cilium on a continuous basis. These molecules include membrane receptors and lipids, as well as effector proteins and second messengers (Nachury et al., 2010). Since the primary cilium is not isolated by membranes from the rest of the cell, this ciliary localisation must be actively maintained. Various trafficking and retention mechanisms have been reported to play a role in the generation and maintenance of ciliary composition. Ciliary proteins can be classified based on the nature of their association, or lack thereof, with the membrane: integral, with permanent membrane binding, soluble, which remain in the cytoplasm, and membrane-associated, which cycle between the membrane and the cytoplasm.

4.1.1.2.1 Integral proteins across the ciliary-plasma membrane divide

Ciliary and plasma membranes exhibit distinct protein and lipid compositions despite being continuous. This is attributed to the presence of a membrane

diffusion barrier that prevents isotropic lateral diffusion between the two membrane compartments (Nachury et al., 2010). Evidence for the presence of such a barrier came from studies of the *Chlamydomonas reinhardtii* motile cilium, or flagellum. Sexual reproduction in these unicellular organisms involves the adherence of gametes of opposite mating types via the interaction of agglutinin glycoproteins. It has been shown that only active agglutinins localise to the flagellum, which is attributed to their ability to cross a selective diffusion barrier (Hunnicutt et al., 1990). Later studies made use of fluorescent probes targeted to the outer leaflet of the plasma membrane of ciliated cells. The probes was found to be absent from the ciliary membrane as well as a small region in the plasma membrane surrounding the base of the cilium. The presence of a diffusion barrier in this region would explain the inhibition of lateral diffusion (Vieira et al., 2006, Nachury et al., 2010).

Under normal circumstances, membrane proteins achieve their localisation through an exocytic route from the Golgi and/or lateral diffusion in the membrane. In the case of the ciliary membrane, these two pathways can take the protein only as far the base of the cilium due to the ciliary restrictions against vesicle entry and diffusion. However, an exception has been reported in the case of Smoothened (SMO), which localises to the cilium upon stimulation of the Hedgehog signalling pathway. The authors of the study noted that the role of lateral diffusion was restricted to early time points following stimulation of the pathway, replaced by the secretory pathway in later stages (Milenkovic et al., 2009). This lateral mode of ciliary entry needs further validation; in some cases, import molecules such as IFT-A appear to selectively facilitate the lateral passage of the membrane-bound cargo across the transition zone (Nachury and Mick, 2019).

Laterally diffusing proteins are generally reported to undergo endocytosis at the ciliary base prior to assisted cilia entry. Alternatively, newly synthesised proteins can be directly targeted by the endocytic pathway to the base of the cilium. Early studies in frog photoreceptors revealed that trafficking of rhodopsin to the modified primary cilium takes place via vesicles targeted to a modified ciliary pocket at which the vesicles then fused to the membrane (Papermaster et al., 1985).

The IFT-B complex component IFT20 localises at the Golgi and on subsequently-formed vesicles destined for the cilium (Follit et al., 2006). IFT20, possibly in conjunction with other IFT-B components, is proposed to help guide the transfer of ciliary cargoes from the vesicles to IFT trains being assembled at the base of the cilium prior to entry and transport along the axoneme. This mode of transport is also linked to the Bardet-Biedl Syndrome proteins (BBSome), which is an 8-protein complex that functions in association with the IFT machinery in transport across the transition zone and within the cilium (Lechtreck, 2015).

The presence of ciliary targeting sequences (CTSs) such as the VxP motif aids in the initial targeting of some ciliary proteins to trafficking vesicles. CTS-containing proteins such as the integral G protein coupled receptor (GPCR) somatostatin receptor 3 (SSTR3) arriving at the ciliary base are recognised by the BBSome, which is recruited to the membrane by ARL6GTP. Together, they drive the endocytosis of the GPCR and direct the transporting vesicle to cilia in hippocampal neurons (Berbari et al., 2008, Garcia III et al., 2018).

The BBSome also functions to remove proteins from cilia. Several integral GPCRs, including GPR161, localise to the primary cilium from the plasma membrane in a process mediated by the tubby-like protein TULP3 and IFT-A. TULP3 also mediates the retention of GPR161 in the cilium, through binding PIP_2 in the membrane (Malicki and Avidor-Reiss, 2014). The ciliary exit of GPR161 has been suggested to involve the following: upon loss of retention due to changes in phospholipid content, activated GPR161 dissociates from the retaining TULP3/IFT-A complex. It is then sensed by ß-arrestin 2 and subsequently removed from the cilia by the BBSome acting in concert with retrograde IFT machinery. These transport the integral GPCR across the transition zone to the base of the cilium where it is removed by endocytosis (Wingfield et al., 2018).

A schematic depicting the aforementioned transport and retention mechanisms of integral proteins is shown in **Figure 4-2**.

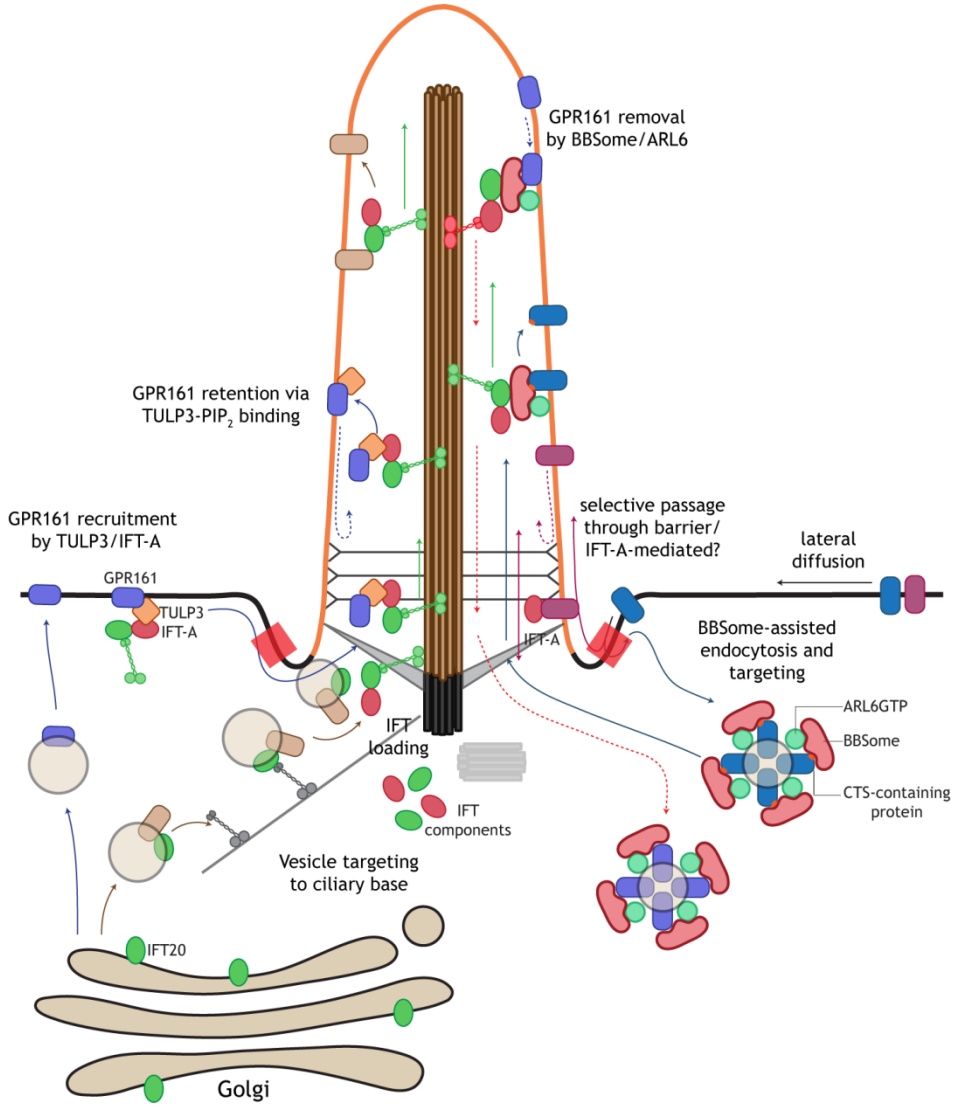

Figure 4-2 Transport of integral membrane proteins to and from the primary cilium. Entry of laterally-diffusing membrane proteins into the cilium appears to be inhibited by the presence of a diffusion barrier (red box). This is circumvented through BBSome-assisted endocytosis and targeting to assembling IFT trains and subsequent ciliary entry. BBSome-mediated transport requires the recognition of ciliary target sequences (CTS, orange circles) on cargo proteins. Few exceptions to the endocytic route have been reported where IFT-A assists in bypassing the diffusion barrier without endocytosis. Integral GPCRs are actively recruited into the cilium by the action of TULP3 and IFT-A components. Membrane proteins can be targeted to the base of the cilium from the site of synthesis via transporting vesicles and IFT-B components. Further entry into the cilium is mediated by IFT trains driven by kinesin motors (green). Similarly, ciliary exit of membrane proteins is inhibited by the diffusion barrier. It may be bypassed by BBSome-assisted IFT transport (driven by dynein motors, red) followed by endocytosis. Solid and dashed arrows indicate processes involved in ciliary entry and exit, respectively. PIP_2, phosphatidylinositol 4,5-bisphosphate; TULP3, tubby-like protein 3; IFT, intraflagellar transport; BBSome, Bardet-Biedl Syndrome proteins; ARL, ARF-like protein; GPR161, G protein coupled receptor 161.

4.1.1.2.2 Soluble ciliary components between the ciliary lumen and the cytoplasm

Diffusion of molecules originating in the cytoplasm into the ciliary compartment is proposed to be subject to regulation mediated by the barrier of the ciliary gate. The nature of this barrier and how it mediates selective entry, however, is a matter of debate.

Soluble proteins can diffuse freely in the cytoplasm to reach the base of the cilium, where a diffusion barrier is proposed to exist. Subsequent entry through this barrier would depend on the size of the protein, where small proteins diffuse freely across the gate into the cilium. The reported maximum freely-diffusing protein size varies between 30 - 100 kDa; this disagreement is likely due to the use of different experimental approaches and models as well as the effect of other properties of the diffusing protein (Takao and Verhey, 2016, Nachury and Mick, 2019). The diffusion barrier has been suggested to exert size exclusion, whereby larger proteins are not allowed entry. Alternatively, a study utilising inducible dimerisation of fluorescently-labelled soluble proteins to ciliary targets indicated that the diffusion barrier may be of a kinetic nature. This dictates that protein size determines only the speed of entry, and not the possibility of passage itself; proteins of up to ~650 kDa were reported to eventually localise to the cilium. Larger proteins are therefore prevented from entering the cilia at earlier time points when signal transduction is underway **(Figure 4-3A)**. Specific localisation of proteins functioning in steady-state processes was suggested to be achieved by selective retention in the cilium, rather than access (Lin et al., 2013). Diffusion rates exhibited by GFP monomers and oligomers of different sizes in photoreceptor cells were also found to be size-dependent (Najafi et al., 2012).

Free diffusion into the cilium opposes enrichment of molecules, unless retention occurs within the compartment. In the case of the *Chlamydomonas* end-binding protein 1 (EB1), free diffusion in the cilium is followed by preferential binding to plus-ends of microtubules at the ciliary tip, resulting in its accumulation; this facilitates its function in aiding IFT trains arriving at the tip to switch to retrograde transport (Harris et al., 2016). Alternatively, cilia-restricted generation of small soluble molecules can also result in their ciliary localisation and enrichment; examples include Ca^{2+} influx through ion channels in the ciliary

membrane, and the production of cyclic AMP (cAMP) by ciliary adenylyl cyclases (ACs) (Nachury and Mick, 2019) **(Figure 4-3A)**.

The presence of an active transport entry mechanism for proteins in the 40 – 70 kDa size range at the ciliary gate has also been proposed. This mechanism has been likened to that of the nuclear pore complex, which allows free movement of small proteins, and requires energy for the selective transport of larger proteins. This was based on reports of the localisation of nucleoporins, which constitute the nuclear pore complex, at the base of the cilium. Furthermore, ciliary localisation of the kinesin family member 17 (KIF17) was found to be dependent on nucleoporin function (Kee et al., 2012). This was attributed to the presence of a localisation signal on KIF17 which is recognised by the transporter protein importin-β2. This shuttles the protein across the ciliary pore in a mechanism regulated by different levels of the GDP- and GTP-bound forms of the GTPase RAS-related nuclear protein (RAN) **(Figure 4-3B)**. Disrupting the RAN-GTP gradient by overexpression of constitutively active RAN was found to inhibit the ciliary localisation of KIF17 (Dishinger et al., 2010). However, the presence of a ciliary pore complex has been questioned by other reports. One study showed that while nucleoporins were observed at the ciliary base, they did not organise into a ring-like structure that would be expected at the pore complex (del Viso et al., 2016). Another study failed to observe any ciliary localisation of nucleoporins. Their data confirms the presence of a size-dependent diffusion barrier with a threshold of ~100 kDa that was independent of active transport (Breslow et al., 2013).

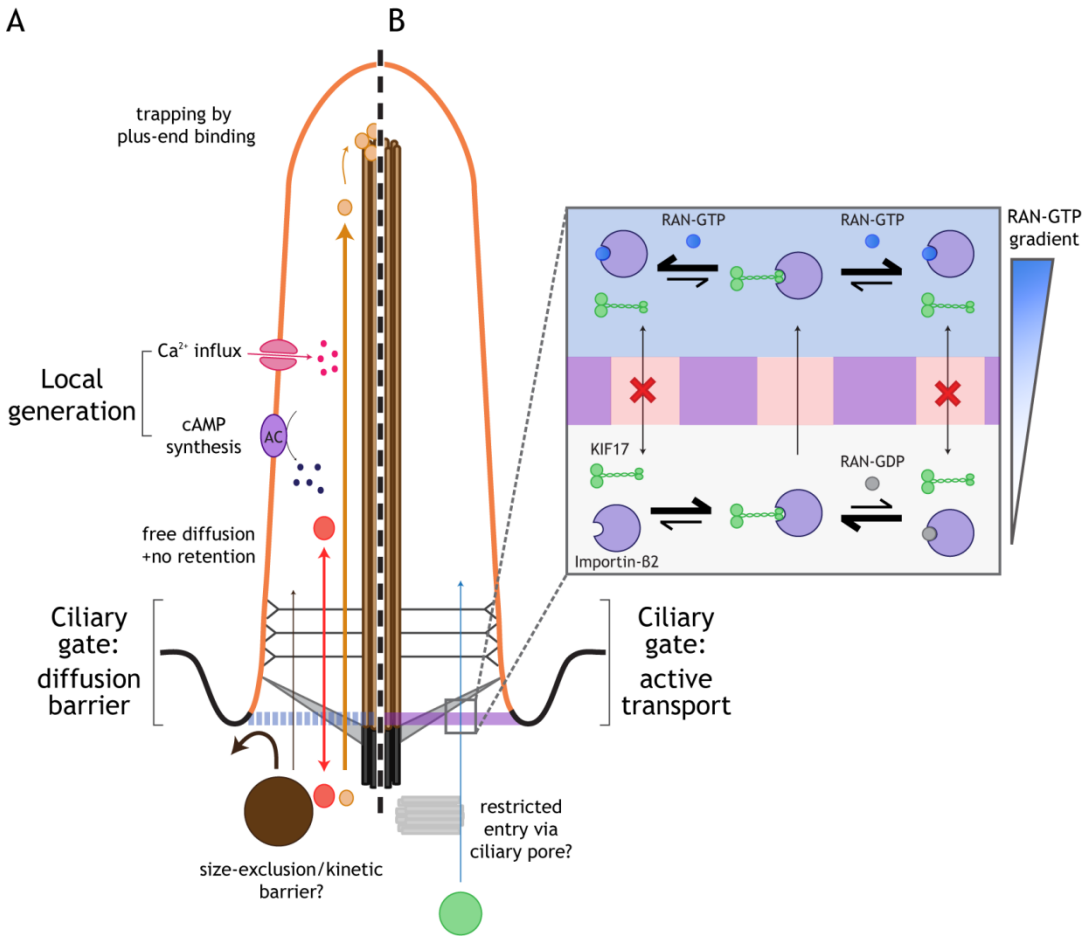

Figure 4-3 Proposed modes of ciliary entry for soluble proteins.

A proposed ciliary gate restricts cytoplasmic diffusion into the ciliary component, with two possible modes of action. **(A)** A diffusion barrier restricts free diffusion either by preventing molecules above a certain threshold to enter (size exclusion barrier), or slowing down their entry compared to smaller proteins (kinetic barrier). Freely diffusing molecules will not be enriched in the cilium unless they are retained. Alternatively, small molecules can be enriched in the cilium by local generation. **(B)** The active transport mode of the ciliary gate suggests the presence of a ciliary pore complex, where cargo proteins bearing a ciliary localisation signal, such as KIF17, are shuttled by the transporter importin-β2 across the pore. Inside the ciliary compartment, high levels of RAN-GTP results in release of KIF17 from the transporter. The released KIF17 cannot cross the gate on its own, and is therefore retained in the ciliary compartment. cAMP, cyclic adenosine monophosphate; AC, adenylyl cyclase; RAN, RAS-related nuclear protein; KIF17, kinesin family member 17.

4.1.1.2.3 The middle-ground: membrane-associated proteins

Membrane-associated proteins have not been as well studied as integral and soluble ciliary components. However, their transport to and from the cilium is likely to combine aspects of membrane and soluble protein trafficking. This is due to the dynamic nature of membrane-associated proteins, which alternate between associating to membranes via their anchoring group, and localising to the cytoplasm as a soluble protein upon the masking of their anchor **(section 1.2.1)**.

During membrane association, lateral diffusion into the cilium is prevented by the diffusion barrier. Photobleaching studies of fluorescently-labelled ciliary membrane-associated proteins have shown that rapid recovery of the ciliary fluorescent signal was only achieved when the bleaching was restricted to part of the cilium. Whole-cilium bleaching failed to show recovery, which would require diffusion of fluorescent proteins associated with the plasma membrane to replace the bleached ciliary counterparts (Hu et al., 2010).

Tubby proteins are recruited to the ciliary compartment by IFT-A. Retention within the cilium is mediated by preferential binding to PIP_2 phospholipids in the membrane, as described in **section 1.1.1** (Mukhopadhyay et al., 2010).

As described in **section 1.3.2**, some lipid-modified proteins are extracted from membranes by GSFs to form a freely-diffusing complex. Ciliary localisation is brought about through localised release that is mediated by ARL3GTP and ARL13B. Cargo release from the GSF complex exposes the acyl/prenyl lipid group which acts as a second binding signal to trap the protein at the ciliary membrane (Stephen et al., 2017).

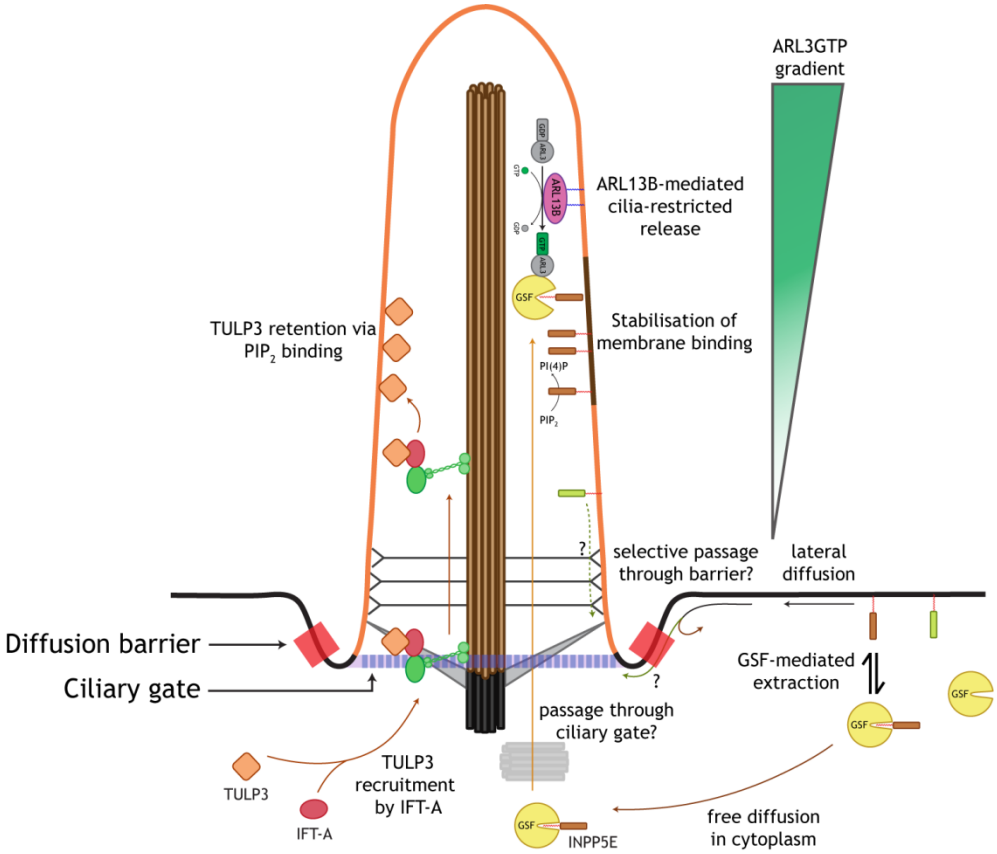

Figure 4-4 Ciliary trafficking of membrane-associated proteins.
Membrane-associated proteins can access the cilium both via the membrane and the cytoplasm, and so they are subject to regulation by both the membrane diffusion barrier and the ciliary gate. Prenylated INPP5E is extracted from membranes by the GDI-like solubilising factor PDEδ to form a freely diffusing complex in the cytoplasm. ARL13B is restricted in the cilium, creating an ARL3GTP gradient. This drives the cilia-specific release of GSF lipidated cargo, which binds to the membrane through the free anchor. INPP5E, inositol polyphosphate-5-phosphatase E; PI(4)P, phosphatidylinositol-4-phosphate ; PIP_2, phosphatidylinositol 4,5-bisphosphate; GSF, GDI-like solubilising factor; TULP3, tubby-like protein 3; IFT, intraflagellar transport.

4.1.2 Function

The ultrastructure of the primary cilium was extensively studied with the advent of electron microscopy. However, its non-motility rendered its potential function challenging to elucidate, and it was considered to be a vestigial organelle. Two other hypotheses were later formulated: that it helps regulate the cell cycle by engaging the centrioles away from the mitotic machinery, or that it functions in the detection of extracellular signals (Satir et al., 2010). The primary cilium is now known to be a highly intricate signalling hub with far-reaching influence. In constructing the primary cilium, the cell essentially extends a miniature antenna

into the surrounding environment. This small surface area and volume aids in the generation of high concentrations of receptors and signalling machinery, which in turn facilitates efficient signal detection and transduction.

As mentioned in the beginning of this chapter, the first clues to the signalling role of primary cilia came from studying cellular detection of light and odour. Olfactory signal transduction is initiated by ligand binding to ciliary GPCRs and propagated by the second messenger cAMP (Boekhoff et al., 1990). Phototransduction takes place in the highly specialised primary cilium of cone and rod photoreceptor cells. Reception of light stimulus is carried out by rhodopsin GPCRs, with cGMP acting as a second messenger (Fesenko et al., 1985).

With the identification of functional roles for the cilium, the recognition of the separation between cytoplasmic sites of protein synthesis and ciliary sites of function led to the question of how cellular delivery of proteins to the cilium was achieved. The discovery of intraflagellar transport in the *Chlamydomonas* flagellum (Kozminski et al., 1993) and the subsequent identifications of the driving motor proteins were the first steps in formulating an answer. Sequencing studies of the *Chlamydomonas* IFT-encoding genes drew the link between an IFT component and a disease-causing gene identified in a mouse model of polycystic kidney disease. The link between ciliary impairment and disease, and the identification of cilia presence on a growing number of cell types opened the door for decades of research into the once-vestigial organelle (Satir, 2017).

Ciliary defects can give rise to issues in left-right asymmetry. Together with their motile counterparts, primary cilia have been proposed to help establish left-right patterning during embryonic development by driving unidirectional extracellular fluid flow. The mechanism of ciliary involvement in this process is under debate; different hypotheses include mechanosensation of the fluid and chemosensation of a morphogen gradient generated by the fluid flow (Hamada, 2016).

The previous hypothesis of a function in cell division has since been supported. Cilia affect the division of the cell independent of its mediated signalling pathways. The central role of centrioles in the process of ciliogenesis links it to

cell division, which requires centrioles for the construction of the mitotic spindle. The dependence of both these processes on the centriole means that they cannot occur simultaneously: the cilium must be disassembled for cell division to occur. Furthermore, several proteins involved in each of these processes have been shown to exert regulatory effects on the other. An example is the IFT-B component IFT88, which is essential for ciliogenesis, and which has been shown to inhibit the G1/S cell cycle transition (Robert et al., 2007).

The transduction pathways mediated by the ciliary receptors give rise to further roles in development and growth of different tissues: among these are the signalling of polycystins and the platelet-derived growth factor receptor-α (PDGFRα), which affect renal and skeletal development, respectively (Fliegauf et al., 2007). Most prominent among the ciliary pathways is that of Hedgehog signalling, which is described in the following section.

4.1.2.1.1 The Hedgehog signalling pathway

Hedgehog (HH) was first described in *Drosophila* as a mutated protein which caused a spiny larval phenotype, which was likened to a hedgehog (Nüsslein-Volhard and Wieschaus, 1980). It was later discovered to be secreted from cells to influence the patterning of the surrounding cells. It carries out this function by triggering a highly conserved developmental signalling pathway that affects cell division and differentiation. In addition to its developmental roles, the Hedgehog pathway is of oncogenic significance as its dysregulation can result in cancer (Bangs and Anderson, 2017). Understanding the ciliary role in this pathway started with the discovery that mutations in murine IFT components gave rise to phenotypes characteristic of Hedgehog signalling defects (Huangfu et al., 2003).

Mammalian signalling of Hedgehog (of which there are three isoforms including Sonic (SHH)) is entirely dependent on the primary cilium. This is due to the ciliary localisation of several essential members of the transduction pathway, including HH-binding receptors and the glioma-associated (GLI) transcription factors, which regulate the expression of HH target genes. The ciliary dependence of mammalian HH is one striking difference from its counterpart in *Drosophila*. This has been attributed to the long-range functionality of mammalian HH, whereby the pathway is initiated at distant cells from the

source of secreted HH. The sensitivity of signal detection afforded by the high receptor concentration in the primary cilium facilitates this mode of action, which is not required in *Drosophila* (Bangs and Anderson, 2017). **Figure 4-5** summarises the events occurring during mammalian Hedgehog signalling in the primary cilium.

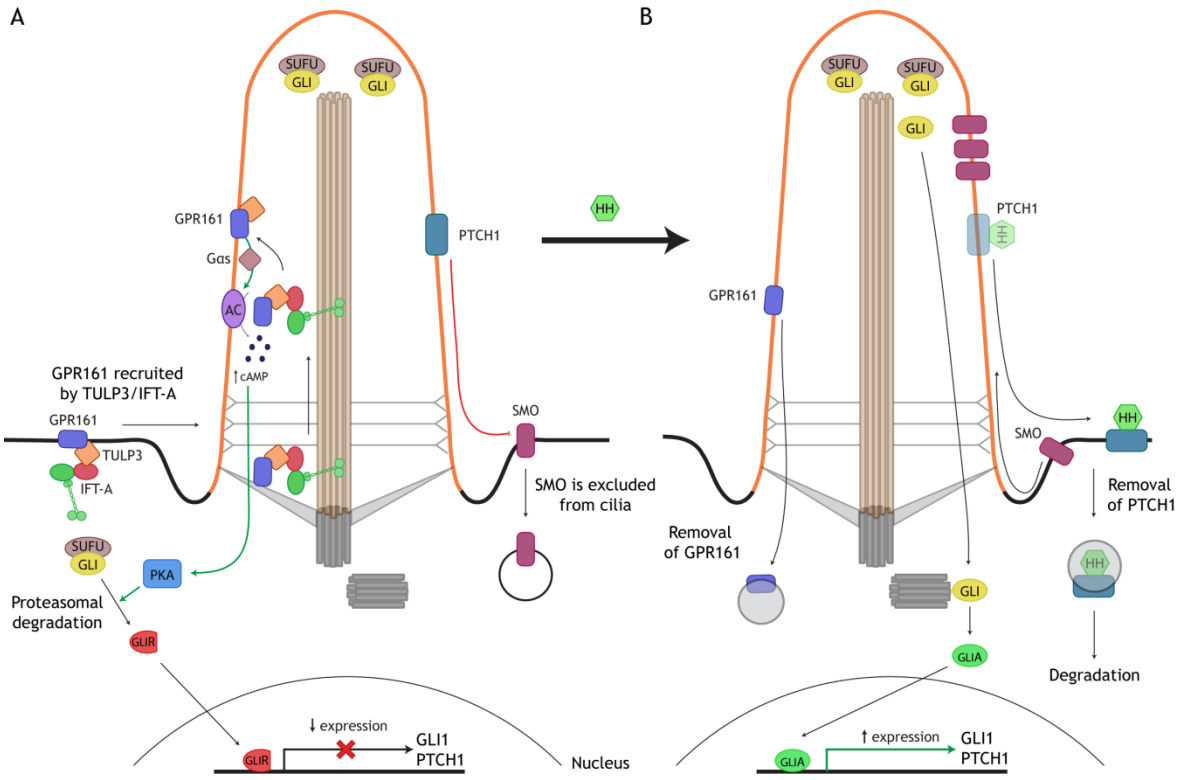

Figure 4-5 Hedgehog signalling in the primary cilium.

(A) In the absence of the HH ligand, Patched 1 (PTCH1) localises to the cilium and excludes Smoothened (SMO), causing its sequestration in vesicles outside the ciliary compartment. Ciliary GLI proteins are inhibited by the binding of Suppressor of Fused (SUFU). In parallel, the GPCR GPR161 is shuttled into the cilium, aided by TULP3 and IFT-A proteins. GPR161 activates cAMP synthesis in the cilium via the action of Gαs. This in turn activates protein kinase A (PKA), which phosphorylates GLI proteins, promoting their degradation to form repressor forms (GLIR) which inhibit gene transcription in the nucleus. **(B)** The binding of HH to PTCH1 results in its removal from the cilium and the cessation of its SMO inhibition. GPR161 is also excluded from the cilium, reducing ciliary cAMP synthesis and subsequent PKA activation. SMO enters the cilium and releases GLI proteins from SUFU. These can then exit the cilium, undergo modifications to form the activator forms (GLIA) and upregulate target gene expression.

In absence of HH, the transmembrane receptor Patched 1 (PTCH1) and the GPCR GPR161 localise to the cilium. As mentioned in **section 4.1.1.2.1**, ciliary localisation of GPR161 is dependent on IFT-A and the tubby-like protein 3 (TULP3). PTCH1 mediates constitutive inhibition of the transmembrane protein Smoothened (SMO) by excluding SMO from the cilium and sequestering it in vesicles. GPR161 activates the alpha subunit of the stimulatory G protein (Gαs), which in turn activates adenylyl cyclase. The resulting increase in ciliary cAMP levels results in activated protein kinase A (PKA) which phosphorylates GLI2 and GLI3 proteins and marks them for proteasomal degradation. This results in the formation of GLI repressors (GLIRs), which translocate to the nucleus and downregulate target gene expression. At the same time, the Suppressor of Fused (SUFU) binds non-degraded GLI proteins and sequesters them at the ciliary tip **(Figure 4-5A)**.

The binding of extracellular HH to PTCH1 results in the removal of the receptor from the cilium and the subsequent entry of SMO. Ciliary localisation of SMO results in the release of GLI proteins from SUFU and their post-translational modifications to form the activator forms (GLIA). These leave the cilium and upregulate target genes, including GLI1 for further response amplification and PTCH1 for regulation of the pathway (Briscoe and Thérond, 2013) **(Figure 4-5B)**.

4.1.3 Ciliopathies

Given the importance of ciliary function, and its scope across most cell types, mutations in ciliary components can have widespread pathological consequences. The link between primary cilia and genetic disease was first made with the finding that mutations in the IFT-B component IFT88 gave rise to ciliary defects which led to polycystic kidney disease (PKD) (Pazour et al., 2000). With the identification of more genetic disorders caused by ciliary defects, these diseases were classified as ciliopathies. Currently numbering over 30, these heterogeneous disorders affect a range of organ systems giving rise to different phenotypes with varying degrees of severity. Ciliopathies are a particularly complex set of pathologies, with overlapping causes and symptoms. Mutations in multiple ciliary genes can give rise to the same ciliopathy, while a single mutation can result in varying ciliopathic presentations in different patients (Hua and Ferland, 2018).

Ciliopathic phenotypes can have complex origins as the effects of multiple defects contribute to their formation. These include retinal degeneration, loss of olfaction, renal cyst formation, mental retardation, and skeletal defects such as polydactyly (Reiter and Leroux, 2017). The severity of these symptoms varies depending on the disorder and its presentation in the individual.

Joubert syndrome (JBTS) is an autosomal recessive neurodevelopmental ciliopathy which has a spectrum of associated phenotypes. CNS-related symptoms such as cognitive defects and hypotonia can also be accompanied with retinal, renal, and hepatic symptoms. While its presentation may vary, it is characterised by the presence of the so-called molar tooth sign in axial magnetic resonance imaging (MRI) of the midbrain. Despite its rare incidence, JBTS exhibits a high degree of genetic heterogeneity, with mutations in over 30 genes being attributed to its incidence (Hildebrandt et al., 2011).

4.1.4 Cilia in cancer

The interplay between ciliogenesis and cell division, as well as the signalling pathways mediated by the primary cilium point to recently growing interest in the role of primary cilia in the development of cancer. The complexity of the cilium extends to this aspect of its function as well: tumour progression favours both the loss and the retention of primary cilia, depending on the type of tumour. Studies of breast cancer have indicated a reduction in the incidence of ciliated mammary cells in invasive tumours (Yuan et al., 2010). On the other hand, HH-driven cancers such as medulloblastoma and basal cell carcinoma seem to favour the retention of cilia. However, primary cilia play dual roles of tumour promotion and suppression depending on the mutational locus on the HH pathway axis: SMO mutation requires the presence of cilia to initiate HH signalling for tumour progression. Mutations in GLI, however, are opposed by the negative feedback exerted by the primary cilium (Liu et al., 2018). Differences in the ciliation of cancer cells and their surroundings may give rise to targeting therapeutic strategies.

The focus of this chapter is twofold: the identification of a new causative JBTS mutation and the basis of its pathology, and investigating the use of manipulation of ciliary trafficking to modulate Hedgehog signalling.

4.2 Results

4.2.1 Joubert syndrome patient mutation in ARL3 affects ciliary composition

Given the complexities underlying ciliary function, the genetic causes of ciliopathies are a continuously expanding pool of suspects. Recently, our collaborators in the Sayer lab identified a novel *ARL3* mutation in several Joubert syndrome affected-individuals, with a homozygous mutation of the arginine residue at position 149 to histidine (*ARL3*^{R149H}) (Alkanderi et al., 2018). We therefore set out to investigate the biochemical pathology arising from this mutation, and how it affects the function of ARL3 in ciliary trafficking.

4.2.1.1 ARL3 R149 is involved in the interaction with ARL13B and the mediation of its GEF activity

The first step in studying the effect of this ARL3 mutation was to locate its position in the protein structure. **Figure 4-6A** shows the crystal structure of murine ARL3 (PDB code: 1FZQ; 98% sequence identity to human ARL3) and the position of R149 between the helix α4 and the ß-sheet ß6 (Hillig et al., 2000). This ARL3 region has been reported to interact with the GEF ARL13B in a study that used ARL13B and ARL3 from *Chlamydomonas reinhardtii* (Gotthardt et al., 2015). The human ARL3-ARL13B complex crystal structure has not been solved. However, *Chlamydomonas* proteins can provide a useful source of information on their human counterparts. *Cr*ARL3 shares 62% sequence identity with the human protein, and the arginine residue in question is conserved in human, mouse and *Chlamydomonas* ARL3 sequences (R149, R149, and R148, respectively) **(Figure 4-6B)**.

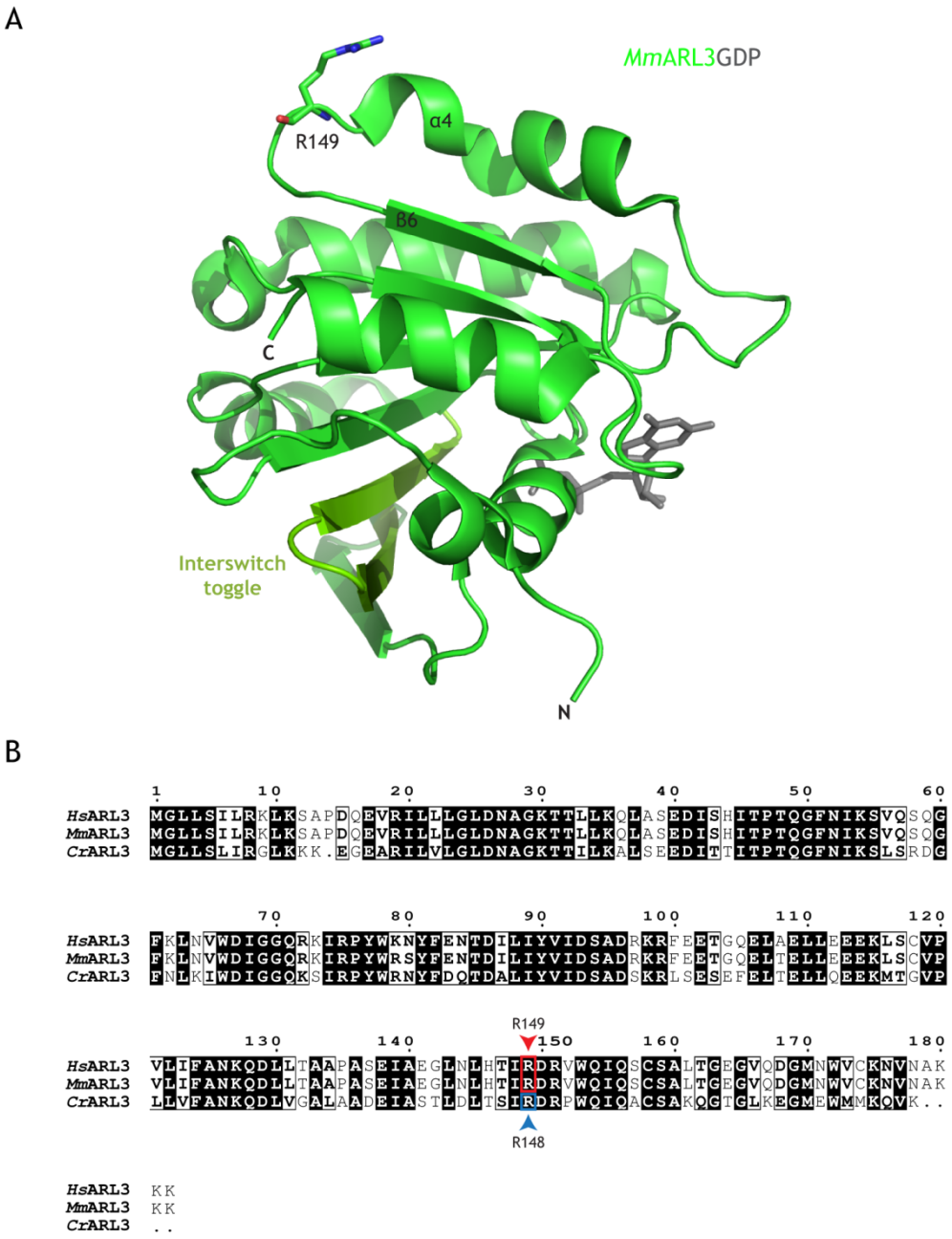

Figure 4-6 Structure of ARL3 and position of patient mutation.

(A) Cartoon representation of murine ARL3 (PDB code: 1FZQ (Hillig et al., 2000)) with bound GDP (grey) and arginine at position 149 between helix α4 and sheet β6 shown in stick form. **(B)** Sequence alignment of human, mouse, and *Chlamydomonas* ARL3 proteins, with residues equivalent to the mutation locus marked in red (human and mouse) or blue (*Chlamydomonas*).

Figure 4-7A shows the structure of the *Cr*ARL3-*Cr*ARL13B complex (PDB code; 5DI3). The *Cr*ARL3 residue R148 is indeed an interacting residue with ARL13B, forming a salt bridge with glutamate 86 in the latter during ARL13B-catalysed nucleotide exchange of ARL3. The mutation can therefore affect the nucleotide exchange, and hence the activation, of ARL3.

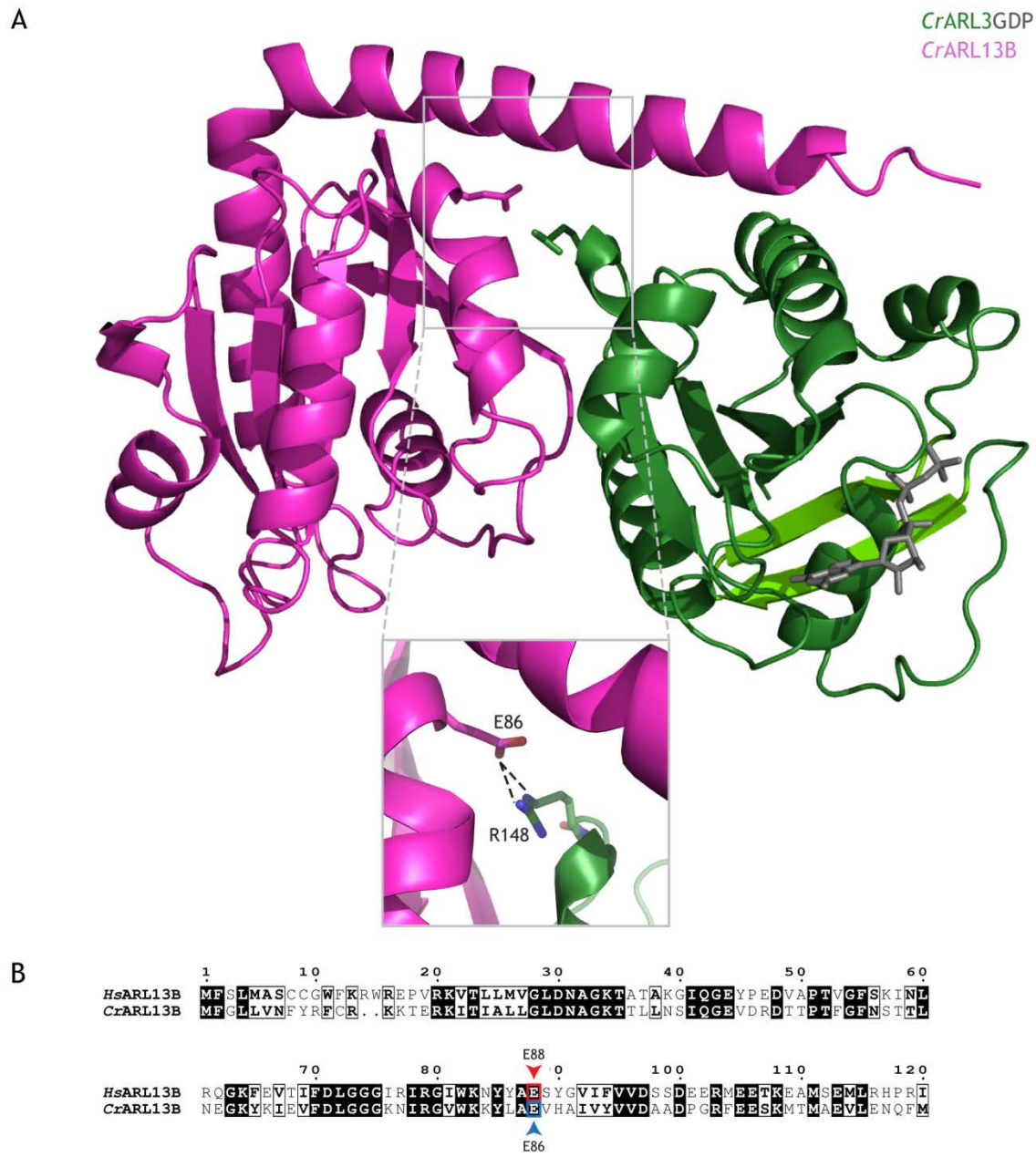

Figure 4-7 Mutant ARL3 arginine residue is located at the ARL3-ARL13B interface. **(A)** Cartoon representation of the *Cr*ARL3-*Cr*ARL13B complex structure (PDB code: 5DI3 (Gotthardt et al., 2015)). Residues R148 and E86 in ARL3 and ARL13B, respectively, are shown in stick form; the zoomed-in inset shows the salt bridge formed between them as black dashed lines. **(B)** Sequence alignment of the first ~120 residues of human and *Chlamydomonas* ARL3, with the glutamate residues interacting with the ARL3 arginine residue marked in red and blue boxes, respectively.

While recombinant murine ARL3 (as a representative of human ARL3) is easily expressed in *E. coli*, purification of human ARL13B (*Hs*ARL13B) has been reported to require expression in insect cells (Gotthardt et al., 2015). As a preliminary

step in our study, we decided to test the mutation with *C. reinhardtii* ARL3 (*Cr*ARL3) and ARL13B (*Cr*ARL13B). Both proteins easy to express and purify in *E. coli*, and were used previously to generate the aforementioned crystal structure. Sequence alignment of human and *Chlamydomonas* ARL3 shows that R149 in the former aligns with R148 in the latter **(Figure 4-6B)**. I generated the wild-type and mutant His-tagged ARL3 proteins: *Cr*ARL3^{WT} and *Cr*ARL3^{R148H}, respectively. Along with *Cr*ARL13B, all three proteins were expressed in *E. coli* and purified as previously reported (Gotthardt et al., 2015).

To compare the ARL13B-catalysed nucleotide exchange of the wild-type and mutant ARL3, I used a fluorescence polarisation-based GEF assay. This involves labelling the ARL3 protein with fluorescently-labelled GDP, mantGDP. The fluorescence polarisation is monitored during the addition of ARL13B to a mixture of the labelled ARL3 and excess unlabelled GppNHp (non-hydrolysable GTP analogue). If the nucleotide exchange is successful, ARL3-bound mantGDP is exchanged for unlabelled GppNHp. A drop in polarisation will occur as the fluorophore is no longer associated with ARL3 and is smaller in size. **Figure 4-8** shows the fluorescence polarisation measurements taken after the addition of ARL13B to wild-type and mutant ARL3. While ARL3^{WT} shows a gradual decrease in polarisation following ARL13B addition, the mutant ARL3^{R148H} does not, and the polarisation remains steady. Nucleotide exchange did not take place in the latter case, indicating that the R148H mutation affects GEF-mediated activation of ARL3.

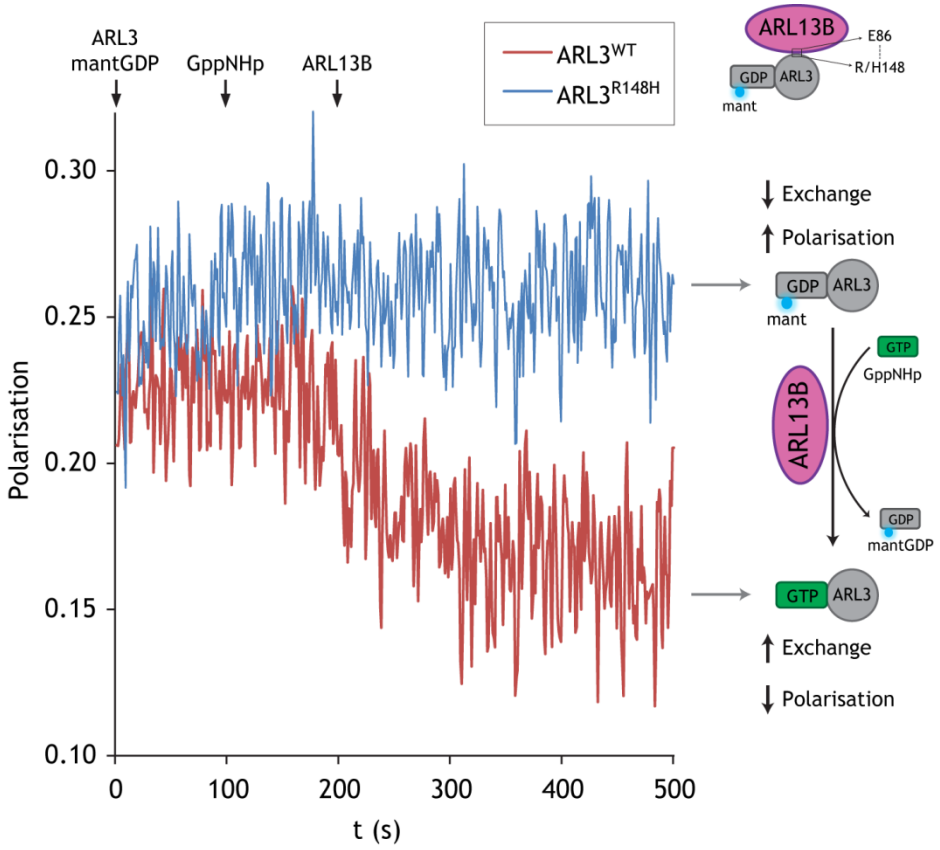

Figure 4-8 R148H mutation in *Cr*ARL3 inhibits nucleotide exchange by ARL13B.
Nucleotide exchange was assessed for both wild-type and mutant *Cr*ARL3 after loading them with mantGDP. Fluorescence polarisation of 0.5 mM of $ARL3^{WT}$ and $ARL3^{R148H}$ was monitored during the addition of 10 mM GppNHp followed by 5 mM *Cr*ARL13B-GppNHp as indicated on the plot. The right-hand side scheme summarises the principle of the assay: the successful exchange of the labelled mantGDP for the unlabelled GppNHp present in excess results in a reduction in polarisation. This is because the fluorescent nucleotide is release from the larger ARL3 and is the case observed for the wild-type ARL3 (red). Mutant $ARL3^{R148H}$ (blue), however, shows no similar decrease in polarisation, indicating the impairment of the ARL13B-catalysed nucleotide exchange.

4.2.1.2 Purification of recombinant *Hs*ARL13B

Having shown that the patient mutation does have an effect on ARL3 nucleotide exchange when tested in the equivalent *Cr*ARL3 and *Cr*ARL13B proteins, the next step was to replicate the experiment with the human equivalents. As previously mentioned, murine ARL3 (being highly similar to the human protein) has been previously used by us and others to study the structure and function of human ARL3. While recombinant *Hs*ARL13B has only been reported to be successfully expressed in insect cells (Gotthardt et al., 2015), we decided to attempt *E. coli* expression, using the 12xHis-tag system that we found to be highly successful in

the purification of another challenging protein, full-length LCK. Therefore, using the truncated ARL13B$^{18-278}$ sequence previously used in insect cells in order to maximise the chances of successful expression **(Figure 4-9A)**, I generated the 12xHis-tagged construct of *Hs*ARL13B and used BL21(DE3)CodonPlus *E.coli* competent cells for expression. **Figure 4-9B** shows the elution profile obtained from nickel affinity chromatography and ARL13B peak obtained. The protein was then further purified by size exclusion chromatography and the ARL13B tested on SDS-PAGE **(Figure 4-9C)**.

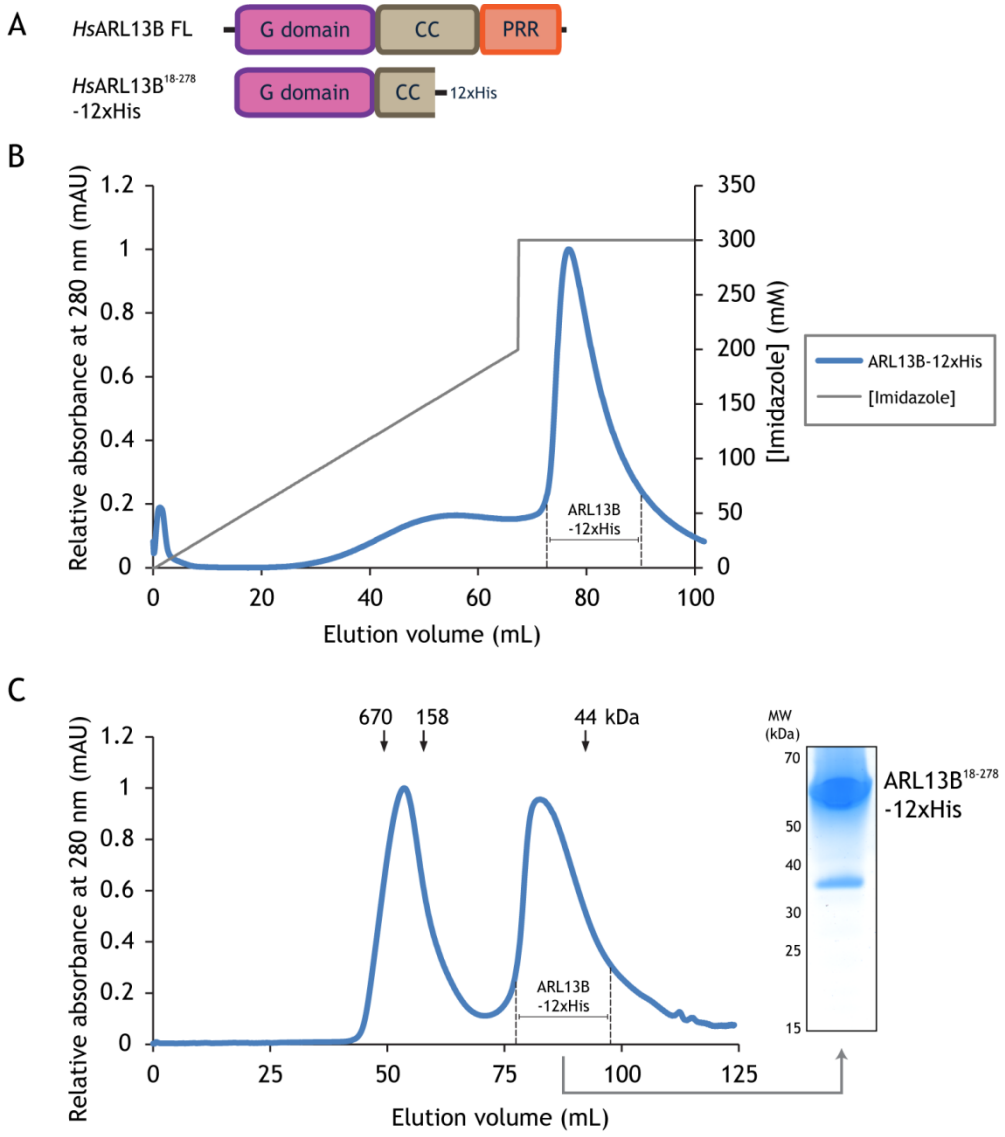

Figure 4-9 Purification of recombinant *Hs*ARL13B.

(A) Domain organisation of full-length ARL13B and the truncated His-tagged construct (ARL13B$^{18-278}$) used for expression in *E. coli*. **(B)** ARL13B$^{18-278}$-12xHis was expressed in BL21-CodonPlus (DE3)-RIL competent cells and separated from the lysate by nickel affinity chromatography. The gradient elution profile of the protein with imidazole is shown, with the major ARL13B peak eluting at higher concentrations of imidazole. Step elution was used to speed up the ARL13B

elution and restrict it to a smaller volume. The eluted ARL13B fraction was further purified by size exclusion chromatography. **(C)** Gel filtration elution profile of the ARL13B fraction obtained after nickel affinity separation. The ARL13B fraction was separated and a sample was run on SDS-PAGE and stained with Coomassie blue (right panel). *Hs*, *Homo sapiens*; CC, coiled coil domain; PRR, Proline-rich region; G domain, GTPase domain.

4.2.1.3 The human ARL3^{R149H} mutant reflects *Cr*ARL3 nucleotide exchange impairment

With the successful ARL13B expression in *E. coli*, I tested the purified protein using the same polarisation-based GEF assay as before, this time using murine ARL3. The wild-type ARL3 did undergo nucleotide exchange **(Figure 4-10)**, confirming that the recombinant *Hs*ARL13B protein is functional. Mutant ARL3^{R149H}, bearing the same mutation as reported in the affected individuals, failed to show nucleotide exchange, confirming the *Cr*ARL3 results.

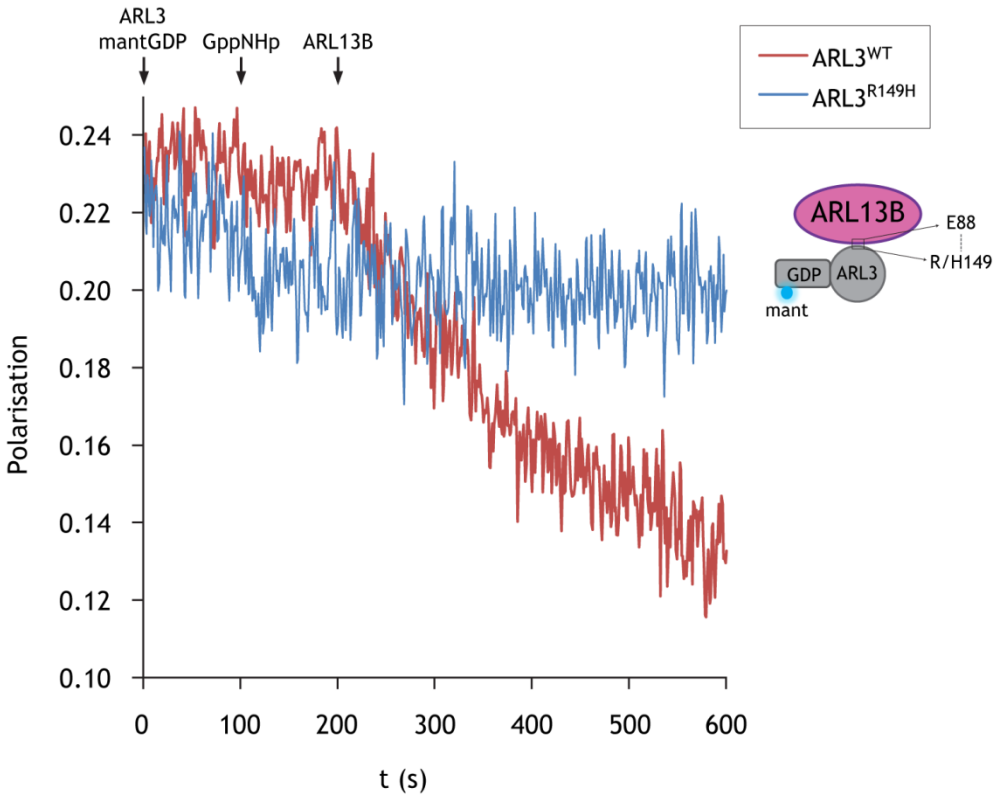

Figure 4-10 *Mm*ARL3^{R149H} exhibits impaired ARL13B-mediated nucleotide exchange. Fluorescence polarisation measurements of 1mM wild-type (red) and R149H mutant (blue) ARL3-mantGDP, with the addition of 400 mM GppNHp followed by 5 mM HsARL13B. Only ARL3WT shows a reduction in polarisation following ARL13B addition, indicating the occurrence of nucleotide exchange.

4.2.1.4 Mutation of interacting residue in ARL13B reproduces GEF activity impairment

Testing the ARL3 mutation in both human/mouse and *Chlamydomonas* proteins indicated that it affected the nucleotide exchange of the protein. The crystal structure of ARL3 and ARL13B in complex indicates that the importance of the ARL3 arginine residue arises from its ionic interaction with a glutamate residue in ARL13B. We can therefore attempt to replicate the mutant condition in ARL13B by disrupting the ionic interaction through glutamate mutation to a residue of opposite charge. I therefore generated the *Cr*ARL13B glutamate-to-arginine mutant (*Cr*ARL13B^{E86R}) and assessed its ability to exchange the nucleotide of wild-type ARL3. As shown in **Figure 4-11**, only *Cr*ARL13B^{WT} resulted in a drop in polarisation, indicating successful nucleotide exchange, while *Cr*ARL13B^{E86R} failed to bring about a similar exchange.

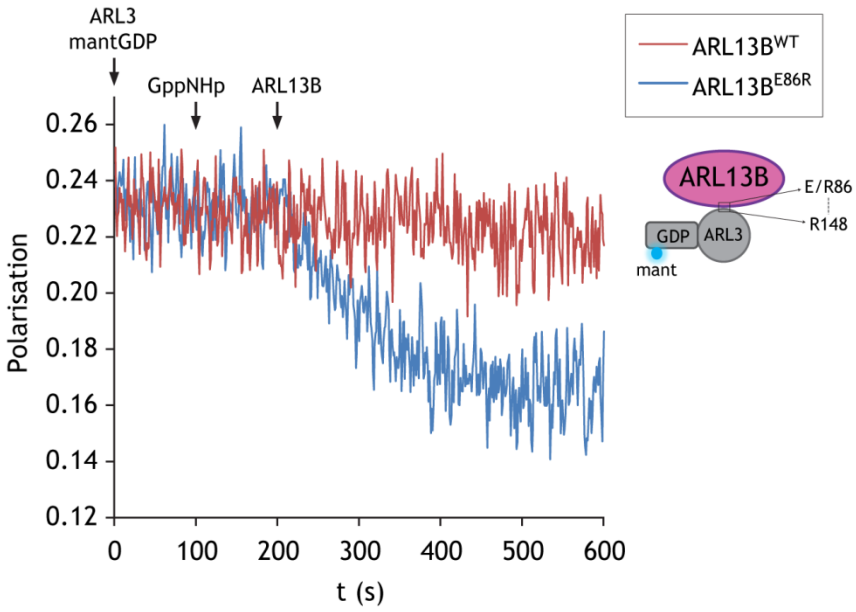

Figure 4-11 *Cr*ARL13B^{E86R} fails to catalyse nucleotide exchange of ARL3.
Fluorescence polarisation-based GEF assay of *Cr*ARL13B^{WT} and *Cr*ARL13B^{E86R}. 10 mM GppNHp was added to 0.5 mM *Cr*ARL3-mantGDP, followed by 5 mM of the indicated ARL13B protein. Nucleotide exchange only occurred with the use of the wild-type *Cr*ARL13B^{WT}.

4.2.1.5 R148H mutation does not affect ARL3 binding to UNC119

To confirm the effect of the ARL3 mutation was restricted to the ARL13B-catalysed nucleotide exchange, I tested the interaction of wild-type and mutant ARL3 with UNC119, which should not be affected. **Figure 4-12** shows the results

of GST pulldown assays using GST-UNC119A to pull down *Mm*ARL3^{WT} and *Mm*ARL3^{R149H}. Both ARL3 proteins interact similarly with GST-UNC119A, indicating the integrity of the purified proteins, despite the presence of the mutation.

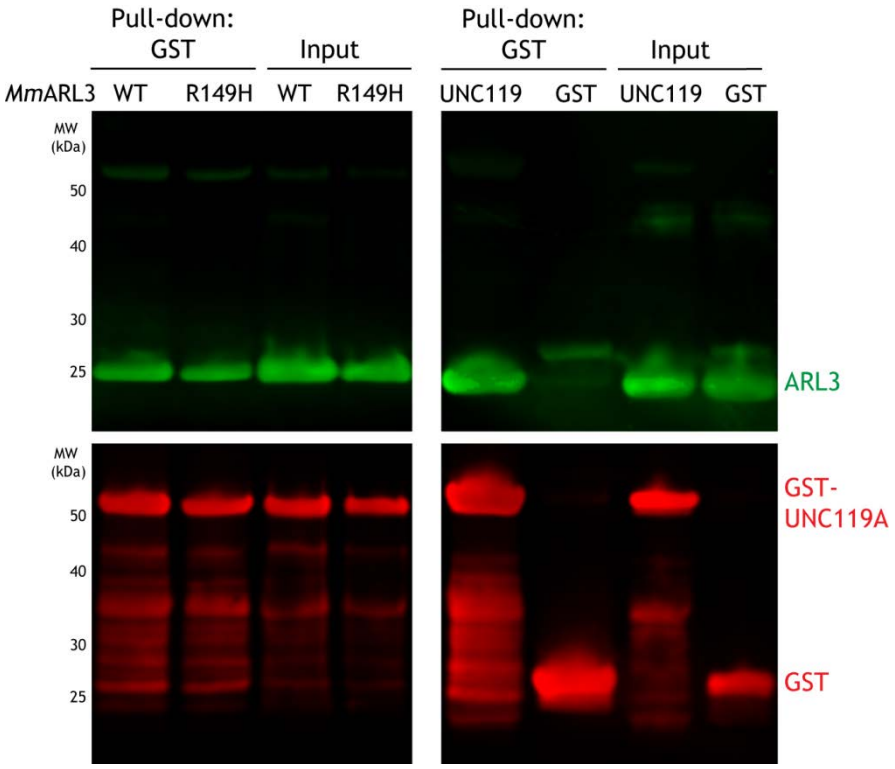

Figure 4-12 Patient ARL3 mutation does not affect its binding to UNC119A.
Pull-down assay with 30 µg of GST-UNC119A FL and 60 µg of either wild-type or R149H mutant *Mm*ARL3. Right-hand side panel shows the GST control experiment used to rule out non-specific binding, where the beads where loaded with GST alone. ARL3 and UNC119 were detected by Western blots using antibodies against His and GST, respectively.

4.2.1.6 Patient fibroblasts show mislocalisation of ciliary GSF cargo

Localisation studies in patient fibroblasts described in this section were carried out by John Sayer and Sumaya AlKanderi and are included here with their permission.

As previously described, the trafficking of high affinity lipid-modified cargo proteins by the GSF-mediated pathway is primarily dependent on the specific release of the cargo due to the activation of ARL3 in the cilium. Having confirmed the effect of the patient mutation on the nucleotide exchange of ARL3, we hypothesised that it would result in the impairment of the GSF-mediated trafficking of lipid-modified cargo. Our collaborators in the Sayer lab

have studied the ciliary localisation of INPP5E and NPHP3, which are GSF cargo of PDEδ and UNC119, respectively. Ciliary localisation was assessed in fibroblasts derived from the affected individuals, and compared to that of control fibroblasts. Ciliary localisation of both GSF cargo proteins was reduced in affected cells bearing the ARL3^{R149H} mutation (Alkanderi et al., 2018) **(Figure 4-13)**.

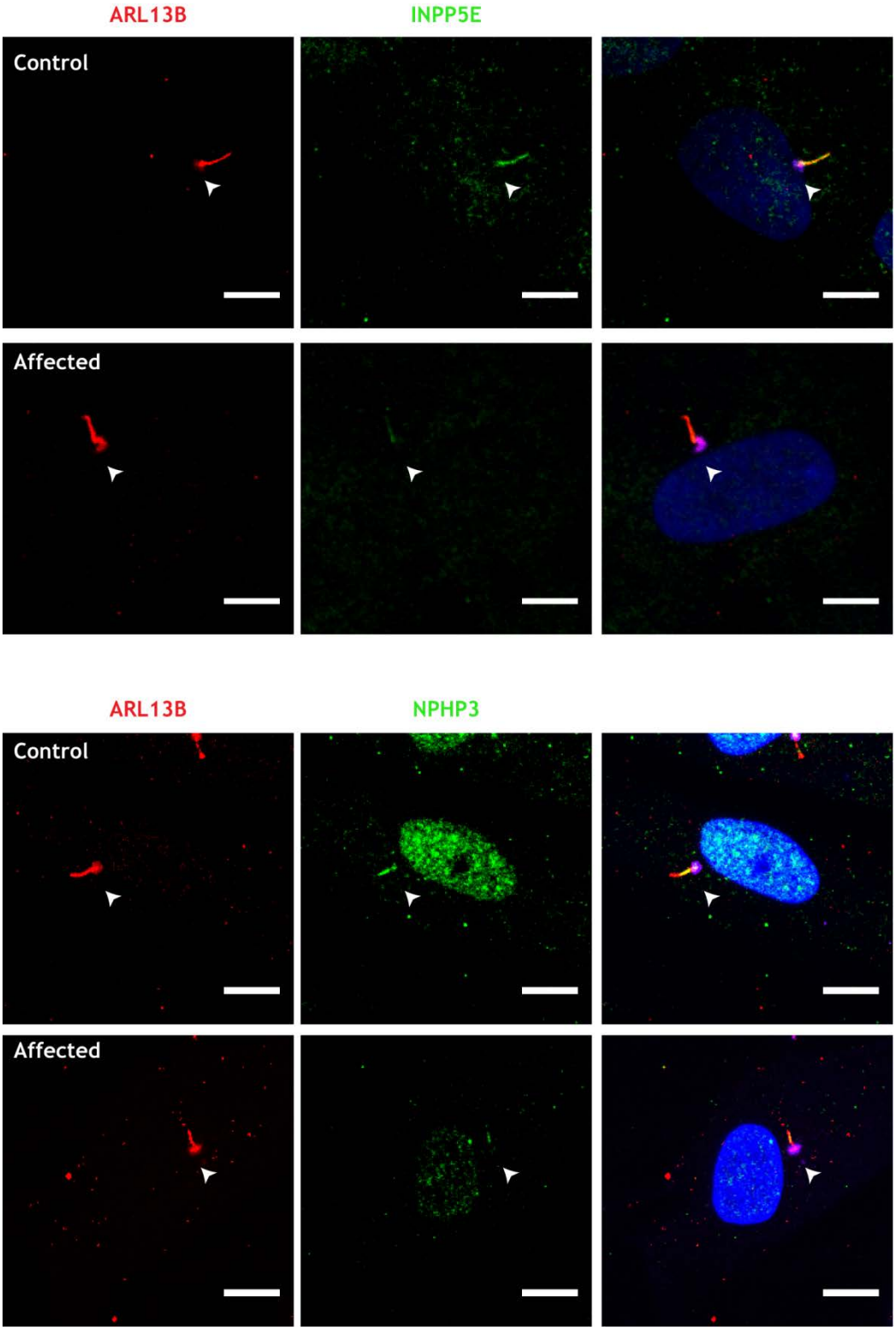

Figure 4-13 Mislocalisation of ciliary GSF-trafficked cargo in fibroblasts derived from affected individuals.

Fibroblasts from control and affected individuals were serum starved and stained for ARL13B and INPP5E (top) or NPHP3 (bottom). Ciliary localisation of the respective PDEδ and UNC119 cargo proteins was reduced in affected fibroblasts compared to that in the control counterparts (Alkanderi et al., 2018). White arrows indicate cilia, and bars represent 10 µm.

4.2.2 Inhibition of PDEδ in Hedgehog signalling

The developmental role of the Hedgehog pathway limits most of its activity to the embryonic stage, in which tissue patterning and differentiation take place. The pathway is mostly inactive once development is complete. Aberrant constitutive activation of Hedgehog signalling renders it an oncogenic pathway which drives the initiation and progression of some cancer types. This pathological activation of the pathway may be due to dysregulation at various points along the signalling axis **(section 4.1.2.1.1)**. HH overstimulation can occur independent of HH ligand levels due to activating mutations in *SMO* and *GLI* or inhibiting mutations in the negative regulators *PTCH1* and *SUFU*. In contrast, ligand-dependent activation involves the overproduction of the HH ligand. Oncogenic HH signalling is a driving factor in a sizeable fraction of cases of basal cell carcinoma and medulloblastoma (Amakye et al., 2013). The pathway has therefore become the subject of pharmacological screens in the search for targeted therapies. These have mainly focused on SMO and, more recently, GLI. However, there have been setbacks due to insufficient response in clinical trials, adverse side effects, and the development of resistance due to mutations in the target proteins (Gan and Jimeno, 2016). The search for additional targets is therefore ongoing, both to develop better inhibitors and to allow more options for combination therapy.

4.2.2.1 Using INPP5E to target the Hedgehog pathway

Recent studies have focused on the role of the phosphatase INPP5E in regulating the phosphoinositide content of the ciliary membrane with respect to HH signalling (Garcia-Gonzalo et al., 2015). As previously discussed, HH signalling is negatively regulated by the action of GPR161 in the primary cilium. GPR161 recruitment is mediated by TULP3 and IFT-A. Crucially, preferential binding of TULP3 to biphosphorylated PIP_2 in the ciliary membrane brings about the retention of GPR161 and its subsequent inhibition of the HH pathway (Badgandi et al., 2017). This INPP5E-TULP3-GPR161 axis, summarised in **Figure 4-14**, provides a potential strategy for targeting the Hedgehog pathway.

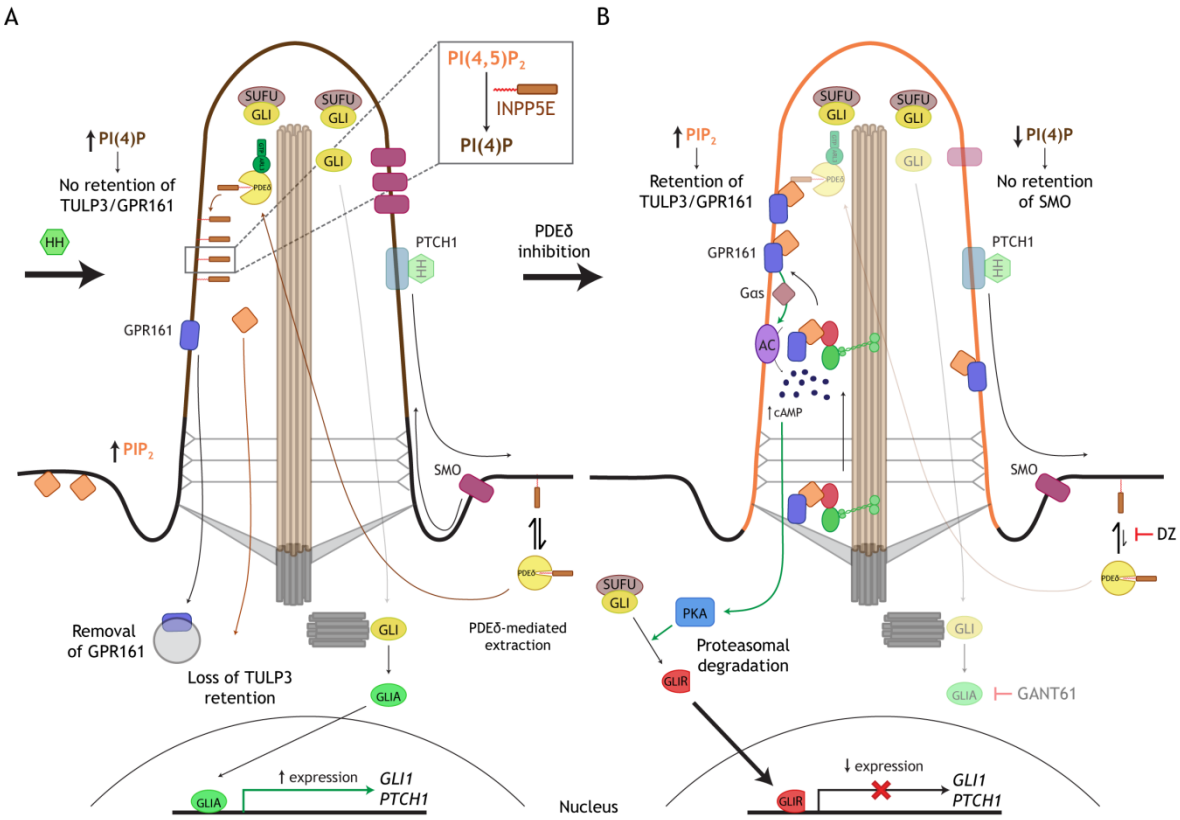

Figure 4-14 Effect of PDEδ inhibition on Hedgehog signalling.

(A) Under normal conditions, ciliary localisation of INPP5E is brought about by PDEδ-mediated trafficking. This results in the depletion of PIP_2 and the generation of PI(4)P (inset). TULP3, which preferentially binds PIP_2, is not retained in the cilium, and so is its interaction partner GPR161. Upon stimulation of the Hedgehog pathway, signalling is further enhanced by the high levels of ciliary PI(4)P, which promotes SMO localisation. In addition, loss of GPR161 retention decreases protein kinase A (PKA)-mediated inhibition of GLI proteins. **(B)** Inhibition of PDEδ by deltazinone (DZ) reduces INPP5E trafficking to the cilium, thereby restoring PIP_2 levels in the membrane. This promotes the retention of TULP3 and GPR161. The latter enhances cAMP production, which through the activation of PKA, promotes generation of the inhibitory repressor forms of GLI proteins (GLIR). In addition, low levels of ciliary PI(4)P reduce SMO localisation in the cilium, and hence release of GLI proteins from SUFU complexes. Signalling is therefore repressed even in the presence of stimulation. INPP5E, inositol polyphosphate-5-phosphatase E; PI(4)P, phosphatidylinositol-4-phosphate ; PIP_2, phosphatidylinositol 4,5-bisphosphate; INPP5E, inositol polyphosphate-5-phosphatase E; PDEδ, phosphodiesterase 6 subunit δ; TULP3, tubby-like protein 3; GANT61, GLI antagonist.

It has also been shown that the loss of ARL13B in medulloblastoma cell lines inhibited HH signalling even in the presence of oncogenic *SMO* mutation and *PTCH1* deletion (Bay et al., 2018). ARL13B is linked to the aforementioned axis as it facilitates the ciliary localisation of INPP5E, being a high affinity cargo protein of PDEδ that undergoes ARL3-specific release in the cilium (Fansa et al.,

2016). Furthermore, inhibitors have been previously developed to block the prenyl-binding pocket of PDEδ. **Figure 4-15** depicts the binding of one of these inhibitors, deltazinone (DZ), to the hydrophobic pocket of PDEδ (Papke et al., 2016).

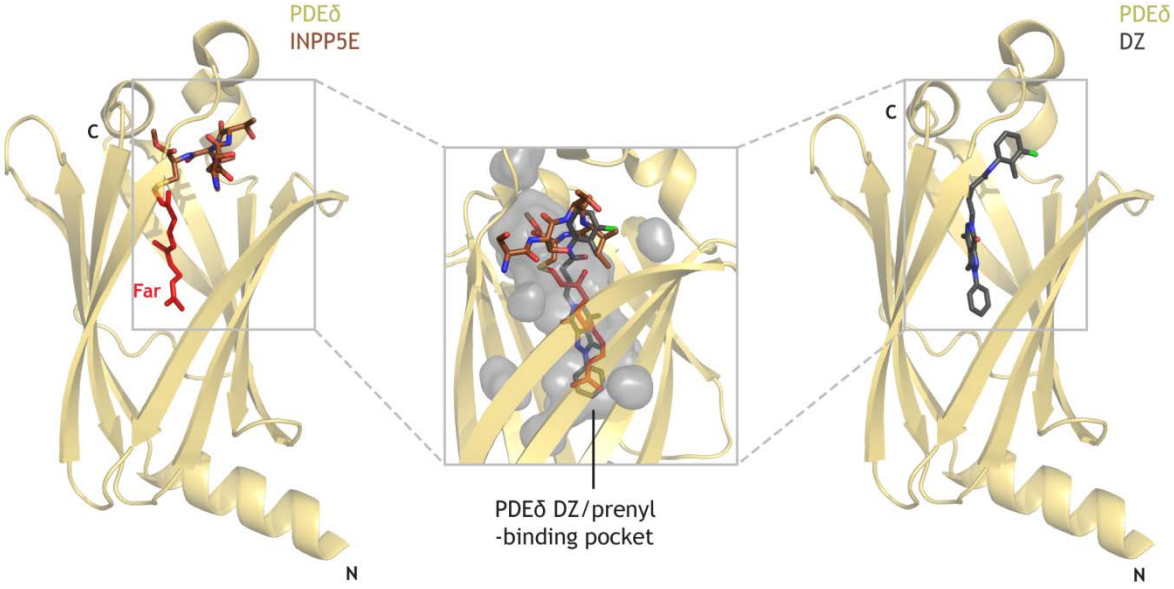

Figure 4-15 Deltazinone is an inhibitor of PDEδ prenyl binding.
Cartoon representations of the crystal structure of PDEδ (yellow) in complex with a C-terminal farnesylated peptide of INPP5E (left, PDB code: 5F2U (Fansa et al., 2016)) and with the compound deltazinone (right, PDB code: 5E80 (Papke et al., 2016)). INPP5E peptide and deltazinone are shown as sticks. Middle panel shows the superimposed close-ups of the PDEδ pocket (grey surface) in complex with the aforementioned ligands.

Inhibiting PDEδ is another strategy by which ciliary localisation of INPP5E may be disrupted. The availability of an inhibiting small molecule makes this approach encouraging in terms of developing a new targeted therapy against the Hedgehog pathway. This section presents my preliminary work in investigating the use of the PDEδ inhibitor deltazinone to target Hedgehog signalling.

4.2.2.2 Effect of deltazinone treatment on ciliated Madin-Darby canine kidney (MDCK) cells

The first cell line I used in investigating the effect of deltazinone (DZ) treatment on the Hedgehog pathway was the canine kidney MDCK cell line. This is an adherent cell line that is frequently used in ciliary studies as it forms tightly packed monolayers that quickly reach confluence to facilitate the formation of primary cilia. Cells grown on glass coverslips were serum starved for 24 hrs to arrest cell division and induce cilia formation. Primary cilia were visualised using acetylated tubulin which marks the axoneme, while nuclei were stained with DAPI. To image the cilia, I took 0.5 µm optical sections covering the entire depth, as visualised by acetylated tubulin staining, of all cilia in the field. The Z-stack was converted to a 2D image by performing maximum intensity projection using Fiji software. I then assessed MDCK ciliation by quantifying the number of ciliated cells compared to the total population, and the total area of the cilia as visualised by acetylated tubulin staining compared to total nuclear area (identified by DAPI staining). These two measurements were used to compare DZ-treated cells to the DMSO-treated controls. As shown in **Figure 4-16**, DZ treatment decreased both the number and area of cilia formed by MDCK cells.

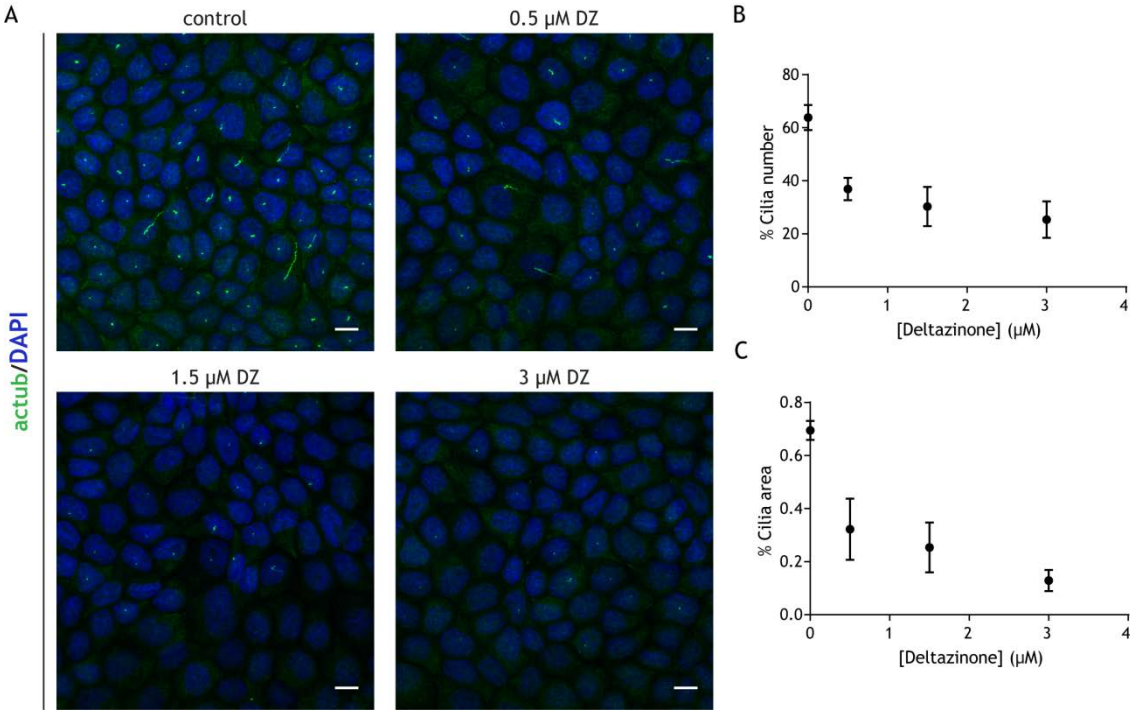

Figure 4-16 Effect of Deltazinone treatment on ciliation of MDCK cells.

(A) MDCK cells were serum-starved (0.5% serum-supplemented medium) in the presence of the indicated concentrations of deltazinone (DZ) for 24 hrs. Following fixation, cells were stained for

acetylated tubulin (actub) to visualise cilia and with DAPI. Scale bars represent 10 μm. **(B)** Quantification of the number of ciliated cells relative to the total number of cells and **(C)** the total area of cilia (indicated by actub) relative to total area of nuclei (indicated by DAPI). Values represent average of three different fields in two experiments (90 cells/field).

Having observed an effect on MDCK ciliation following DZ treatment, the next step was to investigate the effect of the inhibitor on HH signalling in these cells. This was carried out by using quantitative PCR (qPCR) to measure mRNA levels of *GLI1* and *PTCH1* compared to that of *GAPDH.* I designed primers complementary to exon-exon junctions in the canine sequences of the aforementioned genes. It is important for these primers to anneal to the junctions between exons to avoid overestimation of mRNA due to primer annealing to genomic DNA, which retains the introns. I validated the designed primers by confirming that the size of amplification products produced by endpoint PCR matched that predicted by primer design.

In assessing the efficiency of HH signalling, the pathway needs to be exogenously stimulated in cells to mimic the overactivation of HH-dependent cancer. I therefore used a synthetic smoothened agonist (SAG) to activate the pathway (Chen et al., 2002). However, no increase in either *GLI1* or *PTCH1* was observed at all tested concentrations **(Figure 4-17A)**. SAG has been shown to exert a bivalent mode of action, where it binds to both SMO and a downstream effector, thereby enhancing their interaction. Therefore, very high concentrations can saturate both binding partners, resulting in the inhibition of the pathway (Chen et al., 2002). However, since no activation was observed over a range of concentrations, this was unlikely to be the case. Another possibility was that SAG, which has poor aqueous solubility (Niewiadomski and Rohatgi, 2015), was precipitating upon addition to the culture medium. I therefore repeated the treatment with the water-soluble dihydrochloride form of SAG (SAG•2HCl). However, as shown in **Figure 4-17B**, no stimulation was observed.

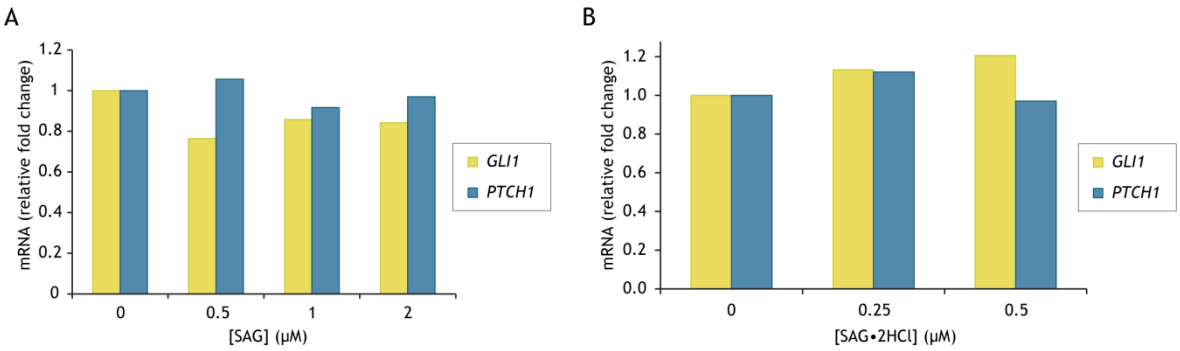

Figure 4-17 MDCK cells fail to show Hedgehog stimulation with Smoothened agonist (SAG).

MDCK cells were treated with the indicated concentrations of **(A)** DMSO- and **(B)** water-soluble smoothened agonist (SAG and SAG•2HCl, respectively) in the presence of serum starvation. Hedgehog signalling was assessed after 24 hrs by quantifying mRNA levels of *GLI1* (yellow bars) and *PTCH1* (blue bars) by quantitative PCR. Fold changes for the indicated mRNA species relative to unstimulated controls are shown for the different SAG concentrations used.

4.2.2.3 Effect of deltazinone treatment on NIH/3T3 fibroblasts

As MDCK cells were not responding to stimulation with SAG, I repeated the aforementioned experiment with NIH/3T3 murine embryonic fibroblasts, which are also commonly used to study the cilium. Using SAG•2HCl to stimulate the NIH/3T3 cells produced a robust increase in both *GLI1* and *PTCH1*, which was comparable to that seen in similar studies. Using SAG•2HCl at a concentration of 0.2 μM gave the highest fold increase in mRNA levels of both genes and so was chosen for further experiments.

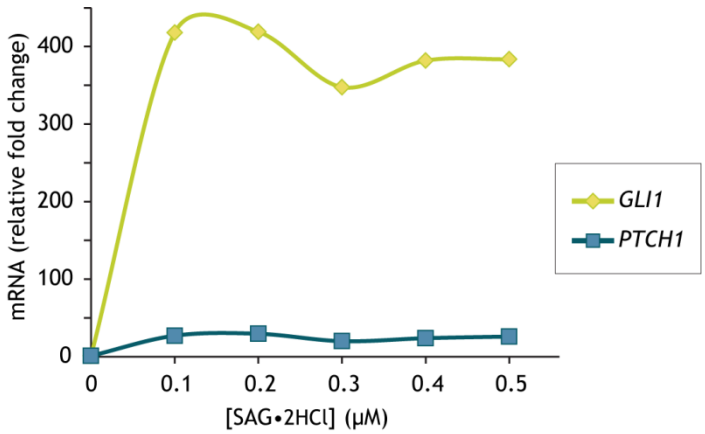

Figure 4-18 Optimisation of SAG-mediated Hedgehog signalling stimulation in NIH/3T3 cells.

NIH/3T3 fibroblasts were treated with the indicated concentrations of water-soluble smoothened agonist (SAG•2HCl) in the presence of serum-starvation for 24 hrs. Hedgehog pathway stimulation was assessed by measuring the levels of the indicated mRNA species by quantitative PCR relative to unstimulated control.

HH signalling was assessed by qPCR in NIH/3T3 cells following serum starvation in the presence of increasing concentrations of two inhibitors: DZ, which inhibits PDEδ, and GANT61, which is a reported GLIA inhibitor (Lauth et al., 2007). GANT61 was used as a positive control, and to assess the effect of using DZ. **Figure 4-19** shows the increase of *GLI1* and *PTCH1* mRNA levels upon stimulating the HH pathway with SAG in the presence of different concentrations of the aforementioned inhibitors. DZ does result in inhibition of HH signalling, if to a lesser extent than GANT61. It remains, however, an encouraging result, providing an initial indication that targeting PDEδ is a valid approach of HH pathway inhibition.

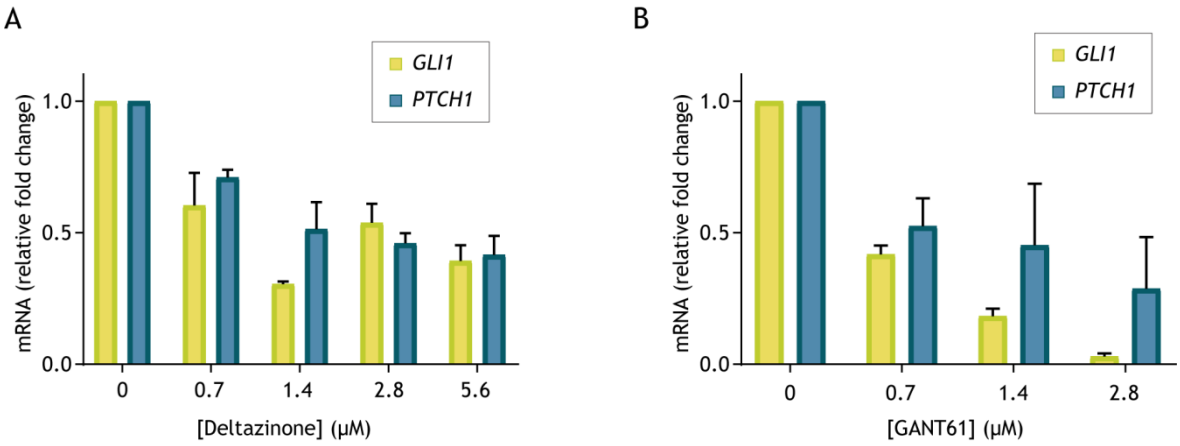

Figure 4-19 Effect of deltazinone treatment on Hedgehog signalling in NIH/3T3 cells. NIH/3T3 fibroblasts were treated with the indicated concentrations of **(A)** PDEδ inhibitor deltazinone (DZ) or **(B)** GLIA antagonist GANT61 in the presence of serum-starvation and 0.2 μM SAG•2HCl for 24 hrs. Average changes in mRNA levels relative to controls (SAG stimulation but without inhibitor treatment) are shown for two separate experiments.

Following the observation of inhibition of the HH due to DZ treatment, the next step was to investigate cilia formation and INPP5E localisation. At the time of writing, this is ongoing work. **Figure 4-20** shows preliminary images of 3T3 cells treated with 1.4 μM DZ. Cilia formation does not appear to be as affected as with MDCK cells, but it still needs to be confirmed, as does the effect on INPP5E localisation.

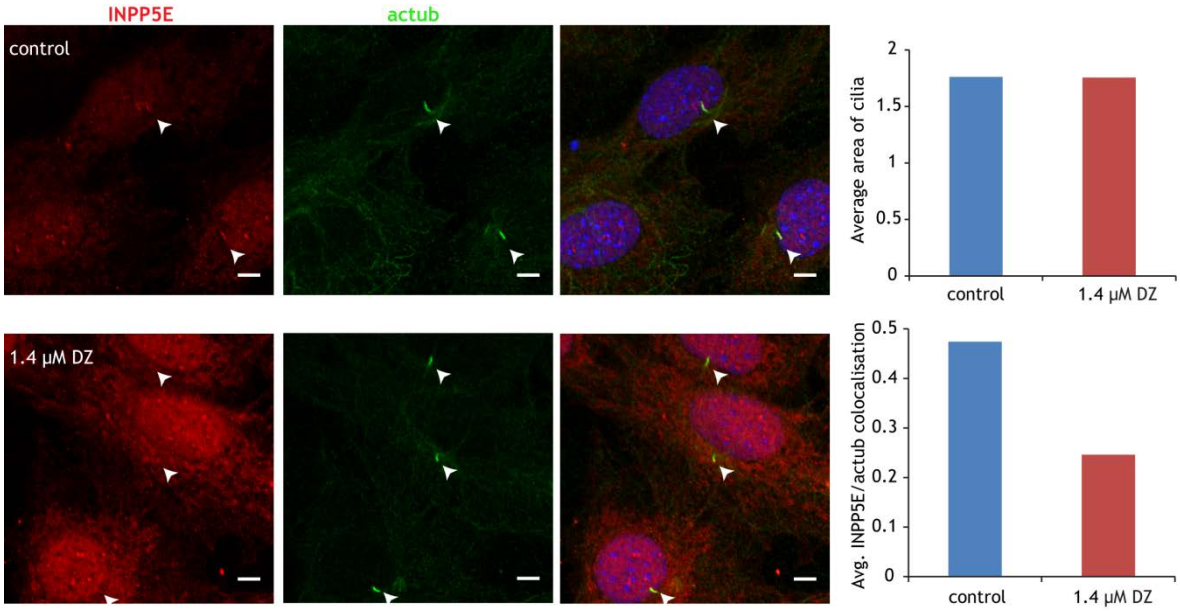

Figure 4-20 Preliminary localisation studies of INPP5E in NIH/3T3 cells.

3T3 fibroblasts were treated with 1.4 μM deltazinone in the presence of serum starvation. After 24 hrs, cells were fixed and stained for INPP5E and acetylated tubulin. Area of cilia (top right) and colocalisation of INPP5E and acetylated tubulin (bottom right) was quantified for a small sample (n<10 cilia).

4.3 Discussion

In this chapter, I presented my work on aspects of GSF-mediated trafficking of ciliary cargo proteins in the context of Joubert syndrome and HH signalling.

4.3.1 GSF-mediated trafficking and Joubert syndrome

We have shown that the ARL3^{R149H} mutation identified in individuals affected with the ciliopathy Joubert syndrome resulted in impairment of its ARL13B-catalysed nucleotide exchange. The mutated residue was found to be involved in an ionic interaction with ARL13B that was critical for successful exchange. I confirmed this hypothesis by assessing the nucleotide exchange of wild type and mutant ARL3 proteins. The mutation greatly decreased the exchange in both *Chlamydomonas* and human proteins. Our collaborators have observed that GSF-trafficked cargo proteins INPP5E and NPHP3 exhibited less ciliary localisation in the presence of the ARL3 mutation (Alkanderi et al., 2018).

The case of this ARL3 mutation highlights the importance of the ARL3GTP gradient generated in cilia by ARL13B on the localisation of ciliary cargo proteins. High cargo affinity to GSFs depends on the restricted localisation of the active displacement factor to facilitate correct trafficking by the GSF-ARL3-ARL13B axis, as summarised in **Figure 4-21**.

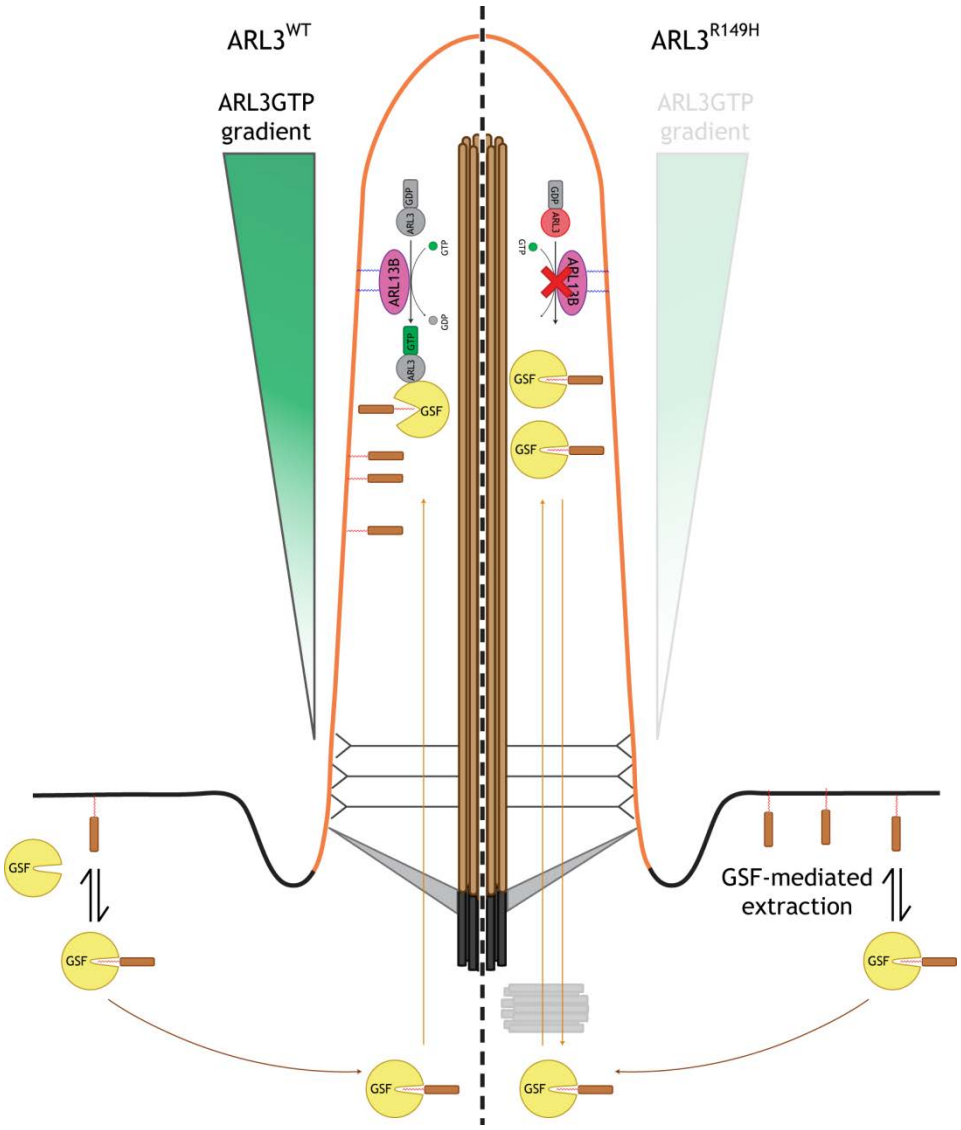

Figure 4-21 ARL3^{R149H} mutation impairs GSF-mediated trafficking to the primary cilium.
A comparison of GSF-mediated trafficking in the presence of wild-type (left) and mutant (right) ARL3. Impairment of nucleotide exchange of ARL3 abrogates the generation of high ciliary levels of ARL3GTP. GSF-cargo complexes are therefore not specifically disrupted within the compartment, resulting in decreased localisation.

Members of this trafficking axis have been implicated as ciliopathy genes; mutations in ARL13B and PDEδ have been reported to cause Joubert syndrome (Cantagrel et al., 2008, Thomas et al., 2014). This also applies to several cargo proteins trafficked to the cilium by this system. Defects in ARL3, which is required for both UNC119- and PDEδ-mediated trafficking, are likely to have devastating effects on the cilium as the transportation of multiple cargo proteins would be impaired. ARL3 mutations may be more likely to be lethal, perhaps accounting for the scarcity of other reports of ciliopathy-causing ARL3 mutations.

In addition, it may be a beneficial strategy in the case of ARL3 defects to attempt artificial GSF cargo release through the use of inhibitors, such as squarunkin A and deltazinone, as previously mentioned. While this approach will not restore the specific ciliary localisation, it should release the ciliary cargo from being sequestered in the cytoplasm, thereby increasing its chances of reaching the cilium from the membrane. This may be possible through pathways taken by membrane proteins, as described in **4.1.1.2.1**.

Finally, the role of UNC119A-trafficking in the immune synapse gives rise to the question of what the effect of this ARL3 mutation would be on the immune response. The incidence of recurrent urinary tract infections was reported for one of the affected individuals (Alkanderi et al., 2018), which may be due to an effect on the immune response. It would be interesting to reproduce the ARL3 R149 mutation in T lymphocytes and study how well the immune synapse functions.

4.3.2 PDEδ-mediated trafficking and HH signalling

Having optimised the assessment of HH signalling by qPCR following DZ-treatment and SAG-stimulation, I plan to focus on elucidating the mechanism of HH signalling inhibition observed upon PDEδ. The primary aim is to study INPP5E localisation in this system, in addition to that of TULP3 and GPR161. Furthermore, the accompanying changes in membrane phosphoinositides are an important aspect of this signalling axis. The effect of PDEδ inhibition can be validated by comparing it to that of knocking down or deleting the protein. Furthermore, I can use SHH-dependent medulloblastoma cell lines such as Daoy (Götschel et al., 2013) to study the effect of PDEδ inhibition in the context of cancer, and compare the effect of DZ treatment on HH signalling and proliferation to that obtained with PDEδ deletion.

The regulation of INPP5E is also an open question. Ciliary localisation of INPP5E suppresses HH signalling, so there must be a cellular mechanism to allow its regulation during HH pathway activity. How is HH signalling initiated in the ciliary compartment in the presence of INPP5E? It may be that that the PDEδ-mediated trafficking is inhibited by an as-yet unidentified mechanism, or that

INPP5E is actively excluded from the cilium (Phua et al., 2018). Exclusion is likely to occur through the membrane, as cytoplasmic exit will also require the solubilisation of the farnesyl group. Alternatively, INPP5E may be subject to degradation or inhibition to stop its activity and allow HH signalling to take place. In that vein, the centrosomal kinase Aurora kinase A (AURKA) has been implicated in a potential regulatory role with respect to INPP5E (Plotnikova et al., 2015).

While the HH pathway has been found to play a role in $CD8^+$ T cell killing (de la Roche et al., 2013), in an oncogenic context, it has also been implicated in suppression of the immune response against cancer cells. This has been reported to be mediated via the downregulation of the interferon γ (IFN-γ) signalling following T cell activation, among other effects (Hanna and Shevde, 2016). This is yet another link between the immune response and ciliary signalling. It would be interesting to investigate how the Hedgehog pathway exerts two opposing effects on T cell responses in the presence and absence of cancer. What happens to T cell cytotoxicity in the presence of HH pathway overactivation? The HH pathway may therefore provide another approach by which to manipulate the immune response.

Concluding remarks

Cellular signalling pathways are orchestrated by the spatial segregation of their various components in relation with each other. The work presented in this thesis has focused on the trafficking of lipid-modified cargo as mediated by a handful of proteins. It is the flexibility of the system to shuttle multiple cargoes to various destinations that results in multi-system ramifications upon impairment of its function.

The presence of common denominators in the mechanisms that bring about these localisations provides a way to identify and understand the links between different cellular processes. The identification of such links requires careful dissection of the multitude of trafficking networks in the cell. This is especially important when it comes to finding new therapeutic strategies for disorders of these processes. Investigations of such approaches must encompass not only the effects of immediate interactors, but also the bigger picture imposed by all the different compartments of the cell that are connected by these trafficking pathways.

List of References

Akimzhanov, A. M. & Boehning, D. 2015. Rapid and transient palmitoylation of the tyrosine kinase Lck mediates Fas signaling. *Proceedings of the National Academy of Sciences,* 112**,** 11876-11880.

Alkanderi, S., Molinari, E., Shaheen, R., Elmaghloob, Y., Stephen, L. A., Sammut, V., Ramsbottom, S. A., Srivastava, S., Cairns, G. & Edwards, N. 2018. ARL3 mutations cause Joubert Syndrome by disrupting ciliary protein composition. *The American Journal of Human Genetics,* 103**,** 612-620.

Amakye, D., Jagani, Z. & Dorsch, M. 2013. Unraveling the therapeutic potential of the Hedgehog pathway in cancer. *Nature medicine,* 19**,** 1410.

Amor, J. C., Harrison, D. H., Kahn, R. A. & Ringe, D. 1994. Structure of the human ADP-ribosylation factor 1 complexed with GDP. *Nature,* 372**,** 704.

Antón, O., Batista, A., Millán, J., Andrés-Delgado, L., Puertollano, R., Correas, I. & Alonso, M. A. 2008. An essential role for the MAL protein in targeting Lck to the plasma membrane of human T lymphocytes. *Journal of Experimental Medicine,* 205**,** 3201-3213.

Araki, S., Kikuchi, A., Hata, Y., Isomura, M. & Takai, Y. 1990. Regulation of reversible binding of smg p25A, a ras p21-like GTP-binding protein, to synaptic plasma membranes and vesicles by its specific regulatory protein, GDP dissociation inhibitor. *Journal of Biological Chemistry,* 265**,** 13007-13015.

Badgandi, H. B., Hwang, S.-H., Shimada, I. S., Loriot, E. & Mukhopadhyay, S. 2017. Tubby family proteins are adapters for ciliary trafficking of integral membrane proteins. *J Cell Biol,* 216**,** 743-760.

Balagopalan, L., Barr, V. A. & Samelson, L. E. 2009. Endocytic events in TCR signaling: focus on adapters in microclusters. *Immunological reviews,* 232**,** 84-98.

Balagopalan, L., Coussens, N. P., Sherman, E., Samelson, L. E. & Sommers, C. L. 2010. The LAT story: a tale of cooperativity, coordination, and choreography. *Cold Spring Harbor perspectives in biology,* 2**,** a005512-a005512.

Ballek, O., Valečka, J., Manning, J. & Filipp, D. 2015. The pool of preactivated Lck in the initiation of T-cell signaling: a critical re-evaluation of the Lck standby model. *Immunology and cell biology,* 93**,** 384-395.

Bangs, F. & Anderson, K. V. 2017. Primary cilia and mammalian hedgehog signaling. *Cold Spring Harbor perspectives in biology,* 9**,** a028175.

Barcia, C., Wawrowsky, K., Barrett, R. J., Liu, C., Castro, M. G. & Lowenstein, P. R. 2008. In vivo polarization of IFN-γ at Kupfer and non-Kupfer immunological synapses during the clearance of virally infected brain cells. *The Journal of Immunology,* 180**,** 1344-1352.

Barnden, M. J., Allison, J., Heath, W. R. & Carbone, F. R. 1998. Defective TCR expression in transgenic mice constructed using cDNA-based α-and ß-chain genes under the control of heterologous regulatory elements. *Immunology and cell biology,* 76**,** 34-40.

Basu, R. & Huse, M. 2017. Mechanical communication at the immunological synapse. *Trends in cell biology,* 27**,** 241-254.

Batista, F. D., Iber, D. & Neuberger, M. S. 2001. B cells acquire antigen from target cells after synapse formation. *Nature,* 411**,** 489.

Bay, S. N., Long, A. B. & Caspary, T. 2018. Disruption of the ciliary GTPase Arl13b suppresses Sonic hedgehog overactivation and inhibits medulloblastoma formation. *Proceedings of the National Academy of Sciences,* 115**,** 1570-1575.

Berbari, N. F., Lewis, J. S., Bishop, G. A., Askwith, C. C. & Mykytyn, K. 2008. Bardet–Biedl syndrome proteins are required for the localization of G protein-coupled receptors to primary cilia. *Proceedings of the National Academy of Sciences,* 105**,** 4242-4246.

Bijlmakers, M.-J. J., Isobe-Nakamura, M., Ruddock, L. J. & Marsh, M. 1997. Intrinsic signals in the unique domain target p56lckto the plasma membrane independently of CD4. *The Journal of cell biology,* 137**,** 1029-1040.

Bijlmakers, M.-J. J. & Marsh, M. 1999. Trafficking of an acylated cytosolic protein: newly synthesized p56lck travels to the plasma membrane via the exocytic pathway. *The Journal of cell biology,* 145**,** 457-468.

Blom, N., Gammeltoft, S. & Brunak, S. 1999. Sequence and structure-based prediction of eukaryotic protein phosphorylation sites. *Journal of molecular biology,* 294**,** 1351-1362.

Blümer, J., Rey, J., Dehmelt, L., Mazel, T., Wu, Y.-W., Bastiaens, P., Goody, R. S. & Itzen, A. 2013. RabGEFs are a major determinant for specific Rab membrane targeting. *J Cell Biol,* 200**,** 287-300.

Boekhoff, I., Tareilus, E., Strotmann, J. & Breer, H. 1990. Rapid activation of alternative second messenger pathways in olfactory cilia from rats by different odorants. *The EMBO journal,* 9**,** 2453-2458.

Boggon, T. J. & Eck, M. J. 2004. Structure and regulation of Src family kinases. *Oncogene,* 23**,** 7918.

Bos, J. L., Rehmann, H. & Wittinghofer, A. 2007. GEFs and GAPs: critical elements in the control of small G proteins. *Cell,* 129**,** 865-877.

Boulter, E., Garcia-Mata, R., Guilluy, C., Dubash, A., Rossi, G., Brennwald, P. J. & Burridge, K. 2010. Regulation of Rho GTPase crosstalk, degradation and activity by RhoGDI1. *Nature cell biology,* 12**,** 477.

Bray, D. 1998. Signaling complexes: biophysical constraints on intracellular communication. *Annual review of biophysics and biomolecular structure,* 27**,** 59-75.

Brdička, T., Pavlišťová, D., Leo, A., Bruyns, E., Kořínek, V., Angelisová, P., Scherer, J., Shevchenko, A., Shevchenko, A. & Hilgert, I. 2000. Phosphoprotein associated with glycosphingolipid-enriched microdomains (PAG), a novel ubiquitously expressed transmembrane adaptor protein, binds the protein tyrosine kinase csk and is involved in regulation of T cell activation. *Journal of Experimental Medicine,* 191**,** 1591-1604.

Breslow, D. K., Koslover, E. F., Seydel, F., Spakowitz, A. J. & Nachury, M. V. 2013. An in vitro assay for entry into cilia reveals unique properties of the soluble diffusion barrier. *J Cell Biol,* 203**,** 129-147.

Briscoe, J. & Thérond, P. P. 2013. The mechanisms of Hedgehog signalling and its roles in development and disease. *Nature reviews Molecular cell biology,* 14**,** 416.

Calabia-Linares, C., Robles-Valero, J., De La Fuente, H., Perez-Martinez, M., Martín-Cofreces, N., Alfonso-Pérez, M., Gutierrez-Vázquez, C., Mittelbrunn, M., Ibiza, S. & Urbano-Olmos, F. R. 2011. Endosomal clathrin drives actin accumulation at the immunological synapse. *J Cell Sci,* 124**,** 820-830.

Cambier, J. C. 1995. Antigen and Fc receptor signaling. The awesome power of the immunoreceptor tyrosine-based activation motif (ITAM). *The Journal of Immunology,* 155**,** 3281-3285.

Cantagrel, V., Silhavy, J. L., Bielas, S. L., Swistun, D., Marsh, S. E., Bertrand, J. Y., Audollent, S., Attié-Bitach, T., Holden, K. R. & Dobyns, W. B. 2008. Mutations in the cilia gene ARL13B lead to the classical form of Joubert syndrome. *The American Journal of Human Genetics,* 83**,** 170-179.

Caron, L., Abraham, N., Pawson, T. & Veillette, A. 1992. Structural requirements for enhancement of T-cell responsiveness by the lymphocyte-specific tyrosine protein kinase p56lck. *Molecular and cellular biology,* 12**,** 2720-2729.

Cevik, S., Sanders, A. A., Van Wijk, E., Boldt, K., Clarke, L., Van Reeuwijk, J., Hori, Y., Horn, N., Hetterschijt, L. & Wdowicz, A. 2013. Active transport and diffusion barriers restrict Joubert Syndrome-associated ARL13B/ARL-13 to an Inv-like ciliary membrane subdomain. *PLoS genetics,* 9**,** e1003977.

Chan, A. C., Irving, B. A., Fraser, J. D. & Weiss, A. 1991. The zeta chain is associated with a tyrosine kinase and upon T-cell antigen receptor stimulation associates with ZAP-70, a 70-kDa tyrosine phosphoprotein. *Proceedings of the National Academy of Sciences,* 88**,** 9166-9170.

Chandra, A., Grecco, H. E., Pisupati, V., Perera, D., Cassidy, L., Skoulidis, F., Ismail, S. A., Hedberg, C., Hanzal-Bayer, M. & Venkitaraman, A. R. 2012. The GDI-like solubilizing factor PDEδ sustains the spatial organization and signalling of Ras family proteins. *Nature cell biology,* 14**,** 148.

Chang, J. T., Palanivel, V. R., Kinjyo, I., Schambach, F., Intlekofer, A. M., Banerjee, A., Longworth, S. A., Vinup, K. E., Mrass, P. & Oliaro, J. 2007. Asymmetric T lymphocyte division in the initiation of adaptive immune responses. *science,* 315**,** 1687-1691.

Chávez, M., Ena, S., Van Sande, J., De Kerchove D'exaerde, A., Schurmans, S. & Schiffmann, S. N. 2015. Modulation of ciliary phosphoinositide content regulates trafficking and sonic hedgehog signaling output. *Developmental cell,* 34**,** 338-350.

Chen, J. K., Taipale, J., Young, K. E., Maiti, T. & Beachy, P. A. 2002. Small molecule modulation of Smoothened activity. *Proceedings of the National Academy of Sciences,* 99**,** 14071-14076.

Chen, L. & Flies, D. B. 2013. Molecular mechanisms of T cell co-stimulation and co-inhibition. *Nature reviews immunology,* 13**,** 227.

Chiang, G. G. & Sefton, B. M. 2001. Specific dephosphorylation of the Lck tyrosine protein kinase at Tyr-394 by the SHP-1 protein-tyrosine phosphatase. *Journal of Biological Chemistry,* 276**,** 23173-23178.

Chih, B., Liu, P., Chinn, Y., Chalouni, C., Komuves, L. G., Hass, P. E., Sandoval, W. & Peterson, A. S. 2012. A ciliopathy complex at the transition zone protects the cilia as a privileged membrane domain. *Nature cell biology,* 14**,** 61.

Collins, R. N. 2003. "Getting it on"—GDI displacement and small GTPase membrane recruitment. *Molecular cell,* 12**,** 1064-1066.

Comrie, W. A. & Burkhardt, J. K. 2016. Action and traction: cytoskeletal control of receptor triggering at the immunological synapse. *Frontiers in immunology,* 7**,** 68.

Constantine, R., Zhang, H., Gerstner, C. D., Frederick, J. M. & Baehr, W. 2012. Uncoordinated (UNC) 119: coordinating the trafficking of myristoylated proteins. *Vision research,* 75**,** 26-32.

D'oro, U. & Ashwell, J. D. 1999. Cutting edge: the CD45 tyrosine phosphatase is an inhibitor of Lck activity in thymocytes. *The Journal of Immunology,* 162**,** 1879-1883.

Davis, D. M., Chiu, I., Fassett, M., Cohen, G. B., Mandelboim, O. & Strominger, J. L. 1999. The human natural killer cell immune synapse. *Proceedings of the National Academy of Sciences,* 96**,** 15062-15067.

Davis, D. M. & Dustin, M. L. 2004. What is the importance of the immunological synapse? *Trends in immunology,* 25**,** 323-327.

Davis, S. J. & Van Der Merwe, P. A. 2006. The kinetic-segregation model: TCR triggering and beyond. *Nature immunology,* 7**,** 803.

De La Roche, M., Ritter, A. T., Angus, K. L., Dinsmore, C., Earnshaw, C. H., Reiter, J. F. & Griffiths, G. M. 2013. Hedgehog signaling controls T cell killing at the immunological synapse. *Science,* 342**,** 1247-1250.

De Robertis, E. 1956. Electron microscope observations on the submicroscopic organization of the retinal rods. *The Journal of Cell Biology,* 2**,** 319-330.

Del Viso, F., Huang, F., Myers, J., Chalfant, M., Zhang, Y., Reza, N., Bewersdorf, J., Lusk, C. P. & Khokha, M. K. 2016. Congenital heart disease genetics uncovers context-dependent organization and function of nucleoporins at cilia. *Developmental cell,* 38**,** 478-492.

Di Stefano, P., Damiano, L., Cabodi, S., Aramu, S., Tordella, L., Praduroux, A., Piva, R., Cavallo, F., Forni, G. & Silengo, L. 2007. p140Cap protein suppresses tumour cell properties, regulating Csk and Src kinase activity. *The EMBO journal,* 26**,** 2843-2855.

Dishinger, J. F., Kee, H. L., Jenkins, P. M., Fan, S., Hurd, T. W., Hammond, J. W., Truong, Y. N.-T., Margolis, B., Martens, J. R. & Verhey, K. J. 2010. Ciliary entry of the kinesin-2 motor KIF17 is regulated by importin-β2 and RanGTP. *Nature cell biology,* 12**,** 703.

Dustin, M. L., Chakraborty, A. K. & Shaw, A. S. 2010. Understanding the structure and function of the immunological synapse. *Cold Spring Harbor perspectives in biology,* 2**,** a002311.

Dustin, M. L. & Groves, J. T. 2012. Receptor signaling clusters in the immune synapse. *Annual review of biophysics,* 41**,** 543-556.

Eck, M. J., Shoelson, S. E. & Harrison, S. C. 1993. Recognition of a high-affinity phosphotyrosyl peptide by the Src homology-2 domain of p56lck. *Nature,* 362**,** 87.

Fansa, E. K., Kösling, S. K., Zent, E., Wittinghofer, A. & Ismail, S. 2016. PDE6δ-mediated sorting of INPP5E into the cilium is determined by cargo-carrier affinity. *Nature communications,* 7**,** 11366.

Farnsworth, C. C., Kawata, M., Yoshida, Y., Takai, Y., Gelb, M. H. & Glomset, J. A. 1991. C terminus of the small GTP-binding protein smg p25A contains two geranylgeranylated cysteine residues and a methyl ester. *Proceedings of the National Academy of Sciences,* 88**,** 6196-6200.

Fesenko, E. E., Kolesnikov, S. S. & Lyubarsky, A. L. 1985. Induction by cyclic GMP of cationic conductance in plasma membrane of retinal rod outer segment. *Nature,* 313**,** 310.

Finetti, F., Paccani, S. R., Riparbelli, M. G., Giacomello, E., Perinetti, G., Pazour, G. J., Rosenbaum, J. L. & Baldari, C. T. 2009. Intraflagellar transport is required for polarized recycling of the TCR/CD3 complex to the immune synapse. *Nature cell biology,* 11**,** 1332.

Fliegauf, M., Benzing, T. & Omran, H. 2007. When cilia go bad: cilia defects and ciliopathies. *Nature reviews Molecular cell biology,* 8**,** 880.

Follit, J. A., Tuft, R. A., Fogarty, K. E. & Pazour, G. J. 2006. The intraflagellar transport protein IFT20 is associated with the Golgi complex and is required for cilia assembly. *Molecular biology of the cell,* 17**,** 3781-3792.

Fujiwara, T., Ritchie, K., Murakoshi, H., Jacobson, K. & Kusumi, A. 2002. Phospholipids undergo hop diffusion in compartmentalized cell membrane. *The Journal of cell biology,* 157**,** 1071-1082.

Fukumoto, Y., Kaibuchi, K., Hori, Y., Fujioka, H., Araki, S., Ueda, T., Kikuchi, A. & Takai, Y. 1990. Molecular cloning and characterization of a novel type of regulatory protein (GDI) for the rho proteins, ras p21-like small GTP-binding proteins. *Oncogene,* 5**,** 1321-1328.

Gambhir, A., Hangyás-Mihályné, G., Zaitseva, I., Cafiso, D. S., Wang, J., Murray, D., Pentyala, S. N., Smith, S. O. & Mclaughlin, S. 2004. Electrostatic sequestration of PIP2 on phospholipid membranes by basic/aromatic regions of proteins. *Biophysical journal,* 86**,** 2188-2207.

Gan, G. N. & Jimeno, A. 2016. Emerging from their burrow: Hedgehog pathway inhibitors for cancer. *Expert opinion on investigational drugs,* 25**,** 1153-1166.

Garcia-Gonzalo, F. R., Phua, S. C., Roberson, E. C., Garcia Iii, G., Abedin, M., Schurmans, S., Inoue, T. & Reiter, J. F. 2015. Phosphoinositides regulate ciliary protein trafficking to modulate hedgehog signaling. *Developmental cell,* 34**,** 400-409.

Garcia-Gonzalo, F. R. & Reiter, J. F. 2017. Open sesame: how transition fibers and the transition zone control ciliary composition. *Cold Spring Harbor perspectives in biology,* 9**,** a028134.

Garcia-Mata, R., Boulter, E. & Burridge, K. 2011. The'invisible hand': regulation of RHO GTPases by RHOGDIs. *Nature reviews Molecular cell biology,* 12**,** 493.

Garcia Iii, G., Raleigh, D. R. & Reiter, J. F. 2018. How the ciliary membrane is organized inside-out to communicate outside-in. *Current Biology,* 28**,** R421-R434.

Garcia, K. C., Degano, M., Stanfield, R. L., Brunmark, A., Jackson, M. R., Peterson, P. A., Teyton, L. & Wilson, I. A. 1996. An αß T cell receptor structure at 2.5 Å and its orientation in the TCR-MHC complex. *Science,* 274**,** 209-219.

Gauen, L., Zhu, Y., Letourneur, F., Hu, Q., Bolen, J. B., Matis, L. A., Klausner, R. D. & Shaw, A. S. 1994. Interactions of p59fyn and ZAP-70 with T-cell receptor activation motifs: defining the nature of a signalling motif. *Molecular and cellular biology,* 14**,** 3729-3741.

Gawden-Bone, C. M., Frazer, G. L., Richard, A. C., Ma, C. Y., Strege, K. & Griffiths, G. M. 2018. PIP5 kinases regulate membrane phosphoinositide and actin composition for targeted granule secretion by cytotoxic lymphocytes. *Immunity,* 49**,** 427-437. e4.

Gomez, T. S., Kumar, K., Medeiros, R. B., Shimizu, Y., Leibson, P. J. & Billadeau, D. D. 2007. Formins regulate the actin-related protein 2/3 complex-independent polarization of the centrosome to the immunological synapse. *Immunity,* 26**,** 177-190.

Gommermann, N., Buehlmayer, P., Von Matt, A., Breitenstein, W., Masuya, K., Pirard, B., Furet, P., Cowan-Jacob, S. W. & Weckbecker, G. 2010. New pyrazolo [1, 5a] pyrimidines as orally active inhibitors of Lck. *Bioorganic & medicinal chemistry letters,* 20**,** 3628-3631.

Gorska, M. M. & Alam, R. 2012. A mutation in the human Uncoordinated 119 gene impairs TCR signaling and is associated with CD4 lymphopenia. *Blood,* 119**,** 1399-1406.

Gorska, M. M., Liang, Q., Karim, Z. & Alam, R. 2009. Uncoordinated 119 protein controls trafficking of Lck via the Rab11 endosome and is critical for immunological synapse formation. *The journal of immunology,* 183**,** 1675-1684.

Götschel, F., Berg, D., Gruber, W., Bender, C., Eberl, M., Friedel, M., Sonntag, J., Rüngeler, E., Hache, H. & Wierling, C. 2013. Synergism between Hedgehog-GLI and EGFR signaling in Hedgehog-responsive human medulloblastoma cells induces downregulation of canonical Hedgehog-target genes and stabilized expression of GLI1. *PloS one,* 8**,** e65403.

Gotthardt, K., Lokaj, M., Koerner, C., Falk, N., Gießl, A. & Wittinghofer, A. 2015. A G-protein activation cascade from Arl13B to Arl3 and implications for ciliary targeting of lipidated proteins. *Elife,* 4**,** e11859.

Grakoui, A., Bromley, S. K., Sumen, C., Davis, M. M., Shaw, A. S., Allen, P. M. & Dustin, M. L. 1999. The immunological synapse: a molecular machine controlling T cell activation. *Science,* 285**,** 221-227.

Griffiths, G. M., Tsun, A. & Stinchcombe, J. C. 2010. The immunological synapse: a focal point for endocytosis and exocytosis. *The Journal of cell biology,* 189**,** 399-406.

Haeseleer, F., Sokal, I., Li, N., Pettenati, M., Rao, N., Bronson, D., Wechter, R., Baehr, W. & Palczewski, K. 1999. Molecular characterization of a third member of the guanylyl cyclase-activating protein subfamily. *Journal of Biological Chemistry,* 274**,** 6526-6535.

Hamada, H. 2016. Roles of motile and immotile cilia in left-right symmetry breaking. *Etiology and morphogenesis of congenital heart disease.* Springer, Tokyo.

Han, Y., Eppinger, E., Schuster, I. G., Weigand, L. U., Liang, X., Kremmer, E., Peschel, C. & Krackhardt, A. M. 2009. Formin-like 1 (FMNL1) is regulated by N-terminal myristoylation and induces polarized membrane blebbing. *Journal of Biological Chemistry,* 284**,** 33409-33417.

Hancock, J. F., Magee, A. I., Childs, J. E. & Marshall, C. J. 1989. All ras proteins are polyisoprenylated but only some are palmitoylated. *Cell,* 57**,** 1167-1177.

Hancock, J. F., Paterson, H. & Marshall, C. J. 1990. A polybasic domain or palmitoylation is required in addition to the CAAX motif to localize p21ras to the plasma membrane. *Cell,* 63**,** 133-139.

Hanna, A. & Shevde, L. A. 2016. Hedgehog signaling: modulation of cancer properies and tumor mircroenvironment. *Molecular cancer,* 15**,** 24.

Harris, J. A., Liu, Y., Yang, P., Kner, P. & Lechtreck, K. F. 2016. Single-particle imaging reveals intraflagellar transport–independent transport and accumulation of EB1 in Chlamydomonas flagella. *Molecular biology of the cell,* 27**,** 295-307.

Hentschel, A., Zahedi, R. P. & Ahrends, R. 2016. Protein lipid modifications—More than just a greasy ballast. *Proteomics,* 16**,** 759-782.

Hermida-Matsumoto, L. & Resh, M. D. 1999. Human immunodeficiency virus type 1 protease triggers a myristoyl switch that modulates membrane binding of Pr55 gag and p17MA. *Journal of virology,* 73**,** 1902-1908.

Hildebrandt, F., Benzing, T. & Katsanis, N. 2011. Ciliopathies. *New England Journal of Medicine,* 364**,** 1533-1543.

Hillig, R. C., Hanzal-Bayer, M., Linari, M., Becker, J., Wittinghofer, A. & Renault, L. 2000. Structural and biochemical properties show ARL3-GDP as a distinct GTP binding protein. *Structure,* 8**,** 1239-1245.

Hoffman, G. R., Nassar, N. & Cerione, R. A. 2000. Structure of the Rho family GTP-binding protein Cdc42 in complex with the multifunctional regulator RhoGDI. *Cell,* 100**,** 345-356.

Holdorf, A. D., Lee, K.-H., Burack, W. R., Allen, P. M. & Shaw, A. S. 2002. Regulation of Lck activity by CD4 and CD28 in the immunological synapse. *Nature immunology,* 3**,** 259.

Hori, Y., Kobayashi, T., Kikko, Y., Kontani, K. & Katada, T. 2008. Domain architecture of the atypical Arf-family GTPase Arl13b involved in cilia formation. *Biochemical and biophysical research communications,* 373**,** 119-124.

Hu, Q., Milenkovic, L., Jin, H., Scott, M. P., Nachury, M. V., Spiliotis, E. T. & Nelson, W. J. 2010. A septin diffusion barrier at the base of the primary cilium maintains ciliary membrane protein distribution. *Science,* 329**,** 436-439.

Hua, K. & Ferland, R. J. 2018. Primary cilia proteins: ciliary and extraciliary sites and functions. *Cellular and molecular life sciences,* 75**,** 1521-1540.

Huangfu, D., Liu, A., Rakeman, A. S., Murcia, N. S., Niswander, L. & Anderson, K. V. 2003. Hedgehog signalling in the mouse requires intraflagellar transport proteins. *Nature,* 426**,** 83.

Hunnicutt, G. R., Kosfiszer, M. G. & Snell, W. J. 1990. Cell body and flagellar agglutinins in Chlamydomonas reinhardtii: the cell body plasma membrane is a reservoir for agglutinins

whose migration to the flagella is regulated by a functional barrier. *The Journal of Cell Biology,* 111**,** 1605-1616.

Huppa, J. B. & Davis, M. M. 2003. T-cell-antigen recognition and the immunological synapse. *Nature Reviews Immunology,* 3**,** 973.

Huse, M. 2012. Microtubule-organizing center polarity and the immunological synapse: protein kinase C and beyond. *Frontiers in immunology,* 3**,** 235.

Irving, B. A. & Weiss, A. 1991. The cytoplasmic domain of the T cell receptor ζ chain is sufficient to couple to receptor-associated signal transduction pathways. *Cell,* 64**,** 891-901.

Ismail, S. 2017. A GDI/GDF-like system for sorting and shuttling ciliary proteins. *Small GTPases,* 8**,** 208-211.

Ismail, S. A., Chen, Y.-X., Rusinova, A., Chandra, A., Bierbaum, M., Gremer, L., Triola, G., Waldmann, H., Bastiaens, P. I. & Wittinghofer, A. 2011. Arl2-GTP and Arl3-GTP regulate a GDI-like transport system for farnesylated cargo. *Nature chemical biology,* 7**,** 942.

Ismail, S. A., Chen, Y. X., Miertzschke, M., Vetter, I. R., Koerner, C. & Wittinghofer, A. 2012. Structural basis for Arl3-specific release of myristoylated ciliary cargo from UNC119. *The EMBO journal,* 31**,** 4085-4094.

Jaiswal, M., Fansa, E. K., Kösling, S. K., Mejuch, T., Waldmann, H. & Wittinghofer, A. 2016. Novel biochemical and structural insights into the interaction of myristoylated cargo with Unc119 protein and their release by Arl2/3. *Journal of Biological Chemistry,* 291**,** 20766-20778.

Jardetzky, T. S., Brown, J. H., Gorga, J. C., Stern, L. J., Urban, R. G., Chi, Y.-I., Stauffacher, C., Strominger, J. L. & Wiley, D. C. 1994. Three-dimensional structure of a human class II histocompatibility molecule complexed with superantigen. *Nature,* 368**,** 711.

Johnson, K. G., Bromley, S. K., Dustin, M. L. & Thomas, M. L. 2000. A supramolecular basis for CD45 tyrosine phosphatase regulation in sustained T cell activation. *Proceedings of the National Academy of Sciences,* 97**,** 10138-10143.

Judokusumo, E., Tabdanov, E., Kumari, S., Dustin, M. L. & Kam, L. C. 2012. Mechanosensing in T lymphocyte activation. *Biophysical journal,* 102**,** L5-L7.

Kappler, J., Kotzin, B., Herron, L., Gelfand, E. W., Bigler, R. D., Boylston, A., Carrel, S., Posnett, D. N., Choi, Y. & Marrack, P. 1989. V beta-specific stimulation of human T cells by staphylococcal toxins. *Science,* 244**,** 811-813.

Kawabuchi, M., Satomi, Y., Takao, T., Shimonishi, Y., Nada, S., Nagai, K., Tarakhovsky, A. & Okada, M. 2000. Transmembrane phosphoprotein Cbp regulates the activities of Src-family tyrosine kinases. *Nature,* 404**,** 999.

Kee, H. L., Dishinger, J. F., Blasius, T. L., Liu, C.-J., Margolis, B. & Verhey, K. J. 2012. A size-exclusion permeability barrier and nucleoporins characterize a ciliary pore complex that regulates transport into cilia. *Nature cell biology,* 14**,** 431.

Kim, J., Shishido, T., Jiang, X., Aderem, A. & Mclaughlin, S. 1994. Phosphorylation, high ionic strength, and calmodulin reverse the binding of MARCKS to phospholipid vesicles. *Journal of Biological Chemistry,* 269**,** 28214-28219.

Kim, P. W., Sun, Z.-Y. J., Blacklow, S. C., Wagner, G. & Eck, M. J. 2003. A zinc clasp structure tethers Lck to T cell coreceptors CD4 and CD8. *Science,* 301**,** 1725-1728.

Kobayashi, A., Kubota, S., Mori, N., Mclaren, M. J. & Inana, G. 2003. Photoreceptor synaptic protein HRG4 (UNC119) interacts with ARL2 via a putative conserved domain. *FEBS letters,* 534**,** 26-32.

Kobayashi, T. & Dynlacht, B. D. 2011. Regulating the transition from centriole to basal body. *The Journal of cell biology,* 193**,** 435-444.

Kozminski, K. G., Johnson, K. A., Forscher, P. & Rosenbaum, J. L. 1993. A motility in the eukaryotic flagellum unrelated to flagellar beating. *Proceedings of the National Academy of Sciences,* 90**,** 5519-5523.

Krummel, M. F., Sjaastad, M. D., Wülfing, C. & Davis, M. M. 2000. Differential clustering of CD4 and CD3ζ during T cell recognition. *Science,* 289**,** 1349-1352.

Kühn, S., Erdmann, C., Kage, F., Block, J., Schwenkmezger, L., Steffen, A., Rottner, K. & Geyer, M. 2015. The structure of FMNL2–Cdc42 yields insights into the mechanism of lamellipodia and filopodia formation. *Nature communications,* 6**,** 7088.

Kumari, S., Curado, S., Mayya, V. & Dustin, M. L. 2014. T cell antigen receptor activation and actin cytoskeleton remodeling. *Biochimica Et Biophysica Acta (BBA)-Biomembranes,* 1838**,** 546-556.

Kusumi, A., Nakada, C., Ritchie, K., Murase, K., Suzuki, K., Murakoshi, H., Kasai, R. S., Kondo, J. & Fujiwara, T. 2005. Paradigm shift of the plasma membrane concept from the two-dimensional continuum fluid to the partitioned fluid: high-speed single-molecule tracking of membrane molecules. *Annu. Rev. Biophys. Biomol. Struct.,* 34**,** 351-378.

Lauth, M., Bergström, Å., Shimokawa, T. & Toftgård, R. 2007. Inhibition of GLI-mediated transcription and tumor cell growth by small-molecule antagonists. *Proceedings of the National Academy of Sciences,* 104**,** 8455-8460.

Lechtreck, K. F. 2015. IFT–cargo interactions and protein transport in cilia. *Trends in biochemical sciences,* 40**,** 765-778.

Lee, K.-H., Dinner, A. R., Tu, C., Campi, G., Raychaudhuri, S., Varma, R., Sims, T. N., Burack, W. R., Wu, H. & Wang, J. 2003. The immunological synapse balances T cell receptor signaling and degradation. *science,* 302**,** 1218-1222.

Lee, K.-H., Holdorf, A. D., Dustin, M. L., Chan, A. C., Allen, P. M. & Shaw, A. S. 2002. T cell receptor signaling precedes immunological synapse formation. *Science,* 295**,** 1539-1542.

Leonard, D., Hart, M. J., Platko, J. V., Eva, A., Henzel, W., Evans, T. & Cerione, R. A. 1992. The identification and characterization of a GDP-dissociation inhibitor (GDI) for the CDC42Hs protein. *Journal of Biological Chemistry,* 267**,** 22860-22868.

Ley, S. C., Marsh, M., Bebbington, C. R., Proudfoot, K. & Jordan, P. 1994. Distinct intracellular localization of Lck and Fyn protein tyrosine kinases in human T lymphocytes. *The Journal of cell biology,* 125**,** 639-649.

Lin, Y.-C., Niewiadomski, P., Lin, B., Nakamura, H., Phua, S. C., Jiao, J., Levchenko, A., Inoue, T., Rohatgi, R. & Inoue, T. 2013. Chemically inducible diffusion trap at cilia reveals molecular sieve–like barrier. *Nature chemical biology,* 9**,** 437.

Linari, M., Hanzal-Bayer, M. & Becker, J. 1999. The delta subunit of rod specific cyclic GMP phosphodiesterase, PDE δ, interacts with the Arf-like protein Arl3 in a GTP specific manner. *FEBS letters,* 458**,** 55-59.

Liu, B., Chen, W., Evavold, B. D. & Zhu, C. 2014. Accumulation of dynamic catch bonds between TCR and agonist peptide-MHC triggers T cell signaling. *Cell,* 157**,** 357-368.

Liu, H., Kiseleva, A. A. & Golemis, E. A. 2018. Ciliary signalling in cancer. *Nature Reviews Cancer,* 18**,** 511.

Lopez-Cabrera, M., Santis, A., Fernandez-Ruiz, E., Blacher, R., Esch, F., Sanchez-Mateos, P. & Sanchez-Madrid, F. 1993. Molecular cloning, expression, and chromosomal localization of the human earliest lymphocyte activation antigen AIM/CD69, a new member of the C-

type animal lectin superfamily of signal-transmitting receptors. *Journal of Experimental Medicine,* 178**,** 537-547.

Low, M. G., Ferguson, M. A., Futerman, A. H. & Silman, I. 1986. Covalently attached phosphatidylinositol as a hydrophobic anchor for membrane proteins. *Trends in Biochemical Sciences,* 11**,** 212-215.

Malicki, J. & Avidor-Reiss, T. 2014. From the cytoplasm into the cilium: bon voyage. *Organogenesis,* 10**,** 138-157.

Martin, G. S. 2001. The hunting of the Src. *Nature reviews Molecular cell biology,* 2**,** 467.

Mcneill, L., Salmond, R. J., Cooper, J. C., Carret, C. K., Cassady-Cain, R. L., Roche-Molina, M., Tandon, P., Holmes, N. & Alexander, D. R. 2007. The differential regulation of Lck kinase phosphorylation sites by CD45 is critical for T cell receptor signaling responses. *Immunity,* 27**,** 425-437.

Mejuch, T., Garivet, G., Hofer, W., Kaiser, N., Fansa, E. K., Ehrt, C., Koch, O., Baumann, M., Ziegler, S. & Wittinghofer, A. 2017. Small-Molecule Inhibition of the UNC119–Cargo Interaction. *Angewandte Chemie International Edition,* 56**,** 6181-6186.

Milenkovic, L., Scott, M. P. & Rohatgi, R. 2009. Lateral transport of Smoothened from the plasma membrane to the membrane of the cilium. *The Journal of cell biology,* 187**,** 365-374.

Mitxitorena, I., Saavedra, E. & Barcia, C. 2015. Kupfer-type immunological synapses in vivo: Raison D'être of SMAC. *Immunology and cell biology,* 93**,** 51-56.

Molla-Herman, A., Ghossoub, R., Blisnick, T., Meunier, A., Serres, C., Silbermann, F., Emmerson, C., Romeo, K., Bourdoncle, P. & Schmitt, A. 2010. The ciliary pocket: an endocytic membrane domain at the base of primary and motile cilia. *J Cell Sci,* 123**,** 1785-1795.

Monks, C. R., Freiberg, B. A., Kupfer, H., Sciaky, N. & Kupfer, A. 1998. Three-dimensional segregation of supramolecular activation clusters in T cells. *Nature,* 395**,** 82.

Mukhopadhyay, S., Wen, X., Chih, B., Nelson, C. D., Lane, W. S., Scales, S. J. & Jackson, P. K. 2010. TULP3 bridges the IFT-A complex and membrane phosphoinositides to promote trafficking of G protein-coupled receptors into primary cilia. *Genes & development,* 24**,** 2180-2193.

Murakoshi, H., Iino, R., Kobayashi, T., Fujiwara, T., Ohshima, C., Yoshimura, A. & Kusumi, A. 2004. Single-molecule imaging analysis of Ras activation in living cells. *Proceedings of the National Academy of Sciences,* 101**,** 7317-7322.

Mustelin, T., Coggeshall, K. M. & Altman, A. 1989. Rapid activation of the T-cell tyrosine protein kinase pp56lck by the CD45 phosphotyrosine phosphatase. *Proceedings of the National Academy of Sciences,* 86**,** 6302-6306.

Nachury, M. V., Loktev, A. V., Zhang, Q., Westlake, C. J., Peränen, J., Merdes, A., Slusarski, D. C., Scheller, R. H., Bazan, J. F. & Sheffield, V. C. 2007. A core complex of BBS proteins cooperates with the GTPase Rab8 to promote ciliary membrane biogenesis. *Cell,* 129**,** 1201-1213.

Nachury, M. V. & Mick, D. U. 2019. Establishing and regulating the composition of cilia for signal transduction. *Nature Reviews Molecular Cell Biology***,** 1.

Nachury, M. V., Seeley, E. S. & Jin, H. 2010. Trafficking to the ciliary membrane: how to get across the periciliary diffusion barrier? *Annual review of cell and developmental biology,* 26**,** 59-87.

Nada, S., Okada, M., Macauley, A., Cooper, J. A. & Nakagawa, H. 1991. Cloning of a complementary DNA for a protein-tyrosine kinase that specifically phosphorylates a negative regulatory site of p60c-src. *Nature,* 351**,** 69-72.

Najafi, M., Maza, N. A. & Calvert, P. D. 2012. Steric volume exclusion sets soluble protein concentrations in photoreceptor sensory cilia. *Proceedings of the National Academy of Sciences,* 109**,** 203-208.

Nancy, V., Callebaut, I., El Marjou, A. & De Gunzburg, J. 2002. The δ subunit of retinal rod cGMP phosphodiesterase regulates the membrane association of Ras and Rap GTPases. *Journal of Biological Chemistry,* 277**,** 15076-15084.

Niewiadomski, P. & Rohatgi, R. 2015. Measuring expression levels of endogenous Gli genes by immunoblotting and Real-Time PCR. *Hedgehog Signaling Protocols.* Springer.

Nika, K., Soldani, C., Salek, M., Paster, W., Gray, A., Etzensperger, R., Fugger, L., Polzella, P., Cerundolo, V. & Dushek, O. 2010. Constitutively active Lck kinase in T cells drives antigen receptor signal transduction. *Immunity,* 32**,** 766-777.

Norcross, M. A synaptic basis for T-lymphocyte activation. Annales de l'Institut Pasteur/Immunologie, 1984. Elsevier, 113-134.

Nüsslein-Volhard, C. & Wieschaus, E. 1980. Mutations affecting segment number and polarity in Drosophila. *Nature,* 287**,** 795.

Onnis, A. & Baldari, C. T. 2019. Orchestration of immunological synapse assembly by vesicular trafficking. *Frontiers in Cell and Developmental Biology,* 7**,** 110.

Osterhout, J. L., Waheed, A. A., Hiol, A., Ward, R. J., Davey, P. C., Nini, L., Wang, J., Milligan, G., Jones, T. L. & Druey, K. M. 2003. Palmitoylation Regulates Regulator of G-protein Signaling (RGS) 16 Function II. PALMITOYLATION OF A CYSTEINE RESIDUE IN THE RGS BOX IS CRITICAL FOR RGS16 GTPase ACCELERATING ACTIVITY AND REGULATION OF Gi-COUPLED SIGNALING. *Journal of Biological Chemistry,* 278**,** 19309-19316.

Padovani, D., Zeghouf, M., Traverso, J. A., Giglione, C. & Cherfils, J. 2013. High yield production of myristoylated Arf6 small GTPase by recombinant N-myristoyl transferase. *Small GTPases,* 4**,** 3-8.

Paige, L., Nadler, M., Harrison, M. L., Cassady, J. M. & Geahlen, R. 1993. Reversible palmitoylation of the protein-tyrosine kinase p56lck. *Journal of Biological Chemistry,* 268**,** 8669-8674.

Papermaster, D. S., Schneider, B. & Besharse, J. 1985. Vesicular transport of newly synthesized opsin from the Golgi apparatus toward the rod outer segment. Ultrastructural immunocytochemical and autoradiographic evidence in Xenopus retinas. *Investigative ophthalmology & visual science,* 26**,** 1386-1404.

Papke, B., Murarka, S., Vogel, H. A., Martín-Gago, P., Kovacevic, M., Truxius, D. C., Fansa, E. K., Ismail, S., Zimmermann, G. & Heinelt, K. 2016. Identification of pyrazolopyridazinones as PDEδ inhibitors. *Nature communications,* 7**,** 11360.

Patino-Lopez, G., Dong, X., Ben-Aissa, K., Bernot, K. M., Itoh, T., Fukuda, M., Kruhlak, M. J., Samelson, L. E. & Shaw, S. 2008. Rab35 and its GAP EPI64C in T cells regulate receptor recycling and immunological synapse formation. *Journal of Biological Chemistry,* 283**,** 18323-18330.

Patwardhan, P. & Resh, M. D. 2010. Myristoylation and membrane binding regulate c-Src stability and kinase activity. *Molecular and cellular biology,* 30**,** 4094-4107.

Paul, W. E. & Seder, R. A. 1994. Lymphocyte responses and cytokines. *cell,* 76**,** 241-251.

Pazour, G. J., Dickert, B. L., Vucica, Y., Seeley, E. S., Rosenbaum, J. L., Witman, G. B. & Cole, D. G. 2000. Chlamydomonas IFT88 and its mouse homologue, polycystic kidney disease gene tg737, are required for assembly of cilia and flagella. *The Journal of cell biology,* 151**,** 709-718.

Pazour, G. J. & Rosenbaum, J. L. 2002. Intraflagellar transport and cilia-dependent diseases. *Trends in cell biology,* 12**,** 551-555.

Peitzsch, R. M. & Mclaughlin, S. 1993. Binding of acylated peptides and fatty acids to phospholipid vesicles: pertinence to myristoylated proteins. *Biochemistry,* 32**,** 10436-10443.

Pepinsky, R. B., Zeng, C., Wen, D., Rayhorn, P., Baker, D. P., Williams, K. P., Bixler, S. A., Ambrose, C. M., Garber, E. A. & Miatkowski, K. 1998. Identification of a palmitic acid-modified form of human Sonic hedgehog. *Journal of Biological Chemistry,* 273**,** 14037-14045.

Pfisterer, K., Forster, F., Paster, W., Supper, V., Ohradanova-Repic, A., Eckerstorfer, P., Zwirzitz, A., Donner, C., Boulegue, C. & Schiller, H. B. 2014. The late endosomal transporter CD222 directs the spatial distribution and activity of Lck. *The Journal of Immunology,* 193**,** 2718-2732.

Philipsen, L., Reddycherla, A. V., Hartig, R., Gumz, J., Kästle, M., Kritikos, A., Poltorak, M. P., Prokazov, Y., Turbin, E. & Weber, A. 2017. De novo phosphorylation and conformational opening of the tyrosine kinase Lck act in concert to initiate T cell receptor signaling. *Sci. Signal.,* 10**,** eaaf4736.

Phua, S. C., Nihongaki, Y. & Inoue, T. 2018. Autonomy declared by primary cilia through compartmentalization of membrane phosphoinositides. *Current opinion in cell biology,* 50**,** 72-78.

Plotnikova, O. V., Seo, S., Cottle, D. L., Conduit, S., Hakim, S., Dyson, J. M., Mitchell, C. A. & Smyth, I. M. 2015. INPP5E interacts with AURKA, linking phosphoinositide signaling to primary cilium stability. *J Cell Sci,* 128**,** 364-372.

Porter, J. A., Young, K. E. & Beachy, P. A. 1996. Cholesterol modification of hedgehog signaling proteins in animal development. *Science,* 274**,** 255-259.

Prive, G. G., Milburn, M. V., Tong, L., De Vos, A. M., Yamaizumi, Z., Nishimura, S. & Kim, S.-H. 1992. X-ray crystal structures of transforming p21 ras mutants suggest a transition-state stabilization mechanism for GTP hydrolysis. *Proceedings of the National academy of Sciences,* 89**,** 3649-3653.

Reiter, J. F. & Leroux, M. R. 2017. Genes and molecular pathways underpinning ciliopathies. *Nature Reviews Molecular Cell Biology,* 18**,** 533.

Resh, M. D. 2013. Covalent lipid modifications of proteins. *Current Biology,* 23**,** R431-R435.

Ritter, A. T., Asano, Y., Stinchcombe, J. C., Dieckmann, N., Chen, B.-C., Gawden-Bone, C., Van Engelenburg, S., Legant, W., Gao, L. & Davidson, M. W. 2015. Actin depletion initiates events leading to granule secretion at the immunological synapse. *Immunity,* 42**,** 864-876.

Ritter, A. T., Kapnick, S. M., Murugesan, S., Schwartzberg, P. L., Griffiths, G. M. & Lippincott-Schwartz, J. 2017. Cortical actin recovery at the immunological synapse leads to termination of lytic granule secretion in cytotoxic T lymphocytes. *Proceedings of the National Academy of Sciences,* 114**,** E6585-E6594.

Robert, A., Margall-Ducos, G., Guidotti, J.-E., Brégerie, O., Celati, C., Bréchot, C. & Desdouets, C. 2007. The intraflagellar transport component IFT88/polaris is a centrosomal protein regulating G1-S transition in non-ciliated cells. *J Cell Sci,* 120**,** 628-637.

Roh, K.-H., Lillemeier, B. F., Wang, F. & Davis, M. M. 2015. The coreceptor CD4 is expressed in distinct nanoclusters and does not colocalize with T-cell receptor and active protein tyrosine kinase p56lck. *Proceedings of the National Academy of Sciences,* 112**,** E1604-E1613.

Rossy, J., Williamson, D. J. & Gaus, K. 2012. How does the kinase Lck phosphorylate the T cell receptor? Spatial organization as a regulatory mechanism. *Frontiers in immunology,* 3**,** 167.

Santagata, S., Boggon, T. J., Baird, C. L., Gomez, C. A., Zhao, J., Shan, W. S., Myszka, D. G. & Shapiro, L. 2001. G-protein signaling through tubby proteins. *Science,* 292**,** 2041-2050.

Sasaki, T., Kato, M. & Takai, Y. 1993. Consequences of weak interaction of rho GDI with the GTP-bound forms of rho p21 and rac p21. *Journal of Biological Chemistry,* 268**,** 23959-23963.

Sasaki, T., Kikuchi, A., Araki, S., Hata, Y., Isomura, M., Kuroda, S. & Takai, Y. 1990. Purification and characterization from bovine brain cytosol of a protein that inhibits the dissociation of GDP from and the subsequent binding of GTP to smg p25A, a ras p21-like GTP-binding protein. *Journal of Biological Chemistry,* 265**,** 2333-2337.

Satir, P. 2017. CILIA: before and after. *Cilia,* 6**,** 1.

Satir, P., Pedersen, L. B. & Christensen, S. T. 2010. The primary cilium at a glance. *J Cell Sci,* 123**,** 499-503.

Schoebel, S., Oesterlin, L. K., Blankenfeldt, W., Goody, R. S. & Itzen, A. 2009. RabGDI displacement by DrrA from Legionella is a consequence of its guanine nucleotide exchange activity. *Molecular cell,* 36**,** 1060-1072.

Scholer, A., Hugues, S., Boissonnas, A., Fetler, L. & Amigorena, S. 2008. Intercellular adhesion molecule-1-dependent stable interactions between T cells and dendritic cells determine CD8+ T cell memory. *Immunity,* 28**,** 258-270.

Seeley, E. S. & Nachury, M. V. 2010. The perennial organelle: assembly and disassembly of the primary cilium. *J Cell Sci,* 123**,** 511-518.

Shahinian, S. & Silvius, J. R. 1995. Doubly-lipid-modified protein sequence motifs exhibit long-lived anchorage to lipid bilayer membranes. *Biochemistry,* 34**,** 3813-3822.

Shaw, A. S. & Dustin, M. L. 1997. Making the T cell receptor go the distance: a topological view of T cell activation. *Immunity,* 6**,** 361-369.

Sigrist, C. J., De Castro, E., Cerutti, L., Cuche, B. A., Hulo, N., Bridge, A., Bougueleret, L. & Xenarios, I. 2012. New and continuing developments at PROSITE. *Nucleic acids research,* 41**,** D344-D347.

Singer, S. J. & Nicolson, G. L. 1972. The fluid mosaic model of the structure of cell membranes. *Science,* 175**,** 720-731.

Singla, V. & Reiter, J. F. 2006. The primary cilium as the cell's antenna: signaling at a sensory organelle. *science,* 313**,** 629-633.

Somersalo, K., Anikeeva, N., Sims, T. N., Thomas, V. K., Strong, R. K., Spies, T., Lebedeva, T., Sykulev, Y. & Dustin, M. L. 2004. Cytotoxic T lymphocytes form an antigen-independent ring junction. *The Journal of clinical investigation,* 113**,** 49-57.

Sorokin, S. 1962. Centrioles and the formation of rudimentary cilia by fibroblasts and smooth muscle cells. *The Journal of cell biology,* 15**,** 363-377.

Sorokin, S. 1968. Reconstructions of centriole formation and ciliogenesis in mammalian lungs. *Journal of cell science,* 3**,** 207-230.

Stephen, L. A., Elmaghloob, Y. & Ismail, S. 2017. Maintaining protein composition in cilia. *Biological chemistry,* 399**,** 1-11.

Stephen, L. A., Elmaghloob, Y., Mcilwraith, M. J., Yelland, T., Sanchez, P. C., Roda-Navarro, P. & Ismail, S. 2018. The ciliary machinery is repurposed for T cell immune synapse trafficking of LCK. *Developmental cell,* 47**,** 122-132. e4.

Stinchcombe, J. C., Bossi, G., Booth, S. & Griffiths, G. M. 2001. The immunological synapse of CTL contains a secretory domain and membrane bridges. *Immunity,* 15**,** 751-761.

Stinchcombe, J. C., Majorovits, E., Bossi, G., Fuller, S. & Griffiths, G. M. 2006. Centrosome polarization delivers secretory granules to the immunological synapse. *Nature,* 443**,** 462.

Straus, D. B. & Weiss, A. 1992. Genetic evidence for the involvement of the lck tyrosine kinase in signal transduction through the T cell antigen receptor. *Cell,* 70**,** 585-593.

Takao, D. & Verhey, K. J. 2016. Gated entry into the ciliary compartment. *Cellular and molecular life sciences,* 73**,** 119-127.

Thelen, M., Rosen, A., Nairn, A. C. & Aderem, A. 1991. Regulation by phosphorylation of reversible association of a myristoylated protein kinase C substrate with the plasma membrane. *Nature,* 351**,** 320.

Thomas, S., Wright, K. J., Corre, S. L., Micalizzi, A., Romani, M., Abhyankar, A., Saada, J., Perrault, I., Amiel, J. & Litzler, J. 2014. A Homozygous PDE 6 D Mutation in J oubert Syndrome Impairs Targeting of F arnesylated INPP 5 E Protein to the Primary Cilium. *Human mutation,* 35**,** 137-146.

Trimble, W. S. & Grinstein, S. 2015. Barriers to the free diffusion of proteins and lipids in the plasma membrane. *J Cell Biol,* 208**,** 259-271.

Turner, J. M., Brodsky, M. H., Irving, B. A., Levin, S. D., Perlmutter, R. M. & Littman, D. R. 1990. Interaction of the unique N-terminal region of tyrosine kinase p56lck with cytoplasmic domains of CD4 and CD8 is mediated by cysteine motifs. *Cell,* 60**,** 755-765.

Udenwobele, D. I., Su, R.-C., Good, S. V., Ball, T. B., Varma Shrivastav, S. & Shrivastav, A. 2017. Myristoylation: An important protein modification in the immune response. *Frontiers in immunology,* 8**,** 751.

Van't Hof, W. & Resh, M. D. 1997. Rapid plasma membrane anchoring of newly synthesized p59 fyn: selective requirement for NH2-terminal myristoylation and palmitoylation at cysteine-3. *The Journal of cell biology,* 136**,** 1023-1035.

Van Der Merwe, P. A., Davis, S. J., Shaw, A. S. & Dustin, M. L. Cytoskeletal polarization and redistribution of cell-surface molecules during T cell antigen recognition. Seminars in immunology, 2000. Elsevier, 5-21.

Veillette, A., Bookman, M. A., Horak, E. M. & Bolen, J. B. 1988. The CD4 and CD8 T cell surface antigens are associated with the internal membrane tyrosine-protein kinase p56lck. *Cell,* 55**,** 301-308.

Veltel, S., Gasper, R., Eisenacher, E. & Wittinghofer, A. 2008. The retinitis pigmentosa 2 gene product is a GTPase-activating protein for Arf-like 3. *Nature structural & molecular biology,* 15**,** 373.

Vieira, O. V., Gaus, K., Verkade, P., Fullekrug, J., Vaz, W. L. & Simons, K. 2006. FAPP2, cilium formation, and compartmentalization of the apical membrane in polarized Madin–Darby canine kidney (MDCK) cells. *Proceedings of the National Academy of Sciences,* 103**,** 18556-18561.

Vorobjev, I. & Yus, C. 1982. Centrioles in the cell cycle. I. Epithelial cells. *The Journal of cell biology,* 93**,** 938-949.

Wan, R., Wu, J., Ouyang, M., Lei, L., Wei, J., Peng, Q., Harrison, R., Wu, Y., Cheng, B. & Li, K. 2019. Biophysical basis underlying dynamic Lck activation visualized by ZapLck FRET biosensor. *Science advances,* 5**,** eaau2001.

Wardenburg, J. B., Fu, C., Jackman, J. K., Flotow, H., Wilkinson, S. E., Williams, D. H., Johnson, R., Kong, G., Chan, A. C. & Findell, P. R. 1996. Phosphorylation of SLP-76 by the ZAP-70 protein-tyrosine kinase is required for T-cell receptor function. *Journal of Biological Chemistry,* 271**,** 19641-19644.

Weil, R., Fournel, M. & Veillette, A. 1995. Regulation of Zap-70 by Src family tyrosine protein kinases in an antigen-specific T-cell line. *Journal of Biological Chemistry,* 270**,** 2791-2799.

Weiss, A. 1993. T cell antigen receptor signal transduction: a tale of tails and cytoplasmic protein-tyrosine kinases. *Cell,* 73**,** 209-212.

Wiedemann, A., Müller, S., Favier, B., Penna, D., Guiraud, M., Delmas, C., Champagne, E. & Valitutti, S. 2005. T-cell activation is accompanied by an ubiquitination process occurring at the immunological synapse. *Immunology letters,* 98**,** 57-61.

Wingfield, J. L., Lechtreck, K.-F. & Lorentzen, E. 2018. Trafficking of ciliary membrane proteins by the intraflagellar transport/BBSome machinery. *Essays in biochemistry,* 62**,** 753-763.

Wright, K. J., Baye, L. M., Olivier-Mason, A., Mukhopadhyay, S., Sang, L., Kwong, M., Wang, W., Pretorius, P. R., Sheffield, V. C. & Sengupta, P. 2011a. An ARL3–UNC119–RP2 GTPase cycle targets myristoylated NPHP3 to the primary cilium. *Genes & development,* 25**,** 2347-2360.

Wright, K. J., Baye, L. M., Olivier-Mason, A., Mukhopadhyay, S., Sang, L., Kwong, M., Wang, W., Pretorius, P. R., Sheffield, V. C., Sengupta, P., Slusarski, D. C. & Jackson, P. K. 2011b. An ARL3–UNC119–RP2 GTPase cycle targets myristoylated NPHP3 to the primary cilium. *Genes & development,* 25**,** 2347-2360.

Wu, Y.-W., Oesterlin, L. K., Tan, K.-T., Waldmann, H., Alexandrov, K. & Goody, R. S. 2010. Membrane targeting mechanism of Rab GTPases elucidated by semisynthetic protein probes. *Nature chemical biology,* 6**,** 534.

Xu, W., Doshi, A., Lei, M., Eck, M. J. & Harrison, S. C. 1999. Crystal Structures of c-Src Reveal Features of Its Autoinhibitory Mechanism. *Molecular Cell,* 3**,** 629-638.

Xu, W., Harrison, S. C. & Eck, M. J. 1997. Three-dimensional structure of the tyrosine kinase c-Src. *Nature,* 385**,** 595-602.

Yamaguchi, H. & Hendrickson, W. A. 1996. Structural basis for activation of human lymphocyte kinase Lck upon tyrosine phosphorylation. *Nature,* 384**,** 484.

Yang, J., Sanderson, N., Wawrowsky, K., Puntel, M., Castro, M. & Lowenstein, P. 2010. Kupfer-type immunological synapse characteristics do not predict anti-brain tumor cytolytic T-cell function in vivo. *Proceedings of the National Academy of Sciences,* 107**,** 4716-4721.

Ye, J., Coulouris, G., Zaretskaya, I., Cutcutache, I., Rozen, S. & Madden, T. L. 2012. Primer-BLAST: a tool to design target-specific primers for polymerase chain reaction. *BMC bioinformatics,* 13**,** 134.

Yokosuka, T., Kobayashi, W., Sakata-Sogawa, K., Takamatsu, M., Hashimoto-Tane, A., Dustin, M. L., Tokunaga, M. & Saito, T. 2008. Spatiotemporal regulation of T cell costimulation by TCR-CD28 microclusters and protein kinase C θ translocation. *Immunity,* 29**,** 589-601.

Yoshida, Y., Kawata, M., Katayama, M., Horiuchi, H., Kita, Y. & Takai, Y. 1991. A geranylgeranyltransferase for rhoA p21 distinct from the farnesyltransferase for ras p21A. *Biochemical and biophysical research communications,* 175**,** 720-728.

Yount, J. S., Zhang, M. M. & Hang, H. C. 2013. Emerging roles for protein S-palmitoylation in immunity from chemical proteomics. *Current opinion in chemical biology,* 17**,** 27-33.

Yu, H., Chen, J. K., Feng, S., Dalgarno, D. C., Brauer, A. W. & Schrelber, S. L. 1994. Structural basis for the binding of proline-rich peptides to SH3 domains. *Cell,* 76**,** 933-945.

Yu, H., Rosen, M. K., Shin, T. B., Seidel-Dugan, C., Brugge, J. S. & Schreiber, S. L. 1992. Solution structure of the SH3 domain of Src and identification of its ligand-binding site. *Science,* 258**,** 1665-1668.

Yuan, K., Frolova, N., Xie, Y., Wang, D., Cook, L., Kwon, Y.-J., Steg, A. D., Serra, R. & Frost, A. R. 2010. Primary cilia are decreased in breast cancer: analysis of a collection of human breast cancer cell lines and tissues. *Journal of Histochemistry & Cytochemistry,* 58**,** 857-870.

Zhang, H., Constantine, R., Frederick, J. M. & Baehr, W. 2012. The prenyl-binding protein PrBP/δ: a chaperone participating in intracellular trafficking. *Vision research,* 75**,** 19-25.

Zhang, H., Constantine, R., Vorobiev, S., Chen, Y., Seetharaman, J., Huang, Y. J., Xiao, R., Montelione, G. T., Gerstner, C. D. & Davis, M. W. 2011. UNC119 is required for G protein trafficking in sensory neurons. *Nature neuroscience,* 14**,** 874.

Zhang, W., Sloan-Lancaster, J., Kitchen, J., Trible, R. P. & Samelson, L. E. 1998. LAT: the ZAP-70 tyrosine kinase substrate that links T cell receptor to cellular activation. *Cell,* 92**,** 83-92.

Zimmermann, L., Paster, W., Weghuber, J., Eckerstorfer, P., Stockinger, H. & Schütz, G. J. 2010. Direct observation and quantitative analysis of Lck exchange between plasma membrane and cytosol in living T cells. *Journal of Biological Chemistry,* 285**,** 6063-6070.